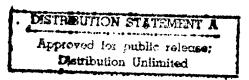
JPRS-CST-89-001 26 JANUARY 1989



JPRS Report



Science & Technology

China

16TH INTERNATIONAL CONGRESS OF THE INTERNATIONAL SOCIETY FOR PHOTOGRAMMETRY AND REMOTE SENSING--VOL I

DTIC QUALITY INSPECTED 3

19980528 130

SCIENCE & TECHNOLOGY

CHINA

16TH INTERNATIONAL CONGRESS OF THE INTERNATIONAL SOCIETY FOR PHOTOGRAMMETRY AND REMOTE SENSING--VOL I

Kyoto Selections from INTERNATIONAL ARCHIVES OF PHOTOGRAMMETRY AND REMOTE SENSING in English Vol 27, 1988 Parts Bl, B2, B4, B5, B6 and B7

CONTENTS

AEROSPACE

A New Holographic Inverse Filtering Method and Its Application to Restoration of Degraded Remote Sensing Images [Cao Haisheng, Chang Xiangqian]	1
A Bistatic Parasitical Radar (BIPAR) [Philipp Hartl, Hans Martin Braun]	11
A Practical Method of Remotely Sensed Digital Image's Resolving Power [Izumi Kamiya]	20
A Conceptual Study of Optical Earth Observation From Geosynchronous Orbit [Hajime Koshiishi, Kohzo Homma]	30
Modelling Orientation Parameters of Sensor Platforms [Joachim Lindenberger]	39
KRASA Danish High Resolution Airborne SAR [Soren Norvang Madsen, et al.]	48
Outline of MOS-1 Verification Program (MVP) [Korehiro Maeda, et al.]	58
Investigation of the Effectiveness and Applications of Japanese ERS-1 Stereoscopic Images [Nobuhiko Mori, et al.]	69

A Satellite Assisted-Tracking System With Real-Time	
Accommodation for Maximal Pointing [Jose Luiz de Barros Aguirre, Valder Matos de Madeiros]	80
Local Area Network and Data Network for the Advanced Earth	
Observing Satellite, ADEOS System	00
[Kohei Arai]	90
SAR Activities at Dornier	
[Hans Martin Braun, Gerhard Hans Rausch]	98
ERS-1 SAR Processing With CESAR	
[Einar-Arne Herland]	105
Jena Photogrammetric Instruments Manufacture From 1984-1988	
[Werner Marckwardt]	114
Experiences in Implementing an Expert System Supported Man-Machine-Interface for the Configuration of the	
Intollicent SAR Processor	
[W. Noack, et al.]	120
EXASExperiment on Autonomous SAR Processor Calibration	
[H. Runge, et al.]	132
Zeiss Digital MappingA New Hardware and Software System	
Concept From Kombinat VEB Carl Zeiss JENA	
[Wolfgang Wallwitz]	141
High Resolution Soviet Space Photographs for Topographic Mapping	
[Romuald Kaczynski, Jan Konieczny]	148
Map Production and Revision With Satellite Photographs Taken	
by the MKF-6 Camera and by the Cameras KATE-140, KATE-200,	
and KFA-1000	
[Joachim Kraemer]	154
An Expert System for Satellite Image Interpretation and	
C T S Resed Problem Solving	
[J. Desachy, et al.]	163
Photogrammetry: A Method for Three Dimensional Inspection	
of Equipment Inside Muclear Installations	
[Alain Martin]	176
National Report of Polish Society of Photogrammetry and	
Daniela Canada (Bordod: Ian 1980 - Dec 1987)	100
[Ryszard Florek, et al.]	183
A Comparison Between the Variability Structure of the Remotely	
Sensed Sea-Surface Temperature and Pigment Distributions	100
[Mati Kahrul	193

A Study on information Analysis Alds for Sea Surface Temperature Image Data	
[Hajime Koshiishi, et al.]	203
Interpretation of Remote Sensing Data From Eastern	
Areas of the Baltic Sea	
[J. Lokk, et al.]	209
Development of Borehole Scanner for Underground Geological Survey	
[Shunji Murai, et al.]	215
An Improving Multispectral Recording Set Analysis Method	
[Nicolae Oprescu, Constantin Borduselu]	220
Development of a Field Radiometer as a Ground Truth	
Equipment for the Japanese ERS-1	
[Yasushi Yamaguchi, Isao Sato]	231
Application of Aerial Side-Looking Radar Imagery in China	
[Yang Pinghe, Wang Lianke]	239

.

ı

A New Holographic Inverse Filtering Method and Its Application to Restoration of Degraded Remote Sensing Images

43070001a Kyoto Selections from INTERNATIONAL ARCHIVES OF PHOTOGRAMMETRY AND REMOTE SENSING in English Vol 27, 1988 pp 37-44

[Article by Cao Haisheng and Chang Xiangqian, Zhengzhou Institute of Surveying and Mapping, No 59 West Longhai Road, Zhengzhou, Henan, China; Commission I]

[Text] I. Introduction

The sharpness and resolution of the remote sensing images are limited by the image motion. In recent years, it was improved by the forward motion compensation. But in many cases, there are also many linear motion blur images. The a posteriori methods of degraded pictures can be categorized under two heads: (a) digital, (b) optical (analog). Digital methods, which are mainly computer assisted, have produced some excellent results and are commended for their ability to realize nonlinear transformations. But when the image to be processed has a large space-bandwidth product, digital techniques become difficult and expensive. This poses a serious limitation to the application of digital techniques. On the other hand, optical image processing is inexpensive and simple in comparison. But there are a serious limitations on the coherent optical image processing techniques: the low efficiencies, the small range of linear response of the filters and the coherent noise. To overcome this disadvantages, a new holographic inverse filtering system has been developed by the authors. The inverse filter is made by recording a hologram in the back of an attenuate mask 1/ |H| and then the filtering operation is done in multi-channel. The theoretical analysis and the experimental result are given.

II. Description of the Optical System

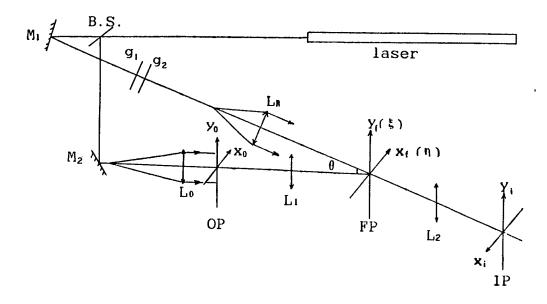


Figure 1. The Experimental System of Filter Generating and Image Processing

The optical experimental system is shown in Figure 1. The 65mw He-Ne laser is used as the coherent source: One bundle of beam splited by the beam spliter BS is collimated by lens L_0 and illuminates the object plane OP, the other beam splited is collimated by L_R and illuminates the filter plane FP at the angle θ as the reference beam. The intensity of the reference beam is controlled by a pair of polarizers g_1 and g_2 . The cameras L_1 and L_2 with focal length equal to 600mm are used as the Fourier transform lenses. The front focal plane of L_1 is the object (input) plane OP, the back focal plane is the filter plane FP, which is also the front focal plane of the lens L_2 .

In the image processing step, the reference beam is blocked. The deblurred aerial image is formed in the image plane IP (the back focal plane of L_2). The frequency of the grating used in this system is 40 lps/mm. The recording material is the Tianjing holographic I plate, its sensitivity is $3.0 \times 10^{-5} \text{J/cm}^2$.

III. Theory

The theoretical background of optical filtering is well known. However, for the sake of completeness, a brief outline of the mathematics involved is given as follows.

The formation of a blurred photograph (for that matter any photographs, blurred or sharp) can be described in general by the superposition integral

$$b(x,y) = \iint_{-\infty}^{+\infty} f(x',y')h(x,y;x',y')dx'dy'$$
 (1)

where f(x,y) and b(x,y) are the image and object intensity distribution respectively, and h(x,y) is the impulse response of the optical system. For certain types of blurs, which include linear motion of the camera under the assumption that the picture occupies only a limited region of the field. Equation (1) can be simplified to a convolution integral

$$b(x,y) = \iint_{-\infty}^{+\infty} f(x',y')h(x-x',y-y')dx'dy'$$
 (2)

In the Fourier plane, Equation (2) can be written as

$$B(\xi,\eta) = F(\xi,\eta) H(\xi,\eta)$$
(3)

where ξ , η are spatial frequencies in the x_f and y_f directions, and the B, F and H are the Fourier transforms of b, f and h respectively. By passing Equation (3) through a filter with transmittance proportional to $H^{-1}(\xi,\eta)$, we can recover $F(\xi,\eta)$ completely, provided H never goes to zero within the region where $F(\xi,\eta)\neq 0$. The operations of multichannel inverse filtering system are as follows.

A. The basic relations

In the filter-generating and image-processing steps, a grating, with spatial frequency \mathbf{p}_0 , is superposed on the transparency representing the PSF (point spread function) and on the transparency representing the blurred picture. The amplitude transmittance of the grating with lines running parallel to the \mathbf{y}_0 axis (perpendicular to the blurring direction) is described by a periodic function $\mathbf{g}(\mathbf{x}_0)$, which can be expressed as a Fourier series

$$g(x_0) = \sum_{n=-\infty}^{\infty} C_n \exp \left\{ j 2\pi n p_0 x_0 \right\} \qquad n=0, \pm 1, \pm 2,$$
 (4)

where the Fourier coefficients are given by

$$C_n = p_0 \int_0^{1/p_0} g(x_0) e^{-j2\pi n p_0 x_0} dx_0$$
 (5)

The amplitude transmittance of the grating and PSF transparency in contact is

$$h^{(p)}(x_0, y_0) = h(x_0, y_0) \cdot g(x_0)$$

its Fourier transform is

$$H^{(p)}(\xi, \eta) = \sum_{n=-\infty}^{\infty} C_n \cdot H(\xi - np_0, \eta)$$
 (6)

Similarly, the Fourier transform of the transmittance of the blurred picture in contact with the grating is

$$B^{(p)}(\xi, \eta) = \sum_{n=-\infty}^{\infty} C_n F(\xi - n p_0, \eta) \cdot H(\xi - n p_0, \eta)$$
 (7)

where we have applied the convolution theorem to Equation (2). Corresponding to the various diffraction orders of the modulating grating, the spectra of the PSF and blurred picture appears in a series of equally spaced islands in the filter plane, the amplitude distributions across each islands vary in proportional to the Fourier transform H and B respectively. The amplitudes of various islands, if compared at points corresponding to the same spatial frequency, are proportional to the Fourier coefficients of the amplitude transmittance of the grating.

In the following, we will assume that the functions h(x,y) and f(x,y) are band-limited in the x_0 direction, as expressed by

$$\frac{H(\xi, \eta) = 0}{F(\xi, \eta) = 0}$$
 for $|\xi| \ge p_0/2$ (8)

It is equivalent to requiring that various islands of the spectrum do not overlap.

B. The attenuating mask

Two parts are involved in the filter-generating step. The first is to get an absorptive mask with the amplitude transparency in proportional to $|\mathrm{H}^{(p)}(\xi,\eta)|^{-1}$, by recording the intensity distribution $|\mathrm{H}^{(p)}(\xi,\eta)|^2$. And then to make the filter by recording a hologram in the back of the absorptive mask $|\mathrm{H}^{(p)}(\xi,\eta)|^{-1}$, with the interference between a weak reference beam and the Fourier spectrum of $h^{(p)}(x,y)$.

In the object plane, the collimated beam transilluminates a transparency representing the function h(x,y) which is in contact with the transmission grating, the distribution of the Fourier spectrum plane is

$$H^{(p)}(\xi, \eta) = \frac{A_0}{i \lambda f} \sum_{n=-\infty}^{\infty} C_n \cdot H(\xi - np_0, \eta)$$
 (9)

where H is a normalized function, A_0 is the peak value of its zero order and λ is the optical wavelength. As a consequence of the band-limited condition (8), the terms in Equation (9) do not overlap, hence can be

squared individually and summed to yield $|\mathtt{A}^{(p)}(\xi,\eta)|^2$. The exposure for the mask $|\mathtt{H}^{(p)}|^{-1}$ can thus be written as

$$E_a(\xi, \eta) = \sum_{n=-N}^{N} E'_{an}(\xi - np_0, \eta)$$

where N is the highest order used in this system. The exposure of the n-th islands is

$$E_{an}^{\prime}(\xi - np_{0}, \eta) = \frac{\Delta t_{1} \cdot A_{0}^{2}}{\lambda^{2} f^{2}} \cdot |C_{n}|^{2} \cdot |H(\xi - np_{0}, \eta)|^{2}$$
 (10)

The amplitude transmittance of the n-th island of the mask, for the case of the ideal recording medium with a Gamma of 1 can be expressed

$$\tau_{n} = \frac{\mathbf{k}_{n}\lambda\mathbf{f}}{\sqrt{\Delta t_{1} \cdot \mathbf{A}_{0}}} \cdot \left| \mathbf{C}_{n} \cdot \mathbf{H} \left(\xi - n p_{0}, \eta \right) \right|^{-1}$$
(11)

where k_n is a constant which is related to the photographic techniques. Now we have got the attenuating mask $|H^{(p)}|^{-1}$.

C. The holographic inverse filter

As mentioned in section B, to make the filter, it is necessary to replace the attenuating mask $|\mathbf{H}^{(p)}|^{-1}$ into its recording position, and it is illluminated by the fields $\mathbf{A}^{(p)}(\xi,\eta)$ and the reference beam Rexp $\{-\mathrm{j}2\pi\xi,\chi_i\}$, ξ , is the spatial frequency of the reference beam. The mask attenuates the $\mathbf{A}^{(p)}$ and reference beam equally, the ratios between the two beams remain unchanged. Now we record the hologram in the back of the mask, the exposure to which the holographic plate in the plane (χ_f, y_f) is subjected is

$$E_{f}(\xi, \eta) = \left| (H^{(p)}(\xi, \eta) + R \cdot \exp\{-j2\pi\xi_{f}x_{f}\}) \cdot \tau(\xi, \eta) \right|^{2}$$
 (12)

 $\mathbf{E}_{\mathbf{f}}$ can be arranged and separated into two terms

$$E_{t} = \vec{E} + \vec{E} = \sum \vec{E}_{n} + \sum \vec{E}_{n})$$

$$\vec{E}_{n} = 1 + \lambda^{2} f^{2} \cdot (R/A)^{2} \cdot |C_{n}|^{-2} \cdot |H(\xi - np_{0}, \eta)|^{-2}$$
(13a)

$$\widetilde{E}_{n} = \frac{\lambda f R / A_{0}}{|C_{n}H|} \sin(2\pi \xi_{r} x_{f} + \Psi_{H_{n}} + \delta_{n})$$
(13b)

where \bar{E} is the d-c part of Equation (12), \tilde{E} is its a-c part, Φ_n and δ_n are defined as the phases of $H(\xi - np_0, \eta)$ and C_n respectively. R/A_0 is the ratio of the reference beam to object beam. Equation (13b) is the term of interest for the inverse filter. If the hologram with a perfectly linear recording medium (amplitude transmittance proportional

to exposure), the ideal amplitude transmittance corresponding to this term is

$$\tau_{fn} = \frac{\lambda \cdot f \cdot R / A_0}{C_n \cdot H} \exp\{-j2\pi \xi_r x_i\}$$
 (14)

D. The deblurring processing

During the image processing step, the blurred image and the grating are placed in contact, which yields an amplitude

$$B^{(p)}(\xi, \eta) = \frac{1}{j\lambda f} \sum_{n=-N}^{N} C_n \cdot F(\xi - np_0, \eta) \cdot H(\xi - np_0, \eta)$$
(15)

incident on the filter plane. The filter is placed precisely to the position where it is recorded. The amplitude component of interest transmitted by the filter is the term-by-term product of Equations (14) and (15)

$$F_{c}(\xi, \eta) = \sum_{n=-N}^{N} R/A_{0} F(\xi - np_{0}, \eta) \cdot \exp\{-j2\pi\xi_{r}x_{f}\}$$
 (16)

After the Fourier transform produced by L_2 , a filtered image appears in the (x_i,y_i) coordinates system. The amplitude in the image plane becomes

$$f_c^{(p)}(x_i, y_i) = r_0 \sum_{n=-N}^{N} f(x_i, y_i) e^{i2\pi n p_0 X_i}$$
 (17)

where all constant are collected in the complex amplitude r_0 . The deblurred image carries a grating structure, which can be removed by the band-pass filtering process.

Finally, linearity of the deblurring process with respect to irradiance is achieved by photographing the output with $Y = -\frac{1}{2}$, with this value of Y, the irradiance transmittance of the film is proportional to $f(x_0,y_0)$.

IV. Feature Analysis of the New System

The multi-channel inverse filtering system has many advantages.

1. The large dynamic range

The dynamic range (DR) of a hologram is defined as the largest range in which the amplitude transmittance is proportional to the exposure. The larger the dynamic range is, the higher the deblurring ratio of the inverse filtering system is. The deblurring ratio is the compression ratio of the blur width. For the absorptive filter, its dynamic range is restrained by straight part of the H-D curve. Because holographic

filter is attenuating light by diffraction, its dynamic range is restrained in the straight part of the t-E curve (the curve of transmittance vs exposure).

It is well-known that the holographic plate has a big Gamma. Therefore, its dynamic range is small. We find a special photographic processing technique which can make the quasilinear recording range to be 500:1, so the mask $|H^{(p)}|^{-1}$ does not affect the dynamic range of the inverse filter.

The small DR is a problem which has not been solved properly, because the capacity of the film is far from enough for the realization of linear holographic recording. So the effects of special photographic processing techniques are limited. The method reported here is to compress the exposure range with the aid of the attenuating mask, so the exposure that the film subjected is almost equal everywhere. It does not require the film to have a large linear region, therefore the filter generated by this system has a large dynamic range than that made by other methods.

2. The high efficiency

If the hologram is used as an inverse filter, the intensity of reference beam must be very small in comparison with that of the object beam. The weaker the reference is, the higher the deblurring ratio is. As general, if we want to get a good deblurring effect, we must choose a smaller ratio of the reference beam to the object beam, the modulations of the fringes are very low, so the efficiency of the filter is small. But in this new system, the inverse filtering function can be got automatically with the help of the mask. We only choose the ratio R/A_0 according to the linear recording condition, so we can get higher modulation interference fringes. The other methods cannot compare with this method in efficiency. And it is verified by experiments that there are big differences in efficiency if different photographic condition is used. So it is very important to optimize the recording and processing conditions.

3. The anti-noise property

The holographic system is damaged by various noise, especially the granularity noise due to random aggregations of the silver grains in the emulsion. Helstrom developed an expression for the optimum filter function, when random zero-mean, additive noise is present. As the criterion for best filtering, the principle of the least mean-squares is used in his derivation. The optimum filter function is

$$t = H^{-1} \frac{\phi_0 / \phi_n}{\phi_0 / \phi_n + 1/|H|^2}$$
 (18)

where ϕ_n/ϕ_0 are the power spectra of the noise distribution and the image respectively. He showed that the smaller the ϕ_n , ϕ_0 is, the stronger the noise is restrained. From part II we can give another form of our filter

$$t_{n} = \frac{2\lambda f R / A_{0}}{1 + (\lambda^{2} f^{2} R^{2} / A_{0}^{2}) / |C_{n} H|^{2}} \frac{1}{|C_{n} \cdot H|}$$
(19)

here $\phi_n/\phi_0 = \lambda^2 f^2 (R/A_0)^2 = 0.0014$ (for λ =6328A, f=600mm, $R/A_0 = 1/10$), it is very small. So the filter we have got is optimal with respect to the additive noise.

Another advantage of this system is that the output image is composed of N pictures. So the SNR of N-channel filtering system is increased by N times than that of a single one. The affection of the system noise is decreased greatly.

V. Experimental

The linear motion blur image (Figure 2a) simulated in the laboratory and the blurred remote-sensing image (Figure 2b) were processed by this system. The over all Gammas of two blurred images were controlled to be 2 approximately. So that their amplitude transmittances are proportional to the irradiation distributions of the blurred objects.

The image shown in Figure 2b was the deblurred one of Figure 2a using the 3-channel inverse filtering system. The sharpness of the restored picture was improved greatly and most of the details blurred was almost restored.

Figure 2 is the restored remote sensing image. In order to evaluate the capacity of the filtering system, we chose a part of the resolution test marks from an aero-photograph. From the ratio of ground speed to the flight height (V/H) of the aeroplane as well as other references the blur width was figured out, which was $100\mu m$. If we observe this photo directly, the sharpness of vision is good enough. But if it is measured at a high magnification, the visual effect and the measurement accuracy are very poor. Figure 3 was magnified by 5 times. From it we can find that the azimuth resolution is half of the cross track. In the restored image, the details of azimuth resolution test object can be distinguished, the sharpness is also improved. It can be seen that the restored image is still damaged by the coherent noise.

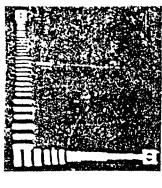


握克定技術 測繪現代化

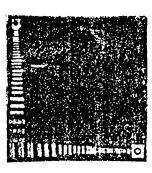
(a)

(b)

Figure 2. The blurred image simulated in laboratory: (a) the blurred image, (b) the deblurred image



(a)



(b)

Figure 3. The image of the resolution test target on an aero-photograph: (a) the blurred image, (b) the restored image

In many cases, the smear length of the filter is not the same as that of blurred image, our experiments showed that even the match error of the smear length is as high as 20 percent, the blurred image cna still be improved clearly.

VI. Conclusion

A new method is presented here in which the filtering operations take place in multi-channel at the same time. The filter generated by this system has a large dynamic range and high efficiency than that from other systems. As a by-product, the new filters can be prepared which are sufficiently efficient to significantly restore linear-motion blur images and other degraded images. So the optical image processing is one of the effective methods to improve the quality of the degraded remote sensing images. It is worth while to study further.

References

- 1. S. I. Ragnarsson, "A New Holographic Method of Generating a High Efficiency, Extended-Range Spatial Filter with Application to Restoration of Defocused Images," Phys. Scr. 2, 145 (1970).
- 2. Y. G. Jiang, Y. R. Xu, "Simple Method for Image Deblurring," Appl. Opt. 22, 784 (1983).
- 3. C. Zetzsche, "Simplified Realization of the Holographic Inverse Filter: A New Method," Appl. Opt. 21, 1077 (1982).
- 4. J. W. Goodman, "Wave-front Inversion Using a Thin Phase Hologram: A Computer Simulation," Appl. Opt. 23, 4575 (1984).
- 5. K. Biedermann, "A Function Characterizing Photographic Film That Directly Relates to Brightness of Holographic Images," Optik. 28, 160 (1968/69).
- 6. G. L. Cai, "The Problem of Resolution Matching in Aero-photographic System," Acta Geodetic et Cartographica Sinica 16, 121 (1987).
- 7. Helstrom, C. W., "Image Restoration by the Method of Least Squares," J. Opt. Soc. Am. 57, 297 (1967).

Abstract

This paper presents a new anti-noise inverse filtering system based on the work of predecessors. In this system the diffraction gratings are superposed on the point spread function (PSF) and blurred images to be restored on the input plane respectively. Then the multi-channel inverse filtering process is done on the Fourier spectrum plane. The SNR of N-channel processing system is increased by N times than that of a single one. In addition, the filter (1/H) is made in the back of an absorptive mask (1/abs(H)), and then the reference beam need not be too low, the modulation of the interference fringes of the filter is increased. Therefore, the filter with high efficiency and extended dynamic range can be achieved. The above mentioned advantages were verified by the theoretical analysis and the experimental results.

/09599

A Bistatic Parasitical Radar (BIPAR)

43070001b Kyoto Selections from INTERNATIONAL ARCHIVES OF PHOTOGRAMMETRY AND REMOTE SENSING in English Vol 27, 1988 pp 45-53

[Article by Philipp Hartl, University of Stuttgart and Hans Martin Braun, Dornier System, Friedrichshafen, FRG]

[Text] Abstract

After decades of remote sensing from aircrafts and satellites with cameras and other optical sensors Earth observation by imaging radars become more and more suitable because of their night and day and all weather operations capability and their information content being complementary to those of optical sensors. The major problem with microwave sensors (radars) is that there are not many of them presently in operation and therefore not enough data available for effective radar signature research for civil applications.

This paper shows that airborne bistatic real aperture radar receivers can be operated with spaceborne transmitters of opportunity. Famous candidates for those systems are high power communications or direct TV satellites illuminating the Earth surface with a power density of more than 10^{-12} Watt per square-meter. The high sophisticated status of signal processing technology today allows the realization of receivers correlating the received direct path signal from a communications satellite with its unavoidable reflection on the ground. Coherent integration can improve the signal to noise ratio up to values where the radiometric resolution can satisfy users needs.

The development of such "parasitical" radar receives could even provide a cost effective way to open up new frequency bands for radar signature research.

Advantages of these quiet systems for the purpose of classical radar reconnaissance are evident.

1. Introduction

Bistatic radars are defined as systems in which spatial separation exists between the transmitting and the receiving radar chain. The fundamental principles of bistatic surveillance radar systems have been known from the beginning of radar history. However, interest in them declined early, doubtless driven by the desire of users, particularly military users, to have radars capable of being operated from a single site. Therefore, up to now, monostatic radars have been developed to a very sophisticated state, whereas bistatic and multistatic radar systems laid dormant for about more than two decades. However, these systems received new interest, when the development of advanced radar processing techniques allowed bistatic radars to deploy their advantages.

2. The System Concept

A BIPAR is a bistatic radar system combining the advantages of spaceborne and airborne imaging radar systems. The transmitter is located in a geostationary orbit with a very low probability of intervention illuminating continuously the area of interest on ground. The quiet receiver is carried on an airborne platform implying a high mission flexibility, high repetition capability and less power requirements compared to a system with spaceborne receivers. It is called "parasitical" because it uses non-radar transmitters of opportunity, such as geostationary communications satellite transmitters or transmitters of direct television satellites. A typical system geometry is shown in Figure 1. A geostationary communications or direct TV satellite is transmitting its RF downlink signal to Earth. Within the beam of its downlink antenna it illuminates the Earth surface and a certain portion of the RF energy is unavoidably reflected back into the The strength of the reflection depends on the reflection coefficient of the target areas on ground, such as the vegetation canape, streets, houses, cars and so on.

An aircraft with a BIPAR receiver onboard, flying within the satellite downlink antenna beam picks up these reflections from the ground with a scanning pencil beam radar antenna and provides real aperture radar images of that part of the Earth surface being covered by the BIPAR scan range.

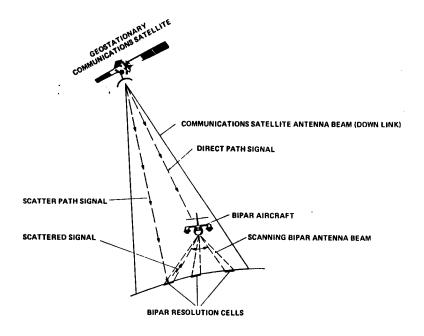


Figure 1. Typical BIPAR System Geometry

In case of a low downlink transmit power of the satellite resulting in a low power density on ground the received signal reflections are far below the BIPAR receiver noise level. Hence correlation with a known reference and coherent integration is required. The necessary reference signal can be provided by receiving the direct path downlink signal with an antenna on top of the aircraft. The differences in doppler shift and round trip delay time can easily be compensated because of its a-priory knowledge, if not-moving targets on Earth were of interest for the users.

The overall block diagram of a BIPAR receiver is shown in Figure 2. scattered signals are received via a scanning pencil beam antenna and routed through the Low Noise Amplifier and the Downconverter, which compensates the doppler shift of the scattered signals. After appropriate gain setting this noisy signal is fed to the coherent detector, where it is correlated with the respective reference signal. The reference signal, received via the telecom antenna on top of the aircraft is routed through a Low Noise Amplifier, a Downconverter compensating its doppler shift, and a variable delay line. The delay line takes care that the reference signal and the scattered signal arrive simultaneously at the detector (correlator) input. After integration, the signal is digitized and routed to the Radar Control Computer. This unit analyses the signals and derives the updates for the gain settings. In parallel, the signals are displayed in terms of a real aperture radar image and stored for further processing on ground. The doppler compensation and delay line control is driven by the Radar Control Unit based on data from the aircraft Position and Attitude

Sensor, on information about the satellite position and downlink frequency, and on the actual BIPAR pencil beam orientation.

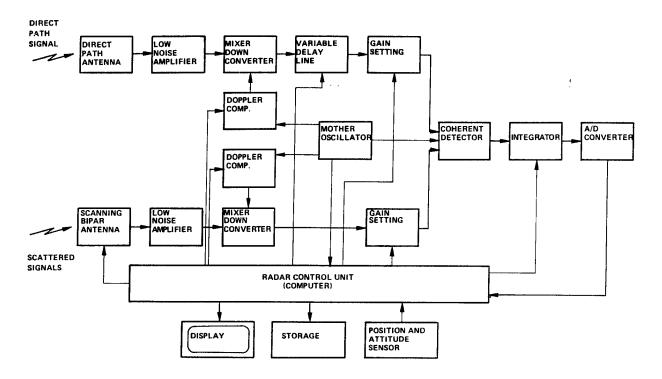


Figure 2. Block Diagram of a BIPAR Receiver

3. Performance Considerations

3.1 Radar Equation

Starting from a given signal power density \boldsymbol{p} on the Earth surface, the received power $\boldsymbol{P}_{\boldsymbol{R}}$ can be estimated by

$$P_{R} \approx \frac{p \, G_{R} \, \lambda^{2} \, \rho_{b} \, G_{i}}{(4\pi)^{2} \, H^{2} \, L_{p} \, L_{s}} \tag{1}$$

where G_R is the BIPAR receiver antenna gain, ρ_b is the bistatic radar cross section, G_i is the signal integration gain, λ the wavelength, H the flight altitude, and L_p and L_s are the propagation loss and other system losses.

The antenna gain ${\sf G}_R$ is a function of the antenna effective area ${\sf A}_R$ and the radar wavelength.

$$G_{R} \approx \frac{4\pi A_{R}}{\lambda^{2}} \tag{2}$$

The bistatic radar cross section $\,\rho_{b}^{}\,$ can be expressed by

$$\rho_{\mathbf{b}} = \delta_{\mathbf{A}} \delta_{\mathbf{E}} \sigma_{\mathbf{ob}} \tag{3}$$

and

$$\delta_{\rm A} \ \delta_{\rm E} \approx \frac{{\rm H}^2 \ \lambda^2}{{\rm A}_{\rm R}} \tag{4}$$

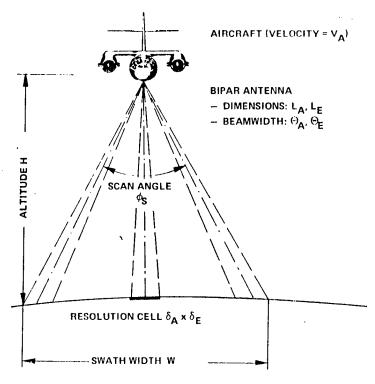
where δ_A and δ_E are the spatial resolution in azimuth and elevation and σ_{ob} is the normalized bistatic scatter coefficient.

The resulting equation for the received power of a BIPAR system indicates, that this power is moreless independent from the BIPAR pencil beam antenna dimensions and the aircraft flight altitude.

$$P_{R} \approx \frac{1}{4\pi} p \lambda^{2} G_{i} \sigma_{ob} \left(\frac{1}{L_{p} L_{s}}\right)$$
 (5)

This is due to the fact that changes in flight altitude and in antenna beamwidth implying loss and gain variations are compensated by resolution cell variations being consequently a result of the above changes.

3.2 Spatial Performance



N_p = NUMBER OF PIXELS IN ELEVATION (INTEGER)
N₁ = NUMBER OF INDEPENDENT LOOKS

Figure 3. BIPAR Scan Geometry

The spatial resolution of a real aperture BIPAR system is defined by the beamwidth of the scanning pencil beam antenna (see Figure 3). The nominal value of the spatial resolution in azimuth δ_A (flight direction) and elevation δ_E (perpendicular to flight direction) is defined at a scan angle of 0 degrees.

$$\delta_{A/E} \approx \frac{H \cdot \lambda}{L_{A/E}}$$
 (for Nadir) (6)

When the pencil beam is pointed to an outermost edge of the swath the spatial resolution is degraded to

$$\delta_{A_{\text{max}}} \approx \frac{H \cdot \lambda}{L_{A} \cos(\varphi_{S}/2)} \tag{7}$$

$$\delta_{E_{\text{max}}} \approx \frac{\frac{H \cdot \lambda}{L_{E} \cos^{n}(\varphi_{S}/2)}}$$
 (8)

where L_A and L_E are the effective antenna dimensions in azimuth and elevation, φ_S is the maximum scan angle between left and right edge of the swath and n is an integer value being n=2 for mechanical and n=3 for electronical scanning of the pencil beam. This difference considers a broadening of the antenna elevation beam toward the swath edges in case of electronical scanning.

The width of the BIPAR swath W is given by

$$W \approx H \left[2 \tan(\varphi_s/2) + \frac{\lambda}{L_E \cos^n(\varphi_s/2)}\right]$$
 (9)

and the available pixel integration time T_{i} is defined by

$$T_{i} \approx \frac{\delta_{A}}{v_{A} N_{p} N_{L}}$$
with $N_{p} \approx (\frac{\varphi_{S} + \Theta_{E}}{\Theta_{E}})$ and $\Theta_{E} \approx \frac{\lambda}{L_{E}}$ (10)

where v_A is the aircraft velocity, N_L is the number of independent looks required for improvement of the radiometric resolution, and θ_E is the antenna elevation beamwidth. The theoretical integration gain is defined by the time bandwidth product $T_i {}^{\bullet} B_{_S}$.

3.3 Radiometric System Performance

Applying the time-bandwidth product and the integration efficiency η_{i} equation 6 can be written as follows:

$$S = P_R \approx \frac{1}{4\pi} p \lambda^2 \sigma_{ob} T_i B_s \left(\frac{\eta_i}{L_p L_s} \right)$$
 (11)

where S is the received signal power and $\mathbf{B}_{\mathbf{S}}$ is the system bandwidth assuming a matched receiver chain.

The system noise power N is defined by

$$N = kT_{O} F_{R} B_{S}$$
 (12)

where k is the Bolzmann's constant, \boldsymbol{T}_{O} is the system temperature and \boldsymbol{F}_{R} the receiver noise figure.

The radiometric resolution ρ_R of an imaging radar is estimated by

$$\rho_{R} \approx 1 + \left(\frac{\left(\frac{S}{N}\right) + 1}{\sqrt{N_{L}} \left(\frac{S}{N}\right)}\right) \tag{13}$$

as a function of the number of independent looks ${\rm N}_{\rm L}$ and the signal to noise ratio being derived from equation 11 and 12.

4. System Example

The following example of a feasible system shall indicate the general capabilities of BIPARs.

The transmitter of opportunity could be an ECS-type communications satellite illuminating the Earth surface with a power density of -120 dBW per squaremeter or a direct TV satellite with about 10 times more output power. The transmit frequency is assumed to be about 11 GHz with a bandwidth of 27 MHz.

The BIPAR uses an electronically scanning antenna of 1 m x 1 m effective area with a scanning angle of plus or minus 30 degrees. It flies on an aircraft at 1000 m flight altitude with a velocity of 100 km/h. The scan repetition rate is 1 Hz. It is a step scan with 40 positions within plus or minus 30 degrees. At each beam position 3 independent looks are assumed resulting in an integration time per look of about 8.3 milliseconds. This leads to a coherent integration gain of 52 dB considering an integration efficiency of 70 percent due to the noisy scattered signal, its doppler spread of about 30 Hz, and misalignments within the time and doppler compensations.

Typical values for the scatter coefficients might be between -10 dB and +6 dB (one sigma) assuming that there is not much difference between 9.6 GHz and 11 GHz and between bistatic and monostatic systems. Under the umbrella of the German/Italian X-SAR project $\sigma_{\rm O}$ values have been researched intensively and these results could be used as a guideline for a preliminary BIPAR performance assessment.

Assuming furthermore a clear air propagation loss of 0.5 dB, a receiver noise figure of 6 dB, and a kTo of -204 dB/Ws, Table 1 shows that a signal to noise ratio between 0 dB and 19 dB could be reached. An overall margin of 3 dB for other systems losses is included in this calculation.

Table 1. Link Calculation

Power density (ECS)	-120 dBW/m³
$(1/4\pi)$	-11 dB
λ^2	-31.5 dBm²
o _o b	-10 dB thru +6 dB
Integration gain	52 dB
Propagation loss	-0.5 dB
(1/kTo)	204. dBWs
(-) Receiver noise figure	-6 dB
(-) System bandwidth	-74 dB/Hz
System loss margin	-3 dB
Signal to noise ratio	0 dB thru 19 dB

If a direct TV satellite is available as transmitter of opportunity the link budget will typically be improved by about 10 dB.

The performance of this BIPAR system based on ECS is summarized in Table 2.

Table 2. System Performance

Spatial resolution

	Nominal: Worst case at swath edges:	27 m x 27 m 31 m x 41 m
•	Swath width	1.2 km
•	Signal to noise ratio per look (for a o of -10 dB thru + 6 dB) ob	0 dB - 19 dB
•	Radiometric resolution for 3 looks	2 dB - 3 dB
•	Scan repetition rate	l Hz
•	Integration time per look	8 ms
•	Number of pixels in elevation	40

5. Conclusion

The objectives of this short paper have been to show that a relatively simple version of a bistatic radar system comprising an airborne real aperture radar receiver operating with the unavoidable ground reflections of geostationary communications satellite downlinks is capable to achieve a satisfactory system performance.

There are several system options under discussion comprising for example a mechanically steered or even fixed pointed antenna. The latter results in a simple 1 pixel system, where the swathwidth is provided by several parallel flights and the signal to noise ratio is improved by 16 dB due to a longer integration time per look.

Another system option is the leasing of one of the satellite transponders during BIPAR operations and the transmission of a cooperatively modulated communications signal. This could reject the need for the reference signal chain within the BIPAR receiver because the structure of the received signal is well known.

Last but not least, arrival time separation (range gating) and synthetic aperture principles (doppler gating) could be applied in order to improve the system performance once again.

All these options are up to further investigations and their viabilities are primarily driven by user requirements and available financial budgets.

Compared to classical monostatic and bistatic radars, it can be concluded that BIPAR systems have the following advantages:

- Low power consumption,
- High operational flexibility,
- Quiet and secret systems,
- Low cost.

BIPAR systems are typically not optimized with respect to radar applications, but they could provide a good compromise between user requirements, their need for a high amount of data, and funds available. BIPARs cannot replace large operational airborne and spaceborne radar systems, but in many cases they can support the scientific research, if no operational system was available.

/09599

A Practical Method of Remotely Sensed Digital Image's Resolving Power

43070001c Kyoto Selections from INTERNATIONAL ARCHIVES OF PHOTOGRAMMETRY AND REMOTE SENSING in English Vol 27, 1988 pp 64-72

[Article by Izumi Kamiya, Geographical Survey Institute of Japan, Kitasato-1, Tsukuba-shi, Ibaraki-ken, Japan, Commission I]

[Text] 1. Abstract

A method which decides resolving power of digital remote sensing sensor in field experiment was developed. It was applied to MOS-1 airborne verification experiment and predicted a resolving power of MESSR on MOS-1 satellite.

An outline of this method is following. An airphoto signal, refrectance of which is like step function, is laid slightly obliquely (angle θ) to perpendicular to flying direction and observed (Figure 1). It is equivalent to observing an object, radiance of which changes like step function, in various phases. A calculation method of PSF and MTF from the data was developed.

2. MOS-1 and MESSR

NASDA (National Space Development Agency of Japan) launched MOS-1 (Marine Observation Satellite 1) in 1987. Before the launching, NASDA conducted MOS-1 airborne verification experiment in order to test sensor equipment. GSI (Geographical Survey Institute of Japan) took part in the experiment, and evaluated resolving power of MESSR (Multi-spectral Electric Self-scanning Radiometer). It is a visible and infrared image sensor on the MOS-1. Table 1 is selected technical data of the MOS-1 and the MESSR.

The MESSR employed linear CCD (Charge Coupled Device) sensor like SPOT HRV. One of the most significant difference between linear CCD sensor and scanner (ex. LANDSAT MSS, TM) is following. Scanner samples incident light in IFOV (Instantaneous Field of View) in a moment. But CCD accumulates incident light in IFOV while satellite moves

corresponding length between two consecutive lines. So, the area that a detector observes changes during the accumulation. It contributes to lower resolving power in flying direction, but no contribution in perpendicular to the flying direction.

3. General Idea of the Method

In order to obtain PSF (Point Spread Function) in certain direction, it is enough to observe airphoto signal, refrectance of which changes like step function in the direction, in various locations of sensor relative to the edge. But it is impossible to design an airplane or satellite based experiment to fix a pixel to certain location. Also it is very difficult to observe the locations of pixeles in sub-pixel order. So, statistical processing of edge observation data, in which every locations were thought to appear in same probability, was used for field experiment to evaluate resolving power. But the statistical processing is not efficient usage of data.

In new method, an airphoto signal, refrectance of which changes like step function, is prepared. Now let us suppose to measure resolving power in flying direction. The airphoto signal is laid as its edge is slightly oblique to perpendicular to the flying direction. In this case, we can observe the edge in various locations of pixels in many columns. And the relative locations of the pixels in the flying direction to the edge (L_i) changes linear to the column number (i) (Figure 2).

$$L_{i} = c + d*i \tag{3-1}$$

Here, constant c is concern to only absolute geometric correction, and it is not important for our purpose. So if the airphoto signal is observed and the constant d is determined, it means that essential data to calculate PSF are obtained.

4. CCT-Column Curve

It is convenient to plot CCT count to column number i of pixeles included in a line near the edge (Figure 3). Let us call it CC curve (CCT-Column curve). Because the edge is straight, and because the image has little distortion in small area even if no geometric correction, observed image of line 1 is similar to one of line 1+1, and CC curves of the line 1 and 1+1 have similar figures. In other words, if the CC curve of the line 1 is transferred in column direction, it overlaps to one of the line 1+1. Using this fact, we can determine the constant d.

$$d = b/n (4-1)$$

Here, b is pixel size in line direction, n is number of columns to transfer in CC curve (real number).

5. Calculation Algorithm

Now, CC curve can be thought usual edge observation data, x axis of which is space coordinate in tangent to the edge, y axis of which is CCT count, supposing one column equal to length d = b/n. So, standard algorithm to calculate PSF from edge observation data can be applied. Radiance (R(x), relative vale) of airphoto signal is

$$R(x) = \begin{cases} Rb & (x < 0) \\ Rw & (x > 0) \end{cases}$$
 (5-1)

Here, x: space coordinate in tangent to the edge. the edge is corresponding to x = 0.

Rw: Radiance of black part of the airphoto signal. Rb: Radiance of white part of the airphoto signal. CCT count of observed image(I(x)) is expressed as following.

$$I(x) = \begin{cases} +\infty & R(x) * PSF(x-x') dx' \\ = Ib + (Iw-Ib) \begin{cases} x & PSF(x') dx' \end{cases}$$
 (5-2)

Here, PSF(x): Point spread function (normalized). Ib = $I(-\infty)$ = Rb : CCT count of the black part of the airphoto signal. Iw = $I(+\infty)$ = Rw : CCT count of the white part of the airphoto signal. Point spread function can be calculated from I(x)

$$PSF(x) = \frac{1}{Tw - Ib} \frac{d}{dx} I(x)$$
 (5-4)

Here, I(x), I_b and I_w can obtain from CC curve, i.e. PSF can calculate from only observed image data.

6. A Constraint Condition Formula

As for flying direction, PSF is broadened by the moving of the satellite through the accumulation as mentioned in section 2. A constraint condition formula on observed image I(x) will be derived. The effect of moving is expressed as follow.

$$PSF(x) = \int \frac{x+b/2}{x-b/2} PSFO(x') dx'$$
 (6-1)

Here, PSFO(x): PSF, assuming the sensor does not move.

Differentiating and using $PSFO(x) \rightarrow O(x \rightarrow -\infty)$, PSFO(x) can calculate from PSF(x)

$$PSFO(x) = \sum_{j=0}^{\infty} \frac{d}{dx} PSF(x-b/2-j*b)$$
 (6-2)

Using $PSFO(x) \rightarrow 0 (x \rightarrow +\infty)$,

$$\sum_{j=-\infty}^{+\infty} \frac{d}{dx} PSF(x+j*b) = 0$$
 (6-3)

As $|(d/dx)PSF(x)| \rightarrow 0$ ($|x| \rightarrow \infty$), (6-3) can be written in finite expression.

$$\sum_{j=-m}^{+m} \frac{d}{dx} PSF(x+j*b) = 0$$
 (6-4)

Here, m and x are supposed m>>b and x<<m.

Substituting (5-4) into (6-4) and integrating twice,

$$\sum_{j=-m}^{+m} I(x+j*b) = A*x + B$$
 (6-5)

Here, A and B are integration constant.

Subtracting (6-5) from (6-5) substituted x+1 in x, value of constant A can be calculated as A = I(x+(m+1)*b) - I(x-m*b) = Iw-Ib. So, (6-5) is expressed,

$$\sum_{j=-m}^{+m} I(x+j*b) = (Iw-Ib)*x + B$$
 (6-6)

This is the constraint condition formula for CCT count of observed image I(x) in flying direction.

7. Application to the MOS-1 Airborne Verification Experiment

The experiment was executed in 1984 winter and 1985 summer (Table 2). The oblique airphoto signals were placed on roof of GSI in the both experiment. Because adjustment of offset was too small in the winter experiment, CCT count of the black part of the airphoto signal (Ib) was 0. It meant that Ib could not be determined correctly, and that the data could not be used for the analysis. All MESSR images of the summer experiment including the airphoto signal were checked, and it appeared

that complete (continue from Ib to Iw) CC curve was obtained from only one image for PSF in the flying direction, and no image for perpendicular to the flying direction. The image was taken on September 6, 1985 (reference number MCC85-278-2). Following analysis was executed to the image. PSF and MTF of all bands were obtained in flying direction.

MESSR images had alternative vertical stripes, which were caused by existence of two shift registers in a semiconductor chip. First, radiometric correction was executed, assuming odd number detectors and even number detectors observed same sample (same mean and same standard deviation). The stripes were removed by the correction. Generally speaking, round error into integer was significant in processing of CCT data. So the CCT count was multiplied by 5 in this correction.

Actually, CC curve of any one line of the image was not complete. Partial CC curves were obtained from two lines 1 and 1+1. They had overlapping part, so n (number of columns to transfer) and d could be measured (Figure 4). The CC curve of line 1 was shifted n columns, and complete CC curve was synthesized. Here after, CC curve and observed CCT count I(x) express this synthesized one. What mentioned above as "complete CC curve was obtained" means these contents.

Next, the CC curve was smoothed. It really important process, because the curve would be differentiated. If there had been no smoothing, effective result had not been obtained because of noise (especially quantization noise). Observed values I(x) were not located in same distance in x coordinate of CC curve, because the curve was synthesized. It is convenient for following processing and application of the constraint condition (6-6) that observed values I(x) was interpolated into linear grid in same time. Distance of the grid (D) was selected near d and diving b (pixel size) into integer N (b=n*d=N*D).

The smoothing was executed minimizing sum of two terms (S) under the constraint condition. The first term was sum of square of difference between observed value and smoothed value. The second term was sum of square of second order differential of smoothed CC curve.

$$S = \sum_{j=1}^{J} (Is(x_{j}) - I(x_{j}))^{2} + W \sum_{k=1}^{K} (2*Is(x_{k}) - Is(x_{k-1}) - Is(x_{k+1}))^{2}$$
 (7-1)

Here, $I(x_j)$: Observed value(CCT count). Index of observed value. J: Number of observed values. Is(x_k): Smoothed observed value. Value of Is(x) was defined only on the linear grid, so it was linearly interpolated to x_j in the first term. Is(x_j =Ib (x_j =Ib (x_j =Ib (x_j =Ib (x_j =Ib) (x_j =Ib) should be determined. Index of smoothed observed value. K: Number of smoothed observed values. x_k : Grid point (x_k =(x_j =(x_j =1)*D+ x_j). Weight of smoothing.

The constraint condition formula (6-6) was transformed into discrete expression and applied.

$$\sum_{k=k0,k0+N,K0+2*N,...}^{M} Is(x_k) = (Iw-Ib)*D*k0 + B$$
 (7-2)

Here, M : The smallest multiple of N greater than or equal to K.
B : Constant.

 $KO: 1,2,\ldots,N.$

Formula (7-2) had N constraint conditions (the formula substituted k0=N+1 was equivalence to k=1). Canceling constant B, (7-2) has N-1 independent constraint conditions. Using Lagrange's method of undetermined multipliers, smoothed observed value $\mathrm{Is}(\mathbf{x}_k)$ were obtained by minimizing formula (7-1) under the N-1 constraint conditions (7-2). Using (5-4), PSF was obtained.

8. Estimation of PSF of the MESSR on the MOS-1 Satellite

The obtained PSF in section 7 was PSF of the MESSR on the airplane. If it had been PSF in perpendicular to the flying direction, or if the MESSR had employed scanner, PSF on satellite had been same without

effect of small angle scattering of atmosphere. But they were not same in this case.

Accumulation and sampling time interval of the MESSR was designed as long as the time to move an IFOV on satellite, i.e., pixel size in flying direction (b) is equal to an IFOV on the satellite. The same sampling interval was used in the air borne experiment, but speed height ratio of platform was different between from satellite. Actually pixel size b was much longer than an IFOV.

The estimation was executed in two steps. The first step transformed PSF from condition of speed height ratio of the airplane to stationary status using (6-2). The second step transformed PSF from stationary status to the ratio of the satellite using (6-1). In the second step, b of (6-1) should changed to a (pixel size in perpendicular to flying direction, it was equal to an IFOV), and unit of length should be interpreted as a is pixel size in satellite case. The ratio of a and b were obtained by measurement of the airphoto signal.

MTF was calculated from PSF by usual algorithm.

$$\mathtt{MTF}(\,\omega\,\,) \;=\; \mathtt{Norm} \;\int\; \mathtt{PSFs}(\,\mathbf{x}\,) \;\; *\; \mathrm{e}^{-\,\hat{\boldsymbol{\mathcal{L}}}\,\omega} \;\; \mathbf{x} \;\; \mathrm{d}\mathbf{x}$$

Here, MTF: Modulation transfer function. .

PSFs : PSF on satellite calculated by above method. Norm : Normalization constant (1 / PSFs(x) dx).

Figure 5 is obtained MTF of the MESSR on the MOS-1 satellite.

9. Conclusion

The practical method to obtain PSF and MTF of digital image sensor in field experiment was developed in this study. The method uses information of phase effectively by slightly oblique airphoto signal. This is the most excellent point of the method, which other methods do not have.

Following conditions of airphoto signal are very important for the method.

- (1) Refrectance of the airphoto signal shall change like step function.
- (2) Black part and White part of the airphoto signal shall be uniform, shall not be saturated in CCT count, shall have great difference in CCT count.
- (3) Edge of the airphoto signal shall be straight line.
- (4) Length of edge and oblique angle shall adjusted in order to obtain complete CC curve.

These conditions are so critical that it is difficult to use natural target instead of airphoto signal. In addition, smoothing mentioned in section 7 and measure against round error are very important, because quantization error cannot be ignored.

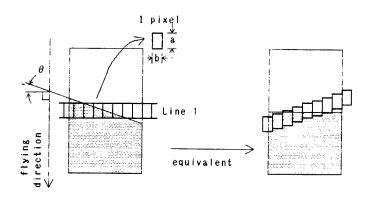


Figure 1. Basic Idea of the PSF Measurement

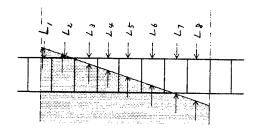


Figure 2. Relative Locations of Pixels to the Edge

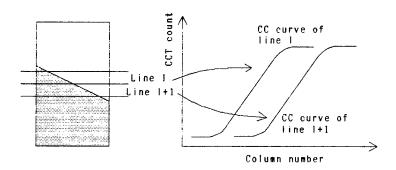


Figure 3. CC Curve of Line 1 and 1+1

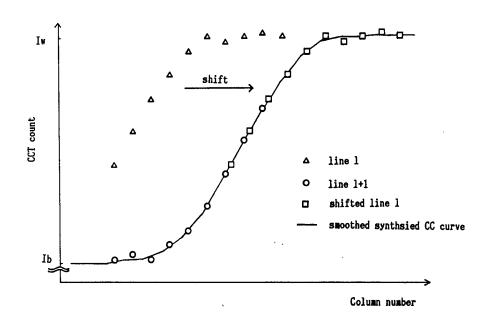


Figure 4. Synthesis of CC Curve

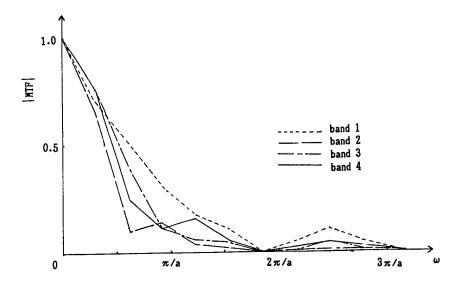


Figure 5. Estimated MTF of the MESSR on the MOS-1 Satellite

Table 1. Selected Technical Data of the MOS-1 and the MESSR

launching	Feb. 19, 1987	IFOV	$54.7 \mu \text{ rad}$ (50 m at ground)
orbit hight	909 km		64 (128 at the veri-
wave length	0.51-0.59(band1)	quantization levels	fication experiment)
(μ)	0.61-0.69(band2) 0.72-0.80(band3) 0.80-1.10(band4)	detector	2048 cells linear CCD
scan width	100km×2 systems	scan period	7.6 m sec.

Table 2. MOS-1 Airborne Verification Experiment

Place	Date	Hight
Tsukuba -	Nov. 22, 1984 Dec. 8, 1984 Dec. 13, 1984	1,000 m / 7,000 m
Kashimanada -	Jul. 18, 1985 Sep. 5, 1985 Sep. 6, 1985	1,000 m / 6,000 m

The airphoto signal was placed at Tsukuba. Experiment at other area is omitted.

/09599

A Conceptual Study of Optical Earth Observation From Geosynchronous Orbit

43070001d Kyoto Selections from INTERNATIONAL ARCHIVES OF PHOTOGRAMMETRY AND REMOTE SENSING in English Vol 27, 1988 pp 73-81

[Article by Hajime Koshiishi and Kohzo Homma, National Aerospace Laboratory, 7-44-1, Jindaijihigashi-machi, Chofu, Tokyo 182, Japan, Commission Number: I]

[Text] Summary

At first we assumed that requisitions of earth observation from geosynchronous orbit are 100 m spatial resolution at 1.1 µm wave length. Then design of telescope system had done with the Schmidt type telescope. The optical parameters of resulted design are 5 m focal length and 1 m aperture. Then we had introduced new scanning scheme: conical scan on image plane. Analytical calculation by wave optics had been done and it became clear that the 100 m spatial resolution can be get with very high OTF with this conical scheme.

Introduction

For various fields of earth observation, an observation from geosynchronous orbit is desired. For example, observation of climate condition and warning, ocean observation and forestry need geosynchronous earth observation satellite. Especially, the Japan islands are covered by clouds steadily and only for 80 days a year can be observed from remote sensing satellites. Therefore the observation from geosynchronous orbit will be particularly useful for the Japanese remote sensing users, nevertheless such a system is usually excluded because of the long distance and the imagined enormousness required for high resolution. If we use some catadioptoric telescope and conical scan scheme on the image plane, can get 100 m resolution with a comparatively small telescope system, and it is realizable even by existing technologies. We have done the conceptual design of the earth observing system from geosynchronous orbit applying a catadioptoric

telescope design. This paper presents the outline of the design studies.

1. To observe the Japan islands from the geosynchronous orbit

There are three schemes of FOV (Field of View) for observation the Japan islands from the geosynchronous orbit. The three schemes are shown in Figure 1, (a), (b) and (c). In the scheme of (a), a usual small circular FOV and scan are used to observe the total area of the Japan islands. That is, some slewing motion of satellite is needed. When the diameter of the FOV and mean distance between the geosynchronous orbit and the Japan islands are assumed to be 600 km and 38,000 km respectively, the angular FOV becomes to 0.9 degree. To utilize the Cassegranian telescope with parabolic primary mirror for this angular FOV may not be good design scheme because of various aberrations at the edge of FOV. This angular FOV may require the Ritchey-Chretien scheme. In the scheme (b) all of the Japan islands is put into one FOV and staring mode observation is possible and there is no need of slewing of satellite. Nevertheless the diameter of FOV may be 2,000 km and the angular FOV will be 3 degree. Assuming the aperture dimension of CCD element and the required ground resolution are 14 µm and 100 m respectively, then the focal length of telescope must be 5.32 m. aperture will be 1.32 m for F-number 5. It is very easy to get 3 degree of FOV by refractive system, but to do it with the focal length and the aperture diameter is not conceivable. On the other hand, this 3 degree of FOV imposes difficulty on Cassegranian reflective scheme. The Makstov type or Schmidt type catadioptoric schemes are only solutions for this telescope. The scheme (c) is a rather exotic scheme which uses the conical scanning on the focal plane. In this scheme the total Japan islands are imaged in some circular arc area of the focal plane as shown in Figure 1 (c). The optical axis of telescope points to somewhere of Chinese continent. To image islands from Hokkaido to Kyusyu, about 3.2 degree of FOV is required, and to image total islands including Okinawa island about 4 degree of FOV is required. According to similar consideration as scheme (b), the pertinent telescope is the Makstov or Schmidt type catadioptoric system. On the focal plane the image of Japan islands are formed along with concentric strips, on which all image points are focused best and have same optical performances.



Figure 1 (a). FOV for Observation From Geosynchronous Orbit

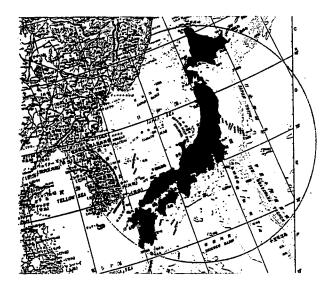


Figure 1 (b). FOV for Observation From Geosynchronous Orbit

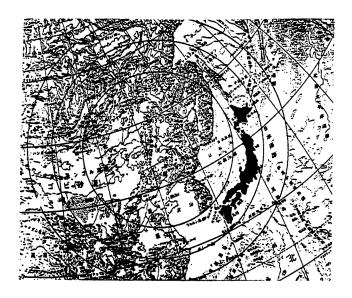


Figure 1 (c). FOV for Observation From Geosynchronous Orbit

2. Design of Schmidt telescope to observe the Japan islands with conical scan from geosynchronous orbit

2.1 The principle of Schmidt telescope

Figure 2 shows the basic principle of Schmidt telescope. S is a primary mirror with spherical surface, and C is an aspheric lens which called the correcting plate and positioned on the center of curvature of the primary mirror. The central part of this correcting plate is forming a convex lens, but the peripheral part is forming a concave lens and there is no power part between these two parts, which does not refract ray. The spherical aberration is removed completely by this correcting plate. Oblique light beam is symmetrical about the principal ray OA. Due to this symmetry there is no coma and astigmatism. The focal plane is spherical surface with 1/2 length radius of curvature compared to the primary mirror. That is, on the spherical focal plane we can get complete image without any aberration.

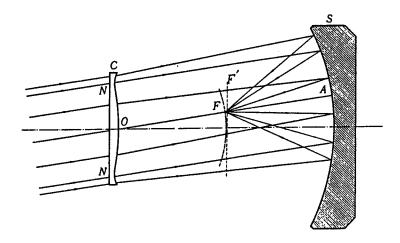


Figure 2. Principle of Schmidt Telescope

2.2 Calculation of optical parameters of the Schmidt telescope

We adopt the scheme (c) and put the image of Japan islands in the concentric strips on the spherical focal plane of Schmidt telescope. Then the projection of telescope FOV on the Earth's surface is a circle, which comes in contact with parallels of latitude 29 degree and 61.5 degree, and the center of FOV is projected on the parallel 45 degree and the distance from satellite on the geosynchronous orbit to the projected image center is $38,140~\rm km$ (cf. Figure 3). The focal length f, the distance between satellite and the center of FOV on the ground D, the spatial resolution on the ground Δx and the aperture of sensor element d are related in formula:



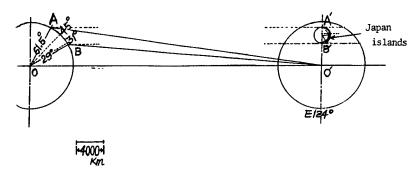


Figure 3. Telescope on Geosynchronous Orbit and Japan Islands

Figure 4 shows this relation with the parameter d. The most small photodiode size is about 7 μ m and usually 14 μ m size photodiode

elements are arranged in a linear array. So, two lines for $7 \mu m$ and 14 μm are shown in the figure. Spatial resolution of telescope is limited by diffraction. The aperture of telescope \emptyset , wave length λ , and an angular resolution Δw are connected as follows:

$$\Delta W = 1.22 \lambda/\phi$$

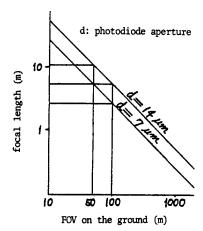


Figure 4. Relation of Focal Length and Ground Resolution

The limited ground resolution Δx_L is D. Δw , then, we have,

$$\emptyset = 1.22 \ \lambda D/\Delta x_{L} \tag{2}$$

Figure 5 shows this relation provided that D is 38,140 km and λ is 1.1 μ m.

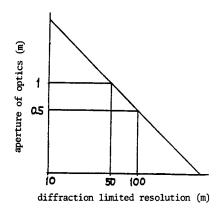


Figure 5. Aperture and Diffraction Limited Resolution

If 100 m ground resolution is required for the observing wave length 1.1 μ m and photodiode aperture 14 μ m, then we can say from Figure 4 and

Figure 5 that the focal length must be 5.35 m and the aperture of telescope 0.5 m at least.

If 50 m ground resolution is required for the same wave length and photodiode aperture, then 10.7 m focal length and 1 m minimum aperture are needed.

2.3 Shape of correcting plate

The shape of correcting plate of Schmidt telescope is given by following equations:

$$Z = \beta y^{4} - \alpha y^{2}$$

$$\alpha = \frac{k}{128(n-1)f - (F_{NO})^{2}}$$

$$\beta = K_{O} \left[1 - \frac{2k}{64(F_{NO})^{2}} \right]^{2}$$

$$K_{O} = \frac{1}{32(n-1)f^{3}}$$
(3)

Here, k is a parameter which determine the radius of neutral zone (no power part between the convex and concave parts), and n is an index of glass (cf. Figure 6). The radius of curvature of the primary mirror R is given by the equation:

$$R = f + \sqrt{f^2 + \frac{k\phi^2}{16}}$$
 (4)

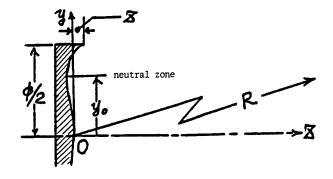


Figure 6. Difinition of Parameters on Correcting Plate

As above mentioned the minimum aperture of telescope for 100 m ground resolution is 0.5 m, however this diameter is required for diffraction limited resolution. If we take into consideration various degradation factors, for example the effect of atmosphere, imcompleteness of hardware system, we must extend the aperture a little more. Therefore, we assumed 1 m aperture as an actually required diameter of telescope. Another assumptions are the glass material BK-7 for correcting plate and 1.5 for parameter k which determines the radius of neutral zone. Then, utilizing equation (3), we can fix the parameters α , β and β as follows:

$$X = 3.68616 \times 10^{-8}$$

$$B = 3.92868 \times 10^{-13}$$

$$R = 1.06825 \times 10^{4} \text{ mm}$$

From these parameters, non-spherical coefficients of correcting plate are determined, and ray trace, aberrations, spot diagram and OTF are calculated.

3. Calculation of optical performances

Calculations of aberrations and OTF are performed by wave optics, so the calculated results will give physical insight of the system performances. Incidentally geometrical optics sometimes gives too superior results for such a reflecting system. The focal plane of Schmidt telescope is spherical as shown in Figure 2, F. The spot diagrams of on axis and semi-field angle 1.65 degree on this curved focal plane are shown in Figure 7, (a), (b) and the spot diagram at 1.65 degree on flat plane F' is shown in Figure 7, (c) for comparison. The former two spot diagrams are smaller than the assumed photodiode aperture 14 µm, but the latter spot diagram on flat plane is large extraordinarily. Figure 8 is the OTF for Figure 7 (b). It is clear that the OTF value at the cut off frequency of photodiode aperture 14 Am is about 0.67 for both tangential and sagital directions. This means that the conical scan utilizes the curved focal plane itself gives sufficient performance for 100 m spatial resolution from geosynchronous orbit.

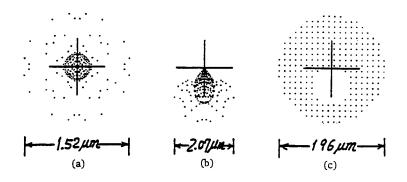


Figure 7. Spot Diagrams of Schmidt Telescope

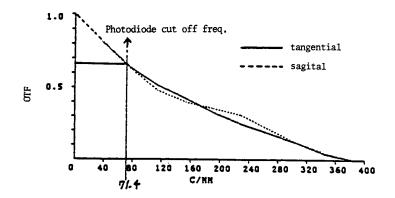


Figure 8. OTF of Schmidt Telescope

4. Conclusion

100 m spatial resolution at 1.1 µm wave length can be realized with good performance utilizing conical scan on the curved focal plane of Schmidt telescope. The diameter of the telescope is 1 m and the focal length is about 5 m. This dimension is rather small compared to the space telescope and it's realization is not so difficult. The observation from geosynchronous orbit is a staring type and sufficient integration time for signal will be obtained. By focal plane construction we can extend the image to surrounding sea area of the Japan islands and to other area, for example, the Chinese continent area.

References

1. Handbook of Optics, Optical Society of America, 1978, McGraw-Hill. /09599

Modelling Orientation Parameters of Sensor Platforms

43070001e Kyoto Selections from INTERNATIONAL ARCHIVES OF PHOTOGRAMMETRY AND REMOTE SENSING in English Vol 27, 1988 pp 82-89

[Article by Joachim Lindenberger, Institute of Photogrammetry, Stuttgart University, Keplerstr. 11, 7000 Stuttgart 1, Fed. Rep. of Germany, Commission I/3]

[Text] 1. Introduction

Recent advances in photogrammetry may be characterized by the introduction of computer technology into all photogrammetric procedures. The first link in such procedures, the primary data acquisition, plays an important role in this development, because the transformation of a classical photography into a computer readable format is a time-consuming and costly process. For this reason the substitution of the photo-chemical layer by photo-electrical sensors is the subject of current research. The three-line scanner and the airborne laser profiling system are two typical examples of the new sensor technologies which are mentioned here as the background to the studies presented in this paper.

Comparing modern scanners with conventional photogrammetry the main principles become obvious: the scanners provide less information per exposure, which must be compensated by a higher exposure rate. In consequence the exterior orientation parameters of the scanner platform must be determined with a higher rate. Closely connected to this point is the problem of a weak geometry of the scanner data. Single spot laser scanning represents an extreme. When only a single measurement is executed at every point of time, no geometric redundancy is obtained. Then the determination of the exterior orientation parameters is not possible in the conventional, indirect manner with the help of terrestrial control points. In this case the exterior orientation parameters must be directly measured by additional devices with a sufficient accuracy. These brief arguments explain why the direct measurement of the exterior orientation parameters of a modern sensor

platform and their consideration in the whole evaluation process is indispensable.

This paper presents a mathematical model describing the dynamic and stochastical properties of any time-dependent parameter. The evaluation of measured data takes full advantage of this model for the solution of a series of problems such as: stochastical description of the measurement process, filtering and smoothing of observations, detection of gross measurement errors, stochastical description of the filtered data. To summarize, the dynamic modelling of measured exterior orientation parameters provides filtered data with their stochastic properties for input into further evaluations of sensor data.

The measured orientation parameters represent a trajectory of the sensor platform, which is disturbed by the observation errors. As the observation errors are unknown, we are unable to reconstruct the true track of the sensor platform. An approach to the true movement will be found by the introduction of a model, which is built up here by the application of autoregressive integrated (ARI-) processes. The time-characteristic of each orientation parameter will be modelled by a specific representation of an ARI-process.

In chapter 2 the theoretical background of the time-series model will be outlined. Chapter 3 will present some applications of the theory:
1) modelling the position parameters of an aircraft flight measured by the Global Positioning System GPS, and 2) modelling the attitude parameters of an aircraft and of a space shuttle measured by an Inertial Navigation System INS.

2. Theoretical Background

2.1 Autoregressive integrated processes

Autoregressive integrated (ARI-) processes are a widely applied class of stochastic processes for various kinds of time-series (Haykin 1979, Kay and Marple 1981).

An autoregressive (AR-) process of order p describes a stationary timeseries \mathbf{x}_{+} by

$$x_t = -\sum_{i=1}^{p} a_i \cdot x_{t-i} + e_t$$
 $V(e_t) = \sigma_e^2$ (1)

The time-series considered in our applications are generally not stationary. These time-series have to be transformed into stationary time-series by the elimination of trends. A usual way is to take derivatives of the time-series. The autoregressive integrated process of order (p,d) is achieved if the d-th derivative of the original time-series can be described by a stationary AR(p) process. Formally, the

derivation can be expressed by an additional number d of process parameters a_i in equation (1). Then the ARI(p,d) process fully describes the dynamic behaviour of any orientation parameter by a number of (p+d) process parameters a_i and by the variance σ_e of the prediction errors.

2.2 The filtering algorithm

Two kinds of equations build up a Gauss-Markov model to estimate the filtered time-series \mathbf{x}_t from the observed series \mathbf{y}_t

$$E(y_t) = x_t \qquad V(y_t) = \sigma_n^2 \qquad (2)$$

$$E(e_t) = 0 = x_t + \sum_{i=1}^{p} a_i \cdot x_{t-i}$$
 $V(e_t) = \sigma_e^2$ (3)

Equation (2) expresses the observation process with σ_n 2 being the variance of the observation noise. Equation (3) presents the ARI model to which the unknown time-series x_t has to correspond.

The estimation of the filtered time-series x_t presumes the knowledge of the stochastic part of the Gauss-Markov model, i.e., the variances σ_n and σ_e . As the variances in general are a priori unknown, they must be estimated by applying the variance component estimation (VCE) technique. The formulation in the frequency domain published by Forstner (1984) is recommended for our application.

Together with the unknown ARI process parameters a_i we obtain a highly nonlinear estimation problem which can be solved in an iterative computation scheme (Lindenberger 1987). The conditions to be fulfilled by the data for successful solution of the GM model and the VCE are mentioned in the same paper (e.g., the variances σ_n ² and σ_e ² have to be of same order of magnitude).

Gross errors in the observations would disturb the validity of the GM model in equation (2). These gross errors are automatically detected and are taken into consideration by individual weights in equation (2). The weights are calculated following the robust estimation theory (Danish method, Krarup, et al. 1980). On the other hand, a robust treatment of equation (3) reduces the influences of edges and discontinuities in the data, which disturb the ARI model.

2.3 Capability of the algorithm

What are the main results from the algorithm? Under the assumption that the true trajectory of the sensor platform can be modelled by an ARI-process, we obtain a filtered data set \mathbf{x}_t which is the most probable representation of the true track. Together with the estimated ARI process parameters, several demands of further evaluation of the sensor data will be satisfied.

In addition, the ARI-model yields important results, relevant for the analysis of the stochastic model. The estimated variance of the observation noise σ_n ² describes the observation process. The variance of the prediction errors σ_e ² gives a fidelity measure how well the ARI-model is suited for the real physical process. The inversion of the normal equation system out of equations (2) and (3) provides accuracy criteria of the filtered data set, especially the variance of the filtered data σ_x ² and the autocorrelation coefficients r(h). It is emphasised here that all stochastic results are obtained without any a priori information.

Any systematic effects in the time-series, such as drifts of the orientation parameters with time, cannot be taken into consideration by the algorithm. For this reason the estimated accuracies must be understood not as absolute but as relative accuracies.

3. Applications

3.1 Position coordinates from NAVSTAR-GPS

The NAVSTAR Global Positioning System GPS enables the determination of the x,y,z position coordinates of one or more GPS receivers. The application of GPS is of particular interest in photogrammetry for the inflight positioning of the aerial camera. This reduces drastically the ground control requirements for aerial triangulation (Frieb 1986).

In the case of a stationary GPS receiver the accuracy estimation of GPS measurements is relatively simple due to the redundancy of the observations. In contrast to this, the application of a GPS receiver in a moving vehicle, such as an aircraft, renders the accuracy estimation more difficult or rather impossible if a non redundant satellite constellation (i.e., 4 satellites or less) is available or if an unsuitable receiver is used. Then the suggested algorithm with ARI-processes can be utilized for stochastic investigations.

As an example some results of an accuracy study on real GPS data are presented in the following. The data for the analysis originate from a photogrammetric test flight with a Sercel GPS receiver TR5SB carried out by the Survey Department of Rijkswaterstaat in the Netherlands on June 10th and 12th 1987 (D. Boswinkel, R. Witmer, J. W. v. d. Vegt 1988). The position coordinates in the earth-fixed WGS system derived from the primary phase measurements are subject of this analysis. Systematic effects which influence the determination of the coordinates are eliminated to a great extent in advance by simultaneous measurements with a second GPS receiver at a stationary reference point. Both receivers recorded with a registration rate of 1 measurement every 0.6 seconds. The data of the whole flight were divided according to the 6 photo-strips with about 130 registrations each. Only the data within

the strips are of interest and the aircraft then shows a very uniform kind of movement.

Each position coordinate is considered separately by it's own ARI-process. The mean ARI process order was found to be (5,2); so 7 ARI process parameters fully describe the model. The parameters of the stochastic model were estimated without any a priori information. In Table 1 the estimated standard deviations of the noise-component in the GPS coordinates are listed. The main result is that the internal accuracy of the positions determined from a moving GPS receiver is about 0.02 m.

Table 1:	Estimated noise	σ_n [m]	of GPS coordin	nates
Strip	Date	x	Y	Z
1	12.06.87	0.027	0.011	0.038
3	10.06.87	0.020	0.009	0.026
4	10.06.87	0.024	0.009	0.027
5	10.06.87	0.020	0.013	0.024
6	12.06.87	0.014	0.011	0.014
7	12.06.87	0.012	0.007	0.010
rms of s	trips 3,4,5	0.021	0.010	0.026
	trips 1,6,7	0.018	0.010	0.021

These results can be compared with an estimation of the internal accuracy out of the least squares adjustment of the GPS positions. The LS adjustment determines the weight coefficient matrix Q and gives in general an estimate of the weight unit sigma naught, i.e., the GPS range measurement accuracy. In the case of a moving GPS receiver observing 4 satellites the sigma naught value is not determinable because of the missing redundancy. Out of different consideration the range measurement precision of the Sercel receiver in dynamic application can be assumed reasonably to be $\sigma_0 = 0.006$ m. This value is twice as large as the precision obtained by a stationary receiver and depends mainly on the velocity of the aircraft. With this assumption the accuracies of the coordinates given in Table 2 are calculated (Frieb 1988).

Table 2: Estimated internal accuracy σ_n [m] of GPS coordinates from least squares adjustment with assumed range measurement accuracy of $\sigma_0 = 0.006$ m

	x	Y	Z
rms of strips 3,4,5 rms of strips 1,6,7	0.022	0.009	0.017
	0.020	0.009	0.020

Comparing the estimated internal accuracies from the ARI model in Table 1 without any a priori stochastic information and from the least squares adjustment with a priori knowledge of the sigma naught (Table 2), we note a very good agreement. It demonstrates that the ARI model is suited to be applied for modelling the dynamic characteristics of GPS coordinates during a photogrammetric flight and that the results are realistic.

All subsequent evaluation of the sensor data, for example the aerotriangulation, is based on the filtered GPS coordinates. These filtered data with their stochastic informations are achieved from the ARI-model. Table 3 summarizes the estimated accuracies of the filtered coordinates and their autocorrelation coefficients. It is an important result that in this example only the correlations from one to the next point (within 0.6 sec.) remain significant.

Table 3: Accuracy crite	ria of <u>filt</u> e	ered GPS dat	a
Estimated accuracies σ_x	of filtered	d coordinate	es [m]
	x	Y	Z
rms of strips 3,4,5 rms of strips 1,6,7		0.007 0.006	0.021 0.016
Correlation coefficients	s of filtere	ed data d=0	.6 sec
	x	Y	z
r(2d)	-0.06	0.69 0.11 -0.15	0.52 -0.01 -0.10

3.2 Attitude data from INS

Attitude data, i.e., the roll-, pitch- and yaw- angles of the sensor body axis to the terrestrial fixed coordinate system can be directly measured by an inertial navigation system (INS) belonging to the equipment of every larger aircraft. The evaluation of INS measurements is in most cases very difficult and depends essentially on the physical model which describes the systematic influences of a large number of physical effects.

The analysis of INS data presented in this chapter examine only the registered attitude angles. Any systematic drift effects caused by remaining errors in the gyros of the INS are not taken into consideration. For this reason the filtered attitudes cannot be estimated as absolute values, but must be rectified for the systematic drifts. Then the estimated accuracies of the measured angles are understood as the precision of one reading of the gyro.

The data for the analysis come from two different dynamic applications of INS. In the first example the attitude data of an INS from a NASA Space Shuttle mission are presented. The analysed data are registered during the metric camera experiment of the ESA/NASA's D1 Spacelab mission on 2nd December 1983. The registrations took place every 2 seconds, the angles are measured in degrees. The attitudes refer to the earth-fixed Greenwich True of Date system. The registrations were subdivided according to 21 photo-strips consisting between 120 and 800 points. As the estimated accuracies are very similar between the strips, only the root mean square values from all the strips are listed in Table 4.

Table 4: INS attitude data from Space Shuttle					
Estimated standard devia	tions in	[deg]			
	YAW	PITCH	ROLL		
observation noise σ_n ARI-model errors σ_e filtered data σ_x	0.0060 0.0019 0.0027	0.0048 0.0012 0.0027	0.0060 0.0014 0.0031		
Correlation coefficients	of filte	red data d=	=2 sec		
r(1d) r(2d) r(3d) r(4d)	0.71 0.46 0.18 0.13	0.62 0.39 0.10 0.13	0.67 0.47 0.15 0.13		

The mean ARI process order in this case is (6,1). The estimated accuracies are not very different between the three angles, so that a common measurement precision can be assumed. The estimated autocorrelation coefficients show a decrease within the first five seconds.

The attitude data of the second example are registered during an aircraft flight with a Litton LTN-72 Inertial Navigation System of a Falcon jet. The registration rate was 10 Hz. The characteristic of the aircraft flight is very different to the space shuttle flight, which is much more smooth. This is expressed by the ARI process parameters; here the ARI process order was only (2,2). The analysis refers to the central part of the flight, not disturbed by take-off and landing maneuvers. The results are presented here with reservation. Some discrepancies in the results caused by unsteadinesses in the aircraft trajectory are subject of further research. During undisturbed parts of the flight the standard deviation of the ARI-prediction errors $\sigma_{\rm e}$ decrease below 0.0001. deg.

Table 5: INS attitude data from aircraft				
Estimated standard devi	ations in	[deg]		
	YAW	PITCH	ROLL	
observation noise σ_n ARI-model errors σ_e filtered data σ_x	0.0023 0.0005 0.0011	0.0035 0.0013 0.0013	0.0030 0.0026 0.0017	
Correlation coefficient	s of filte	red data d	=0.1 sec	
r(1d) r(2d) r(3d) r(4d)	0.86 0.57 0.29 0.09	0.79 0.40 0.09 -0.07	0.80 0.41 0.08 -0.09	

The estimated observation noise σ_n is in full accordance with other investigations from a stationary INS of same type. In the stationary mode the precision of the attitude measurement is about four times higher than in the dynamic mode, which was expected in advance.

4. Conclusions

This paper introduced autoregressive integrated stochastic processes for modelling the dynamic characteristics of the exterior orientation parameters of a sensor platform. The ARI-Model in combination with a

variance component estimation enables the entire functional and stochastical description of the orientation parameters. The main advantages of this model are the easy handling, the low number of necessary ARI process parameters and the dispensation of any a priori information concerning the stochastical model.

The successful application of the ARI model to very different kinds of sensor orientation parameters improves the power of the concept. Comparisons to other methods for accuracy estimation demonstrate that the obtained results are realistic.

5. References

- Boswinkel, D.; Witmer, R.; v. d. Vegt, J. W. (1988): Utilisation of GPS in large scale photogrammetry; presented paper ISPRS Congress Kyoto Commission I.
- Forstner, W. (1984): Determination of the additive noise variance of observed autoregressive processes using variance component estimation technique; Schriftenreihe Heft 10; Institut fur Photogrammetrie Universitat Stuttgart.
- Frieb, P. (1986): The effects of camera position and attitude data in aerial triangulation--A simulation study; pres. pap. ISPRS Commission I Symposium: Progress in imaging sensors; esa SP-252 pp 101-111.
- Frieb, P. (1988): Empirical accuracy of positions computed from airborne GPS data; pres. pap. ISPRS 16th Congress Kyoto Commission I.
- Haykin, S. ed. (1979): Topics in applied physics vol 34: Nonlinear methods of spectral analysis; Springer-Verlag 1979.
- Kay, S. M.; Marple, S. L. (1981): Spectrum analysis--A modern perspective; proceedings of the IEEE, Vol 69, No 11, Nov 1981.
- Krarup, T.; Juhl, J.; Kubik, K. (1980): Gotterdammerung over least squares adjustment; pres. paper ISP Congress Hamburg Comm III, Int. Arch. of Photogr. Vol 23 B3, pp 369-378.
- Lindenberger J. (1987): Consideration of observation errors when modelling digital terrain profiles; Proceedings of the ISPRS WG III/3 International Colloquium: Progress in terrain modelling; TU Denmark Lyngby.

/09599

KRAS--A Danish High Resolution Airborne SAR

43070001f Kyoto Selections from INTERNATIONAL ARCHIVES OF PHOTOGRAMMETRY AND REMOTE SENSING in English Vol 27, 1988 pp 90-97

[Article by Soren Norvang Madsen, Erik Lintz Christensen, and Niels Skou, Electromagnetics Institute, Technical University of Denmark, Building 348, DK-2800 Lyngby, Denmark]

[Text] Abstract

The Electromagnetics Institute, the Technical University of Denmark, is presently constructing a C-band high resolution airborne SAR. The main purpose of the project, which is called KRAS, is to develop the knowledge base required to build advanced coherent radars. The paper will present the design rationale. The design of the radar is based on digital technology to the largest possible degree. This results in a very flexible radar system, with most of the system parameters being software controlled. Variable waveforms of bandwidths larger than 100 MHz and durations up to 20 $\mu \rm s$ can be generated. Calibration of the system has also been given much consideration, and design principles usually applied in radiometers have been implemented. The significant flexibility and the calibration is of major importance since the system is intended for applications ranging from medium resolution wide swath mapping, i.e., sea ice mapping or oil pollution surveillance, to high resolution narrow swath mapping for cartography or reconnaissance.

I. Introduction

The Electromagnetics Institute has been involved in the development of specialized radar systems for nearly 30 years. It all started when the Institute undertook the development of a 60/300 MHz radar sounder for measuring the thickness of the inland ice of Greenland and Antarctica [Gudmandsen, 1980]. In cooperation with a number of foreign institutes such as the Scott Polar Research Institute, U.K. and with the support from the National Science Foundation, U.S.A., the ice sounder has surveyed more than 200,000 km of bed-rock under the two major ice caps

of the world, and a thickness of up to 3.2 km was measured in Greenland and 4.8 km was measured in Antarctica.

Since then, a number of special purpose radars have been developed at the Electromagnetics Institute, e.g., a number of weather radars for measuring both horizontal and vertical distribution of rain. Other studies have involved marine radar systems and sea clutter studies [Maaloe, 1982], a coherent 1.5 GHz earth penetrating radar system, and design studies for the European Space Agency of planetary radars. Simultaneously passive microwave radiometers were developed.

Ten years ago the Institute modified a conventional incoherent marine radar so that it could be used as an X-band SideLooking Airborne Radar (SLAR). This system was improved a number of times and it was successfully used in a number of field experiments. In one of these experiments the system was modified to acquire HH and VV polarized images simultaneously. The system is today commercially available.

The Electromagnetics Institute's activities within the Synthetic Aperture Radar field started in 1977, where the breadbording of a real-time digital processor for a medium resolution airborne SAR was initiated [Sondergaard, 1977]. In 1982 a study of the basic properties of SAR images was initiated. This study involved speckle theory, procedures for estimating the power transfer function of the SAR system as well as postprocessing algorithms for edge detection and adaptive speckle filtering [Madsen, 1986], [Madsen, 1987]. This study also resulted in the development of digital off-line processors for both the airborne SAR-580 system and the SEASAT satellite SAR system. Since 1984 the Institute has also conducted a number of studies of the feasibility of using SAR for scientific and commercial sea ice mapping [Skriver, et al., 1986].

The project that will be described in this paper was officially commenced in January 1986. Its title is Coherent Radar Techniques and Advanced Signal Processing (KRAS). The formal goal of the project is to establish a Danish research group with a solid knowledge base within the field of advanced coherent radar technology and high speed digital electronics. The concrete goal is to fly an experimental high resolution airborne C-band SAR in 1989. However, the system holds so much flexibility, that it can accommodate more general experiments with coherent radars. Flexibility is given high priority in the design. It is expected, that the applications of the system will span from geophysical science, which require wide swath but only medium resolution, to mapping experiments that calls for the highest achievable resolution. It is also considered important, that the radiometric fidelity of the images is the highest achievable. Hence, special attention has been given to build in calibration loops in the radar and to some extent radiometer design techniques has been used to obtain the best possible component stability.

II. The KRAS SAR System

The radar is a single frequency system operating at 5.3 GHz. It is designed to obtain a resolution down to 2 m by 2 m. The maximum range of the system is 80 km and the swath width is between 10 and 50 km depending on the resolution. Both maximum range and swath width are prepared for later upgrading. It is expected that the initial experiments will involve an installation on a Gulfstream G-3 aircraft from the Royal Danish Air Force.

The KRAS system parameters are listed in Table 1 and the system block diagram is shown in Figure 1.

Table 1: KRAS System Parameters

Frequency:		5.3 GHz
Transmitter peal	c power:	2 kW
Receiver noise f	igure:	2.5 dB
Total system los	ses (estimated):	3 dB
Pulse length:		from 0.64 to 20 μs
Maximum bandy	width:	100 MHz
Antenna	gain:	27 dB
	azimuth beamwidth:	2.7 °
İ	elevation pattern:	20° section of cosec sqr. pattern
	polarization:	VV
Resolution	range:	Variable 2, 4, 8 m
	azimuth:	Variable 2, 4, 8 m
Slant range map	ping width:	Variable 9.3, 21.6, 46.2 km
Range:		80 km

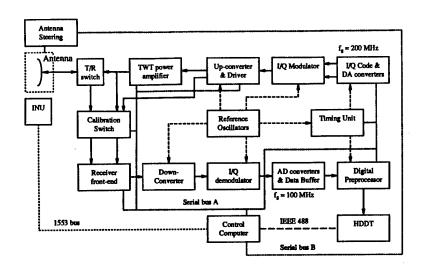


Figure 1. Block Diagram of KRAS Radar

The Control Computer is based on a VME data bus. The main control CPU's are based on the Motorola 68010 and 68020 processors. The Control Computer is linked to the individual subunits through two serial busses A and B. Bus A connects all "sensitive" units and is always shot down during echo reception. The Control Computer also includes IEEE-488, RS-232 and MIL-STD-1553 interfaces. Most of the radars subunits are also equipped with a number of BITE (Build In Test Equipment) facilities, which the Control Computer monitors. The Control Computer can initiate radar operation by down loading the code to be transmitted. The code can be up to 4096 samples long and each sample consist of 8 bit I and 8 bit Q data.

The digital codes are converted to analog signals at a 200 MHz sampling rate in dual DA converters and the analog I and Q channels are transformed to a 300 MHz IF signal in the quadrature modulator. up-converter the signal is converted to 5.3 GHz and the signal is amplified to a level sufficient to drive the TWT tube (22 dBm). 100 MHz, 300 MHz and 5 GHz local oscillator signals are generated in a reference oscillator unit, while 200 MHz is derived in the timing unit. Following the driver the signal is injected into the TWT power amplifier and a sample is directed into the Calibration Switch. The power level of the drive signal is controlled by a variable attenuator in a closed control loop. The power amplifier is a 2 kW Traveling Wave Tube amplifier with low phase noise. Following the TWT the signal is guided to the antenna. Both the power level of the signal injected into the antenna, and the signal reflected from the antenna is monitored using a -60 dB cross coupler. The reflected signal will shut down the TWT Electronic Power Conditioner (EPC) if the level is excessive.

The slotted waveguide array antenna consist of four separate panels to provide large bandwidth. Seven waveguides are stacked in elevation and the elevation pattern is shaped to give a modified cosecant squared illumination over a 40° sector, with sidelobes suppressed 24 dB. This is of major importance to insure that reflections from fuselage and wings will not give rise to two-way propagation, and thereby interference fringes.

The received signal is, after passing a solid state receiver protection unit, amplified by a low noise amplifier (LNA) with a noise figure of 2 dB, and following bandpass filtering a sensitivity time control (STC) is applied before the signal is down-converted to IF, hence limiting the dynamic range already at the RF level. At the IF level the signal is bandlimited and then the signal is down-converted to video in a quadrature I/Q demodulator. The I and Q signals are digitized to 8 bits per channel in dual AD converters running at a sampling rate of 100 MHz. The digitized echo is stretched to a high duty cycle signal in the data buffer, which holds 8192 complex samples, before the data flows into the digital preprocessor. The digital preprocessor performs Doppler tracking, initial motion compensation, and prefiltering of the data to reduce the effective pulse repetition frequency. A digital range filter that accepts complex data at a 100 MHz sampling rate facilitating programmable low-pass filtering and downsampling is presently being developed and this filter will be inserted between the AD converters and the buffers. Finally the signal is transferred to a HDDT system for later processing at the off-line facilities at the Institute.

III. The Digital Signal Generation System

The purpose of coding the transmitted pulses is in short that thereby a good signal-to-noise ratio and a fine resolution can be achieved simultaneously. There are many different coding schemes of which phase and frequency coding are most relevant to radars using power amplifiers in their saturated power range.

Originally it was planned to use SAW (Surface Acoustic Wave) dispersive filters for generation of linear FM pulses in the KRAS radar as well as for pulse compression in the receiver. It was soon realized that to obtain reasonable flexibility a number of pulse codes with different bandwidths and pulselengths were required. Likewise it was found that in situations where low sidelobes are required non-linear FM will give better performance than the usual linear FM chirp. However, since the SAW filters characteristics are fixed such flexibility can only be obtained by using a significant number of SAW devices. By using a digital data generation system it was found that the required flexibility could be supported by a single system.

Likewise the application of digital pulse compression in the receiver gives a number of advantages though at the expense of quite heavy processing requirements. The most important property is probably that

the dynamic range measured as the ratio between the largest point target and the noise floor is improved by the processing gain relative to the dynamic range of the AD converters themselves.

There are a number of ways to generate the digital codes and similarly there are several ways to transform the digital numbers to analog signals. Assume that the desired analog signal is:

$s(t) = a(t)\cos(2\pi f_{RF}t + \phi(t))$

(where a(t) will be an on-off keying and $\phi(t)$ is the phase modulation of the signal), then this signal can be generated by one of the systems outlined in Figure 2.

The system shown in Figure 2(A) implements a direct phase modulation on the RF carrier. Such a system is fairly simple and very attractive when phase codes with only few different phasors and moderate sidelobes are required. This coding process, however, introduces phase errors whose effect must be included in the design, [Iglehart, 1978]. Both Figure 2(B) and 2(C) use DA converters and low-pass filters to generate the modulation function, the main difference being that the one channel implementation (B) requires a digital carrier frequency which means that to generate signals of bandwidth B the sampling rate must be larger than 2 B. This implementation has been proposed for a simple pulse generator using a one bit DA converter [Johnston, 1984]. The quadrature modulator shown in Figure 2(C) generates the complex modulation function $m(t) = a(t)exp\{j\phi(t)\}\$ at baseband, and hence the DA converters need only a sample rate larger than B. The latter implementation is well suited for high bandwidth signals with low sidelobes and was therefore chosen for the KRAS signal generator.

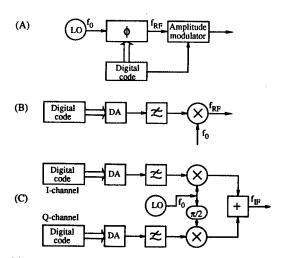


Figure 2. Digital Signal Generator Mechanizations: (A) RF phaseshifter, (B) Direct IF generator, (C) Quadrature baseband modulator

Also the digital codes can be generated in a number of ways. One method to generate the quadratic phase of a linear FM is for instance to implement a digital double integration of a constant, [Eber and Soule, 1975], [Postema, 1987]. By changing the constant the FM rate can be varied. Alternatively the pulsecode can be generated off-line and down loaded in a fast buffer memory. This approach gives significantly more flexibility and the software generating the codes can be designed to calculate non-linear FM with specified pulselength, bandwidth and sidelobe level. The price paid for this flexibility is that a fairly large and very fast buffer memory is required.

It is important to note that high quality signals with low sidelobes can only be obtained if the gain of the quadrature channels are equal and if the phase difference between the channels is 90°. Also the characteristics of the DA converted signals (i.e., digital signals have a periodic spectrum, and the "box" representation of the individual numbers in the code gives a sinc ($\pi\,f/f_s$ weighting of the spectrum) must be taken into account as well as other system components such as filters.

The KRAS digital signal generator is based on a quadrature modulator with the converters running at a 200 MHz sampling rate. The low-pass filters have a cut-off frequency of 150 MHz and a nearly linear phase characteristic. 4096 complex code words are stored in a RAM buffer, hence supporting pulses of a length up to 20 μs . The codes are generated by a C-program that supports both linear and nonlinear FM codes. This program also hold the capacity for incorporating predicted or measured system properties, by generating predistorted signals, so that the signal that drives the TWT will be correct. It is also intended to use the calibration system described below to perform online measurements of transfer functions thereby enabling dynamic predistortion if required. How this can be implemented is presently subject to a Ph.D. study at the Electromagnetics Institute.

IV. System Calibration

Calibration is a very important issue in modern remote sensing radars, especially when data from different radars or multitemporal data from one sensor are to be compared or if measurements have to be compared to models. Several precautions are taken in the KRAS radar design to enable fairly accurate system calibration. The main ingredients in the calibration of the KRAS radar are:

- 1) Design for maximum stability of the analog radar front end;
- 2) Internal calibration loops;
- 3) Accurate antenna calibration;
- 4) Comparison with a 5.3 GHz noise scatterometer.

First of all the stability of the system is ensured by applying design techniques usually applied in radiometer systems. One of the important

factors is that all RF components including the TWT+EPC will be temperature stabilized to an accuracy better than 1°C. Another important feature of radiometers is that of frequent automated calibration. This is implemented in the KRAS radar design by using a number of internal calibration loops. Both a sample of the TWT drive signal and the TWT high power output (sampled via a -60 dB cross coupler) is injected in the calibration switch. The calibration switch includes a programmable precision attenuator and an average power monitor, and the sample of the drive signal or the attenuated high power signal can be injected in the receiver either before or after the LNA. There is still some doubt whether the RF leakage can be kept sufficiently low to enable simultaneous calibration of the TWT and the LNA. All these measurement options are supported by the digital signal generator, that allow the transmission of extra calibration pulses concurrent with normal SAR operation.

The slotted waveguide antenna which is presently being developed will be calibrated in the Electromagnetics Institutes Radio Anechoich Chamber using spherical near field antenna measurement techniques. It will be attempted to include the antenna pod/radome in the measurements.

Finally the collected SAR data will be compared with data gathered with a C-band noise scatterometer that was recently developed at the Electromagnetics Institute, [Skou, 1987].

V. Project Status

The project is presently in the construction and test phase. The RF generator/calibration switch and the receiver have been finished and have passed initial tests. The TWT+EPC system will be integrated and tested mid 1988. The antenna system is presently being developed at the institute and measurements on test samples show good results, so the antenna construction and test is expected before the end of 1989. The control computer is presently in the software development phase. Major parts of the high speed digital electronics have been finished already. Integration and test will take place in the first half of 1989, and the first flight test will be carried out in the summer 1989.

The subsequent phase of the project, which includes real-time processing is planned to be finished late 1990.

It is finally noted that the funding for the project including the realtime processing has already been granted.

Extensions of the project might include polarometric measurement.

VI. Conclusion

This paper reports some features of the Danish KRAS radars design. The system is a C-band high resolution airborne SAR. The top level system

parameters and system block-diagram are presented. Two subjects of main concern in the design is maximum flexibility and system calibration. The flexibility has been achieved by applying digital technology to the largest possible degree. The transmitted pulses are coded in a digital signal generator that can generate any pulse modulation up to a maximal length of 20 μs . It is presently being studied how predistortion of the pulses can be used to compensate for different system errors. The calibration efforts have led to the inclusion of radiometer design techniques such as temperature stabilization and internal calibration loops. Other calibration tasks includes precision measurements on the antenna and comparison with the scatterometer system. The first test flights are expected in the summer 1989.

Acknowledgments

The KRAS research programme is supported financially by the Thomas B. Thriges Foundation. Without that support the project would not have been.

The authors would especially like to thank their colleagues A. Netterstrom, K. Woelders and A. Ostergaard for their contributions to the radar design.

References

Eber, L. O. and Soule, H. H., 1975; Digital Generation of Wideband LFM Waveforms, Proc, IEEE International Radar Conference 1975, pp 170-175.

Gudmandsen, P. E., 1980; Electromagnetic Studies of Ice and Snow, 2, Radio Echo Sounding in Proceedings of JRC seminar on Remote Sensing Applications in Agriculture and Hydrology, Ed. G. Fraisse, pp 401-416.

Iglehart, S. C., 1978; Some Results on Digital Chirp, IEEE trans. on Aerospace and Electronics Systems, Vol AES-14, No 1, pp 118-127.

Johnston, J. A., 1984; Generating Analogue FM Pulses Using a 1 Bit Digital Technique, IEE proc., Vol 131, Pt. F, No 4, July 1984, pp 349-356.

Maaloe, J., 1982; Sea Clutter Statistics, RADAR-82, IEE Conf. Publ. No 216, pp 193-197.

Madsen, S. Norvang, 1986; Speckle Theory, Modelling, Analysis, and Applications Related to Synthetic Aperture Radar Data, LD 62, Electromagnetics Institute, Tech. Univ. of Denmark.

Madsen, S. Norvang, 1987; Spectral Properties of Homogeneous and Nonhomogeneous Radar Images, IEEE trans. on Aerospace and Electronic Systems, Vol AES-23, No 4, pp 583-588.

Postema, G. B., 1987; Generation and performance Analysis of Wideband Radar Waveforms, RADAR-87, IEE Conf. Publ. No 281, pp 310-314.

Skou, N., 1987; A Very Accurate C-band Noise Scatterometer/Radiometer System, Int. J. Remote Sensing, 1987, Vol 8, No 11, pp 1717-1723.

Skriver, H., Gudmandsen, P. E., and Ulander, L., 1986; Active Microwave Observations of Sea Ice and Icebergs, Proceedings of the SAR Applications Workshop, Frascatti, Italy, 16-18 September 1986, ESA SP-264, pp 13-24.

Sondergaard, F., 1977; A Dual Mode Digital Processor for Medium Resolution Synthetic Aperture Radars, RADAR-77, IEE Conf. Publ. No 155, pp 384-390.

/09599

Outline of MOS-1 Verification Program (MVP)

43070001g Kyoto Selections from INTERNATIONAL ARCHIVES OF PHOTOGRAMMETRY AND REMOTE SENSING in English Vol 27, 1988 pp 98-108

[Article by Korehiro Maeda, Hiroyuki Wakabayashi, Kazuyuki Tasaki, Masanobu Shimada, and Hideo Sato, Earth Observation Center (EOC), National Space Development Agency of Japan (NASDA), 1401 Ohashi, Hatoyama-machi, Hiki-gun, Saitama-ken, 350-03, Japan, Commission I, presented at the 16th ISPRS held in Kyoto, Japan in July 1-10, 1988]

[Text] Abstract

Marine Observation Satellite 1 (MOS-1) was successfully launched from Tanegashima Space Center, NASDA by N-II launch vehicle at 10:23 JST (1:23 UT) on February 19, 1987. The MOS-1 has 4 mission instruments: (1) Multi-Spectral Electronic Self Scanning Radiometer (MESSR), (2) Visible and Thermal Infrared Radiometer (VTIR), (3) Microwave Scanning Radiometer (MSR), and (4) Data Collection System Transponder (DCST). All mission instruments were found to be satisfactory during mission check period (three months after the launch) though there was interference problem in DCS due to the outer radio interference source which was resolved by changing the frequency of Data Collection Platform (DCP).

NASDA planned and initiated MOS-1 Verification Program (MVP) to evaluate MOS-1 observation system since March, 1987. NASDA is conducting MVP in collaboration with joint research organizations, domestic and foreign organizations. As a part of the MVP, NASDA conducted airborne experiments in summer and winter in several test sites in FY 1987 in Japan on passing days of MOS-1 and will conduct summer airborne experiment in FY 1988. The first symposium for MVP was successfully conducted by NASDA on November 10 and 11, 1987 in Tokyo. The second symposium will be held in July 12, 13 and 14, 1988 in Tokyo Yubin Tyokin Kaikan in Hamamatsucho, Tokyo near NASDA Headquarter and the third final symposium will be held in February, 1989.

In this paper, the outline of MVP will be described and some initial results of MVP will be presented.

1. Introduction

NASDA developed space and ground segments of Marine Observation Satellite-1 (MOS-1) observation system and succeeded in launching the MOS-1 from Tanegashima Space Center by N-II rocket at 10:23 JST (1:23 UT) on February 19, 1987. This was launched into specified sunsynchronous orbit and called "Momo (Peach) 1". The MOS-1 carries 4 mission instruments (1) Multi-Spectral Electronic Self Scanning Radiometer (MESSR), (2) Visible and Thermal Infrared Radiometer (VTIR), (3) Microwave Scanning Radiometer (MSR), and (4) Data Collection System Transponder (DCST). It was confirmed that all mission instruments are very good during mission check period (three months after the launch) though DCS suffered from harmful radio interference due to outer source which was eliminated by changing the center frequency of Data Collection Platform (DCP).

In order to evaluate MOS-1 total observation system, NASDA planned and initiated MOS-1 Verification Program (MVP) since March, 1987. NASDA is conducting MVP in collaboration with joint research organizations, domestic and foreign organizations. As a part of MVP, NASDA conducted airborne experiments on MOS-1 passing days in 1987-1988.

In this paper, the outline of MVP will be described and the some initial results of MVP will be presented.

2. The Outline of MVP

Main mission objectives of MOS-1 are to establish fundamental earth observation technology and to observe ocean, land and atmosphere by using three radiometers (MESSR, VTIR, MSR) covering visible, near-infrared, thermal infrared and microwave wavelengths.

In order to achieve these mission objectives and to evaluate MOS-1 observation system, NASDA conducted field experiments by using MSR breadbord model (BBM) on the ground, tower and others in 1981-1983, airborne verification experiments by using MOS-1 sensor engineering model (EM) mounted on an aircraft in 1984-1985. Based upon these experiments NASDA planned MOS-1 Verification Program. The content of the MVP is shown as follows.

2.1 Purpose of MVP

Purpose of the MVP is as follows:

(1) Evaluation of geometoric and radiometoric distortion compensation accuracy;

- (2) Evaluation of performance of MOS-1 observation system;
- (3) Evaluation of effectiveness of MOS-1 observation parameter from various fields of remote sensing;
- (4) Reflection of the above results in the development and operation of advanced earth observation system in the future.

2.2 Methodology of MVP

In order to evaluate MOS-1 observation system, MOS-1 data, airborne data, truth data, other earth observation satellite data are required in the framework of the MVP.

Verification items of MVP are classified into (1) verification for instrumentation and (2) verification for physical measurement. The former is evaluation of geometric and radiometric performance such as various distortion, spatial resolution, signal to noise ratio (S/N), dynamic range. The latter is evaluation of physical measurement accuracy. These verification items are shown in Table 1. The MVP consists of the following activity.

(1) Verification experiment

Based upon field experiments in 1981-1983 and MOS-1 airborne verification experiments in 1984-1985, NASDA conducted MVP airborne experiments in summer, 1987, in winter, 1987 and 1988, and NASDA will conduct airborne experiment in coming summer, 1988. Figure 1 shows the schedule of MVP. In these airborne experiments, aircraft Merlin IV A flys over several test sites in Japan on MOS-1 passing days where observation equipments equivalent in performance to MOS-1 sensors are mounted and comparison between MOS-1 data, airborne data and truth data is made. Table 2 shows outline of MVP airborne experiments and Figure 2 shows test sites for MVP airborne experiments.

(2) Routine-base verification

MOS-1 data is evaluated routinely by using various processing and analyzing software installed in MOS-1 processing facility.

(3) Overall evaluation

Based upon test results in the laboratory obtained before the launch, results obtained during mission check period and results for compatibility test, considering the above-mentioned (1) and (2), overall evaluation must be made.

2.3 Cooperative relationship

In order to evaluate MOS-1 observation system from various point of view, NASDA is conducting the MVP in collaboration with joint research organizations, domestic and foreign organizations which were selected at MOS-1 verification committee. The selected organizations and themes are domestic 60 organizations 73 themes foreign 11 countries (Belgium, Canada, France, India, Italy (ESA), Korea, Philippines, Singapore, Sri Lanka Thailand, U.S.A.) 17 organizations 22 themes.

3. Initial Results

3.1 MESSR

The MESSR is an electronic-scanning radiometer using CCD detector elements with the four bands (1) 0.51-0.59 μ m, (2) 0.61-0.69 μ m, (3) 0.72-0.80 μ m, and (4) 0.80-1.1 μ m. Nominal spatial resolution is 50 m. The main mission objectives of the MESSR is to observe land surface and sea conditions such as transparence.

(1) Radiometoric distortion compensation evaluation

In case of radiometrically corrected imagery (level 1), it was confirmed that residual radiometric distortion (RMS of the difference of neighboring intensity) were 0.75, 0.67, 0.25, 0.38 for band 1, 2, 3 and 4 which meet the one quantized level.

(2) S/N evaluation

By applying the two dimensional Fourier transformation to uniform area such as snow field, S/N are 24.0, 24.7, 24.0, 21.5 dB for band 1, 2, 3 and 4, respectively.

(3) Geometric distortion compensation evaluation

The geometric compensation accuracies measured by using 8-10 GCPs 4.7 km, 46 m, 17 m for level 2, 3 and 4 were obtained which is under the specified value 7.5 km, 50 m, 25 m for level 2, 3 and 4. By eliminating bias error of attitude, the position error for level 2 decreases to be 666 m.

(4) Spatial resolution evaluation

By using edge in reclaimed land in Tokyo Bay, line spread function (LSF), modulation transfer function (MTF) were obtained. Example of MTF is shown in Figure 3. In Japan it is very difficult to find uniform area neighboring to edge. So, it is necessary to develop method applicable to non uniform area.

3.2 VTIR

The VTIR is a mechanical scanning type radiometer to observe in one visible (band 1:0.5-0.7 μ m) and three thermal infrared bands (band 2:6.0-7.0 μ m, band 3:10.5-11.5 μ m, band 4:11.5-12.5 μ m). The nominal spatial resolution is 900 m for band 1 and 2700 m for band 2, 3 and 4. The main objective of VTIR is to observe sea surface temperature, cloud, upper atmosphere and others.

(1) Radiometric distortion compensation evaluation

By comparing VTIR data and VISSR data for uniform sea, it was confirmed that radiometoric distortion is under two quantized level. When VTIR thermal band was evaluated by using standard black body, this distortion was found to be under one quantized level.

(2) S/N evaluation

Three methods: Mean-deviation method, APR (Adaptive Peak Rejection) method and one dimensional Fourier transform method were applied to VTIR data in uniform sea area to obtain S/N. By using mean-deviation method, S/N are 20.2 dB, 33.6 dB, 43.2 dB and 42.9 dB for band 1, 2, 3 and 4, respectively. It was confirmed that S/N for band 3 is larger than that for band 4. This is because atmospheric transparence is larger in band 3 than in band 4 and S/N of VTIR hardware measured in the factory was larger in band 3 than in band 4.

(3) Geometric distortion compensation evaluation

By using 20 GCPs in one pass scene, position error of level 2 imagery was measured to be $3.1-4.7~\rm km$ which is under specified value 7 pixels (6.3 km).

(4) Spatial resolution evaluation

By using edge of coast, spatial resolution was measured as follows:

	line direction	pixel direction		
Band 1	1.4 pixel	3.3 pixel		
Band 3	3.0 pixel	4.8 pixel	_	
Band 4	3.3 pixel	5.4 pixel	1	pixel:900m

In case of band 2, spatial resolution cannot be obtained because earth surface cannot be observed. Concerning thermal band (Band 2, 3, 4), three pixel is nominal spatial resolution.

(5) Sea surface temperature extraction evaluation

LOWTRAN 6 was applied to VTIR thermal band imagery (path 21, May 31, 1987) and the following results were obtained.

	level 2 data	Atmospheric data	compensated	Truth data	
Band 3 17.85 18.00	Band 4 16.40 16.35	Band 3 19.65 20.50	Band 4 18.85 19.35		(Omaezaki) (Oshima)

Remark: Radio sonde data was used. unit: °C

3.3 MSR

The MSR is a Dicke type radiometer to measure very weak earth radiation noise at the 23 GHz and 31 GHz. Beam width of MSR is 32 km (23 GHz) and 23 km (31 GHz). Main nission objective of the MSR is to measure water vapor and liquid water, snow cover, sea ice distribution.

(1) Radiometric distortion compensation evaluation

By measuring mean and standard deviation in level 2 imagery, the following results were obtained.

23	GHz	10msec	1.14	K
23	GHz	47msec	1.13	K
31	GHz	10msec	1.33	K
31	GHz	47msec	1.30	K

In case of evaluation of internal calibration source, the $0.579~\rm K$ (23 GHz) and $0.616~\rm K$ (31 GHz) were obtained.

(2) S/N evaluation

S/N for MSR imagery (path 21, April 10, 1987) are as follows:

23	GHz	10msec	36.1	dΒ
23	GHz	47msec	37.7	dΒ
31	GHz	10msec	32.2	dΒ
_		47msec	32.5	dΒ

(3) Geometric distortion compensation evaluation

Position error is measured by using GCPs in one path scene and mean value of this error is 25 km (23 GHz) and 17 km (31 GHz) which is under the specified value 60 km (23 GHz) and 40 km (31 GHz).

(4) Spatial resolution evaluation

By using edge of coast, the following results for MSR imagery (level 2, path 25, April 14, 1987) were obtained.

	pixel direction	line direction
23 GHz 10 msec	64.6 km	74.6 km
23 GHz 47 msec	63.1 km	68.4 km
31 GHz 10 msec	43.7 km	48.0 km
31 GHz 47 msec	49.0 km	45.6 km

3 dB down width

(5) Physical value extraction evaluation

a) water vapor and liquid water

By using recurrence equation developed for extraction of water vapor and liquid water, the following results were obtained.

	May 27,1987	Nov.29,1987
Water vapor	55.2 (43.7)	43.6 (31.8)
Liquid water	1.2	1.1

unit:kg/m

():truth data obtained by using radio sonde data in Titizima (very distant small island in Pacific Ocean)

It was found that bias error was about 10 kg/m. It is necessary to accumulate MSR data from now on.

b) typhoon, front, rain

Example of front, rain region and typhoon were observed in MSR data obtained in path 21, April 27, 1987, path 25, April 4, 1987 and path 24, August 27, 1987, respectively. Rain region obtained by using MSR data corresponds with the region obtained by using rain radar.

c) sea ice

Example of sea ice was observed through cloud in MSR data obtained in path 21, April 10, 1987. Since sea brightness temperature of sea ice is very high, sea ice distribution can be obtained under all weather condition. MSR data is routinely used to forecast drift sea ice in northern ocean of Hokkaido.

3.4 DCS

The DCST transponds data from buoys to Earth Observation Center, where the position of the buoys are determined utilizing doppler frequency measurement. Bit error rate, position estimation error and DCS success rate are 7.3×10 , 500 m and 90 percent. Transmitting frequency of DCP was changed from 401.53 MHz to 401.47 MHz to prevent from outer radio interference.

4. Conclusion

As a result of initial evaluation of MOS-1 data, MOS-1 observation system was found to show satisfactory condition. NASDA continue evaluation in collaboration with domestic and foreign investigators.

Acknowledgment

The authors would like to thank investigators who participated in the MVP and related staff in NASDA.

References

- 1. Announcement of Opportunity for MOS-1 Verification Program, National Space Development Agency of Japan (NASDA).
- 2. K. Maeda, et al., "Airborne observation experiments for MOS-1 Verification Program (MVP)," Proceeding of the fifteenth International Symposium on Space Technology and Science (ISTS), pp 1659-1670, Tokyo, 1986.
- 3. K. Maeda, et al., "Geometric and radiometric performance evaluation methods for Marine Observation Satellite-1 (MOS-1) Verification Program (MVP)," Acta Astronautica, Vol 15, No 6/7, pp 297-304, 1987.
- 4. K. Maeda, et al., "Some results of MOS-1 airborne verification experiment-Multispectral Electronic Self-Scanning Radiometer (MESSR)," IEEE Transactions on Geoscience and Remote Sensing, Vol 25, No 6, pp 788-795, Nov 1987.
- 5. K. Maeda, H. Wakabayashi, and H. Sato, "Some results of MOS-1 airborne verification experiment-MSR (Microwave Scanning Radiometer).

Table 1. Verification Items for MVP

Γ	Multispectral Electronic Self-scanning Radiometer (MESSR)		Visible and Thermal Infrared Radiometer (VTIR)		Microwave Scanning Radiometer (MSR)		Data Collection System (DCS)	
_	Verification Item	Parameters	Verification Item	Parameters	Verification Item	Parameters	Varification Item	Parameters
Verification for Instrumentation	11	Deviation of CCD sensitivity Input/output performance Image quality evaluation	21 Radiometric performance	Temperature resolution Input/output performance Image quality evaluation	31 Radiometric performance	Receiver sensitivity Input/output performance Effect of antenna pattern Image quality evaluation	41 Transmission performance	Transmission quality Multiple accessibility
	12 Geometric performance	Accuracy of distortion correction Spacial resolution	22 Geometric performance	Accuracy of distortion correction Special resolution	32 Geometric performance	Accuracy of distortion correction Spacial resolution	42 Determination accuracy of DCP position	Estimation of DCP position
Verification for Physical measurment	13 Atmospheric and solar effects	Atmosheric effect Sun glitter	23 Atmospheric and solar effects	Atmospheric effect Rim darkening Effect of cloud Sun glitter	33 Atmospheric and solar effects	Sky radiation Effects of water vapor, cloud, rain, wind and sea surface temperature Sun glitter	43 Verification of effectiven- ess of DCS parameters	Data trans- mission of oceanogra- phic and meteoro- logical information
	geophysical information (Including	Applicability of high-gain and compression mode Comparative usage with other sensor data Applicability for land and sea area	24 Derivation accuracy of geophysical information (Including verification of effectiveness of sensor parameter)	Estimation of sea surface temperature Estimation of cloud top height Applicability for 6-7 µm band Usefulness of gain selection for particular area with other sensor data	34 Derivation accuracy of geophysical information (Including verification of effective- ness of sen- sor parame- ter)	Estimation of water vapor content Estimation of liquid water content estimation of snow sover Estimation of sea ice cover Effect of sea surface widn Comparative usage with other sensor data Applicability for land and sea area, and for weather		

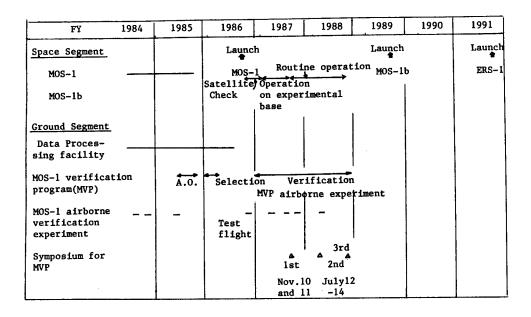


Figure 1. Schedule of MVP

Table 2. Outline of MVP Airborne Experiment

Test Site	Observation Date	Altitude	Objectives
Boso-Hachijo	Aug.5,1987	6000m	MSR antenna pattern
Hachijo-Miyake- jima	Aug.8,1987	500m	VTIR sea surface temperature
Suruga Bay Ensyunada	ditto	6000m	evaluation VTIR spatial resolution
			evaluation
Kasumigaura	Dec.3,1987	500m/	MESSR atmospheric
Tsukuba		3000m/ 7000m	compensation, radiometric
Kashimanada	Dec.4,1987	500m	evaluation, spatial resolution evaluation VTIR sea surface temperature evaluation
Monbetsu	Feb.9,1988	500m/	MSR sea ice
Asahikawa- Nayoro Sapporo	Feb.10,1988	5000m 500m/ 5000m	evaluation MSR snow evaluation
Biwa Lake (planning)	Summer,1988	-	MESSR radiometric evaluation

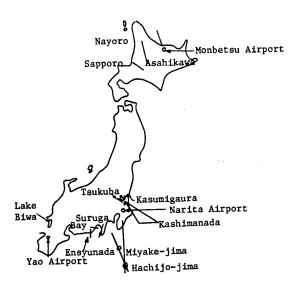


Figure 2. Test Sites for MVP Airborne Experiments

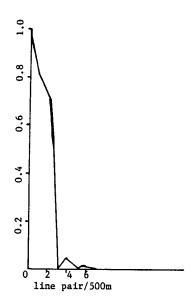


Figure 3. Example of Calculation of MTF for MESSR /09599

Investigation of the Effectiveness and Applications of Japanese ERS-1 Stereoscopic Images

43070001h Kyoto Selections from INTERNATIONAL ARCHIVES OF PHOTOGRAMMETRY AND REMOTE SENSING in English Vol 27, 1988 pp 109-119

[Article by Nobuhiko Mori, NEC Corp.; Hidetoshi Takaoka, Sumitomo Metal Mining Co., Ltd.; Kunishige Tonoike and Jiro Komai, Earth Resources Satellite Data Analysis Center; and Shunji Murai, University of Tokyo, NEC Corp. (space, ground system), 4035, Ikebe-cho, Midori-ku, Yokohama, 226 Japan, Commission 1, WG 1]

[Text] Abstract

A remote sensing satellite named Japanese Earth Resources Satellite-I (JERS-1) is scheduled to be launched in 1992 in Japan. The satellite will be able to take stereoscopic images continuously by two linear array sensors. In this work, we developed a system to make JERS-1 simulation stereoscopic images by computer, and then using this system, we produced stereoscopic images from a Large Format Camera (LFC) photograph taken from the space shuttle. We investigated the quality and the usefulness of the JERS-1 stereoscopic images using these simulation images. The result of this work is that we can get high quality stereoscopic vision to explore earth resources from JERS-1 stereoscopic images which have about 20 m ground resolution and 0.3 base-to-height ratio.

1. Introduction

Recently stereoscopic images taken from satellites are drawing the attention of the world. SPOT-1, which was launched in 1986, was essentially the first satellite to have the function of stereoscopic viewing and many investigations about SPOT stereoscopic images are being executed now. Japan is planning to launch another stereoscopic viewing satellite, JERS-1, in 1992. The main difference between SPOT-1 and JERS-1 is that SPOT-1 takes stereoscopic images in two different orbits using a side-looking image sensor but JERS-1 takes them in the same orbit using nadir and forward looking image sensors. This

difference in the image-taking method causes some differences in image features. So it is necessary to investigate the feature of JERS-1 stereoscopic images in detail.

The projection method of satellite images is different from photographic images, the satellite image is a cylindrical projection but the photographic is a central projection. Therefore, there are many new problems to be resolved in satellite stereoscopic images. It is the main purpose of this work to make simulation stereoscopic images to investigate the features and the quality of JERS-1 stereoscopic images. Another purpose of this work is to evaluate some parameters of JERS-1 stereoscopic viewing to confirm the adequacy of the design. The third purpose of this work is to investigate the usefulness of JERS-1 stereoscopic images to develop their application fields.

2. Japanese Earth Resources Satellite-1 (JERS-1)

JERS-1 is a remote sensing satellite designed to gather image data which are useful to explore earth resources. It will be launched in 1992 in Japan. Its weight is 1.4 tons and the altitude of its orbit will be $568 \, \mathrm{km}$.

JERS-1 has two kinds of imaging systems. One is synthetic aperture radar (SAR) and the other is optical sensor. The wavelength of SAR is L band and the resolution of SAR image is 18 m. The swath width of both sensors is 75 km. The ground resolution of optical sensor is 18.3 m x 24.0 m for the nadir looking sensor and about 19.1 m x 24.0 m for the forward looking sensor. The nadir looking sensor takes seven band images in the wavelengths of visible, near infrared and shortwave infrared. The forward looking sensor takes one band image in shortwave infrared wavelength.

The combination of a nadir looking sensor image and a forward looking sensor image produces stereoscopic vision. The base-to-height ratio of JERS-1 stereoscopic images is fixed to 0.3. This ratio cannot be enlarged because the nadir looking sensor and the forward looking sensor must be placed in the same telescope due to considerations of weight limitations, etc.

3. Development of a System to Make JERS-1 Simulation Stereoscopic Images

We developed a system to make JERS-1 simulation stereoscopic images from photographs by computer. The quality and usefulness of JERS-1 stereoscopic images can be investigated using the output of this system. Figure 1 shows the general flow of this system. The details of the components of this figure will be explained next.

LFC photo (Large Format Camera photo)

The input image data of this system is photographic, particularly by LFC photograph taken from the space shuttle. LFC photograph is very suitable for this system because it covers a very large area with high ground resolution (about $15 \sim 20$ m) similar to JERS-1 stereoscopic images. Moreover a photograph has another merit in that the image distortion of a photograph can be corrected more exactly than that of a satellite image.

Digital image

The input LFC photograph is converted to a digital image by drum-scanner.

Exterior orientation parameters

The exterior orientation parameters are extracted from a positive-film of the LFC photograph using the aerotriangulation method.

Мар

Maps with contours are used to make a digital terrain model (DTM). In this work we used maps of 1:50,000 scale. The contours of the map are converted to a digital image by drum-scanner.

DTM

DTM with 18.3 m interval is made from the digital image of contours using computer. But the height information of each contour must be attached line by live manually.

Orthophoto image

A digital image of a photograph is converted to an orthophoto image using DTM and exterior orientation parameters. In this conversion the earth curvature is taken into account.

Parameters of JERS-1

Some parameters of JERS-1, such as ground resolution, base-to-height ratio and the angle of the forward looking sensor are used to make JERS-1 simulation stereoscopic images.

JERS-1 stereoscopic images

An orthophoto image is converted to JERS-1 stereoscopic images using DTM and parameters of JERS-1. The base-to-height ratio of JERS-1 stereoscopic images is fixed to 0.3, but in this system we can select

any other base-to-height ratio of stereoscopic images. The details of this part will be explained in the next section.

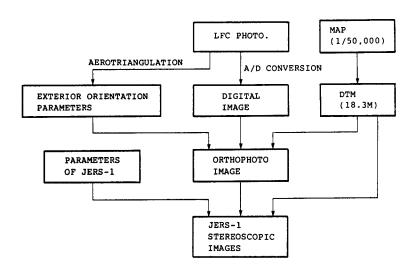


Figure 1. General Flow of the System to Make JERS-1 Simulation Stereoscopic Images

4. Mathematical Method to Make JERS-1 Simulation Stereoscopic Images

JERS-1 simulation images are made point by point determining the earth's surface points sensed by sensor elements in a linear array sensor at any time. We will explain the way to determine the sensed point by a sensor element in this section.

Figure 2 shows the relationship between the ground co-ordinates (X, Y, Z) and the satellite co-ordinates (Xst, Yst, Zst). Both sets of co-ordinates are rectangular plane co-ordinates and are defined on the earth's surface and on the satellite respectively.

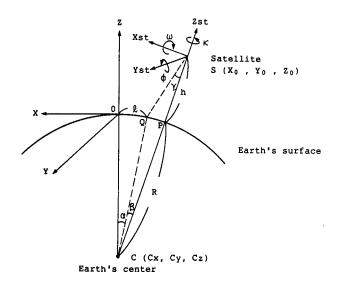


Figure 2. Relationship Between the Ground Co-ordinates (X, Y, Z) and the Satellite Co-ordinates (Xst, Yst, Zst)

The X-Z plane and the Xst-Zst plane are the same and the satellite flies on the plane towards the Xst axis direction. R is the earth's radius. h is the satellite altitude. Point C (Cx, Cy, Cz) is the earth's center in the ground co-ordinates. Point P on the earth's surface is directly below the satellite and the nadir looking sensor faces here. Point Q on the earth's surface is where the forward looking sensor is directed. Angle γ can be determined from the base-to-height ratio of this stereoscopic imaging system. Angle β can be determined from the angle γ . Length 1 is the length along the earth's surface between the origin 0 and the point Q. Angle α can be determined from the length ℓ . The satellite always faces the earth because the satellite rotates once when it flies around the earth. From these conditions, mentioned above, the satellite position S $(X_0,\,Y_0,\,Z_0)$ in the ground co-ordinates and the satellite altitude, that is, the rotation angle ω , ϕ , κ around the axes X, Y, Z, can be expressed as follows.

Satellite $x_0 = Cx - x_0 = Cy - Cz -$	position + (R + h) + (R + h)	cos	$(\frac{\pi}{2} + (\frac{\pi}{2} +$	α + α +	β) β)	(1) (2) (3)
Satellite $\omega = \kappa = 0$ $\phi = -(\alpha - 1)$	0					(4)

The co-ordinates transformation equation between ground co-ordinates (X, Y, Z) and satellite co-ordinates (Xst, Yst, Zst) can be expressed as follows.

```
\begin{bmatrix} X \\ Y \\ Z \end{bmatrix} = \begin{bmatrix} a_{11} & a_{12} & a_{13} \\ a_{21} & a_{22} & a_{23} \\ a_{31} & a_{32} & a_{33} \end{bmatrix} \cdot \begin{bmatrix} Xst \\ Yst \\ Zst \end{bmatrix} + \begin{bmatrix} x_0 \\ y_0 \\ z_0 \end{bmatrix}
\begin{bmatrix} a_{11} & = \cos \kappa \cdot \cos \phi \\ a_{21} & = \sin \kappa \cdot \cos \phi \cdot \cos \phi + \sin \omega \cdot \sin \phi \\ a_{31} & = \sin \omega \cdot \sin \kappa \cdot \cos \phi - \sin \phi \cdot \cos \omega \\ a_{12} & = -\sin \kappa \\ a_{22} & = \cos \omega \cdot \cos \kappa \\ a_{32} & = \cos \kappa \cdot \sin \omega \\ a_{13} & = \cos \kappa \cdot \sin \phi \\ a_{23} & = \cos \omega \cdot \sin \kappa \cdot \sin \phi - \sin \omega \cdot \cos \phi \\ a_{33} & = \sin \omega \cdot \sin \kappa \cdot \sin \phi + \cos \omega \cdot \cos \phi \end{bmatrix}
(6)
```

Using this transformation equation we can express the position of the linear array sensor and the center of projection in the ground coordinates.

Figure 3 shows the method to determine the earth's surface point sensed by a sensor element in a linear array sensor. Point I is the center of projection. Point J is a position of sensor element in the linear array sensor. There are about 4,000 sensor elements in the linear array sensor. The position K sensed by the sensor element J can be determined as the cross point of the line I-J and the DTM, that is, the earth's surface. The line I-J shows the beam of light from the point K on the earth's surface to the sensor element J. This point K can be calculated using the successive approximation method as follows.

At first the height of the point K is hypothesized as a certain value and the cross point with the line I-J, M, is calculated. Then the true earth's surface at the position M, here the point N, is calculated and the second height of the point K is hypothesized between the points M and N. We can determine the approximate height of the point K by repeating this process.

The point sensed by a sensor element at any time can be determined like this and the brightness of that point can be determined from the orthophoto image made from the LFC photograph. A JERS-1 simulation image can be made by determining the brightness of all the picture elements point by point like this.

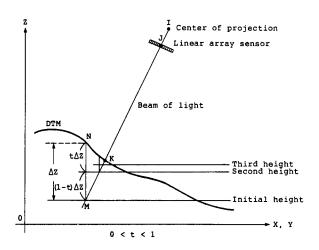


Figure 3. Method to Determine the Earth's Surface Point Sensed by a Sensor Element in a Linear Array Sensor

5. Production and Evaluation of JERS-1 Simulation Stereoscopic Images

We produced some JERS-1 simulation stereoscopic images using this system. As an input image we used an LFC photograph of the Izu peninsula in Japan taken from the space shuttle. Photo l is the photograph but only the left side is printed.

Photo 2 is one output of our system which simulates the JERS-1 nadir looking sensor image. Photo 3 is another output which simulates the JERS-1 forward looking sensor image. These two images produce a stereoscopic vision of 0.3 base-to-height ratio. We derived some significant results from the evaluation of these stereoscopic images.

One of them is that the base-to-height ratio of JERS-1, 0.3, is a little small, but we can get an acceptable vertical exaggeration to see the shape of the earth's surface. Another result is that the ground resolution, about 20 m, is more than adequate to extract the terrain features of the earth's surface.



Photo 1. LFC Photograph of the Izu Peninsula in Japan Taken From the Space Shuttle $\,$

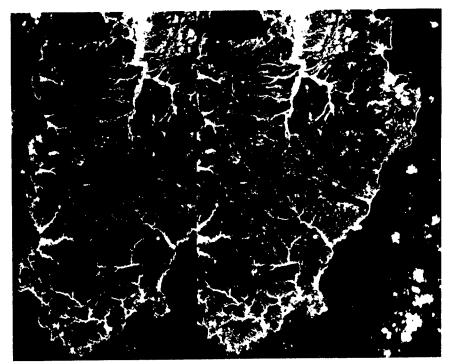


Photo 2 JERS-1 simulation image of the nadir lokking sensor

Photo 3 JERS-1 simulation image of the torward looking sensor

It should be noted that the picture element size of the images which we produced as JERS-1 simulation stereoscopic images was $18.3~\text{m} \times 18.3~\text{m}$. This means that we produced not raw images but geometrically corrected images because the picture element size of the raw image is $18.3~\text{m} \times 24.0~\text{m}$ at the nadir looking sensor image and about $19.1~\text{m} \times 24.0~\text{m}$ at the forward looking sensor image.

6. Lineament Extraction Experiment From JERS-1 Stereoscopic Images

We carried out some experiments to investigate the usefulness of JERS-1 stereoscopic images from the standpoint of the earth resources exploration. One of the results of the experiments is shown in Figure 4. The four maps are the results of lineament extraction from four stereoscopic images which differ in base-to-height (B/H) ratios. These stereoscopic images of different B/H ratios were made by changing the angle of the forward looking sensor at the developed image production system. These lineaments were drawn professionally using a stereoscope. Table 1 shows the total numbers and lengths of these lineaments in each map. From these results we can say as follows.

- (1) We can extract the maximum amount of lineaments from 0.5 B/H ratio stereoscopic images, but 0.3 images are not very inferior to 0.5 images.
- (2) The B/H ratio of 1.0 is too large to extract lineaments in this area where the slope of the earth's surface is somewhat steep.

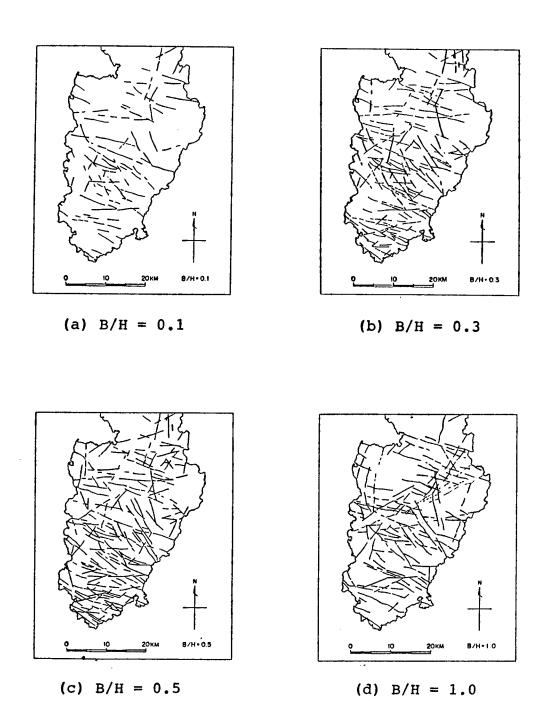


Figure 4. Results of Lineament Extraction From Four Stereoscopic Images Which Differ in $B/H\ Ratios$

- (3) The B/H ratio of 0.1 is too small to extract lineaments even in this somewhat steep slope area.
- (4) We can extract many unknown lineaments from 0.3 images, so it can be said that the stereoscopic images of JERS-1 are very useful to explore earth resources.

Table 1. Total Value of Lineaments Extracted From Four Stereoscopic Images Which Differ in B/H Ratios

B/H ratio	0.1	0.3	0.5	1.0
Total number	135	284	330	262
Total length (km)	305.86	594.13	730.10	610.36

7. Conclusion

We developed a system to make JERS-1 simulation stereoscopic images from photographs. Using this system, we produced JERS-1 simulation stereoscopic images of the Izu peninsula in Japan from an LFC photograph taken from the space shuttle. From the evaluation of these stereoscopic images, it is confirmed that the stereoscopic images of JERS-1 produce fine stereoscopic vision with acceptable vertical exaggeration, and the ground resolution of JERS-1 is more than acceptable to extract terrain features of the earth's surface.

We carried out some experiments to investigate the usefulness of these images. One of them was lineament extraction from four stereoscopic images with different base-to-height ratios. From these experiments we found that JERS-1 stereoscopic images are very useful to explore earth resources.

But our work has not been sufficient to investigate all the possible applications of JERS-1 stereoscopic images. We hope that many other investigations of JERS-1 stereoscopic images are executed and many application fields of these images are developed.

Reference

Shunji Murai, Ryosuke Shibasaki; Geometric Correction of Linear Array Sensor; Proceedings of International Symposium on Advances in the Quality of Image Data, Com. I, Camberra, Australia, Apr 1982.

/09599

A Satellite Assisted-Tracking System With Real-Time Accommodation for Maximal Pointing

43070002a Kyoto Selections from INTERNATIONAL ARCHIVES OF PHOTOGRAMMETRY AND REMOTE SENSING in English Vol 27, 1988 pp 1-10

[Article by Jose Luiz de Barros Aguirre, MSc DDS--Systems Development Department and Valder Matos de Medeiros, MSc DCG--Guidance and Control Department, INPE--Instituto de Pesquisas Espaciais, MCT--Ministerio da Ciencia e Tecnologia, Caixa Postal 01, 12630 Cachoeira Paulista, SP, Brazil; prepared for the XVI Congress of the International Society for Photogrammetry and Remote Sensing, Commission II, Working Group 4]

[Text] Abstract: An operational difficulty of ground receiving stations is to reacquire a satellite in high elevation after a loss due to a zenithal pass (when employing an El-over-Az antenna), a receiving chain malfunction or another cause that breaks reception. Traditional recovery schemes employ rate memory or precalculated pointing data (programmed tracking) to command the antenna movement after a tracking loss. The system described in this paper has been implemented at the Brazilian Landsat receiving station. It does not require a fast computer and takes very little memory, yet has proven extremely effective, with significant advantages over previously available systems. Extensions to the method, to be employed for the upcoming Brazilian satellites, are discussed.

1. Introduction

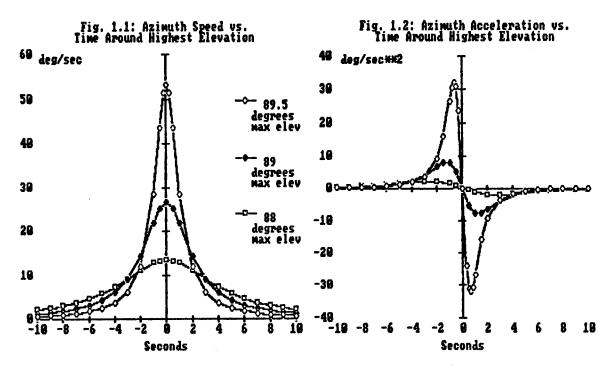
1.1 Initial Motivation for Development: the Zenith Pass Problem

Every Remote Sensing Specialist is familiar to some extent with the need for tracking low-orbit remote sensing satellites with parabolic antennas in order to receive and utilize the data they transmit down to Earth.

Most antennas employed for this purpose have automatic tracking capabilities, i.e., they can "follow" automatically a passing satellite since the moment it is "found" on the sky. However, most such antennas

in operation employ Elevation-over-Azimuth pedestals, which have a serious limitation for near-zenith passes.

Figures 1.1 and 1.2 show typical azimuth speed and acceleration patterns in El-over Az antennas for high elevation passes as a function of time near the overhead. With the existing systems, limited at about 20 degrees/sec maximum turning speed and about 10 degrees/sec² maximum acceleration, we can see that 89 degrees elevation is a practical limit.



Although apparently a low-probability event, this may turn out to be a serious problem for ground stations that happen to lie too near to one of the repetitive ground tracks of satellites such as the Landsats.

This condition determined the initial motivation for the development of the assisted-tracking system described herein. The first Brazilian Landsat Station, installed in 1973 at Cuiaba, just 17 km west of Landsat-1 WRS Path 243, spent several months without being able to acquire images south of its location, because it systematically lost the satellite, coming from the North, at 88.8 degrees elevation. Only after the motor power drives were modified to allow a little more current, raising the maximum turning speed to about 22 degrees per second, the problem was settled. However, if Path 243 was just a little closer to the Station the overhead loss could not be avoided.

The devised assisted-tracking system, in opposition to programmed tracking, took into account the antenna elevation and azimuth readings while locked on the satellite to compute its position in the immediate future, achieving much higher accuracy than an analytical predictor

could do based on mean orbital elements two or more days old. This would allow, even after an unavoidable overhead loss, to recover after a few seconds instead of minutes, which was the case when available precalculated pointing data were not accurate enough to allow catching up still in high elevation.

The implementation was carried in 1982, when Brazil was preparing for the Thematic Mapper era and a new antenna system was being purchased to receive Landsat 4 in X-band at the Cuiaba Station. This implementation is described in Chapter 2 of this paper.

1.2 New Motivation: the "Silence Zones" of the First Brazilian Satellites

Although present antenna systems have already overcome or minimized the zenith pass problem with either motorized tilt pedestals or servocontrolled subreflectors, a new motivation for an assisted-tracking system arose with the characteristics of the first Brazilian satellites, which shall start flying in 1989. A third antenna system is being purchased for installation at Cuiaba for the tracking and command of these satellites.

The two first satellites, devoted to platform data collection, will be near-equatorial rather than near-polar orbiters, while motorized tilt mechanisms like the one to be employed in the purchased antenna system are normally mounted to work in the east-west direction. This will limit the efficacy of such device and assisted tracking may still be necessary near the zenith.

However, the most important service that an assisted-tracking system can provide to the early Brazilian satellite program relates to the absence of active attitude control on the satellites (except for an initial spin-stabilization). This means that at certain periods the satellite orientation can be such that during a pass the Receiving Station will enter the "silence zone" of the satellite irradiation pattern. The resulting signal loss can take from several seconds up to a few minutes.

The initial idea to reacquire the satellite after a silence zone was to move the antenna to the predicted reacquisition position and wait there for the satellite. This approach was abandoned after two problems were pointed out: first, the predicted recovery could be inaccurate, since prediction errors can affect not only the coordinates but also the RF downlink calculation; and second, if reacquisition should occur in high elevation the antenna acceleration capability would certainly not be big enough to suddenly start following the satellite, even if it passed in front the antenna main lobe with signal strength above the required level.

Thus, an assisted-tracking scheme may be employed to command the antenna, keeping it pointed to the satellite during the whole loss

period, guaranteeing the earliest reacquisition. Chapter 3 of this document presents possible modifications that can be made onto the present design for the Brazilian mission.

- The Implementation Carried for Landsat-4 in 1982
- 2.1 Characteristics of the Antenna Control Unit (ACU)

The ACU to be delivered with the Brazilian Thematic Mapper subsystem was a Scientific-Atlanta model 3842. It had, of course, autotrack capability, which was the primary mode of operation, and a backup mode selectable among rate memory, position memory and remote command. For this last mode it included a computer interface to allow reading out pedestal angles and commanding antenna positions from an external computer.

The ACU was designed to work in autotrack mode and switch automatically to the selected backup mode in the event of a signal loss. The acquisition/loss status was also available to the external computer through the interface. While in autotrack mode, the ACU would ignore any remote command received. Due to its internal processor constraints, the maximum remote command rate was about 10 times a second, or a command issued every 100 milliseconds.

2.2 Characteristics of the Station Computer

The Receiving Station did not have a computer on site before the Thematic Mapper subsystem was delivered. The one then bought, chosen to be software- and hardware-compatible with the Processing Station, installed in another facility, was a DEC PDP-11/34 minicomputer and its initial role was just to allow local computation of the antenna pointing data.

Taking into account its limited speed (about 0.2 Mips and no floating point hardware) and internal memory (56 Kbytes), a numerical integrator was out of consideration. Therefore, the pass calculation would have to keep being analytical and based only on the Brouwer Mean Elements then sent via telex by NASA's Goddard Space Flight Center 3 or 4 times a week. For the same reasons, any assisted-tracking software would have to be simple and efficient enough to perform the calculations in real time and still keep ahead of the satellite, i.e., produce predicted Elevation and Azimuth values faster than they might be needed in case of a satellite loss.

2.3 The Calculation Algorithm Employed

If you have a set of orbital elements (which are six for the general case) for a satellite at a given instant, you can use them to compute its position along time and therefore, knowing an antenna location, derive the corresponding pointing angles. In the case of Brouwer Mean

Elements, some of them (semi-major axis a, eccentricity e and inclination i) are almost constant in the course of a few days and could therefore be used as operator inputs. Our problem was to derive or adjust the other three (longitude of the ascending node, argument of the perigee and mean anomaly) based on observations of Elevation and Azimuth during a pass.

To simplify as much as possible the computation, the basic idea was to use a circular rather than elliptical model for the satellite orbit, assuming that its eccentricity (typical value 0.0002) was small enough to be disregarded for a very short term prediction. With this approach the orbital elements would be reduced to five, since there would no longer be a "perigee." Therefore, a single observation of El/Az would allow resolving the two remaining elements. The sequence of calculus would be:

- 1 find the satellite position at the intersection of the antenna pointing direction with a sphere of radius a, concentric with the Earth ellipsoid;
- 2 use this position to derive the longitude of the ascending node and the mean anomaly M (which would coincide, since e = 0, with the true anomaly u);
- 3 use the derived elements, together with a and i, to compute the satellite positions for a time series of N seconds in the immediate future;
- 4 calculate and store the pointing angles for this time-series.

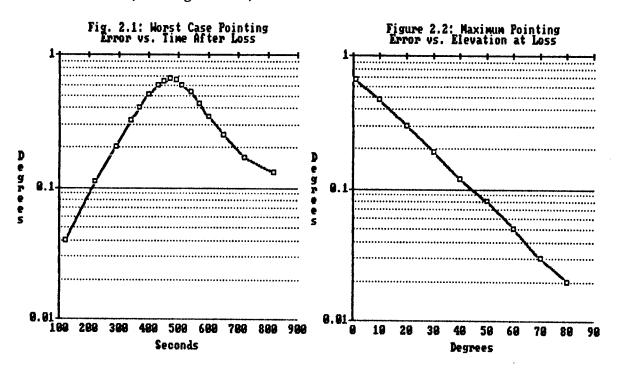
Presenting the full mathematical derivation for the above mentioned procedure is outside the scope of this paper since it involves only well-known equations and formulas of trigonometry, coordinate transforms and orbital calculus. For reference, the interested reader can see Brouwer¹ and Escobal, ² chapters 1 thru 4.

2.4 The Simulations Carried to Check the Model Performances

The model was implemented firstly as a simulation program on the processing Station's PDP-11/34, identical to the one to be installed at the Receiving Station, in order to validate the intended approach against the performance requirements.

2.4.1 Accuracy (Requirement: less than 0.1 degrees of pointing error, for at least 10 seconds to allow reacquisition in Band X after an overhead loss.) -- To verify the delivered accuracy, the model was checked against different Elevation/Azimuth time series, produced by a full model numerical integrator running on a mainframe computer, for high and low elevation passes. Several experiments involving different loss conditions were conducted.

It was found that the worst case conditions for the model, i.e. where the prediction deviated fastest from reality, happened near the zenith. However, even in the worst case the pointing error took at least 2 minutes of loss to exceed 0.1 degrees. Across a full pass (simulating a loss just after the satellite was acquired), the error never exceeded 0.7 degrees (see Figure 2.1), which is enough for a reacquisition in Band S. The maximum error observed near the zenith presented an interesting behavior as a function of the elevation at which the loss was simulated (see Figure 2.2).



2.4.2 Speed (Requirement: less than 100 msec computing time per El/Az pair to allow commanding the antenna at the maximum ACU rate.) -- The computing times were measured and the results showed 1) less than 7 milliseconds for deriving the desired orbital parameters from an observed El/Az pair, and 2) less than 27 milliseconds to compute a pair of predicted pointing coordinates.

2.4.3 Sensitivity to Input Parameter Inaccuracy (Requirement: no degradation of accuracy beyond specification for unaccounted-for typical time drifts in the operator-introduced parameters.) — The operator input parameters (orbit inclination i and semi-major axis a, which would have to be taken from sources 2 or more days old) were changed with respect to those used to produce the time series. The model was found to be practically insensitive to errors up to a hundred times greater than the typical day-to-day change figures, which are about 0.05 Km for the semi-major axis and around 0.001 degrees for the orbit inclination.

The above performances were considered far more than enough to satisfy all the requirements of the devised assisted tracking system. Therefore, a green light was set for the implementation.

2.5 The Real-Time Structure

Considering that in real life conditions the computer would have not only to calculate and store the orbit extrapolation data but also to handle all the traffic of data and statuses between itself and the ACU, the software was designed with a background/foreground architecture.

The synchronous part of the program (background) would take the last available El/Az observation to derive the corresponding orbital elements and then compute and store N_1 seconds of future pointing data. After that it would sit in a wait loop, going back when either a loss was detected or less than N_2 seconds of predicted pointing data remained in the buffers with the satellite still being acquired. N_1 and N_2 are parameter variables set respectively to 90 and 30 based on the simulation behavior.

The asynchronous part of the program (foreground) would read the acquisition status under the pace of an external clock and then, depending if in autotrack or not, either read and store the antenna elevation and azimuth positions or command them from the prediction buffers filled by the background part.

The two parts would communicate through a common area in memory where all flags, pointers and buffers would reside.

The real-time logic was tested by attaching the external clock interrupt routine to the computer real-time clock and implementing a dummy ACU driver to take the El/Az "readings" from the stored time series and take the acquisition "status" from a flag changed asynchronously at another interrupt routine attached to the terminal keyboard.

2.6 The Real-Life Constraints

Certain real-life constraints determined some modifications to the logic used in the simulations:

- a) although El/Az during acquisition state could keep being read once a second, to obtain as smooth an antenna movement as possible a decision was taken to command it at 10 Hz instead of once a second as in the simulations. The external clock pace must be then 10 Hz instead of 1 Hz and the interrupt routine in the foreground software and the prediction interval in the background were adapted accordingly.
- b) due to the ACU characteristics it was important, during normal acquisition, to keep its remote $\rm El/Az$ command registers updated consistently with the current antenna position. Otherwise, when falling

automatically to the remote command backup mode at a signal loss, the ACU would find and use dummy El/Az values to command the antenna before the first predicted values were sent in by the computer, which could impose unnecessary strain to the antenna drives. The decision was to keep the command logic active at all times, loading the ACU command registers with predicted values which would be ignored by the ACU logic during acquisition but would be immediately available when needed.

- c) to reduce the effect of the small potential antenna jitter around the satellite position while tracking it, steps 1 and 2 of the calculations (see Section 2.3) should be repeated a few (3 to 8) times for consecutive El/Az readings, so that the derived elements could be averaged.
- d) to avoid that potentially inaccurate readings made during high antenna acceleration periods impacted the calculations, the software was built not to take into account El/Az pairs above a given elevation, which was initially set to 80 degrees. This value could be certainly higher but its maximum could not be determined by simulation without modelling into it the antenna inertia and servo response. Since satellites at altitudes below 1000 km cannot spend more than about 45 seconds above 80 degrees elevation for a given station and our assisted tracking was safe for at least 2 minutes, the cost/benefit ratio of this investigation did not justify it.

2.7 Integration and Checkout

The Thematic Mapper subsystem was installed at Cuiaba in August, 1982 and the developed simulation program was then adapted to work in real life environment.

As, by chance, the Landsat-4 WRS coverage pattern did not have a ground track close enough to the Receiving Station, there were no near-zenith passes and therefore losses had to be simulated by disconnecting the tracking receiver during a pass. This had advantages over a real loss: first, of course, because no data was lost; and second, because the signal level at the data receiver could be monitored while the assisted tracking was in command.

It could be checked that there was not a single dB of fading for more than one minute in that condition. For comparison, the ACU Rate Memory backup mode would lose the satellite in less than 15 seconds for a loss around 30 degrees of elevation, or 5 seconds above 80 degrees.

3. Extensions of the System for the Brazilian Data Collection Satellites ${\bf Collection}$

3.1 The New ACU and Antenna System

The receiving system purchased for the Brazilian missions includes an ACU of the same manufacturer and model as the one with which the assisted tracking was implemented, although of a more recent design. Its operation will be basically the same, with the addition of a motorized tilt mechanism for the antenna pedestal. Therefore, the basic characteristics of our assisted tracking system can be maintained. Its usefulness, as mentioned in the introduction, will be in helping the antenna across the "silence zones" and perhaps also across overhead passes if the tilt axis must be mounted North-South.

3.2 The New Station Computer

The new Station computer will be a DEC MicroVAX II, more than 10 times faster than the existing PDP-11/34, although with a heavy multitask role of monitoring and recording statuses of all station and satellite subsystems, supporting on-line data communications with the Control Center and sending preprogrammed or emergency commands to the satellite during each pass. Nevertheless, in a signal loss situation, which is when assisted tracking will have to take over, this task is expected to be highly alleviated.

3.3 Changes in the Calculation Algorithm

It is expected that the first Brazilian satellites have an orbit eccentricity well above Landsat's, reaching perhaps 0.05 or a little more. Therefore, the algorithm described at Section 2.3 may not be able to disregard eccentricity. On the other hand, the argument of the perigee will be better defined and can be used as an additional operator input, keeping still at 2 the number of "missing" elements.

As the intersection of the antenna pointing direction with an ellipsoid not concentric with the Earth cannot be analytically explicited, a rigorous solution to find the distance r from the satellite to the Earth center would require numerical methods. However, utilizing steps 1 and 2 of the mentioned algorithm using the semi-major axis a as a first approximation to r, the obtained true anomaly u would allow a new value for r through the equation

$$r = a (1 - e cos E),$$

where

$$(E = 2 \text{ atan}(tg(u/2) \text{ sqrt}((1-e)/(1+e)))$$

is the eccentric anomaly. This makes out a quickly converging series to yield reliably updated values for the desired orbital elements.

From there on, steps 3 and 4 would be exactly the same.

3.4 Changes in the Real-Time Logic

To minimize CPU demand during normal acquisition periods, the real-time logic of the assisted-tracking model can be modified to perform just the orbital element updates, at specified intervals. In a loss event, predicted El/Az pairs will start being needed at a 10 Hz rate, which is something the MicroVAX can compute and command with plenty of margin, based on the last adjusted orbital elements. In fact, since it is unlikely that the condition that caused the loss will disappear before at least some seconds, even the orbital elements adjustment, taking into account the last El/Az readings while still in "lock" state, could be performed right after the loss without delaying recovery.

In any case, as mentioned in Section 2.6.b, it will be necessary, during normal acquisition, to keep the ACU remote El/Az command registers updated, for instance with a copy of the El/Az readings.

4. Conclusion

Although not having been effectively needed after its first implementation, the assisted tracking system described herein was certified for effectiveness and efficiency. The authors are confident that, although representing a very minor part of the system being developed for the Brazilian satellite program, the concepts presented herein can give an important contribution for the successful operation of the first Brazilian satellites and perhaps to other countries' ground systems that might face similar problems.

References

- 1. Brouwer, D.: Solution of the Problem of Artificial Satellites Theory Without Drag. "The Astronomical Journal," 64(9):378-397 (Nov., 1959).
- 2. Escobal, P.R.: "Methods of Orbit Determination." New York, NY, John Wiley & Sons (1965).

/09599

Local Area Network and Data Network for the Advanced Earth Observing Satellite, ADEOS System

43070002b Kyoto Selections from INTERNATIONAL ARCHIVES OF PHOTOGRAMMETRY AND REMOTE SENSING in English Vol 27, 1988 pp 11-19

[Article by Kohei Arai, Earth Observation Center, National Space Development Agency of Japan, presented at the ISPRS held in Kyoto, Japan, in July 1988]

[Text] Abstract: NASDA is planning the next generation of earth observation satellite, following MOS-1, MOS-1b, JERS-1, so called Advanced Earth Observing Satellite, ADEOS. ADEOS will carry Ocean Color and Temperature Scanner, OCTS, Advanced Visible and Near Infrared Radiometer, AVNIR and Announcement Opportunity sensors, AO sensors and will require a quick data distribution. Not only direct broadcasting, but also data distribution through a network are useful for the dissemination of such data. Therefore a data network of which users can access a quicklook image data base in a quasi real time basis is now considered.

In order for the preoperational data handling, a local area network is taken into account for an ADEOS ground facility. The processed data are sent to the film recorder through the LAN together with histograms for the generation of look up table for the gamma correction. Key items of the processed data are also transmitted to the information retrieval subsystem for the registration. The acquired quick look data are transmitted to not only the film recorder but also quick look image data base and the information retrieval subsystem in a real time basis.

The aforementioned ideas and concept for the development of the ADEOS ground facility will be described in the proposed paper.

Introduction

Primary purposes of the development of the Advanced Earth Observing Satellite: ADEOS are

- i) to provide opportunities to onboard mission instruments and collect information using the instruments for the countries in the world,
- ii) to ensure earth observing data starting with MOS-1 through MOS-1b, JERS-1.
- iii) to establish the fundamental technologies on development of the Polar Orbiting Platform. Outline of the ADEOS system has been introduced in Reference 1.

In order to respond to requirements or social demands for earth observation from space, earth observation system consists of not only satellite but also ground facilities including data networks for transmission of mission data, should be matured and improved. For instance, there must exist a strong desire of real time or quasi real time data transmission for the purpose of finding of the fishery ground area, disaster prevention, monitoring sea ice, and so on. Therefore satellite orbit should be determined to increase the observation frequency, namely, subcycle of satellite orbit should be minimized, furthermore, quick transmission of the mission data such as direct transmission for local users' stations, data transmission of the acquired and processed data through a network, should be taken into account. On the other hand, efficiency of ground facilities on data handling and processing should also be improved.

Regarding with image data networks, NOAA has a plan of NOAA-port (Reference 2), ESA also has a TIROS-net (Reference 3), and NASA has a plan of EOSDIS: EOS Data and Information System (Reference 4) while NASDA has a plan of SODS: Space Operation and Data System (Reference 5).

This paper will deal with local area network for improvement of the efficiency of ground facilities on data handling, and data network for quick data transmission for ADEOS system, and will describe the relationship between SODS and image data network. Furthermore Direct Transmission for Local Users' stations: DTL system for decimated OCTS data transmission will also be described.

2. The Communication Link for ADEOS Data Transmission

2-1 The ADEOS data link system

The ADEOS data link system is illustrated in Figure 1. Mission data are directly transmitted to receiving stations via X-band, and are also transmitted to the specified receiving stations through the Data Relay

and Tracking Satellite: DRTS via Ka-band. As the DRTS, NASDA is now planning ETS-VI (available data rate would be 120 Mbps) as is indicated in Table 1. ETS-VI will be launched in 1992 followed by ADEOS in 1993, and EDRTS in 1994. Design life for the ADEOS satellite would be three years. Therefore, until the EDRTS is launched, only Ocean Color and Temperature Scanner: OCTS data (data rate for OCTS data would be 2.6 Mbps) might be transmitted through ETS-VI. After the launching of the EDRTS satellite, full operation at data transmission through the DRTS satellites will be available.

The ADEOS satellite will carry not only OCTS but also Advanced Visible and Near Infrared Radiometer; AVNIR featuring CCDs as the core sensors while Announcement of Opportunity: AO sensors will also onboarded on the satellite. These sensor data will be transmitted directly to the receiving stations and will also be transmitted to the specified receiving stations through the DRTS satellites.

2-2 Direct Transmission for Local Users

In order for real time data transmission, decimated OCTS data will be transmitted directly to the Local Users' stations such as fishermans' ships, etc., via UHF band.

(1) Channel selection

Chrolophil concentration: Cc, in general, can be expressed by the following equation.

$$Cc = a (B1 / B4)$$
 (1)

where a and b are coefficients, and Bl and B4 are Digital Count Values: DCVs of band 1 and 4. OCTS will have 6 bands in the visible wavelength region, while 2 bands for near infrared, 1 band for middle infrared, and 3 bands for thermal infrared. On the other hand, it is difficult to have a wide bandwidth in the UHF-band for the direct data transmission to local users. Therefore DTL system will deal with 2 channels of the decimated OCTS data. One of those is the channel corresponding to the chrolophil concentration expressed by equation (1). The other is one of the thermal infrared bands data. The expected specification of OCTS is shown in Table 2.

(2) Decimation and adjustment of the pixel interval

Instantaneous Field of View: IFOV of OCTS would be 0.85 mrad corresponding to approximately 690 m on the ground at nadir viewing. On the other hand, the acceptable ground resolution of OCTS type of sensors is around 4 km. Therefore the decimation factor of 6 is determined. IFOV on the ground is changed by not only the viewing angle but also tilt angle so that the pixel interval will be adjusted by using Look Up

Tables: LUTs to compensate the pixel intervals in the scanning direction.

(3) Bandwidth and modulation scheme for DTL

Data rate of the decimated OCTS data would be 20.6 kbps. Modulation scheme would be PCM (Bi-phase) - PM with the modulation index for PM of 1.2 radian so that bandwidth would be 181.28 kHz.

- 3. Local Area Network: LAN for ADEOS ground facility
- 3-1 Block diagram of the ground facility for ADEOS system

Figure 2 shows the system block diagram of the ADEOS ground facility. In the time frame of ADEOS operation, Earth Observation Center: EOC of NASDA will acquire the data from LANDSAT-6, SPOT-4, JERS-1, ADEOS, and will also receive the relayed mission data through ETS-VI and EDRTS satellites. Antenna system at EOC will be composed with two antennas for direct reception of mission data via X-band with a buckup function, and two antennas for the reception of data relay and tracking satellites (East and West). These antenna systems will be supervised by Mission Management Organization: MMO. MMO will gather information and mission requests from Spacecraft Control Center through SODS, Ground Stations: GSs and Users through NOAA-port, TIROS-net, and the other links or networks, and will make operation schedules for ground facility then distribute to each subsystems in a real time basis through LAN. The acquired high bit rate data will be stored in HDDTs in a real time basis for the data will also be processed quick look images and quick look imagery data will be transmitted to the Mass Storage System: MSS as a quick look image data base through LAN in a real time basis. users may access the quick look image data base with an authorized users' ID codes. Meanwhile low bit rate data will be stored in optical disks in a real time basis and then processed at a small sized processors. At this moment, optical tape is one of the tradeoff items as an archiving media.

3-2 Data should be transmitted

Data types, required data rate, amont of data should be transmitted are shown in Table 3. Amont of quick look image is data transmitted within a day, through LAN are shown in Table 4. In Table 3, decimation factors for AVNIR and OCTS are, respectively, 10 and 6 in both line and pixel directions. Therefore the standardized low bit rate networks such as the ethernet (the effective transmission rate is about 1 Mbps) would be enough. In the future (the time frame for POP), LAN futuring optical fiber with the transmission rate of 100 Mbps will be installed at EOC. At that time, the ethernet will be connected with a node of the optical fiber LAN.

- 4. Data Network System: DNS
- 4-1 Basic idea for DNS
- (1) Utilize the established or installed networks such as telephone links with MODEMs, VAN: Value Added Networks, WAN Wide Area Networks, and so on.
- (2) Basically users access to the catalog data base and quick look image data base will be installed at EOC. EOC will not transmit such types of data.
- (3) Data link between SODS and EOC will be necessary for the purpose of the site diversity function for acquired data from DRTS satellites.
- 4-2 Users to access

Users who wish access to the data bases can be categorized into the following four types.

- (1) The specified users: with the specified links;
- (2) General users: with the telephone links;
- (3) External users in the foreign countries (EOSDIS, NOAA-port, TIROS-net, etc.): through the KDD Vienus-p links for instance;
- (4) Internal users (SODS, etc.): optical fiber links, or communication satellite channels, and so on.
- 5. Concluding Remarks

A conceptual design of ground facility for ADEOS system is now on going. For more details, we will report at the other opportunity.

Earth observation system, essentially, can world wide observation. In some application fields, there must exist a strong desire of data transmission in real time or quasi real time basis. In order to encourage users community, and to improve efficiency of ground facilities on data handling, world wide remote sensing data networking is getting more important.

References

- 1. Koizumi, S. and K. Arai, A future program on remote sensing satellite in Japan-Advanced Earth Observing Satellite: ADEOS, International Space Year Conference in Hawaii, 19-21 Aug. 1987.
- 2. NOAA, CEOS Working Group on Data meeting, 1987.

- 3. ESA, CEOS Working Group on Data meeting, 1987.
- 4. NASA, CEOS Working Group on Data meeting, 1988.
- 5. NASDA, personal correspondence, 1988.

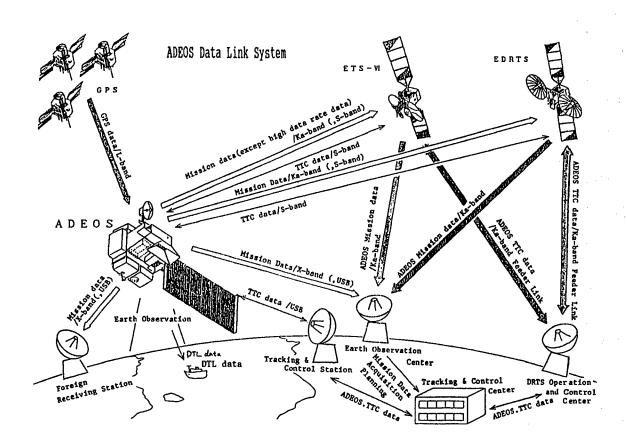


Figure 1. The ADEOS Data Link System

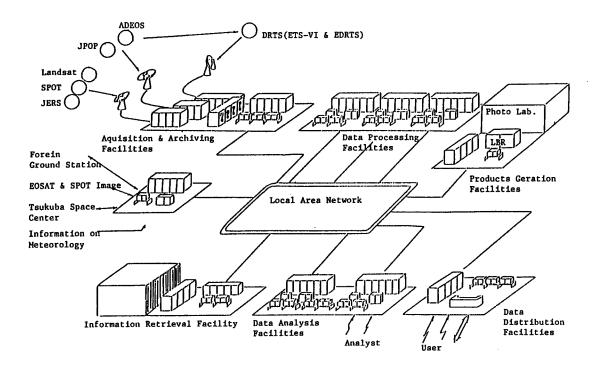


Figure 2. Data Acquisition System for ADEOS

Table 1. Communication Link to Access to ADEOS

Item	Frequency band	Data Rate	Content
VIA EDRTS	Ka band A - E:S band E - G:Ka band	120 Mbps 1 - 2 Kbps	Mission data TTC data
VIA ETS-VI	Ka band A - E:S band E - G:Ka band	2 Mbps 1 - 2 Kbps	A part of Mission data
EOC/Forein Ground Station	X band	60 Mbps x 2	Mission data
TACS/Forein Tracking Station	USB	1 - 2 Kbps	TTC data
Direct Access	UHF or VHF	1 - 100 Kbps	DCS or DTL data

A - E:ADEOS to EDRTS or ETS-VI E - G:EDRTS/ETS-VI to DRTS ground station

Table 2. Specification of OCTS

Item	Specification(Goal)			
Wave Length Region	Visible:6 bands, Middle IR:1 band, Near IR:2 bands, Thermal IR:3 bands			
Scan Angle	Approximately +/- 40 deg.			
IFOV	0.85 mrad(1.7 mrad for mid. IR)			
Tilting Angle	+/- 20 deg.(5 deg. step)			
Scanning Sytem	Mechanical Mirror Vibration			
Optics	Reflection type			
Weight	Approximately 180 kg			
Power Consumption	n Approximately 240 W			

Table 3. Data Types and the Required Data Rates

Data	Amont	Frequency	Media	Data Rate
Satellite Operation Schedule	30 KB	2 / day	Telephone link	
Orbital Elements	1 KB	2 / day	"	"
Data Reception Requests	30 KB	1 / day x 10 St.	"	"
Data Processing Requests	1 KB		"	"
On-line retrieval	300 KE	1 ' ' '	**	11
Satellite Operation Requests	30 KB	· · · · ·	"	11
Acquisition Schedule	30 KB		LAN	100 Kbps
Acquisition Schedule	30 KB	1 = 7	"	. "
Data Processing Schedule	1 KB		"	"
Orbital Elements	30 KB	1	Telephone Link	1200 bps
Path Bliefing Message	20 KB		LAN	100 Kbps
Telemetry Data		1	111	" "
Q/L Data	300 KI		"	1 "
Data Acquisition History	1 KB		! ,,	117
Data Recording History	1 KB		i	
Processed Data	250 M		1 "	,,
Auxial Data for Photo Products	s 1 KB	1	",	,,
Data Processing History	1 KB		**	i ii
Media Conversion History	1 KB	10/ day	11	

Table 4. Q/L Data Amont Within a Day

	AVNIR data	OCTS data	NSCAT data
Case 1	3.4 GB	0.264 GB	0.953 MB
Case 2		0.025 GB	

Case 1.: The relayed data through DRTS are included Case 2: Without consideration of DRTS data

/09599

SAR Activities at Dornier

43070002c Kyoto Selections from INTERNATIONAL ARCHIVES OF PHOTOGRAMMETRY AND REMOTE SENSING in English Vol 27, 1988 pp 44-50

[Article by Hans Martin Braun and Gerhard Hans Rausch, Dornier System GmbH. P. O. Box 1360, 7990 Friedrichshafen, FRG]

[Text] Abstract: Radar remote sensing from space was a key element in the German and the European Earth Observation Programmes for more than a decade now. From the beginning, Dornier-System was involved in these activities. It is the prime contractor of the major German and European space projects being concerned with radars. Supported by the German Ministry of Research and Technology (BMFT) and by the "Deutsche Forschungs- und Versuchsanstalt fur Luft- und Raumfahrt" (DFVLR) Dornier-System has developed important key technologies and extensive system design tools for many spaceborne radars with special emphasis on radars with synthetic aperture (SAR). This paper shows briefly the main space SAR activities in which Dornier was involved and indicates that these demanding programmes again need a creative engagement of innovative industries in future.

1. Introduction

Since that time, when NASA's SEASAT started the area of civil radar imagery from space, Germany initiated an intensive development programme for spaceborne radar instruments and their dedicated technologies. On behalf of the German Ministry of Research and Technology (BMFT) Dornier System has developed the German Microwave Remote Sensing Experiment (MRSE) to be flown on the first SPACELAB mission. This was the first civil radar in space, which has been developed outside the USA. As it happened to SEASAT, the MRSE did not survive the planned mission schedule indicated once again, that high power radar technology for space applications is one of the most critical elements in space radars.

After that, Dornier System overtook the prime contractorship for the first ESA Remote Sensing Satellite (ERS-I) focusing its technological

investigations onto the radar subsystems High Power Amplifier (HPA), Synthetic Aperture Radar (SAR) Processing and SAR Antenna.

A growing interest of remote sensing users in multifrequency and multipolarization SAR imagery led to the German/Italian cooperation with NASA/JPL (Jet Propulsion Lab) on a multifrequency/multipolarization SAR facility (SIR-C/X-SAR) to be flown on Shuttle. Dornier System is leading the German/Italian part.

Furthermore, Dornier System is presently using the technological spinn off of these space programmes for its development of an airborne dual frequency/dual polarization Synthetik Aperture Radar (DO-SAR), which can be flown on the Dornier-aircraft DO-228.

In parallel to these projects, Dornier System is continuously improving its software tools for design, analysis and simulation of space radars and its capabilities for development of new technologies (See Figure 1).

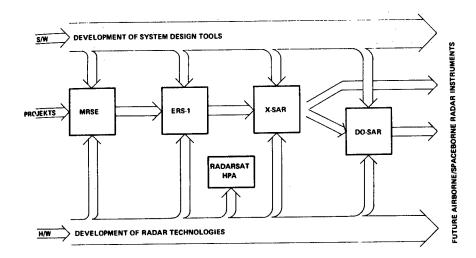


Figure 1. Programme Overview

2. SAR System Design

In 1980 Dornier System conducted a study on a multifrequency/dual-polarization spaceborne SAR facility for the German Ministry for Research and Technology (BMFT). After some analysis work along traditional lines it was understood that a task of such proportions could only be coped with by large computer support. More so, as tradeoffs between system options were part of the study goal.

Therefore, sets of radar equations and design assumptions were derived that eventually linked more than 100 parameters involved in system design. These may roughly be divided into:

1) those derived from user requirements,

- 2) those arising from the technical state-of-the-art and provisional WARC regulations,
- 3) consequential or output parameters of technical nature as subsystem design guide-lines and for final feasibility of user requirements.

A large computer program "SARA" was arranged to work in a synthesis rather than an analysis manner (knowledge based system, KBS). More specifically, after parameters of the first and second category are entered tentatively into the program a range of system solutions is offered by the computer. These are quickly evaluated by the scientific operator. From some kind of "orientation print-out" he has the choice of one or more solutions being nearest to the design goal.

Depending on the mutual compatibility of the initial input values usually two or more of the consequential parameters turned out to be unacceptable or suboptimal. Typically this procedure had to be iterated twice in order to arrive at a quasi-final system layout. The whole trade-off job illuminating more than a dozen inherently feasible system solutions could be accomplished in about half an hour. Classical trade-off approaches need days in order to derive these results.

This short reaction time of our system synthesis computer program saves time for further system optimization. The system synthesis is followed by an extensive computer aided analysis procedure analysing in detail the performance of each radar subsystem taking all possible error contributions into consideration. Iterations of these analyses allow radar parameter fine tuning. After each system layout and especially after development of radar hardware, we use to improve the performance of our KBS "SARA" by implementing new know-how gained during these analysis and test phases and today we have reached a system synthesis accuracy of better than one decibel.

3. Major Projects

The first European spaceborne SAR developed at Dornier was the "Microwave Remote Sensing Experiment" (MRSE). This instrument was flown on the first SPACELAB mission in 1984. It was an X-ban radar operating in three modes:

- a SAR mode,
- a two frequency scatterometer mode,
- a radiometer mode.

As shown in Figure 2, this instrument was characterized by a mechanically steerable 2 m \times 1 m Cassegrain reflector antenna. After successful operation in radiometer and scatterometer mode a HPA failure stopped its operation on Shuttle. Back on Earth, the HPA was operating perfectly again. The problem in orbit had been created by an unexpected

high air pressure within the Shuttle cargo bay during the SPACELAB mission.

After MRSE, under leadership of Dornier System on behalf of the European Space Agency, a large industrial team started the development of the first "ESA Remote Sensing Satellite" ERS-1 (see Figure 3). Its mission objectives concentrate on ocean and ice monitoring for scientific as well as for economic purposes. Planned to be launched in 1990, its core payload consists of the following two instruments. The Active Microwave Instrumentation (AMI) is a C-band radar combining a Synthetic Aperture Radar and a Microwave Scatterometer. The Radar Altimeter (RA) is a Kuband pulse limited altimeter. In line with Dornier's development strategy, Dornier is responsible for the development of the most critical SAR subsystems High Power Amplifier and SAR Antenna.



Figure 2. Microwave Remote Sensing Experiment

In parallel to the ERS-1, Dornier-System started the development of the X-SAR on behalf of the BMFT. THE X-SAR (shown in Figure 4) is an "X-Band Synthetic Aperture Radar" planned to be flown in a joint mission with NASA's Shuttle Imaging Radar (SIR-C) which is designed for L- and C-band measurements. The first flight of X-SAR is aimed to be in 1991.

Simultaneous observations of ground areas with 3 frequencies (L-band and C-band: SIR-C, and X-band: X-SAR) will provide experimenters radar images with different signatures from the same target scene. Thus, the joint X-SAR/SIR-C experiment will be a new step towards multispectral/dual-polarization SAR measurements from space. The X-SAR is developed in cooperation between Italy and Germany. Italy provides the RF-part and the electrical antenna design. Germany, the system architect, develops the High Power Amplifier, the 12 m long slotted waveguide array antenna made from carbon fibre reinforced plastics, and the onboard data handling. Last but not least, Dornier is developing a realtime SAR processor, which will be located on ground and will provide a quick overview over the amount and the quality of data being collected by the SAR.

4. Key Technologies

The development of new technologies for spaceborne radar systems is a real challenge for industry. The main areas of involvement of Dornier-System are

- SAR antennas,
- high power amplifiers,
- and realtime SAR processing.

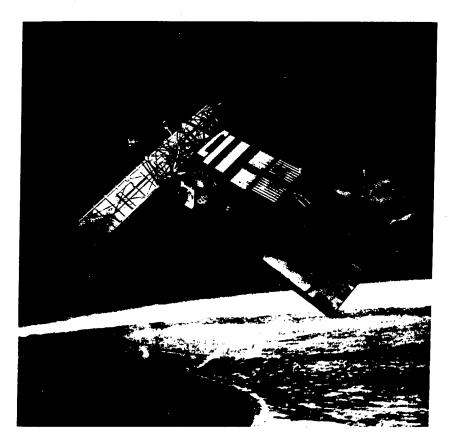


Figure 3. ESA Remote Sensing Satellite, ERS-1

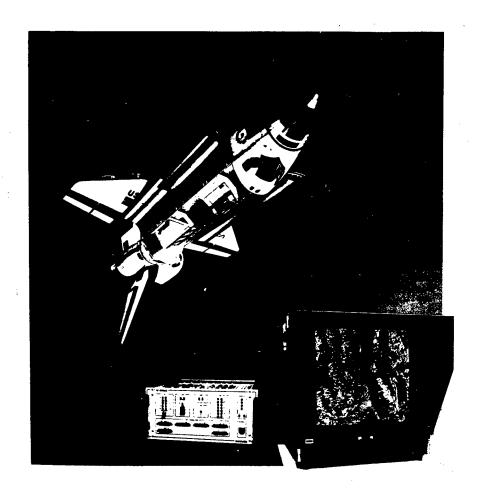


Figure 4. X-Band Synthetic Aperture Radar, X-SAR

In 1978, Dornier-System initiated the technological research on slotted waveguide array SAR antennas made from carbon fibre reinforced plastics due to the need for large lightweight array antennas with extremely high stiffness and thermal stability. This antenna technology is used today for the ERS-1 SAR and for the X-SAR. In parallel to this, a development programme in Germany made high power travelling wave tube amplifiers available for space radar applications. These amplifiers are presently used in all European space radars which need more than 1 kW peak output power. Their use in the Canadian RADARSAT and in some airborne radars is envisaged.

These two technology areas are presently superseded by the demanding technology of the "Distributed Amplifier Active Array Antennas." Large arrays of this kind can provide very high output power in distributing the amplification task to many amplifiers on the rare side of the antenna. These amplifiers can be designed for remote phase control providing a high antenna beam agility with respect to beam steering and forming. The radiating surface of such antennas is typically realized

in microstrip batch technology in order to allow dual polarization operation. The key technological problem of these antennas is the space qualification. Miniaturized solid state power amplifiers, fibre optics antenna feeding and beam forming networks, new substrate materials together with advanced microstrip antenna structures and new in orbit antenna calibration methods must be developed and space qualified, before the next generation spaceborne SAR systems can start their operations on the polar Earth observation platforms in the 90th.

In line with the continuously growing SAR user community, SAR realtime processors are under development at Dornier-System in order to serve the users with high performance SAR images within a reasonable time delay after data collection. The raw data rates of multichannel SAR sensors of the next generation highly exceed 100 Mbps that requires dedicated array processors matched to this application.

5. Outlook

Many on-board and on-ground features are still to be developed in order to provide SAR systems being a viable scientific tool for the remote sensing user community. The attractiveness of SAR systems in future will directly be related to their various operational capabilities, their availability, and the flexibility and effectivity of their onground infrastructure. This concerns user service, data calibration, and image processing. Demanding technological developments are necessary in all of these areas. Dornier-System is prepared to take this challenge.

/09599

ERS-1 SAR Processing with CESAR

43070002d Kyoto Selections from INTERNATIONAL ARCHIVES OF PHOTOGRAMMETRY AND REMOTE SENSING in English Vol 27, 1988 pp 191-199

[Article by Einar-Arne Herland, Division for Electronics, Norwegian Defence Research Establishment, P. O. Box 25, N-2007 Kjeller, Norway]

[Text] Abstract: A vector processor called CESAR (Computer for Experimental Synthetic Aperture Radar), is now in the final stage of development at the Norwegian Defence Research Establishment. It is connected to a supermini computer, and has a maximum performance of 320 Megaflops. This is achieved through parallelism and pipelining, and the processor is fully programmable. This paper describes the architecture of CESAR and the implementation of a set of algorithms for processing of images from the ERS-1 synthetic aperture radar.

1. Introduction

Processing of SAR raw data into images is computationally very demanding, and regular use of SAR images requires a very high processing capacity. With a series of satellite-based SARs planned for the next decade, efficient utilization of the systems requires that suitable processors be available soon. The main objective for developing CESAR is to make possible the use of the coming SARs for surveillance of the Norwegian economic zone, and the first of the available platforms will be ERS-1 to be launched by the European Space Agency (ESA) in the first half of 1990. A prototype of CESAR will be ready by the end of this year, but through extensive simulation and testing of the parts that are already completed, a very accurate estimate of the performance can be given.

2. The CESAR System

2.1 System overview

An earlier version of CESAR has been described in [1]. Figure 2-1 shows a block diagram of CESAR. The processor is connected to a host computer

via the data port module (DAP), which handles the transfer of both data and programs to CESAR. All programming is done on the host computer, which also takes care of communication with surrounding systems, like high density digital recorders (HDDR), discs, graphic displays and output media. This is done via the multiport memory (MPM) on the host computer.

Application programs run in the control processor (CP), which is a Motorola 68020 microprocessor. The application program is written in CESAR PASCAL, which is an extension of standard PASCAL. This is necessary in order to allow parallel processes to run in CESAR, like data transfers between memory modules, and the actual processing. A special extension is also used to allow the CP to refer to data residing outside its own local memory. The CP also controls the other parts of CESAR by sending control information over the VMEbus, which in addition can be used for low capacity data transfers.

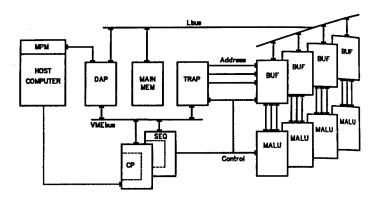


Figure 2-1. CESAR Block Diagram

The actual processing is done in the microprogrammable arithmetic-logic unit (MALU). This module is described in more detail in section 2.2. The CP can also be used for data processing on small amounts of data if it has spare capacity, or if a particular task is not suitable for implementation on the MALU. The MALU gets its input data from and stores its output data in a buffer memory (BUF). BUF is divided into three banks of equal size, and when running a program in the MALU, two of the banks are connected to the MALU input, and the third receives the output data. The connections between the BUG data banks and the MALU I/O-lines is under full program control. CESAR contains four identical, parallel sets of MALU-BUF, which work completely synchronously, always with identical programs, but on different data sets. Addressing in the BUFs is performed by the triple address processor (TRAP), where "triple" refers to the three data banks in BUF. The same addresses are fed to all four BUFs. Synchronization of MALU, BUF and TRAP is performed by the sequencer (SEQ).

The main memory module (MAIN MEM) is used to store intermediate data, and in the case of SAR processing it is used as corner turn memory. Input data from MPM is typically fed directly to the BUFs and output data is transferred directly from the BUFs to MPM, while the MAIN MEM is used for data transfers to and from the BUFs. MAIN MEM and the BUFs are connected via the Lbus, which is controlled by the DAP. The DAP can transfer data between any two memory modules connected to it.

Data transfer capacities are 40 Mbytes/sec locally on the Lbus, 10 Mbytes/sec for transfers from MPM to Lbus, and 6 Mbytes/sec from Lbus to MPM. Each of the three I/O-lines between BUF and MALU transfers data at a rate of 40 Mbytes/sec. In the present configuration MAIN MEM contains 32 Mbytes of dynamic RAM, and each BUF has 6 Mbytes of static RAM equally divided on three banks. CESAR thus contains 56 Mbytes of memory in addition to CP's local memory, which is mainly used for storing system information.

In order to run an application on CESAR, four sets of programs must exist. Three of them are inside CESAR, and the fourth is running in the host, taking care of data communication with peripheral devices as mentioned above. It is also possible to do actual data processing on the host. The host programs are typically written in FORTRAN. The three program sets in CESAR are the CP program and the TRAP and MALU programs. A library of MALU and TRAP programs exists, and if this library is sufficient, only the CESAR PASCAL program has to be written, and the MALU and TRAP programs are implemented as function calls. Both compilers and simulators exist for MALU and TRAP in case a user wants to write programs for these modules. There also exists a simulator for the CP program, whereby bottlenecks in the program can be detected and performance estimated.

2.2 The microprogrammable arithmetic-logic unit, MALU

The actual computations are performed by the MALU. This module consists of a matrix with 128 identical S-elements, connected as a cylinder, as shown in Figure 2-2. The right-hand view shows the data matrix and the interconnections between the 16 by 8 S-elements, while the left-hand view shows how the matrix is connected into a cylinder. Data is fed to the top of the cylinder on parallel form, where it is converted to serial form and clocked bitwise down into the cylinder. On the output the reverse operation is performed. Two 32-bit data words enter and one 32-bit word exits the cylinder every 100 ns when a program is running.

Each S-element is a single VLSI chip, and it has a repertoire of 32 instructions implementing floating point, fixed point and logical operations. It works with bit-serial data, and uses on-chip pipelining to implement the instructions. It has 4 input lines, two from above and one from each of the horizontally neighboring elements, and 6 output lines, two vertically downwards, two horizontally and two diagonally downwards. For the elements in the bottom row only one output exists

vertically. The routing of data along these I/O-lines is programmable, and data can move horizontally and downwards through the matrix. On the top of the cylinder data is input from one or two of the data banks in BUF, and the output data from the bottom row is written back to the third data bank of the BUF.

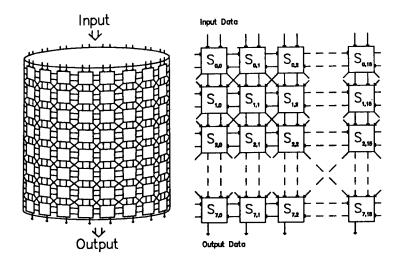


Figure 2-2. The Systolic Array MALU

When MALU is running a program, each S-element performs a single operation with a fixed routing combination given by the instruction word. The S-element contains delay registers in order to insure synchronous arrival of the operands, and it can store 32 different instruction words, which gives rapid change of MALU program. By combining the operations in different S-elements, complex algorithms can be implemented by a single pass through the MALU. Division is not implemented in the present version of MALU.

The actual throughput depends on the algorithm implemented. If a simple addition of two vectors is performed, only one cylinder row is used, and the throughput is accordingly only 1/8 of maximum performance. The more complicated the operation, the better the performance. Figure 2-3 shows how a radix-2 FFT butterfly is implemented. It uses three rows, and the rest of the rows are not shown, since data only is routed directly through them. Since the width of the algorithm is four S-elements, four butterflies fit around the cylinder. The W's are twiddle factors, while X and Y are the complex input data.

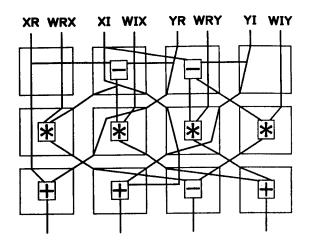


Figure 2-3. Radix-2 Butterfly

3. SAR Processing on CESAR

The implementation considered here is the one which is going to be used for processing of SAR images from ESA's ERS-1 satellite. This is a C-band SAR, which is reflected in some of the algorithm parameters. It has less range curvature than L-band SARs, but more than an X-band SAR. Yaw steering will also reduce the range cell migration (RCM). In spite of these differences, the structure of the algorithms would be much the same for all wavelengths. Highly squinted systems, however, may require different processing algorithms.

3.1 Processing algorithm

The algorithm used here is the socalled range/doppler algorithm, where the two-dimensional compression of the target signal histories is divided into two one-dimensional operations, range compression and azimuth compression. Range dependence of the azimuth signal is handled by changing azimuth filters across the swath, while range cell migration correction (RCMC) is done in the azimuth frequency domain. This is valid for SARs with small squint angles.

Processing is done in terms of reference scenes of 100 km by 100 km. In order to achieve this, the scene is broken down into a number of smaller processing blocks. This is described in more detail in section 3.2. The algorithm described in this section applies to a single processing block.

Figure 3-1 shows a block diagram of the algorithm. The first step is to unpack the raw data from the packed 2 x 5 bit per complex sample used in the input, and convert to 32-bit floating point format used in the computations. The next step is to range compress the data, which consists in fourier-transforming the range vector, multiplying with a

reference filter, and inverse transforming the result. At this stage the data is converted to 16-bit integer format and intermediately stored in MAIN MEM. By properly scaling the range reference filter, the full dynamic range of the range compressed data is retained. The conversion is done to save memory space and data transfer capacity on the Lbus.

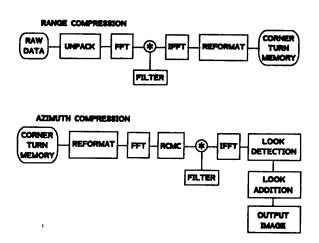


Figure 3-1. Block Diagram of SAR Algorithm

When the processing block has been range compressed, azimuth compression is performed. Corner turning of the data is done by reading back the range compressed data from MAIN MEM in azimuth direction. The first operation is to convert the data from 16-bit integer form back to 32-bit floating point format. The azimuth vectors are then fourier-transformed and RCMC is performed by interpolating in the transformed data in range direction according to the target trajectory. The straightened azimuth vectors are then multiplied with the look filters and inverse transformed. Look detection is done by taking the absolute value of the compressed data, and the looks are added together. Overlapping parts from previous processing blocks are read back from MAIN MEM and added to the present data. The part containing the full number of looks is then output to the host, and the incomplete part is written to MAIN MEM.

The processing chain described above is not complete, and it is only valid for a fast-delivery type product which is not geometrically corrected. In addition to what is shown above, doppler centroid frequency estimation is performed, but only on a small part of the data, and if orbit data is not available, autofocusing must be applied to estimate the azimuth doppler rate. The processing necessary to implement these steps is only a few percent of the total processing load. Geometric correction of the compressed image, however, is a major operation which can be quite time consuming depending on the level of accuracy desired.

3.2 Implementation

The input data matrix for a 100 km by 100 km scene consists of about 6000 by 25000 complex samples, in range and azimuth, respectively. This is divided into 4 by 35 processing blocks of identical size. Figure 3-2 shows this division into processing blocks.

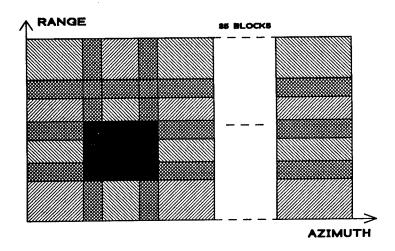


Figure 3-2. Division of Scene Into Processing Blocks

CESAR processes the four blocks lying at the same azimuth position in parallel, with one block for each of the four MALU-BUF sets. The block length is 2048 in range and 1024 in azimuth, suitable for multilook processing. Range overlap is approximately 700 and azimuth overlap is 256, corresponding to one out of four looks. Since a single block is too big to fit into one BUF, it is processed by dividing it into smaller blocks of f.ex. 32 vectors at a time. When possible, these vectors are considered as one long vector, thereby effectively eliminating the importance of the pipeline tails in MALU.

A set of different MALU programs is needed to implement this algorithm. If a specific operation, e.g. unpacking of raw data, cannot be performed in one pass through MALU, more passes will be needed, and the programs for these passes may or may not be different from the programs in previous passes. In the case of FFT, the number of passes depends on the vector length. One pass implements a single butterfly, which means that a radix-4 lK FFT needs 5 passes, but in this case all passes use the same program. A 2K FFT needs the same 5 passes and in addition a radix-2 pass, which uses a different program. Multiplication of two complex vectors is done in a single pass, while unpacking of raw data needs two passes. The reason for this is the cyclic nature of the input. Since the cylinder input row has 16 S-elements, the input data must also be cyclic with a period of 16. If unpacking is to be done in a single pass, the input will lose its cyclic nature. Vector addition

is done in one pass, while the square root in the detection operation needs 3 passes with different programs. It turns out that the total number of MALU programs needed for SAR fast delivery images is 10-15, which means that all the programs can be downloaded into the MALU before processing starts.

3.3 Performance

Since MALU works synchronously, it is easy to calculate the performance of a specific algorithm. The time used is proportional to the vector length, except the pipeline tails at the beginning and end of the vector, which only depend on the algorithm, and is longer the more complex the algorithm. The vector lengths used here are long enough to justify neglecting the tails.

Unpacking a 2K vector of raw data requires two passes, where the first pass is shorter than the second. The total time is

 $25000(512 \times 200 \text{ ns} + 2048 \times 200 \text{ ns}) = 12.8 \text{ s}$

A 2K FFT needs 6 passes through the MALU, which gives

 $2048 \times 6 \times 200 \text{ ns} = 2.5 \text{ ms}$

for a single MALU. CESAR thus uses 0.6 sec on a 2K FFT. A 1K FFT is performed in 0.25 sec on the average in CESAR. Filter multiplication takes 0.2 ms for a 1K vector, and conversion from 32-bit format to 16-bit format the same. Unpacking, range compression and format conversion accordingly require 160 seconds for the whole scene.

Azimuth compression is performed on 35×5400 lK vectors = 189000 lK vectors. The forward and inverse FFTs and filter multiplications are done in 110 seconds, if it is assumed that the multilook processing requires the same time as onelook processing. If range cell migration correction uses a four-point interpolation filter in range, this operation consumes 40 seconds for the whole scene. When reformatting of the input data, look detection and addition are added, the total time for azimuth compression will be approximately 175 seconds.

The calculations above assume that data is always available in the BUFs. This is achieved by using double buffering, where data I/O between BUF and the Lbus is done simultaneously with the MALU processing. The Lbus is able to feed the four MALU-BUF sets with data because many passes are applied to all the data before it is output to the Lbus again, and the data format is more compact for the Lbus data than for the MALU data. The goal for processing of a reference scene is 8 minutes, which will be achieved with the system described above.

4. Conclusion

During the design of CESAR, SAR processing has been the main application area. The system can, however, be used in a wide range of application areas, notably signal and image processing. It is a vector processor, and is especially efficient for complicated computations where many operations are to be performed on the data.

References

1. V. S. Andersen, T. Haugland, O. Sorasen: "CESAR--A programmable systolic array multiprocessor system." The first International Conference on Supercomputing Systems, Dec 1985, St. Petersburg, FL.

/09599

Jena Photogrammetric Instruments Manufacture from 1984-1988

43070002e Kyoto Selections from INTERNATIONAL ARCHIVES OF PHOTOGRAMMETRY AND REMOTE SENSING in English Vol 27, 1988 pp 317-323

[Article by Dr. sc. techn Werner Marckwardt, Kombinat VEB Carl Zeiss JENA, GDR, Manufacturers Forum]

[Text] 1. Introduction

The history of Jena photogrammetric instrument manufacture started with the development of the first test models of a stereocomparator in 1901 and its series production from 1903. Up to the year 1945, there were more than hundred developments for recording, restitution and auxiliary instruments which were, for the most part, based on optical and precision-mechanical principles. After several years of After several years of interruption in the production and development of photogrammetric equipment after the end of World War II, there was a new start in 1949 when the former traditional developments had first to be continued. It was not before the sixties that the photogrammetric instrument system could be completely redesigned, with the electric and electronic components gaining a growing importance. Some instruments from this stage of development, like the Interpretoscope, the universal analogue Topocart Stereoplotter, the Transmark Laser Point Transfer Instrument as well as the UMK 1318 Universal Measuring Camera, achieved particular success and are, still today, included in the production programme of the Jena Works.

Nearly all developments of the eighties comprise modern microcomputer control systems, in addition to the proven opto-mechanical components. The ever-growing and rapid advances in the field of microelectronics permitted an increasing extension and perfection in designing technological procedures and instrument lines for data acquisition and analysis. In the four years following the ISPRS-Congress in Rio de Janeiro, the main emphasis in developing the Jena photogrammetric instrument production was laid on equipment systems for aerial photography and multi-spectral photo analysis as well as components for

analytical evaluation. Table 1 shows the essential new and further developments of photogrammetric instruments.

2. LMK Aerial Survey Camera System

With the introduction of forward image compensation (FMC) for compensating the forward motion of the airplane in the photogrammetric survey cameras, the Jena Works made possible a substantial quality improvement of the airphotos. Rich experience gained with the LMK system on all continents over the past few years could then be used in the new LMK 1000 System.

LMK 1000 Aerial Survey Camera System (1986)

- cones of 9, 15, 21, and 30 cm focal length,
- maximum speed of forward motion compensation of 64 mm/sec.,
- exposure of camera data onto the film edge (when using special interfaces, also external data, e.g. from a navigation system, can be exposed).
- control of two systems with the aid of one control unit,
- connection facility for the exposure of fiducial marks,
- automatic exposure control with half f-stop intervals.

NCU 2000 Navigation Control Unit (1987)

- combination of navigation telescope and control unit for regulating drift and overlap in airphotos taken with the LMK or LMK 1000, resp., $+80^{\circ}$ to -10° angular aperture,
- turret for different navigation line patterns according to the cone used,
- -luminous travelling marks in the telescope image.

3. Multi-Spectral Photo Analysis

A particularly efficient method of photo analysis is the mixing of picture information obtained from different sources and spectral ranges. The further improvement of the Rectimat C and Kartoflex has, thus, taken into special account the possibilities of multispectral projection and vision.

Rectimat CM Precision Colour Rectifier (1987)

- multispectral projection of the three channels of an MKF-6/MSK-4 photograph according to the additive method,
- automatic vanishing point control,
- programme for the automatic rectification by measuring image coordinates through shifting the projected image and by internal computation and transfer of setting values,
- improved illumination of the projection table.

Kartoflex M Computer-Assisted Interpretation and Map Revision Instrument (1988)

- optimized multispectral vision by means of novel illumination systems for all three input channels of the optical viewing system,
- parallax measuring facility and programme for determining the height differences from parallax differences,
- improved connection possibilities for workplace computers by extending the serial interface.

4. Components for Analytical Evaluation

Due to economical aspects, it is not possible yet to do without analogue memories (photos) and visual interpretation methods in photo evaluation.

The computer-assisted, analytical stereo evaluation of photographs has, thus, gained a growing importance over the past few years, a local interconnection of systems taking place. For these tasks, the Jena Works designed several hardware and software components.

MTU 5300/P Magnetic Tape Unit (1984)

- data buffers,
- recording on 1/2" magnetic tape on the basis of the CM 5300 Drive Unit.
- parallel interface,
- connectable to Coordineter H, Orthophot E, DZT 90 x 120 and DZT 90 x 120/RGS Digital Plotting Tables.

ZIF 2 Digital Interface Unit (1985)

- connectable to Dicometer, Stecometer C, Topocart D, Stereometrograph G and Stereoplot for the acquisition and transfer of maximally 4 coordinates via a serial interface (programmable),
- double foot switch,
- display of four coordinates and control panel with 32 buttons as an addition.

Dicometer Precision Stereocomparator (1985)

- -23×23 cm maximum format,
- viewing magnification 8x, 14.5x and 24 x (Galilean telescope),
- drive of measuring spindles via selsyns,
- incremental shaft-angle digitizers (IGR) directly coupled with the spindles (resolution $1 \mu m$),
- six selectable luminous measuring marks,
- mean error of the measured photo coordinates less than or equal to plus or minus 2 μ m,
- special version with shaft-angle digitizers for the controls x,y,z and py for an extension to the Analytical Plotter.

DICOP Programming System (1986)

- computation of the model or national coordinates, resp. obtained from stereocomparator measurements with programme modules for correcting instrument errors and for interior relative and absolute orientation.

STRAUS Programming System (1986)

- on-line aerotriangulation programme for analogue plotters with strip adjustment for the computer-assisted stereomapping system DZT 90 x 120/RGS,
- additional programmes for determining the coordinates of projection centres and for the graphical presentation of results, including residual mismatches.

DZT 912 Digital Plotting Table (1988)

- advanced version of the known family of digital plotting tables with extended applicabilities for drawing tools (Indian ink, engraving, fibre-tip tracer, ball-point-pen).

Table 1. Photogrammetric Instruments from JENA 1984-1988

Year	Instrument/Programme	Application
1984	MTU 5300/P	Magnetic tape unit with parallel interface as peripheral unit for Coordimeter H, Orthophot E, DZT 90 x 120 and DZT 90 x 120/RGS
1985	Dicometer	Precision stereocomparator for the picture format 23 x 23 cm
	ZIF 2	Digital interface for connecting units with 2 or 4 encoders to computers via a serial interface
1986	DICOP	Programme package for the on-line evaluation of Dicometer measurements
	STRAUS	Programme package for on-line aerotriangulation with the DZT 90 x 120/RGS
	LMK 1000	Advanced model of the LMK Aerial Survey Camera System
1987	NCU 2000	Navigation control unit for the LMK and LMK 1000 Systems
	FEAG 400	Photoscan/photowrite system with special facilities for the direct writing of scanner data
1988	DZT 912	Advanced model of the family of digital plotting tables DZT 90 x 120
	Kartoflex M	Computer-assisted interpretation and map revision instrument with improved image mixing possibilities

Literature

- 1. Muller, G., Beck, B.: New equipment for logging photogrammetric data. Jena Review 31 (1986) 4, pp 179-180.
- 2. Starosczik, H., Tiedeken, W., Beier, L.: Highest accuracy in photogrammetry: the new DICOMETER Stereocomparator. Jena Review 31 (1986) 4, pp 175-178.
- 3. Riedel, H.-J.: On-line Mebwerterfassung und -verarbeitung mit DICOP. Vermessungstechnik 34 (1986) 7, pp 227-229.
- 4. Bauer, G.: On-line strip triangulation with the DZT 90 x 120/RGS Computer-Assisted Stereoplotting System. Jena Review 31 (1986) 4, pp 163-166.
- 5. Vob, G., Zeth, U.: New features of the LMK Aerial Camera System. Journal for Photogrammetrists and Surveyors (JPS), Jena 1988.
- 6. Rulf, I.: RECTIMAT-CM, an additive colour viewer and precision rectifier. Journal for Photogrammetrists and Surveyors (JPS), Jena 1988.
- 7. Schumann, R.: Die Entwicklung der photogrammetrischen Gerate in Jena von der Jahrhundertwende bis zum Jahre 1945. Kompendium Photogrammetrie XVIII, Leipzig 1986.

/09599

Experiences in Implementing an Expert System Supported Man-Machine-Interface for the Configuration of the Intelligent SAR Processor

43070002f Kyoto Selections from INTERNATIONAL ARCHIVES OF PHOTOGRAMMETRY AND REMOTE SENSING in English Vol 27, 1988 pp 344-356

[Article by W. Noack, A. Popella, R. Konjack, DFVLR, German Aerospace Research Establishment, D-8031 Oberpfaffenhofen, Federal Republic of Germany, Commission II, WG II/5]

[Text] Summary

In view of ERS-1 and X-SAR, DFVLR is establishing a high throughput Processing and Archiving Facility (PAF) for high precision SAR products. Concerning the requirements throughput and product quality, it has been realised that the SAR processing task needs a distributed and dedicated computer system to be controlled by an expert system. The solution is called ISAR, the Intelligent SAR processor.

During the first development phase, a prototype of the man-machine-interface has been implemented. It is the task of this interface to monitor, control and debug the whole processing system. Especially, there has been investigated the configuration capability of this expert system controlled man-machine-interface with relation to SAR processing.

This paper presents the experiences gathered during the development with emphasis on structuring the knowledge domains and the realisation of facts and rules applying frame based methods. Additionally it will demonstrate the use of an expert system shell for software engineering. Recommendations for future work will also be given.

Keywords: ERS-1, X-SAR, Processing and Archiving Facility (PAF), Intelligent SAR Processing (ISAR), expert system, software engineering, man-machine-interface.

1. Introduction

The upcoming new generation of spaceborne SAR sensors like ERS-1 or X-SAR has been designed to be able to acquire a huge amount of SAR scenes which is in the range of several ten thousand scenes per year. However, according to experience 1,2 it is unrealistic to handle such a fload of data by computer systems which take care of a pure throughput optimisation only. In this case, just simple problems anywhere in the system can lead to unsolvable situations at the man-machine-interface. The term real time processing 3 could be applied and situations similar like those in the operations of a satellite ground station 4,5 will occur at the "system console."

In the first stage of the ISAR development a top-down decomposition of the basic functional requirements has been performed. The guidelines during this process have been determined to characterise the algorithms in terms of their inherent parallelism. Henceforth, the parallelism can be found and sorted in decreasing order of granularity:

- job execution,
- task execution,
- process execution,
- instruction execution,
- register transfer and,
- logic device.

The decomposition order has been followed down to the level of process execution, allowing a system implementation, using high level programming languages. The result is a distributed system where the overall work has to be shared between market available computer systems connected by standard communication links. The required ISAR functions have been mapped onto the best suited architecture which is sketched in Figure 1.

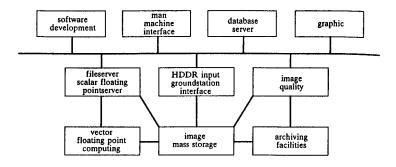


Figure 1. ISAR Functional Decomposition

Now, for each of these functions a reasonable computer system had to be selected. It is evident that the most demanding element of the distributed system is the man-machine-interface.

It has been found² that the realisation of the idea could best be accomplished by applying technology, developed and available in the field of knowledge based systems. From a great variety of definitions of a knowledge based system, the following one, which was given in, offers the necessary scope: a knowledge representation system provides a set of conventions for encoding some class of facts plus facilities for retrieving the stored facts and/or drawing some class of inferences from them. Three different issues have been distinguished:

- Knowledge representation issues:
- -- completeness,
- -- expressive power,
- -- well-defined semantics,
- -- inferential validity.
- Programming issues:
- -- editing,
- -- debugging,
- -- efficiency.
- Human factors:
- -- explanation,
- -- robustness,
- -- user models.

The geometry part of the SAR-processor has been intentionally chosen as the representative sub-domain. This domain contains a considerable amount of quantities and possesses a close inherent connection to SAR processing and simulation. Moreover, already before project start, a full understanding of the domain has been developed, a complete mathematical formalisation was available as well. The idea was, that a full-scale implementation of a control system for the geometry domain would reveal the techniques and problems concerned with knowledge representation, structure of knowledge base, size, etc.

The geometry model describes, with respect to a set of suitable coordinate systems, a satellite-SAR in orbit, looking at a target fixed on the moving earth. A full description of the domain will be given in Chapter 3. The ISAR "prototype" should henceforth prove the feasibility of the ISAR "expert system," realised as the control system equipped with a selection of (sub-) expert systems. Particularly, the possibility of the retrieval of relationships between the quantities of geometry should be demonstrated. As a side-effect the system should evaluate numerical values for them, given a set of input parameters and constraints. The results will be demonstrated in Chapter 4.

2. Objectives

The root idea in the design of the ISAR processor is to improve the operation of the man-machine-interface of a computer scientific application package constrained by the requirements of high throughput, high precision and flexibility. The term man-machine-interface is not being looked at as a static one, instead the whole programming of ISAR is considered an evolutionary process, which means the inclusion of operations and maintenance as the driving sources for further requirements once the development has been finished. The resulting demand of this idea comes quite close to some aspects of the intelligent man-machine-interface proposed by the Fifth Generation Computer Project. At this stage especially, the separation of the man-machine-interface from the signal processing machine (and other subsystems) should be stressed.

The basic function of the ISAR expert system is that of a control system. It manages the overall processing environment, including all interfaces to other PAF-systems and allows for a far-reaching automatic and unattended processing operation. 8 Looking at the expert system as a control system, it has to make use of a series of other (sub-) expert systems, such as systems for interpretation (analysis), diagnosis, design, planning monitoring and others.

But the basis for all this is the existence of a proven SAR processor and data flow theory. This theory is expressed by a set of rigorous formulae and accompanying descriptions, modelling the behaviour of an ideal processing machine. With the occurrence of any problems, the human operator is now able to detect that the behaviour of the processor is not in accordance to the requirements of the theory, by comparison to actual and ideal status.

For expert system development, it is recommended that a representative sub-domain be selected and implementation trials be performed. This phase is considered to be more an experiment than a real software phase. The results shall confirm the feasibility of the expert system with respect to knowledge representation, structure of the knowledge base, evaluating the size of that base and identifying the constraints on hardware and software.

Additionally, but no less important, the human aspects 10,11 of the expert system development had to be experienced thoroughly. First of all new forms of teamwork and cooperation have to be explored. It is well known that the number of people comprising the team is larger than in conventional software projects. Furthermore, close attention of everyone involved over a relatively long period is required. The importance of online and up-to-date documentation has to be especially stressed. It is clear that everyone involved in the exploration of new terrain has individual expectations which can differ from the project

goals. The question is, how would the human aspect influence the expenditure of time, man power and machine resources?

Moreover, the prototype shall allow the calculation of the cost for the overall ISAR expert system and establish control instruments with respect to time, goals and success. The definition of quality measures and the set-up of quality control procedures should be achieved as well.

3. Domain Description

In this chapter the problem or domain knowledge specific to the particular kind of task that the expert system was set up to solve is shortly described.

The ISAR overall system, besides the SAR processor itself, is comprised of a SAR simulator for generating raw data for arbitrary orbiting imaging radar systems. Designed as a flexible engineering test tool, such a validated simulator is to be considered an indispensable part of the ISAR system because it allows a controllable verification of all important processor subsystems during the installation and operational phase as well as a reliable performance demonstration of the overall processor characteristics.

The mathematical simulation of SAR raw data on a computer is based upon the approach to transform a fully described target into the radar space, with respect to its properties, taking into account the relative motion between SAR sensor and target, and scattering— and propagation effect as well. Complex equations describe the SAR components and their physical interactions. The result is the two-dimensional signal response, stored on a data carrier.

Within a close loop, the processor could now access this data set and process it by means of complex algorithms in such a way that the result—a final SAR image—is a measure for the scattering properties of targets at the point of time of maximal illumination. Ideally, the processor gives geolocation information for the processed targets, which is equal to the target position given as a simulator input.

The simulator needs the geolocation of a target as an input, the processor gives it as a result. Both subsystems, however, achieve their results due to the knowledge of the dynamic illumination process between sensor and target. This means, that both systems must know the complete motion of a sensor carrier (six degrees of freedom) with respect to the illumination time interval.

Therefore, regarding the geometrical aspects of SAR, different functions have to be performed by the simulator or the processor, respectively. However, they can use the same basic mathematical model. Only one flexible model has to be developed and integrated in the knowledge

base--processor and simulator commonly use it, however, with a different representation and parameterisation.

For the prototype development, only a subset of the complete geometry model was chosen. Under the objective of studying how to build up a knowledge base, to establish an explain component etc., the basic SAR equations, with respect to geometry, were taken: Equations to compute slant range and Doppler frequency between target and sensor.

The expert system shall now enforce a complete and, as far as possible, error-free input of the mathematical parameters as well as the model parameters regarding orbit, earth, platform motion, etc.

Furthermore, it shall support the selection of hardware and software components for computation of the equations, depending on the input data and system properties given so far. In case, a confused user should be tracked by the system.

4. Software Engineering Methods

The development of the expert system has been split into four consecutive phases. These phases are called preliminary studies, mock-up phase, prototype phase and operational phase. During the preliminary studies some main questions have to be answered:

- does the considered application involve knowledge, judgment and expertise of human experts?
- where are the sources for this expertise?
- who should be the user of this expert system?
- what are the expected advantages of the expert system versus the conventional approach?
- how should the expert system be tested and validated?

Two documents have been published at the end of this phase. The first one is the "Users Requirements Document" (URD). It identifies the domain of expertise and the main functions of the expert system. The second document is a draft of the "Software Requirements Document" (SRD). It classifies the sources of expertise like human experts, books, etc. and defines the hardware and software environment in which the prototype is developed, tested and executed. It also explains the relationship to the operational environment.

The production of the URD and SRD is rather different. The production of the URD is straightforward but the "artificial intelligence" part of the software (knowledge base, reasoning, etc.) has to be specified precisely. The draft SRD will deal mainly with those parts which can be considered as conventional software.

The main objective of the mock-up-phase is to consolidate the SRD. The aims of this phase are to confirm the feasibility of the system and to

take decisions concerning knowledge representation and structure of the knowledge bases. This phase is like an experiment, it is performed by successive iterations, reopening issues until the objectives described earlier are met satisfactorily.

The prototype is the first full-scale implementation of the expert system. The objective of this phase is to evaluate its functions before developing an operational system. The prototype is developed iteratively, each iteration involving some modification of the knowledge base together with testing and evaluation.

The operational phase consists of the integration of the expert system in the target environment. Developing the operational system will be closer to classical software engineering than to knowledge engineering.

Any software development includes the preparation of documentation. The iterative development of the prototype and the progressive build up of the knowledge base imposes a strict software configuration control. Henceforth, additional documentation is produced for that purpose.

5. Results and Experiences

The development has been carried out in two phases. The first phase was mainly dedicated to the setting up of a knowledge base by which calculations of certain parameters could be performed. Given a situation defined by earth model, satellite movement by orbit characterisation and point target, the related SAR-relevant parameters like slant range and Doppler frequency could be calculated. The resulting values could then be compared to the ones which had been derived manually and therefore, the verification of the mathematics implemented could be performed. The formulae have been implemented by using tools from the expert system shell or LISP functions. Additionally, the first phase was used to experience an explanatory machine which allowed for an online inspection of parameters, variables and functions in the related formulae.

In phase two a reexamination of the knowledge base constructed so far has been performed. On this foundation, the knowledge base could be enlarged. Some amendments have been added. However, the most important knowledge representation concept to be studied was that of a rule system. The fundamental idea in the usage of the rule system was to make the man-machine-interface robust. Robustness shall be defined as the ability to deal with new facts not yet included within the current knowledge base. However, the fundamental prerequisites for achieving this, are to have the accessability of high level principles down to simple facts.

Three different knowledge bases have to be distinguished:

- ISAR-PRO: domain knowledge about geometry,
- ISAR-IMG: images and graphics for the user interface,
- DOCUMENTATION: all information needed to provide automatic technical documentation.

The structure of the knowledge base basically distinguishes between several classes. Among these are classes for

- the computational elements for the calculation of geometry related parameters,
- the computing facilities used in the calculation (hardware and software),
- the models (e.g., earth, sensor, orbit...) of the object,
- rules allowing for reasoning about geometry,

and others. The class of the computational elements is the biggest one. As can be seen from Figure 2, the mathematical structure of a formula has been used as a characteristic criterion for the objects. This led to the subclasses of parameters, transformation-matrices and vectors as the major constituents of formulae.

The prototype has been developed completely on a LISP machine. The software configuration was supported by a customary in the market available expert system shell. Some parts of the prototype have also been implemented using pure LISP code.

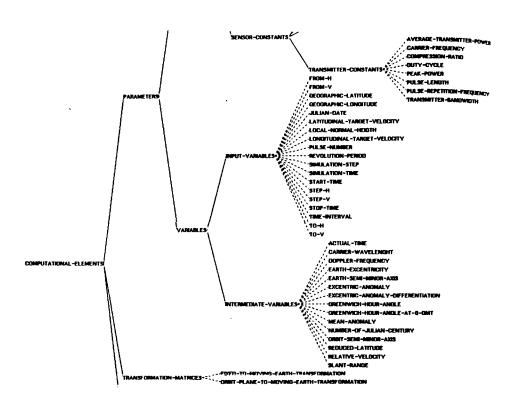


Figure 2. Formula Part of the Knowledge Base

The knowledge domain has been represented using frames. This technique allows for a standardised mapping of the object domain into its representational model. Once the object domain, and this is in our case the underlying apparatus of formulae, has been proven, regarding completeness and semantics, then other knowledge representation issues, as stated in the requirements for the expert system itself, can be investigated. Besides the two mentioned issues, the expressive power of the model as well as the inferential validity have to be considered in comparison to the theory.

The frames could easily be arranged into a meaningful hierarchy by exposing the obvious building blocks of the objects. Attributes, which can either be inherited down the hierarchy relationship or stay static at the level of definition, completed the basic level of knowledge representation. At this stage it was now possible to perform a verification of the implemented system by simply running computations for slant-range or Doppler, giving well defined start-conditions to the system.

At the following stage rules have been introduced to allow for the inference of the type of answer. A sample of a rule which works at the initialisation of a reasoning process is given in Figure 3.

IF ((THE ITEM OF EXPLAIN-PANEL IS ?ITEM)

AND (THE QUESTION OF EXPLAIN-PANEL IS VALUE)

AND (CANT.FIND (THE PARAMETER.VALUE OF ?ITEM IS ?VALUE))

AND (THE INPUT.PARAM OF ?ITEM IS ?INPUT))

THEN (ADD (THE ANCESTORS OF COMPUTATIONS IS ?INPUT)
USING ROOT-RULES) (THE NEXT.RULE.CLASS OF COMPUTATIONS
IS COMPUTE-VALUE-RULES))

Figure 3. Start Rule

The type of answer can be determined by the type of user posing the question and the type of question itself. According to the configuration task requirements, it is possible to reason about

- the definition of objects,
- the defining formula,
- the dimension,
- relationships between objects, and
- values.

Rules also make the man-machine-interface robust against false operation.

As mentioned in Chapter 1 and 2, the main goal in the realisation of the expert system is to improve the operation of the man-machine-interface. Unfortunately, due to shortage of time it was not possible to experiment with different levels of operator education. It has been shown that there are very valuable measures of operator work-load estimation like time-stress ratio or work-load ratio. In order to avoid the overloading of operators, the work-load must be kept at a moderate level. In the worst case, exceeding the schedule in a real time environment can lead to a loss of data.

Commonly, and this has been confirmed in, 12 the objective operator work-load varies in connection with performing subtasks. By experience, in many situations false operation in subtasks most likely leads to systemwide problems. Therefore, a criterion to distinguish between superior and poor operator could be the definition of the ability to perform certain subtasks in a predefined context. This ability would then reflect the level of understanding of the model. Vice-versa, the system then had first to determine which model the user wants to apply and then derive the appropriate answer. Figure 4 shows the answer to a user, experienced in the geometry domain, to the question for a specific formula. As a result the question has been answered but the representation of the subject is not adequate. Therefore, the capabilities should be enhanced in the direction of pure mathematical formula output, that means that the system should be able to distinguish between different levels of user directed representations.

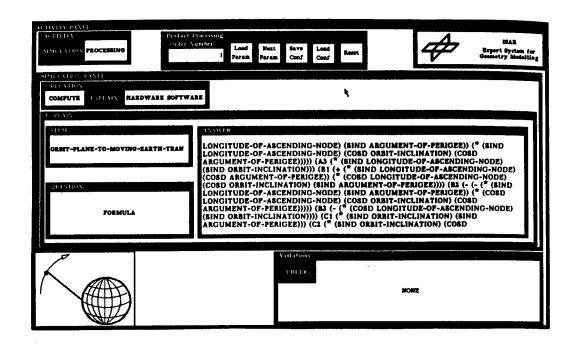


Figure 4. Reasoning About Formulae

Furtheron, the loading of a new context is in the range of minutes. It is even worse when a new start-up procedure has to be done. However, it is clear that with the processing of real time data one cannot afford any waste of time. This means that knowledge at a higher level, where subsystems communicate, has to be used to implement a reasonable system. Therefore, in order to achieve a better system performance, it is necessary to apply traditional and proven software development methods. Finally, parallel processing could help a lot if objects and their relationships could be represented physically.

The size of the system can be given to about 200 objects which have been represented as frames. It comprises less than 50 rules, several display images and additional mathematical support. The physical size is less than 1 MByte, including all additional knowledge bases. It has to be stressed that during the development the system has grown very rapidly. This caused a problem in keeping track with the documentation which has been prepared on another system.

One of the most important experiences during the prototype development phase covered the fact that at the beginning of the project, the role of the expert system user was not fully clarified. Due to that, problems occurred with respect to the design of the explain component, as well as to the construction of a knowledge base (what has to be included?). To avoid all this, the classification of the final user—the person who operates the expert system—has to be done explicitly before any decision is taken regarding knowledge representation and structuring the knowledge base.

He should be included into the development process from time to time. In this way it will be possible to prepare a user-specific screen layout. Generally, other important issues to be implemented would be a formula which allows reasoning about dimensions of parameters and a data dictionary.

6. Conclusion

As a very first step in the direction of DFVLR's Intelligent SAR processor ISAR, an expert system prototype, covering a small sub-domain of the ISR processing system has been developed. It has been found that, especially with respect to the configuration task, the formal classification of the expert system user is superior to any development of a man-machine-interface. The final user has to be involved already in the mock-up and prototype phase because his behaviour influences the development of the prototype. The explain component has to consider the user class and must allow the relation between the mathematical model (knowledge base in the Al part) and the implemented counterpart (procedural part).

The evaluation of the ISAR prototype expert system has shown that the project objectives should be achievable using the applied methods and technologies.

Bibliography

- 1. Noack, W., Pich, M., Popella, A., Runge, H., Konjack, R. "Correlation of Synthetic Aperture Radar Data Using a Knowledge Based Processing System," 2nd Int. Conf. Expert Sys., London, 1986, pp 221-228.
- 2. Noack, W. "Defining a Knowledge Base SAR Processor," Proceeding TROC Symp. Photogrammetric Remote Sensing Systems and Data Processing Analysis (Baltimore), pp 381-388, 1986.
- 3. Le May, M., Hird, E. "Operator Workload: When is enough enough?" Communications ACM, (29) 7 1986, pp 638-642.
- 4. O'Reilly, C. A., Cromarty, A. S. "'Fast' is not 'real-time': Designing effective real-time Al Systems," SPIE, Vol 548, Applications of Artificial Intelligence II (1985), pp 245-257.
- 5. Golden, M., Siemens, R. W. "An Expert System for Automated Satellite Anomaly Resolution," priv. comm.
- 6. Kleinrock, L. "Distributed Systems," Communications ACM, (28) 11 1985, pp 1200-1213.
- 7. Mostow, J. "Workshop Review--Principles of Knowledge-Based Systems," SIGART Newsletter, 92 April 1985, pp 15-27.
- 8. Noack, W., Popella, A., Schreier, G. "Knowledge-Based SAR Processing and Geocoding: The Elementary Components of the German Processing and Archiving Facility for High-Throughput and High-Precision Processing of ERS-1 SAR Data," Transactions on Geoscience and Remote Sensing, Vol GE-25, No 6, Nov 1987, pp 758-769.
- 9. Moto-oka, T., Kitsarega, M. "The Fifth Generation Computer--The Japanese Challenge," J. Wiley, 1984.
- 10. Weizenbaum, Joseph. "Computer Power and Human Reason From Judgment to Calculation," W. H. Freeman, 1976.
- 11. Good, M. D., Whiteside, J. A., Wixon, D. R., Jones, S. J. "Building a User-Derived Interface," Communications ACM, (27) 10 1984, pp 1032-1043.
- 12. Carroll, J. M., McKendree, J. "Interface Design Issues for Advice-Giving Expert Systems," Communications ACM, (30) 1 1987, pp 14-31.

/09599

EXAS--Experiment on Autonomous SAR Processor Calibration

43070002g Kyoto Selections from INTERNATIONAL ARCHIVES OF PHOTOGRAMMETRY AND REMOTE SENSING in English Vol 27, 1988 pp 369-377

[Article by H. Runge, A. Popella, W. Noack, DFVLR WT-DA, German Aerospace Research Establishment, D-8031 Oberpfaffenhofen, F.R.G., Commission II, WG II/5]

[Text] Abstract: Future SAR missions like SIR-C with the German X-band radar will acquire multifrequency and multipolarisation data with various incidence angles. In order to exploit the mission's full scientific potential DFVLR is going to calibrate both its "Intelligent SAR Processor" ISAR and the final image products. The idea of the EXAS proposal is to use extra data gained from an independent Doppler measurement. These data will be gathered at a geolocated receiver in order to tune and finally to calibrate the ISAR processor. The receiver will be adjusted to the sensor carrier frequency, the signals will be mixed down to baseband, be digitised and transferred to the ISAR hardware system. This can be performed in parallel for three frequencies with two different polarisations. Immediately after the fly-over the data will be analysed. The azimuth antenna pattern will be computed and fed back into the processing chain. The replica of the chirps radiated by the sensor will be recorded by the ground receiver. Therefore, the exact range reference function is known and can be used for the processing. The calibrated processor will produce images with a very accurate absolute pixel location. In order to verify this, a cluster of geolocated point reflectors shall be positioned over the swath and the SAR image will be compared with a cartographic map. The paper describes the experiment plan and the contributions of three institutes.

Keywords: SAR, SIR-C, X-SAR, ERS-1, ISAR, Calibration, Multifrequency, Multipolarisation.

1. Introduction

The combined SIR-C/X-SAR mission will be the first spaceborne Synthetic Aperture Radar System to acquire high quality radar data from earth

using multifrequency, multipolarisation sensors with variable incidence angles. Furthermore, the european ERS-1 satellite will be an operational SAR sensor with an expected lifetime of about three years. In order to contribute to the achievement of the scientific goals of these missions, the resulting data products have to be calibrated. This is all the more true if one also attempts to compare data resulting from different radar channels with optically acquired data such as that from SPOT. Therefore, the main goal of this experiment is to install a closed calibration loop for the processing system. For this purpose several research institutions will start a cooperative effort which combines knowledge and experience from different research and application areas.

If the calibration of a Synthetic Aperture Radar imaging system is considered, the whole data acquisition and processing chain must be understood as an end-to-end system.

The different components are:

- the target itself,
- the electromagnetic interaction with the target,
- the atmospheric propagation effects,
- the sensor platform,
- the sensor itself,
- the SAR signal processor, and
- the SAR post-processor for geocoding.

This proposal is aimed at calibrating one part of this chain, namely, the SAR signal processor and especially, some modules which estimate various key processor parameters, like the Doppler Centroid and the PRF Ambiguity Band. In order to accomplish this, extra and independent reference measurements, which are supposed to be more accurate, will be performed for data takes at a test site.

A ground microwave receiver and a signal processor shall be used to perform high precision Doppler frequency measurements, which will then be used to calibrate the SAR processor modules. Furthermore, it is shown that the proposed receiver has more benefits for SAR missions. It turns out that deterministic error sources like the antenna pattern can be corrected in the SAR processor on a routine basis. Another goal of the experiment is to use the receiver to collect reference data from all sensor fly-overs in order to contribute to a long term sensor performance accessment.

2. Experiment Plan

2.1 The ISAR Processor

The "Intelligent SAR Processor" ISAR, currently under development at DFVLR's Data Processing Division (WT-DA) will be used to generate high

precision SAR images from future SAR missions. These are in particular the european ERS-1 satellite and the NASA SIR-C mission with the German X-band radar. The design goals of the processor are high throughput and high precision. The generated images shall have high geometric and radiometric resolution as well as high map projection fidelity. 1,2 Figure 1 depicts the ISAR hardware configuration with a high performance array processor, a host computer, various workstations, the Corner Turn Memory (CTM), the Real Time Input Facility and the EXAS receiver with an interface to the CTM.

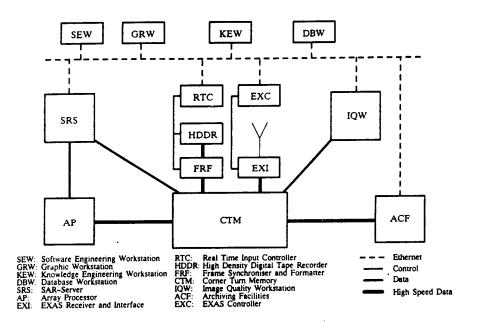


Figure 1. The ISAR Processor Hardware Configuration

2.2 ISAR Product Validation

In order to assure the delivery of good products to the user community various image quality checks and processor validations are planned. In particular the geolocation accuracy will be verified by means of active reflectors, which receive, amplify and retransmit the signals back to the sensor. It is assumed that these reflectors are much more visible in the SAR image than passive corner reflectors. They will be delivered by the University of Stuttgart's Institute for Navigation and will be deployed over the swath at a test site. The position of the reflectors will be determined very precisely, with the possible use of the Global Positioning System GPS. The remote sensing laboratories of the University of Zurich will use these spots as Ground Control Points and verify the geometric fidelity of the ISAR processor products.

2.3 Calibration of the ISAR Processor

The geometric and radiometric resolution of a SAR image is mainly determined by a proper Range and Azimuth filter generation, which in turn needs precise attitude and orbit data. Unfortunately, the sensor attitude is by far not as precisely known as it should be. A very dramatic example is the yaw angle of the SIR-C sensor which can vary in a range of plus or minus 1. In the case of the X-band this is equivalent to approximately 4 km on the ground. Nevertheless, a map projection fidelity of about one resolution cell of 30 m is desired.

The main contributory factor towards the error in the geolocation of an image pixel is the uncertain estimation of the sensor look-direction. As sensor attitude data cannot be used, the sensor look-direction must be determined by using the SAR data itself, knowing that the Doppler frequency shift changes with the variation of the look-direction. By analysing the Doppler frequency, the sensor attitude and the antenna look-direction can be reconstructed. Within one PRF-band a so called "Doppler Centroid" routine can be used and in order to determine the valid PRF-band a "PRF Ambiguity Resolver" may be used.

A common method of determining the Doppler Centroid is a clutter lock technique, where several power spectras of azimuth lines are averaged and then correlated with the antenna pattern. This method has some inherent drawbacks because a large array of data has to be analyzed. Therefore, scatterers with many different Doppler shifts are involved in the measurement. Furthermore, bright targets which are partially covered by the spectral analysis or scene inhomogeneities like a contrast edge, orthogonally oriented to the sensor flight track, can lead to severe estimation error. It does not matter which Doppler Centroid algorithm is used, the designer always faces the problem of not knowing the exact and actual Doppler Centroid value when he wants to tune and finally to calibrate its estimation algorithm. In addition, the "PRF Ambiguity Resolver" can only be calibrated with exact absolute Doppler reference values.

The idea of the EXAS proposal is to use extra information gained from an independent measurement. This will be accomplished by a geolocated microwave antenna connected to a receiver and a data storage device. This passive receiver chain acquires a signal which is identical to the radar return of the particular spot on the earth's surface where the antenna is mounted. The received pulses from the SAR system will be analysed and used to tune and calibrate the ISAR processor Doppler Centroid and PRF Ambiguity Resolver Modules. These ISAR modules will be applied on SAR raw data as well as on EXAS received data in order to compare the results. The parameters estimated from the EXAS measurement are expected to be much more accurate because:

 A data set acquired with the EXAS receiver is the two-dimensional point spread function of only one particular target on the ground. In contrast the SAR raw data which are normally used for the parameter estimation are a superposition of an infinite number of ground reflectors. Most of the infinite number of reflectors have a different relative motion to the sensor and therefore, different Doppler shifts. If SAR raw data are used for the measurement of the absolute Doppler frequency and the determination of the PRF-band, the result will always be uncertain.

- Data acquired by the EXAS receiver will be less noisy than SAR raw data, because the signals have travelled only once from the sensor to the ground. Furthermore, they are not overlayed with background clutter.
- In the EXAS receiver a much better analogue to digital conversion can be performed than by the sensor. The signals may be sampled with up to $150 \, \text{MHz}$ or with a resolution of up to $10 \, \text{bits}$.

2.4 The Data Receiving and Recording System

The reception and recording chain for the EXAS experiment consists of an antenna, a microwave receiver, a digitiser and the Corner Turn Memory to store the received pulses. This is depicted in Figure 2. The system can be enlarged to acquire data from different frequency channels or different polarisations at the same time (Figure 3).

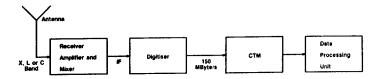


Figure 2. The Data Acquisition Chain

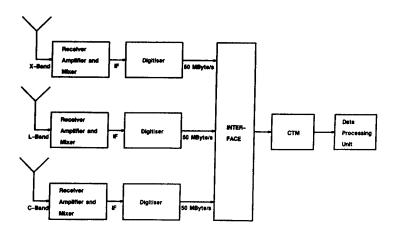


Figure 3. A Three Channel Receiver

In order to avoid an antenna steering mechanism, an antenna with an omnidirectional characteristic could be used. Therefore, the receiving angle of the antenna does not need to be adapted for each fly-over. It may turn out that the noise from other microwave sources is too high and an antenna with a narrower opening angle must be used. In any case it will be valuable for the SIR-C mission to use horizontally and vertically polarised antennas.

The receiver must have a high sensitivity and low noise level in order to be able to detect the signals coming from the SAR platform in space. The receiver must have a narrow input bandwidth so that noise from other microwave sources can be suppressed. The receiver shall be tuneable to adjust it to the three frequency bands of SIR-C, X, L and C and the C-band of ERS-1. The receiver's amplifier must be capable of precise adjustments, because this equipment will in turn be used for calibration. The IF stage of the amplifier must have a bandwidth of 20 MHz because of the high X-SAR chirp bandwidth of 19 MHz.

The industry offers digitisers with a sampling rate of up to 200 MHz and a resolution of 10 bits. For the Corner Turn Memory a standard 3-channel interface with a sampling rate of 50 MHz per channel and a resolution of 8 bits is available.

The Corner Turn Memory (CTM) of the ISAR processor hardware system will be used for data recording. It is a huge semiconductor bulk memory of 512 Megabytes and able to provide a high speed memory access in the row and column direction of a matrix. It has interfaces to the ST-100 array processor and the host computer. Therefore, the gathered data can be easily processed as soon as they are in the CTM. The achievable data rate of the CTM is 40 Mbytes/s for both row and column access of a data matrix. In a sequential data acquisition mode the memory can run with a speed of 150 Mbytes/s. With an input data rate of 150 Mbytes/s and 512 Mbyte storage capacity the data take can be as long as 3.4 seconds.

In order to obtain a time reference, a high precision time code receiver shall be used. It is sufficient to store only one time sample at one data take, because the sampling frequency of the digitiser is controlled very precisely. Therefore, the exact timing for each sample is determined.

If it is desired that the SAR azimuth reference function be obtained with the ground equipment, the received pulses must be aligned very precisely. In order to accomplish this, a stable oscillator may be synchronised with the sensor on-board oscillator and the received signals can be I/Q detected.

The data acquisition unit shall be equipped with an automatic trigger function. This will enable the unattended use of the calibration facility. It would be misleading to trigger only on the amplitude of

the incoming signal because alien microwave sources could easily cause a triggering. Therefore, the incoming data stream shall be recorded continually anyway, but if SAR data are detected a "post triggering" shall be performed as soon as the CTM is filled with useful data. The post triggering unit may also initialise the recording of an actual time sample from the time reference unit.

In order to detect whether the received signals are SAR data or alien signals, the pulses may be correlated with the nominal sensor chirp replica. This can be performed by a simple real time hardware correlator or with the ST-100 array processor. Because of its 100 MFLOPS performance, the array processor can correlate a signal with a chirp replica of lk samples in the timeframe of only lms.

2.5 Choice of the Test Site

Data acquisition with the ground receiver requires a data recording facility of at least 40 MSamples per second. This high data rate can only be achieved with a fast semiconductor memory, like the "Corner Turn Memory" of the ISAR hardware system.

However, the ISAR processor is located at DFVLR in Oberpfaffenhofen and is not portable. Therefore, the receiver must also be placed in Oberpfaffenhofen, very close to the ISAR processor. This is a benefit for a SAR mission because the received signals can already be analysed during the campaign and eventual sensor malfunctions can be detected. Furthermore, DFVLR owns equipment for high precision orbit tracking and determination, which can provide a very precise state vector required for the processor calibration. In addition, DFVLR's Institute for Radio Frequency Technology can supply extensive facilities for radiometric and geometric SAR calibration.

3. Benefits of the Experiment

The original idea of the EXAS proposal was to gain absolute Doppler frequency measurements for the calibration and tuning of key SAR processor modules. However, it turned out that the system has several more benefits for a SAR mission.

- The exact replica of the chirps radiated by the sensor can be recorded, therefore, the exact range reference functions is known. From our experience with the Convair-580 experiment in 1981 this can be extremely helpful, if the range chirp is distorted for any reason. The range chirp will be extracted and compared with a nominal chirp. Furthermore, it will be saved on a disk file and used when the particular scene of raw data is processed later.
- The exact azimuth antenna pattern can be measured and fed back into the processing chain for calibration purposes. If three receivers are used, the X, L and C-band antenna pattern can be obtained in parallel

and the difference between the pointing angles between the three antennas can be determined.

- If two receivers and two suitable antennas are used, pulses with different polarisation can be received and stored for further analysis.
- The EXAS receiver chain can record all data from three channels for a timeframe of 3.4 seconds. This covers the SAR pulses themselves and the gaps between the pulses. In these gaps, the pulses from alien microwave sources can easily be detected and analysed. From the experiences with SIR-B, this jamming can be very extensive and may influence the final SAR image.
- The data set received with the EXAS system can be used to verify the output of a SAR simulator. If the simulator is set up with the conditions of the EXAS data take, the measured two-dimensional point spread function and the simulated one should be equal in their main parameters.
- All actions mentioned above can be performed immediately after the satellite fly-over. The data are stored for online access to the ISAR processor, including advanced engineering workstations, the ST-100 array processor, the ISAR knowledge base and the SAR simulator.

4. Future Prospects

The measurement results like absolute Doppler frequency, azimuth antenna pattern and the range chirp replica, can be fed directly into the ISAR processing chain for immediate analysis. The aim is to calibrate key SAR processor modules autonomously and on an operational basis. However, this requires a regular fly-over of the sensor.

It is believed that it would be worthwhile thinking about a cheaper and portable version of the receiver and data recording system described in this paper. Several of these compact systems could be deployed in the field at test sites along or across the swath. The EXAS proposal will be a first step in the direction of a long term and autonomous SAR processor calibration.

References

- 1. W. Noack, H. Runge, "DFVLR's Intelligent SAR-Processor ISAR," COSPAR, Advances in Space Research, Vol 7, No 11, pp (11) 273 (11) 279, 1987.
- 2. W. Noack, A. Popella, M. Pich, "ISAR--A New Concept for High Throughput and High Precision Digital SAR Processing," Proceedings of IGARSS '86 Symposium, Zurich, 8-11 Sep 1986, ESA SP-254.

- 3. Ph. Hartl, M. Reich, S. Bhagavathula, "An Attempt to Calibrate Air-Borne SAR Image Using Active Radar Calibrators and Ground-Based Scatterometers," Proceedings of IGARSS '87 Symposium, Ann Arbor, 18-21 May 1987.
- 4. C. Wu, J. C. Curlander, A. DiCenzo, "Determination of Spacecraft Attitude Using Synthetic Aperture Radar Data," Presented at AIAA Sensor Systems for the 80's Conf, Colorado Springs, CO, Dec 2-4, 1980.
- 5. F. K. Li, D. N. Held, J. Curlander, C. Wu, "Doppler Parameter Estimation for Synthetic Aperture Radars," IEEE Transactions on Geoscience and Remote Sensing, Vol GE-23, No 1, Jan 1985.
- 6. H. Runge, "PRF Ambiguity Resolver for SAR," ISPRS 1988, Commission II, WG II/5.
- 7. H. Seichter, H. Runge, "Operational Experience of the Beam Tracking in the MDA SAR Processor, "Proceedings of the 3d SEASAT-SAR Workshop on 'SAR Image Quality,' Frascati Dec 1980, (ESA SP-172).

Footnotes

(1) The only difference between this and real SAR raw data is that only a one-way Doppler shift has appeared.

/09599

Zeiss Digital Mapping--A New Hardware and Software System Concept from Kombinat VEB Carl Zeiss JENA

43070002h Kyoto Selections from INTERNATIONAL ARCHIVES OF PHOTOGRAMMETRY AND REMOTE SENSING in English Vol 27, 1988 pp 441-449

[Article by Wolfgang Wallwitz, Kombinat VEB Carl Zeiss JENA, GDR, Commission II]

[Text] Mapping and map production as the main tasks of geodesy/photogrammetry as well as of remote sensing are characterized by rapid advances, which are essentially aimed at the generation of digital maps. These advances have been made possible, on the one hand, by the development of computer hardware including most sophisticated firmware and the resulting possibilities of efficient software solutions, but on the other hand also by revolutionary solutions in the equipment systems. ZEISS JENA has made its contribution to this trend with the LMK aerial camera, the first commercially available camera with forward motion compensation (1982) as well as with the efficient plotting machines STEREOMETROGRAPH, TOPOCART and STEREOPLOT, of which the two lastmentioned systems will also in the era of analytical plotters have a strong foothold for a long period in the field of stereoplotting because of their favourable price/performance ratio.

In the following a system is presented which is characterized by its capability of being connected with equipment existing at the user and by its high utility value in all its parts and which radically changes the traditional process of map production and map use. The block diagram shows the structure of ZEISS DIGITAL MAPPING in a generalized form.

Modern digital mapping systems are distinguished by homogeneity relative to the accuracy of data acquisition and data processing. Moreover, the user expects complete solutions which are immediately applicable after a short period of familiarization and with the experience of the existing personnel. In other words, the user expects a solution dedicated to his needs, that is based on the practice to which he is accustomed.

User-friendliness is guaranteed by the experience of ZEISS JENA regarding the development of photogrammetric camera and restitution systems and the long experience of the software developer, Messrs. Walter Bonne DIGITAL MAPPING SYSTEMS gained over decades in the field of applied photogrammetry for the production of maps of all kinds, including digital maps. The incorporated instruments of such companies as HEWLETT PACKARD, INFOTEK, CALCOMP and others are a solid basis of the performance in every partial solution of the system.

ZEISS DIGITAL MAPPING shall be demonstrated in the following by the example of map production from aerial photographs. A few remarks on the use of digital maps will round off this article.

- 1. Map Production From Aerial Photographs
- 1.1 Aerial photography in the ZEISS DIGITAL MAPPING system

No evidence need be given of the fact that the accuracy of the map is decisively influenced by the photographic process. The ZEISS JENA LMK 1000 in their design variants with 90, 150, 210 and 300 mm focal length has in the past 5 years proved to be an ideal camera system. Unlike traditional cameras, which utilize the efficiencies of high-performance lenses only under favourable conditions, the LMK 1000 boasts of considerably improved features. For example, the forward motion compensation allows:

- photography from a relatively low height, i.e., with the largest possible image scale and hence increased restitution accuracy;
- photography under light conditions of an overcast sky, where conventional cameras fail to produce useful pictures or where highly sensitive emulsions become necessary which entails a reduced resolving power;
- photographs with high-resolution, relatively insensitive emulsions under normal light conditions and hence better detail recognizability and higher restitution accuracy as compared with conventional photographs;
- unusually high image sharpness at increased flying height and hence smaller image scales. Compared with conventional camera systems this leads to larger model areas and hence increased ground coverage without loss of information, resulting in increased photoflight economy.

These benefits are completed by the computerized exposure control. It ensures

- optimum matching of film parameters and flight parameters.
- optimum exposure of dark image regions, and
- largest possible relief of the photoflight operator and optimum control of the photoflight parameters.

A valuable supplement to this equipment configuration is the NCU 2000 Navigation Control Unit which is functionally a combination of the AEROSKOP navigation telescope and the control unit of the LMK.

Attendant consequences are:

- The photograph can be flown with a two-man crew, i.e., with pilot and camera operator.
- The number of holes in the aircraft's fuselage is reduced from hitherto three to two.
- The reduced load and the saving in space permits better working conditions for the crew, increases the useful load and also allows the use of smaller aircraft.
- The optimized auxiliary images with perspectively running travelling marks along the flight line create the best prerequisites for the visual navigation in forward and backward view.
- All camera controls are clearly arranged for convenient manipulation.

The 4- and 6-channel Multispectral Reseau Cameras (MSK 4/MKF 6) of ZEISS JENA featuring also forward motion compensation are increasingly of interest for the purposes of mapping from photographs taken from high-flying aircraft or from satellites. Of decisive importance is the high resolution in the spectral ranges and the geometric accuracy of the individual pictures as well as their combinations from selected channels.

1.2 Airphoto restitution in the ZEISS DIGITAL MAPPING system

The restitution of aerial photographs is that part in map preparation which requires a maximum of equipment and is at the same time the bottleneck in the map production process. The analytical plotters offered so far were not capable of leading to a significant reduction of the process times, but first of all involved an increase in price of the final product. Also image correlators could so far not bring about a radical solution, especially when the restitution at large scales was concerned. At the moment a preliminary solution can only be found technologically. This means that the plotting machine issues all data immediately into the data bank and that these data can then be used in the production process for different map types. The acquisition of the data must be possible in a straightforward way partially with equipment existing at the user.

The ZEISS JENA TOPOCART D equipment which is distinguished by universality and precision as well as its comfortable observation system, has become a standard machine. We merely refer to the following conspicuous parameters: $c_k = 45 \dots 310 \text{ mm}$, large z range, m_{xy} less

than 10 mm, maximum observation magnification 12 times. For users working with focal lengths of 90, 150 and 210 mm it is recommendable to employ the ZEISS JENA STEREOPLOT, an equipment for stereomapping with optimum price/performance ratio. This is a machine of streamlined design doing away with all superfluous mimickry, but a high value was set on convenient manipulation and sufficient accuracy in stereomapping.

Any other plotting machine, whose model coordinates are fitted with TTL-compatible digital encoders, can without any problem be used for data acquisition.

Importance should be attached to the homogeneity of the measurement relative to its accuracy, since differences in the acquisition or recording jeopardize the value of the data bank being created.

1.3 The data bank in the ZEISS DIGITAL MAPPING system

The hardware of the data bank comprises the HP 9000/Series 300 computer optionally with 16 or 32-bit processor with 5 Mbyte RAM and a Winchester drive of minimally 20 Mbyte as well as a colour monitor (12, 16 or 19 inches).

The MERCATOR D.M.S. software of Messrs. Walter Bonne organizes the data acquisition process (CAPTOR), data management including interactive work (ACTOR) and the graphic data output (PLOTTER).

Data acquisition is performed with CAPTOR via photogrammetric plotting machines, via digitizing tables (e.g. of Messrs. CALCOMP), via ZEISS JENA electrooptic tacheometers RECOTA, RETA and others as well as scanners (see schematic).

Data acquisition can be ON-line or OFF-line. In the first case, data is stored in the previously selected coordinate system, e.g. ground coordinates. In OFF-line, however, data is temporarily stored in a machine coordinate system, with the position of the control points being taken into consideration. If the control point coordinates are measured at a later date, the temporarily stored modules are transformed into the particular system. Also the fitting of the models into the data bank system, for example a geographic information system (GIS), is made automatically. This kind of parallel stereoscopic restitution and geodetic supplementary measurement leads to a considerable saving in time for many projects. Especially when delays in geodetic point determination occur caused by climatic or seasonal reasons, the restitution process will not be delayed by this.

The capturing of the restituted objects in different colours on the monitor ensures a complete checking of the state of restitution. Thus, CAPTOR immediately accelerates the process of restitution. Erroneously recorded data is simply deleted in the data bank. Drawing tables are no longer needed for checking.

ACTOR automatically checks the data bank completely and in all its important parts. In this program section the digital map is completed, corrected and finished. More than 170 interactive functions which are called up from a graphics console ensure a fast and comfortable processing of the map in all its details. Text, symbols, line types, hatchings, fillings, line forms, etc. are easily producible by users and can then at any time be used according to standard. In the software part FRAMER as a constituent of ACTOR all kinds of map frames and legends are prepared and applied according to the map type.

If the final product is required to be a digital map, an appropriate extraction is stored on diskette, with data quantities of several Mbyte on tape cassette. A graphic printout on a DIN A3 printer (e.g. Thinkjet) completes the result.

For many purposes the drawn map is preferred to the digital map or a combination of both is desired. With the PLOTTER program every extraction from the data bank can be produced "as printed" or as an original for print.

Maps in low quantities are directly issued or duplicated in monochrome or multicolour. The Hewlett Packard plotter equipment with 8 drawing tools and in formats of up to DIN AO enables the PLOTTER-optimized output with a maximum drawing speed of up to 600 mm/s with sufficient accuracy. For map sheets in appropriate quantities the originals are output on dimensionally stable film. Laser printers can be used for the most exacting demands. Combined outputs of text and graphics e.g. for cadastral extractions are likewise possible.

The high quality of the graphical output by PLOTTER renders the engraving technique practically superfluous.

Each graphical final product is called up directly from the data bank. Such work as compositions, tracing on overlay sheets, pasting of single or area-covering symbols and text as well as other work to be done by cartographic tracers become superfluous or are prepared under the control of ACTOR and any tracing operations are performed by the plotter. The times saved in the map preparation and production process are of considerable orders of magnitude. The technical personnel saved in this section may be used for the interactive work with ACTOR and can accelerate the total process with incomparably higher effectivity.

2. Map Utilization with ZEISS DIGITAL MAPPING

It must be considered as a great advantage that the utilization of the digital map in the form of the data bank established in coded planes is enabled on the basis of the same hardware and software. The size, performance and the required investment for a system range within an order of magnitude, which enables wide utilization.

The logical, staggered data bank structure allows the user to work in that plane, which is necessary for the solution of his task. Hence, it is for example possible to handle separately the inland waterways system, the road network, residential and industrial premises, cabling systems and pipe lines, different vegetation, etc. The data bank structure proves to be particularly favourable for land register (cadastre), whether centralized or decentralized. The combination of topographic and administrative data renders ZEISS DIGITAL MAPPING into an ideal working tool for planners of cities and highways, for project engineers concerned with water, energy and communication routes (telephone, TV cable systems), for agriculture and forestry and for municipal and regional cadastres, to mention only a few of the major applications. The application spectrum includes road accident surveys, environmental protection as well as the wide field of thematic map production.

The output of accurate data ensures the quick graphic availability of the required documentation.

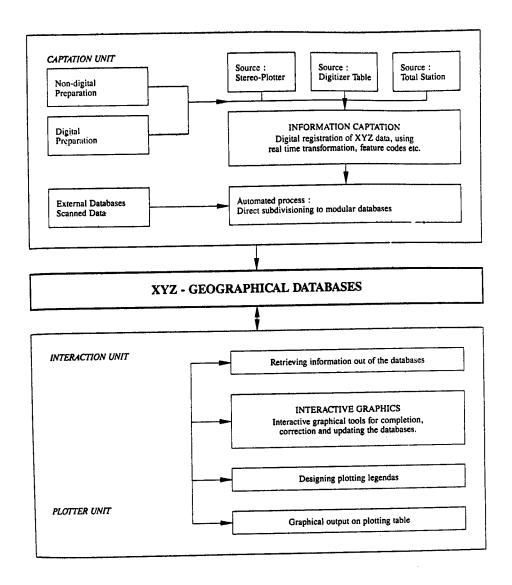
Map revision can be implemented by central institutions and by the user himself, with the procedure doing away with any tracing work and ensuring a high degree of up-to-dateness.

If ZEISS DIGITAL MAPPING works as a geographic or land information system (GIS or LIS), the SHARED RESOURCE MANAGEMENT of HEWLETT PACKARD offers the prerequisites for an optimum hardware/software configuration as well as an efficient periphery.

The ZEISS DIGITAL MAPPING system offers users of ZEISS JENA remote sensing equipment or of ZEISS JENA MSK 4/MKF 6 4- and 6-channel Multispectral Reseau Cameras the most favourable prerequisites for the processing of data gained from photographs taken from high-flying aircraft or satellites. The geometric accuracy of the interpretation results ensures a reasonable transfer of the results into the data bank for creating the digital map.

3. Summary

The article presents the concept of the ZEISS DIGITAL MAPPING system, which consists of aerial photography and restitution equipment and the hardware and software of a data bank. All parts of this modular system are efficient and user-friendly. The MERCATOR D.M.S. software rationalizes the map compilation and utilization process by eliminating several process steps cutting the remaining processing times and improving the accuracy and usefulness of the final product, whether this is a data bank extraction on a data carrier, a plotted map, or an original for monochrome or colour printing. All processes of compiling and utilizing digital maps are fully supported by software and hardware.



Zeiss Digital Mapping /09599

High Resolution Soviet Space Photographs for Topographic Mapping

43070002i Kyoto Selections from INTERNATIONAL ARCHIVES OF PHOTOGRAMMETRY AND REMOTE SENSING in English Vol 27, 1988 pp 501-505

[Article by Romuald Kaczynski and Jan Konieczny, Centre for Remote Sensing of the Institute of Geodesy and Cartography, Jasna 2/4, 00-950 Warsaw, Poland, Commission I/II]

[Text] Abstract: The results of evaluation of high resolution panchromatic photographs acquired from Cosmos satellite and multispectral space photographs taken by the MKF-6 camera installed on Salyut space station are discussed.

High resolution space photographs taken from 220 km orbit have been evaluated on analytical plotters and orthophotoprojectors. The achieved accuracy is satisfactory for topographic mapping in the scale 1:50 000 and map revision up to the scale 1:25 000.

Introduction

The paper describes some results of evaluation of satellite panchromatic and multispectral photographs taken from the Soviet spacecraft. It also includes the cartometric analysis of the high resolution space photographs. The types of the stereophotographs under consideration are:

- 1. multispectral photographs taken from the SALYUT-6 orbital station at the scale of 1:2 652 000 from the orbit of 338 km,
- 2. panchromatic photographs taken from the COSMOS satellites at the scale of approximately 1:1 050 000 from the orbit of 210 km,
- 3. panchromatic photographs taken from the COSMOS satellites at the scale of approximately 1:220 000 from the orbit of 220 km.

The photographs have been elaborated by using analytical methods including DTM for orthophotomaps elaboration. The achieved results have

been compared with the existing topographic maps at the scales from 1:200 000 up to 1:10 000.

Space multispectral photographs at the scale of 1:2,6 mln.

The multispectral photographs have been taken by the MKF-6M camera with FMC in 6 channels /0.48 - 0.84 µm/. Two stereogrammes of band No 4 /0.66 µm/ have been selected for analytical elaboration using the stecometer C Jena. About 40 control points in each stereogramme have been measured for the investigation of cartometric analysis. These points were the topographic details identified on the photographs and on the existing topographic maps at the scale 1:200 000. To reduce the influence of the Earth's curvature the geocentrical coordinate system was applied. The accuracy of coordinates of topographic details /points/ identified and measured on the two stereogrammes was checked by comparison of the some points which coordinates were determined from the topographic maps. The results are listed below:

$$RMS_{x} = \pm 46 \text{ m}$$

$$RMS_{y} = \pm 54 \text{ m}$$

$$RMS_{z} = \pm 75 \text{ m}.$$

The investigation of these photographs proved their satisfactory accuracy for updating topographic maps at the scale 1:200 000 or smaller.

2. Space panchromatic 18 x 18 cm photographs at the scale of 1:1 mln.

The photographs have been taken with the metric camera, equipped with reseau grid of the focal length c_k = 200,622 mm from the COSMOS satellite with the orbit of 220 km.

For the evaluation a part of strip consisting of 4 photographs at the scale approximately 1:1 050 000 with 60 percent end lap was chosen. The base ratio $\frac{B}{H}$ = 1/3. About 35 GCPs on each photographs, clearly identified on the existing topographic maps at the scale 1:50 000 were selected with the accuracy of RMS_{x,y} = plus or minus 15m, RMS_z = plus or minus 5,0 m. From the total of 140 GCP_s, 14 points have been used for strip adjustment, 126 points were used as reference /check/ points. The achieved accuracy is shown in the Table 1.

Table 1

	RMS in the terrain	RMS in the photoscale 1:1 050 000	No of check points		
×	<u>+</u> 20 m	0.02 mm	126		
Y	<u>+</u> 22 m	0.02 mm	126		
Z	<u>+</u> 25 m	0.12% H	126		

The strip adjustment was completed using the "OTR COSMOS" triangulation program.

These photographs can be used for elaboration and updating of topographic maps at the scale up to 1:50 000.

3. Space panchromatic photographs 30 \times 30 cm at the scale of 1:220 000.

The original photographs 30×30 cm have been taken on the board of COSMOS satellite with the photographic camera of focal distance 1012,83 mm, from the orbit of 220 km.

The obtained photographs are vertical or obligue / approximately 19^g . The end lap of the photographs is 60 percent and the base ratio $\frac{B}{H} = 1:8,5$.

In the experiment on analytical plotter planicomp Pl the originals $30 \times 30 \text{ cm}$ have been used. In the planicomp c-120 and orthocomp Z-2, the original size was reduced to $24 \times 24 \text{ cm}$. The new, reduced scale of the $24 \times 24 \text{ photograph}$ is approximately 1:284 000. The data of the photographs are given in the Table No 2.

Table 2

Data	24 x 24 cm	30 x 30 cm
scale approx. c _k /mm/ omega fi H approx. Planicomp	1:284 000 785.040 -18 ^g .80 ^c 0 ^g 22 ^c 214 km c -120	1:226 000 1012.82 -18 ^g .40 ^c 4 ^g 22 ^c 220 km P- 1
Software Mean parallaxe mq /mm/ No of points for absolute orientation	PAT M 0.001	BINGO 0.001 7

The GCP $_{\rm S}$ have been identified as topographic details, from the maps at the scale 1:50.000 and 1:10.000, as well as from the aerial triangulation of photographs in the scale 1:26.000. The RMS of the coordinates XYZ from the above mentioned sources are shown in Table 3.

Table 3

Source	Х	Y	Z	
map 1:50 000 map 1:10 000 aerial triangula-	± 15 m ± 4 m	<u>+</u> 15 m + 4 m	± 2 m	
tion 1:26 000 better then	<u>+</u> 1 m	± 1 m.	<u>+</u> 1 mm	

The interior accuracy on the Planicomp c - 120 with the PAT-M programe is shown in Table 4.

Table 4

-	control points from the map 1:10 000	points from the map 1:50 000
RMS	<u>+</u> 2.5 m	<u>+</u> 49 m
RMS $_{\mathbf{Y}}$	± 2.1 m	<u>+</u> 55 m
RMS _Z	<u>+</u> 1.7 m	± 53 m

DTM has been created on the c - 120 Planicomp. Three orthophotomaps at the scales 1:100 000, 1:50 000, 1:25 000 were produced on the Zeiss Orthocomp Z-2 analytical orthoprojector. Film Agfa Gevaert Gevatone N 31 P was used. Scan speed 50 mm/s, slit 8 and 7, 4 control points were used. The accuracy of the orthophotomaps were checked by the comparison of 50 points which coordinates were digitized in the orthophoto and in maps at the scale of 1:10 000. The results are given in Table 5.

Table 5. Accuracy of the Rectified 24 x 24 Reduced Space Photographs

control points	1:100 000		1:50 000		1:25 000	
taken from:	^m x	m _y	m _x	m _y	m _x	^m y
1. Coordinates from aerial triangulation Photos in the scale of 1:26 000, N = 48	7.9	7.Om	8.0 m	7.1	6.9m	7.0m
2. Coordinates taken from maps 1:10 000 N = 19	8.4m	10.3m	7.8.m	7.9	8.9m	4.2m

Conclusions

Satellite photographs can help to generate accurate topographic maps much quicker and cheaper which is very important for the developing countries.

Acknowledgments

The authors wish to thank the OPTON Oberkochen for the use of equipment and support. Special thanks are due to specialists from the Photogrammetry Division whose efficient helped to complete this project.

/09599

Map Production and Revision with Satellite Photographs Taken by the MKF-6 Camera and by the Cameras KATE-140, KATE 200, and KFA-1000

43070002j Kyoto Selections from INTERNATIONAL ARCHIVES OF PHOTOGRAMMETRY AND REMOTE SENSING in English Vol 27, 1988 pp 506-512

[Article by Joachim Kraemer, VEB Kombinat Geodaesie und Kartographie, Mapping and Plotting Center Leipzig, Gohliser Strasse 4, 7022 Leipzig, German Democratic Republic, Intercommission WG I/II]

[Excerpts] In the practical work done so far with space photographs in our country has been proved that for many problems in principle the equipment and methods commonly used in photogrammetry can be employed. The methods are partial enlargement or rectification, graphic photogrammetric stereoplotting, and digital photogrammetric restitution. Photogrammetry and remote sensing viewed as related sciences very often provide a definitive photogrammetric or cartographic final-product. These are map products as photo maps or in vector format, thematic or topographic maps.

Thematic maps between 1: 50,000 scale and 1: 500,000 scale and smaller produced from space photographs are mainly used for special purposes such as geological exploration, for agriculture, forestry, ecological or local planning purposes.

Until recently, we have to consider the fact, that the resolution of satellite image data was inadequate for mapping or revision of topographic maps at a scale of 1: 25,000. Since 1987 we now have got high resolution Soviet space photographs taken with the camera KFA-1000 which have been the subject of various theoretical and practical studies in photogrammetry.

Since 1976 we are producing photo maps from space photographs taken with the MKF-6 multispectral camera and taken with USSR-cameras made in the last years. Its technical data are:

Type of space vehicle	SOYUZ 22/ SALYUT	SALYUT	COSMOS (unmanned)	COSMOS (unmanne	d)
Camera	mkf-6 m	KATE-140	KATE-200	KFA-1000	
Image format (mm)	55 x 81	180 x 180	180 x 180	300 x 30	0
Calibrated fo- cal length (mm)	125	140	200	1,000	
Spectral ranges, channels (nm)	6 460-520 520-560 580-620 640-680 700-740 790-900	1 black/white false colou 500-700		1 false col 570-670 670-800	our
Photo scale 1:	2,500,000	1,500,0	000 1,00	0,000	270,000
Ground re- solution (m)	10 to 15	50	15 t	o 30	5 to 10

an area o

We receive these space photographs from the Soviet Union in an acceptable period at acceptable costs for our user community.

The photographs from all these space cameras have a 100 per cent cloud-free coverage of the territory of our country.

Because of its geometrical properties the space photographs from the MKF-6 or KFA-1000 are especially suited for planimetric mapping and less for height representation. In previous missions for photogrammetric surveying the photographs were taken with about 60 per cent and more foreward overlap and adequate side overlap for areal coverage.

Since 1978 we have mainly produced photo maps between 1: 50,000 and 1: 500,000 scale from space photographs for an area of about 75,000 km². Photomaps have a high information content which can be geared to the varying needs of different users with elements known from the traditional line maps and with additional cartographic symbols. These maps are equipped with a grid, a map frame, and marginal data.

In a space photo map 1: 200,000 scale just a part of the original photograph size of the space camera is used, for instance, to cover a $\sqrt{}$ map format 50 cm x 50 cm, an image part from a photograph taken with the

MKF-6 camera of about 4 cm \times 4 cm, or an image part from a photograph taken with the KATE-200 camera of about 10 cm \times 10 cm is used.

For partial enlargement or rectification the RECTIMAT C rectifier has given evidence of its excellent performance; it is equipped with an additional device especially for the processing of MKF-6 photographs. The rectifier is an instrument of the new generation for colour and black-and-white photographs. High resolution and the wide range of magnification 0.85 ... 8.0 power or 3.0 ... 18.0 power allow processing of photographs taken with different photographic systems and a maximum photo-size of 30 cm x 30 cm. Its performance parameters satisfy the requirements of photogrammetry as well as those of remote sensing of the earth.

For differential rectification the TOPOCART D - ORTHOPHOT E has proved to be good. In addition to the rectification of black-and-white photographs, also colour photos can be rectified on colour film in the full magnification range without additional aids, the same applies to spectrozonal and infrared films.

Interpretable superimposed colour photographs may be produced with the multispectral projector MSP-4 C from photographs taken with the multispectral camera MKF-6 M. The MSP-4 C is a four-channel colour synthesizer for the interpretation of multispectral black-and-white photographs with a maximal picture size of 70 mm to 91 mm using a constant 5.0 times magnification. Superimposed colour photographs from the multispectral photographs taken with the MKF-6 and the multispectral camera KATE-200 with an image format of 18 cm x 18 cm can also be produced by a special method on the rectifier RECTIMAT C in the full magnification range on colour film.

From the 6 spectral ranges of the space camera MKF-6 M it was channel 4 (from 640 ... 680 nm) and channel 6 (from 790 ... 900 nm) which proved to be most suitable for interpretation in most object categories of complex thematic mapping at the scale 1: 200,000. Mainly larger villages, settlements and important single buildings are clearly visible with regard to their boundaries and inner structures. Industrial plants, airports, dumps of building material, lignite opencuts etc. can be well recognized. The road network with highways, motorways, and communication roads can be compiled in more detail than it is represented in the general map 1: 200,000 scale. The road net, the network of railway communications, rivers and ponds, canals, inland lakes, and coastal lines can be identified and well demarcated by the contrast of the contiguous different vegetation covers or built-up areas in the multispectral photographs. Many possibilities are obtained especially for the special, detailed interpretation of forests and agricultural areas and for the determination of different classes of growth with simultaneous measurement of their sizes and positions for planning and controlling the foodstuff production in agriculture and for territorial planning with the aid of colour mixture and pseudo-colouring.

The graphic photogrammetric stereoplotting of the photographs from the space cameras MKF-6 or type KATE of the scales 1: 1,000,000, 1: 2,000,000, or 1: 2,500,000 for the map scale 1: 100,000 and 1: 200,000 can be carried out on the STEREOMETROGRAPH G precision stereoplotter. This precision stereoplotter with a range of calibrated focal length from 85 mm to 310 mm and 7 times viewing magnification allows the restitution of cosmic image material. Supplementaries such as recorders, tilt calculator or model corrector for the graphical plotting with correction of distortion, earth curvature, and refraction can be connected electrically via selsyns. The MKF-6 photographs can be placed into the machine either in their original size or magnified by 2.4 times in the precision enlarger. The absolute orientation of the image model is made partially by means of map control points. stereoscopic compilation of the map elements to be represented is performed in partial sections and by line-by-line engraving on an engraving foil directly on the computer-aided digital plotting system DZT 90 x 120. With this technique it is possible to compare the photogrammetrically restituted photograph directly with the existing maps and to represent quite different map elements on separate engraving foils.

In the last time we have got high resolution space photographs taken with the camera KFA-1000 during the years 1985, 1986, and 1987 from the territory of our country. The photographs have a photoscale 1:270,000, a calibrated focal length of 1,000 mm, a resolution of 5 to 10 m, an image format of 30 cm x 30 cm, also more than 60 per cent foreward overlap whereby the positive film material is false colour film. The photogrammetrists and cartographers would like to have a cosmic sensor resolution of about 5 m. In the GDR, for example, topographic maps must meet state map accuracy standard which requires about 66 per cent of well defined points, such as road intersections, to be within plus or minus 0.35 mm of the correct photogrammetric map location.

These are plus or minus 8.75 m in nature for the topographic map 1:25,000 scale. Many customers require topical topographic data and, increasingly, the ability to generate them in a short time. The major problem we have encountered with high resolution space photographs and the present topographic map 1:25,000 scale is the "shortened updating."

First experiences have shown that the high resolution space photographs taken with the camera KFA-1000 can be used for the revision of topographic map products 1: 25,000 scale using conventional photogrammetric techniques such as the map revision system KARTOFLEX, the precision stereoplotter STEREOMETROGRAPH or the instrument system TOPOCART D.

The map revision instrument KARTOFLEX is universally applicable to the updating of maps of any scales, interpretation, and calculation of areas with fast operating mode. The original documents are predominantly aerial photo pairs and space photographs irrespective of the exposure focal length with maximum format size of 30 cm x 30 cm. The extended version of the instrument is equipped to solve the following problems:

- Correction of affine and perspective distortions occuring between original photograph and map can be activated through the microcomputer;
- Fast correlating of photo and map by an orientation program;
- Digitizing of map points and image points with coordinate output via standard interface.

The viewing magnification on the KARTOFLEX is continuously variable for photographs from 2.4 to 12 times and for the map from 0.8 to 4 times. The viewing modes to be changed over:

- Stereoscopic viewing of photos with superimposed map in the left or right eyepiece;
- Binocular viewing of one of the two photos with superimposing map;
- Binocular superimposed viewing of multispectral photos in three channels.

The main field of application of KARTOFLEX with space photographs are the production of thematic maps of any scales and the "shortened updating" of topographic maps 1:50,000 or 1:25,000 scale. For instance, the correlation of the space photo model from the camera KFA-1000 with an image format of 30 cm x 30 cm with the existing topographic map 1:25,000 scale is made partially by means of 3 to 5 map control points. The interpretation of the new elements to be represented is performed in partial sections with maximum area of about 5 to 8 cm 2 in the map 1:25,000 scale. This corresponds to an area of 4 to 7 mm 2 in the original image of 1:270,000 scale.

For large areas, for instance new housing areas, of about $100~\rm cm^2$ in the map 1:25,000 scale the photogrammetric stereoplotting from high resolution space photographs of the scale 1:270,000 can be carried out effectively on the STEREOMETROGRAPH G precision stereoplotting machine with model corrector. The absolute orientation of the image model is made partially by means of 6 map control points. The affine stereoscopic compilation of the new map elements to be represented is performed in partial sections and by line-by-line engraving on an engraving foil directly on the computer-aided stereoplotting system.

The combination of photogrammetric mapping with the KARTOFLEX and with the STEREOMETROGRAPH G from the high resolution space photographs may be utilized now with other source information for the "shortened updating." The only one year old, new topographic information from the space photographs on the combination foil may be coloured imprinted in the existing topographic map 1:25,000 scale. This is an effective method. (Figures 3.1...3.3)

For the digital photogrammetric restitution of the space photographs can be made use of the STECOMETER C precision stereocomparator. It allows the point-by-point restitution of the cosmic photographic material in an image format of 23 cm x 23 cm with a total magnification of 6 to 18 times. The photo coordinates of single points measured in digital photogrammetric restitution are recorded in machine readable form and subsequently processed in a computer with the block triangulation program SAMT. Here, too, map control points from existing topographic maps of the scale 1: 25,000 or 1: 10,000 are introduced, with street crossings being well suited as map control points. In the computer program consideration of influences of the earth's curvature and refraction can be satisfied. For the STECOMETER measurement for one photo pair from the space camera MKF-6 M for instance a mean position error of plus or minus 32.5 m or plus or minus 16 m in the original image yielded. The results are represented cartographically in the usual form in off-line operation on the DZT 90 x 120 Digital Drawing Table.

It is a fact that for many problems in the production of thematic maps and in the revision of topographic maps with space photographs the photogrammetric equipments and systems from VEB Carl Zeiss JENA in our mapping and plotting centre can be employed.

The photogrammetric and cartographic methods as we practise them with aerial photographs and the analogue and analytical plotting instruments can also be used for space photogrammetry in the next time.

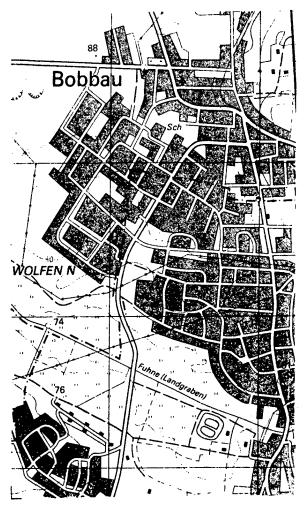


Fig. 3.1.: Existing topographic map (1980) Stand der Ünterlagen 1980

P47/88 Topographische Karte 1: 25 000

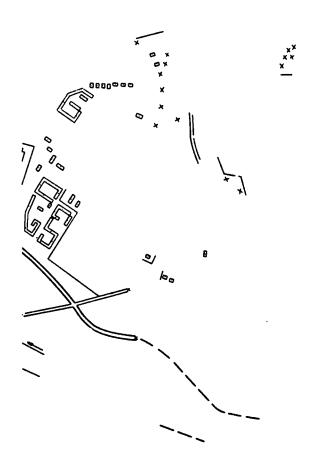


Fig. 3.2.: New topographic information from the high resolution space photographs (1986)

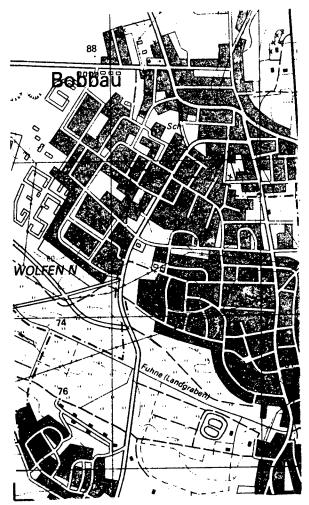


Fig. 3.3.: "Shortened updating" (combination 3.1. and 3.2.)

Stand der Unterlagen:
1 : 1980
Erganzt mit Kosmischen Aufnahmen
vom August 1986
LFB 12/86

/09599

An Expert System for Satellite Image Interpretation and G.I.S. Based Problem Solving

43070003 Kyoto Selections from INTERNATIONAL ARCHIVES OF PHOTOGRAMMETRY AND REMOTE SENSING in English Vol 27, 1988 pp 518-528

[Article by J. Desachy, P. Debord, and S. Castan, Laboratoire CERFIA, Universite Paul Sabatier, 118 route de Narbonne, 31062 TOULOUSE CEDEX-FRANCE]

[Text] Abstract: This paper describes an expert system for satellite image interpretation and thematic mapping.

The thematician knowledge is kept in a data base as a set of production rules with certainty factors. The facts data base for a given problem is composed of the image to be interpreted and the associated geographic information system.

The system can handle two kinds of reasoning depending on the nature of the given problem:

- data-driven reasoning for classification problems.
- goal-driven reasoning for object possible location mapping.

In addition we plan to include a learning process in our expert system.

1. Introduction

Nowadays most cartographic applications manage with satellite imagery, but almost all of them limit themselves to in-image information (spectral or textural features, multitemporal images...).

In fact when somebody analyzes a satellite image, he takes into account a lot of "a priori," "out-image" knowledge to reach a satisfactory interpretation.

A photointerpreter who wants to produce a vegetation map for example, will manage with three types of information sources.

first: of course the satellite image

second: available cartographic information (topography, soils quality...)

third: his knowledge of local vegetation types characteristics

So it's quite an evidence that one should "add" to image information, the domain expert "know-how" and the cartographic data in order to "understand" the image.

The expert systems methodology [FAR 3] [VOY 10] is well adapted to solve this kind of approach.

It's not the first time that expert systems technique is used to solve remote sensing problems but they solve as we know quite different problems.

So GOLDBERG deals with this technique to estimate if computed changes in multitemporal images are valid or not [GOL 5].

GOODENOUGH [GOO 6] presents two systems, one of them (MICE) is used to manage with the "registration" or aerial images extracted objects with the corresponding objects in maps; the other one (LDIAS) is a multiexpert system, which after an analysis of a given image related problem will make an adapted choice of algorithms among an image processing procedures set.

In a synthesis paper, MCKEOWN [MCK 8] presents an analysis of the role of the Artificial Intelligence in the joined management of remote sensing data and Geographic Information System.

He submits data bases quite different from classical G.I.S. (MAPS, CONCEPTMAP) but well fitted to model guided object finding and to object spatial context searching (airport scene for example).

He handles object models and abstract descriptions of scenes by spatial relations between objects.

In this domain we got some experience too in scene analysis and understanding systems [DEB 1].

As far as we know other authors have used expert systems in image processing but generally by the mean of model guided research of objects (in most cases in aerial images) (the image is preprocessed and a segmentation is obtained, then the presence of searched objects is decided by the way of match with a model).

In the Edinburgh symposium of C IV ISPRS of September 1986, we presented a paper [DES 2] about an experimental system of automatic remote sensing imagery interpretation.

It allowed us to show on a particular test zone the interest of such an approach to improve a supervised vegetation classification, but the integration in the processing method of the three sources of information (image, geocoded information, expert know-how and knowledge) was quite empirical, just as the uncertainty management in the knowledge representation.

In order to produce a general system we chose the expert system technique as well as a less empirical method of uncertainty management in knowledge handling.

We can solve classification problems (vegetation cartography for example) by using our inference engine in forward tracking; moreover we can manage with geographic information related problems by using backtracking (for example to determine where it would be optimal to set that or that type of plant knowing that...).

2. The First Steps to the Expert System:

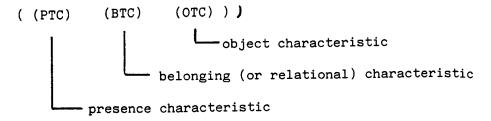
Let's remind of the experimental procedure we applied to a LANDSAT MSS image of Palni hills, India [DES 2] in order to obtain a vegetation map of that region.

We managed then with three different types of knowledge:

- 1. The LANDSAT MSS image (and related computed features: spectral and textural features)
- 2. Geocoded information (digital terrain model, climates map...)
- 3. Expert knowledge about searched classes of vegetation.

The knowledge of types 1 and 2 is typically a fact data base and knowledge of type 3 is the knowledge data base.

In this experiment the expert knowledge concerning each class of vegetation was coded in the form of logical expressions (Λ and \mathbf{V} operators) and each basis operand had the general following appearance:



Example: ((mainly) (bottom of (valleys)))

The PTC and BTC characteristics permitted to code uncertainty in natural language.

The whole procedure of the experiment is presented in Figure 1 (appendix).

First the MSS image was preprocessed (orthogonal transform), then a "preclassification" was made which was a barycentric type supervised classification, managing with spectral and textural features (cooccurrences matrices based features).

For each pixel and for each searched vegetation class we obtained a belonging probability.

Introduction of expert knowledge consisted to modify these computed probabilities taking into account each pixel context in connection with expert knowledge, with relatively empirical methods.

(In fact these methods were quite analogous with the methods used in the medical expert system MYCIN [FAR 3] [VOY 9] to manage with the uncertain knowledge and facts.)

The expert knowledge stepped in at two levels (pixel or spatial level).

3. Presentation of the Expert System

First we are going to present our system in a classification problem context.

The general scheme is presented Figure 2 (see appendix). Let's detail each part:

3.1. What is an elementary fact in our system?

It is the whole set of available informations for each pixel (some of them may not be immediately available but can be computed). The preclassification is supposed done.

So, one fact appears as follow:

Successive application of knowledge base rules will update the certainty factors CF1, CF2... when no more first level rule is eligible a conclusion can be made on the first step of the classification process. Then second level rules can be activated (involving spatial features).

3.2. Knowledge base:

Figures 3 and 4 give the expert knowledge in natural language form, then in the corresponding production rules form.

The number between parenthesis indicates the certainty factor of the rule itself (confidence factor) and is a value from -1. (you are sure it is not...) to 1. (you are sure it is yes...).

The possible forms of rules are as follow:

A and B
$$\longrightarrow$$
 C (CF)

(A or B) and C \longrightarrow D (CF)

A and B \longrightarrow C or D (CF_C) (CF_D)

For purpose of knowledge base construction, which is quite variable for each type of region, it is necessary to have an expert-computer interface.



It must be made possible for the expert to express his knowledge in his natural language. However the expert will have to express with predefined keywords related to objects that can be extracted from G.I.S. and to knowledge description.

Keywords relating to objects:

```
valley, versant, ridge, plateau...(DTM)
road, villages, river...
clay...(SOILS)
```

Keywords for belonging (relational) characteristics:

```
far away, near, around...
upper, bottom...west, south...
```

Keywords for presence characteristics and corresponding certainty factor CF

```
only (1.) principally (0.8) frequently (0.5) present (0.) uncommon (-0.6) never (-1.)
```

Keywords for spatial characteristics (level 2)

remains, large surfaces, elongated surfaces...

The purpose of the interface will be to catch the expert text, to look for keywords and their logical relations and to produce the corresponding production rules and to feedback the expert for corroboration.

The presence characteristics induce the certainty factor of the corresponding production rule.

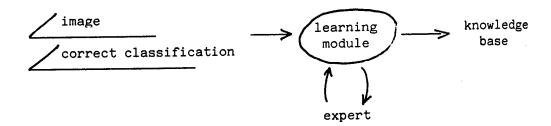
On the other hand, the belonging characteristics (NEAR roads, BOTTOM OF valleys, FAR AWAY FROM...) induce certainty factors for the corresponding premises.

These latter factors can be computed for one pixel on request, or systematically for all pixels at the beginning of the process. This is done by special procedures oftenly using fuzzy sets logic [DES 2].

We anticipate to conceive a learning module. Having images and the corresponding correct classifications, the module will extract knowledge

in relation with possible objects and belonging, presence and spatial characteristics permitted.

The produced rules will be presented to the expert for confirmation.



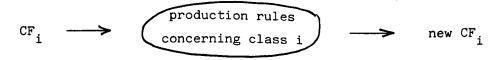
3.3 Inference engine:

If the given problem is a classification one, the inference engine will be used in "forward tracking" in the following way:

For each fact of the facts data base (coordinates, certainty factors that it is belonging to each possible class, description of pixel context in terms of G.I.S. objects) all level 1 production rules will be activated since each pixel "belongs to" each possible class with different certainty factors.

(Eventually a threshold on certainty factors may be used in order to omit the corresponding searched classes and restrict the number of selectable production rules for each pixel.)

For each pixel and for each class we have the following process: CF_i being the certainty factor that the pixel is belonging to class i, each production rule concerning class i, is applied in order to obtain a new CF.



3.4. Dealing with knowledge uncertainty:

We saw that each pixel is considered as belonging to each class with a corresponding certainty factor. This factor has a range from -1. (certainty the pixel is not belonging to class) to 1. (certainty the pixel is belonging to class).

Moreover all production rules admit certainty factors for each possible conclusion (range -1. to 1.) which indicates the confidence in that conclusion.

The effect of activation of a production rule admitting certainty factors on conclusions, with uncertain premises will be to modify the corresponding act (that is to modify the pixel class belonging certainty factors) for that aim we used MYCIN-like uncertainty management [FAR 3].

Premises computing examples

if A and B and C ...
$$(CF_A)$$
 (CF_B) (CF_C) A and B and C \longleftarrow min (CF_A, CF_B, CF_C)

Rules computing examples

Let us suppose we have one pixel already belonging to class i with certainty CF_{class} i then

$$^{\text{CF}}_{\text{class i}}$$
 $^{\text{min (CF}}_{\text{class i}}$, $^{\text{CF}}_{\text{A}}$) * $^{\text{CF}}_{\text{RULE i}}$

If more then one production rule can be activated for identical conclusions (on class i for example), the conclusion will be assigned a combined certainty factor computed by the following commutative and associative operations

ex:
$$\begin{cases} \text{application of Rule 1 gives class i (CF}_{1i}) \\ \text{application of Rule 2 gives class i (CF}_{2i}) \end{cases}$$

then the combined certainty factor CF_i will be:

$$CF_i \leftarrow 1$$
 if $CF_{1i} * CF_{2i} < 0$ and $|CF_{1i}| * |CF_{2i}| = 1$

$$170$$

_..

In a further approach for uncertainty management we plan to take into account the possibility theory to avoid the empiricism of such operations [GRA 7].

3.5. Problem solving context:

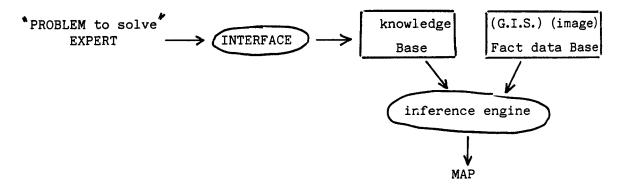
We previously presented our system in a classification, data driven context with the inference engine used in "forward tracking."

The same system can be used in a totally different objective which consists in:

Considering a goal (i.e. a "problem to solve"), connected with the type of informations our system is able to deal with, the geographical zones corresponding to the problem solution can be then determined. In order to do so, the inference engine is used in "back tracking" (in a goal driven context).

The fact data base is G.I.S. information, eventually connected with corresponding images.

The knowledge base will be considered as composed of the sole knowledge on the specific problem to solve



Example of problem to solve: "Where to plant rice?"

Connected knowledge (imaginary...we are not experts!)
"No rice at more than 1500 m of height"
"Not too far from villages or roads," "sunny versants"
"No slopes at more than 40%"...

When the corresponding knowledge base is built, the inference engine is started in "backward tracking."

(If problem connected rules have premises involving spectral signatures of objects or other image linked characteristics...then it is possible to use a regional image.)

At end the system will produce a map. Each point of the map will be assigned a certainty factor related to its ability to solve the problem.

A review of that type of approach can be found in [ROB 9].

4. Conclusion

We propose an expert system able to solve two types of problems:

- classification, cartography problems where accuracy is improved by expert knowledge integration.
- particular problem solving with problem related knowledge integration.

We plan to improve our system in its classification cartography approach by homogenizing the processing techniques:

The preclassification would join the expert system itself; production rules could be computed concentrating information we have on spectral signature of searched classes (as well as textural features), so the expert system could drive the whole processing.

References

- [DEB 1] DEBORD, DALLE, CHAMBON: "configuration de base du systeme SACSO: interpretation de scenes a partir de modeles 2D" Congres RFIA AFCET INRIA (janvier 1984 PARIS).
- [DES 2] DESACHY, CASTAN, FISSE: "Introduction of thematician knowledge in remote sensing imagery interpretation." Proceedings symposium C IV Edinburgh Sept. 1986.
- [FAR 3] FARRENY: "Les systemes experts: principes et exemples." CEPADUES editions, 111 rue Vauquelin, 31100 TOULOUSE FRANCE.
- [FIS 4] FISSE, DESACHY, CASTAN: "Utilisation de donnees exogenes pour la classification d'images en teledetection." Congres RFIA AFCET INRIA, Janvier 84 PARIS.
- [GOL 5] GOLDBERG, KARAM, ALVO: "A production rule-based expert system for interpreting multitemporal Landsat imagery." IEEE 1983.
- [GOO 6] GOODENOUGH, GOLDBERG, PLUNKETT, ZELEK: "An expert system for remote sensing." IEEE Geoscience and remote sensing ge 25, n° 3, May 87.
- [GRA 7] GRANGER -"Fuzzy reasoning in classification expert systems" tutorial 4 Congres RFIA AFCET INRIA Antibes Nov. 87.

[MCK 8] MCKEOWN: "The role of Artificial Intelligence in the integration of remotely sensed data with G.I.S." IEEE geoscience and remote sensing. Ge 25, May 87.

[ROB 9] ROBINSON, FRANCK: "Expert Systems applied to problems in G.I.S.: introduction, review and prospects." AUTOCARTO 8 pp 510-519.

[VOY 10] VOYER: "Moteurs de systemes experts." Eyrolles editions 61, Bd. St.-Germain 75005 PARIS (1987).

Appendix

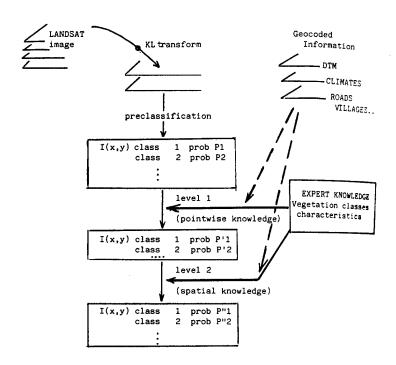


Figure 1. Experimental Classification Procedure

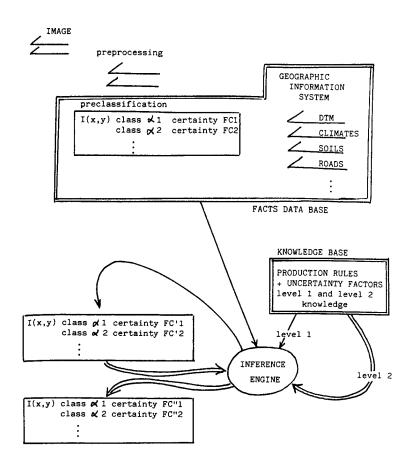


Figure 2. General Schema of the Expert System

- only (top of ridges or bottom of valleys) and remains class 1:
- class 2: only plateau
- only bottom of valleys and principally east and south versants class 3:
- class 5: only near villages
- class 6: only near villages
- highly predominating on the plateau class 7:
- class 8: principally valleys of north global versants
- class 9: only abrupt versants or upper versants
 class 10, 11: no characteristics
- class 12: frequent near villages and roads
- class 13: frequent on all versants
- class 14: principally south and south east versants

Figure 3. Vegetation Characteristics for Palni Hills (INDIA) LEVEL 1 RULES rule 1: if top of combs then C1 (1.) rule 2: if bottom of valleys then Cl (1.) rule 3: if plateau then C2 (1.) rule 4: if bottom of valleys and (east versants or south versants) then C3(0.8)rule 5: if bottom of valleys and non (east versants or south versants) then C3 (0.3) rule 6: if abrupt versants then C4 (1.) rule 7: if near villages then C5 (1.) or C6 (1.) rule 8: if plateau then C7 (0.9) rule 9: if valley and north global versant then C8 (0.8) rule 10: if abrupt versants or upper versants then C9 (1.) rule 11: if near village or near road then C2 (0.7) rule 12: if versant then Cl3 (0.7) rule 13: if south versant or south east versant then C14 (0.8)

rule 1: if remains then C1 (1.)

LEVEL 2 RULES

Figure 4. Knowledge Base Production Rules for Palni Hills /09599

Photogrammetry: A Method for Three Dimensional Inspection of Equipment Inside Nuclear Installations

43070004 Kyoto Selections from INTERNATIONAL ARCHIVES OF PHOTOGRAMMETRY AND REMOTE SENSING in English Vol 27, 1988 pp 385-390

[Article by Alain Martin, Framatome BP 3083, 69398 Lyon Cedex 03, France, Commission V]

[Text] Industrial photogrammetry is a method of dimensional inspection whose main advantages are: rapid acquisition of elementary data (photos), inspection without contact and deferred analysis.

Its basic principle means that photogrammetry is well suited to work in hostile environments, and particularly for maintenance of nuclear power stations.

Since 1983, FRAMATOME has been developing various applications of photogrammetry for its three-dimensional inspection needs and for expert evaluation with a view to preparing repair work.

Up to now, three different types of applications have already been regularly carried out (see Figure 1)

- inspection of tube sheets of steam generators,
- dimensional inspection of steam generator nozzle support rings,
- inspection of positioning pins of fuel elements for Upper Internals in the reactor vessel.

The first two applications were performed in air in a restricted and confined space (1/4 of a sphere of 1.6 m radius), the third application on the 10 m of contaminated water.

In all three cases, the radiation level was such that:

- the human operator could in no case remain near the equipment while the photos were being taken,

- positioning had to be as quick as possible to avoid having a shadow on the film.
- as many operations as possible had to be by remote control,
- in no case was it possible to go back to take the photos again in case of failure while the shots were being taken.

These extreme operating conditions required rigorous preparation, purpose made tools, operator training beforehand and in order to ensure the quality of the measures taken, work with Quality Assurance.

It must also be noted, that in all cases only photogrammetry was enable to make possible these inspections with acceptable precision.

1. Inspection of steam generator tube sheets

This is in order to determine the damage caused by a "loose part" over a tube sheet (a plate drilled with 3388 holes to which are welded the exchanger tubes—1/2 circle of 1.6 m radius).

As the loose part had squashed in the ends of the tubes, inspection enables in particular, the following to be determined:

- inside tube diameter--this data is necessary to perform routine inspection of the state of these tubes,
- the excess height of these tubes in order to know, to what extent they may be machined without deteriorating the component,
- the profile of the most deformed tubes to be able to justify the harmlessness of this damage to the components (see Figure 2).

The operating principle consists of:

- using a non-metric camera calibrated to medium size,
- a manipulating arm which positions the camera in 12 different positions,
- the mosaique thereby created enables a stereoscopic view of all the tube sheet to be obtained,
- metrology is performed on each tube at about 20 points,
- inside diameter and residual height is deducted by means of an optimization calculation,
- on request, a profilommetry can be performed as indicated in Figure 2 in order to characterize the most impacted tubes.

This application has already been performed on more than 10 tube sheets in France and in Europe, allowing:

- in less than 8 hours, usable photos to be obtained,
- in approximately 48 hours, the most appropriate means of repair to be indicated,

- in one week, a photographic and dimensional file indicating the state of the tube sheet to be supplied to the utility, thereby making it possible to request the safety authorities to authorize the startup of the reactor.

The accuracy of the measurements are:

- 0.2 mm for the tube diameter, (7/8"),
- 0.2 mm for the residual tube height (5 mm nominal value).
- 2. Dimensional inspection of steam generator nozzle support rings

The role of these rings is to accommodate a plug which allows work to be carried out in the steam generator, while the power station is shut down for its annual refueling, at this time obligatory movements of water, associated with loading and unloading operations, would prohibit any activity within the steam generator were it not for the presence of the plug.

Whenever a reactor has never been fitted with such plugs, it is necessary to check the generator nozzle support rings to check that:

- the plug can really be clamped to the ring by means of 20 screws in the 20 holes which are tapped around the ring,
- the levelness of the ring will be acceptable for the kind of plug joint and that water tightness at a pressure of 0.2 MPa will be guaranteed.

Depending on the results of this inspection either the standard plug will be compatible with the ring, or it will be necessary to adapt it to the ring, or finally a plug will have to be specially designed for that ring.

The operating principle is as follow:

- the ring is prepared by fixing studs into the tapped holes, by making the lodging standout and by placing reference in the field of vision (see Figure 3). To do this, an operator works in the steam generator for a maximum of two minutes.
- the photo is taken from the outside with the help of a manipulating arm which places a medium size metric camera in two positions.

The process gives (see Figure 3):

- the ring drilling plan,
- levelness defects of the lodging at about 200 points.

The operation lasts about:

- 4 hours for the photo,
- 24 hours for the analysis.

This operation has been performed on around 20 rings in France and in Europe. Its use can be extended to checking levelness of flange lodgings for various components.

The accuracy obtained for a 1 m diameter ring taking into account the environment and the medium sized apparatus is 0.3 mm.

3. Inspection of the fuel rod positioning pins in the Upper Internals of the reactor vessel

The positioning pins of the Upper Internals are used to keep the fuel rods in place in the reactor vessel.

During maintenance operations of the upper internals in the reactor cavity during refuelling, it may happen that these pins become damaged if they come into contact with part of the cavity, in this case they can no longer carry out their function and they may, if badly bent, damage the upper flange of the fuel rod. Although this damage does not bring about any safety problems, it is very expensive, since the fuel rod is itself damaged and must therefore be replaced. When such an incident becomes known therefore, it is important to be able to quantify the pin defect in order to determine the most appropriate kind of repair work: machining, straightening, or removal.

As the upper internals are in contact with the reactor fuel rods, it is impossible to remove them from the water (this acts as a screen against radiation). To perform this inspection it is therefore necessary to take all the photos under water, moreover as the pins are situated under the upper internals, the operations must be guided by an underwater video system.

The photo equipment consists of:

- 2 underwater metric cameras of medium size, coupled to obtain a base of 0.5 m for 1.2 m shooting distance,
- a system of flash lighting set up on the camera support,
- a set of reference scales linked to the camera support,
- a video camera which acts as a viewfinder to correctly position the cameras on their objective,
- a set of poles and brackets to position the set as desired under the upper internals.

Following the operation, the analysis enables the state of the pins to be seen as shown in Figure 4: each pin's distortion and positioning are given.

This information is then used as guide to repair work on the pin. During the first operation, with pins showing a distortion of about 3° , they were using the photogrammetric indications to direct the effort which was to be exerted. During the second operation, the distortion reached 10° and was judged excessive for the mechanical resistance of the pin, which was simply cut off. In both cases, the inspection enabled, within 48 hours approximately information of prime importance on damages to be given and to help in the choice of the means of repair.

Accuracy with medium sized cameras and mediocre operating conditions is about 20' for distortion values.

In all the applications described above, photogrammetry has been a great help for maintenance work on nuclear power stations. It can be seen that ease of use is a prime factor in the choice of photogrammetry as a method of inspection. It must however be noted that two handicaps remain to be overcome:

- the accuracy obtained is only just sufficient for the needs of repair operations,
- process delay may be a reason for rejecting the method.

In the majority of cases however, photogrammetry is obligatory as it is the only possible method taking into account working conditions in a very hostile environment. These are the reasons which have enabled FRAMATOME to perform its inspections on more than 30 installations in France and in Europe in 4 years.

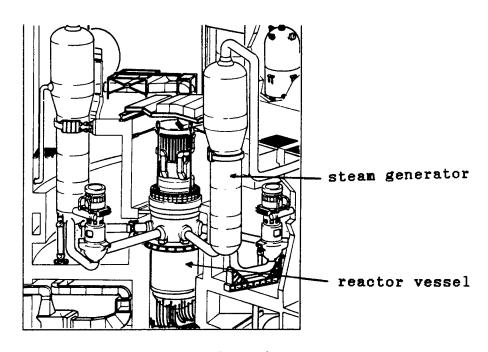


Figure 1

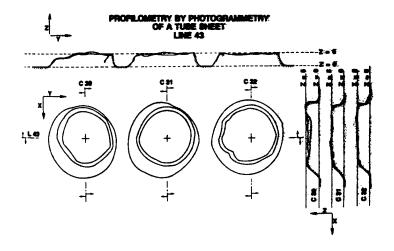


Figure 2

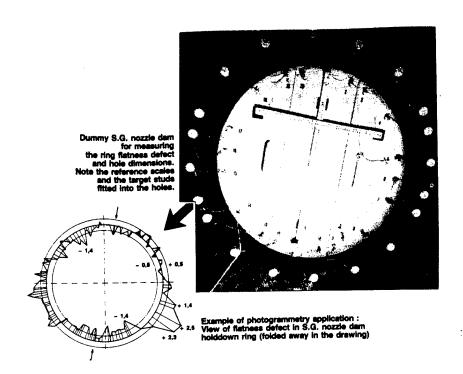
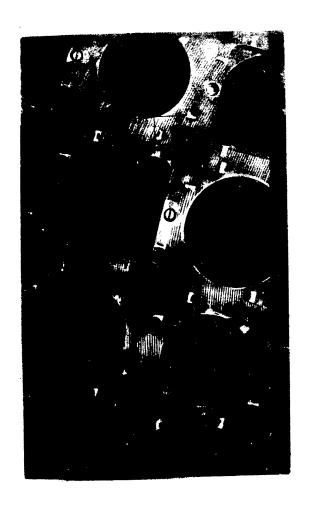


Figure 3



PHOTOGRAMMETRY OF UPPER INTERNALS

GRAPHICAL REPRESENTATION OF PIN DISTORTION

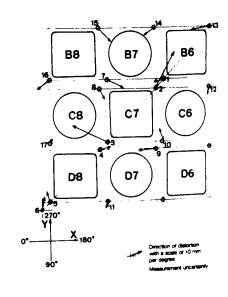


Figure 4

/09599

National Report of Polish Society of Photogrammetry and Remote Sensing (Period: Jan 1980 - Dec 1987)

43070005 Kyoto Selections from INTERNATIONAL ARCHIVES OF PHOTOGRAMMETRY AND REMOTE SENSING in English Vol 27, 1988 pp 52-59

[Article compiled by Ryszard Florek, Jozef Jachimski, Romuald Kaczynski, Wladyslaw Mierzwa, Stefan Papiernik, Ryszard Preuss, Zbigniew Sitek, Andrzej Swiatkiewicz, Jacek Uchanski and accepted by the Council of the Polish Society of Photogrammetry and Remote Sensing; Commission VI]

[Text] 1. Topographic Operations

Projects executed

Topographic operations in Poland are executed exclusively by state enterprises. The aerial photographs are taken by one enterprise which delivers the photos to the eight regional enterprises.

New maps are now produced only in the following scales: 1:5000 to 1:500. The area covered by these maps differs in each year e.g. in 1981 they covered 5893 km^2 , while in 1987 only 1380 km^2 . The maps in scale 1:5000 are plotted for 50 percent of mapped areas, 1:2000 for 34 percent, 1:1000 for 11 percent and 1:500 for 5 percent of areas being mapped. As the full coverage of the whole country by maps in scale 1:10000 was achieved in 1974, only revision of these maps is being done now. An average of 30 000 km² of these maps is revised each year.

Photographic coverage

For large scale mapping and for photointerpretation purposes, the panchromatic aerial photographs in scales from 1:4000 to 1:18000 are mainly used. The number of taken photographs depends mainly on weather condition which limits the number of days appropriate for photogrammetric flights.

The area covered by these photographs vary in each year. For instance in 1981 area of 4880 $\rm km^2$ only was covered, while in 1987 17 213 $\rm km^2$.

Furthermore each year the area of 30 000 $\rm km^2$ for 1:10 000 maps revision, the photographs in scales 1:18 000-1:35 000 are used. Moreover, in each year an average area of 120 $\rm km^2$ is photographed on colour infrared film, area of 320 $\rm km^2$ is covered by multispectral photographs, and for area of 1000 $\rm km^2$ a thermal scanerimageries are taken.

Instrumentation

In Poland the following frame cameras are used: Wild RC-8 and RC-10, Zeiss Jena MRB, Multispectral-Zeiss-Jena MSK-4 and Japan NAC.

For analytical solutions, the following precision stereocomparators are used: Zeiss-Jena stecometers and Opton PSK-2 stereocomparators.

For map compilation the following stereoplotters are used: Wild A10 and A8, Zeiss-Jena Stereometrographs, Stereoplanigraphs and Topocarts.

Manpower

Majority of photogrammetric staff have high or technical university education.

2. Non-Topographic Operation

The non-topographic applications of photogrammetric methods concern various domains of the national economy and science. The photogrammetric methods have found in Poland many applications for mining, industry and other purposes such as:

- measurements of dislocations and deformations of industrial and mining constructions (e.g., a gasholder, gantry pillar, boring tower, coal bunker, roof trusses of industrial halls, radar antenna);
- terrophotogrammetric measurements of a TV mast to determine tension forces of guy-ropes;
- application of single-image photogrammetry to examine sewerage pipeline deformations;
- investigation of a model of a river bottom using stereophotos taken with UMK 10/1318 through water;
- photogrammetric measurements of water waves on hydrotechnic models;
- volume determination of excavated masses on open pits by analytical photogrammetry;
- application of analogue or/and analytical photogrammetric plotting for revision of data on open pits;

- investigation of ship launching process;
- determination of geometry and density of powder spreaded out by a jet fire extinguisher;
- diagnosis and monitoring of rehabilitation process by stereophotogrammetry and "Moire technique" in medicine;
- stereophotogrammetry measurements of photomicrographs taken with an electron and microscope.

There were applied different methods and ideas as:

- development of the method based on time parallax concept for photogrammetric determination of displacements;
- technology of photogrammetric determination of the building displacements based on block adjustment of the stereophotograms taken from a time base;
- attempt to substitute the glass plate 13x18 cm by a cut-film in the terrestrial cameras UMK;
- using of non-metric cameras for investigation of model of physical phenomena or objects.

Moreover, "Technical Instructions" for documentation of monuments of architecture" was published in Poland in 1981. It gives a main lines how to measure and present: urbanistic and architectonic units, small architecture, interiors and furnishing, details, historical sites, etc. The instructions contain methods and technologies, accuracy requirements, and some examples of final drawings.

Non-topographic projects have been carried out by photogrammetric sections or institutes of universities, technical or agriculture academies, state and local enterprises. Totally, about 20 units are involved in non-topophotogrammetry in Poland. Following cameras have been used: Zeiss Jena UMK, Photheo, Wild P3O, and non-metric cameras. Photographs are measured mainly on Zeiss Jena stereocomparators as steco 1818 and stecometer, and are plotted on different analogue instruments of Zeiss Jena or Wild Stereoplotters.

3. Remote Sensing Activity

The main activity in this field is carried out at the Polish Remote Sensing Centre (OPOLIS)—department of Institute of Geodesy and Cartography Warsow. Some activity take place at the universities in Cracow, Gdansk, Olsztyn, Poznan, Stettin, Warsow and Wroclaw. Interesting remote sensing applications (including close-range methods)

have been done by regional surveying enterprises (KPG-Cracow and OPGK-Stettin).

OPOLIS has been established in 1976. The modern methods of data acquisition and analysis are applied. MSS, TM Landsat, SPOT data as well as Soviet satellite photographs are basic source from space for interpretation. Airborne data including panchromatic, colour, colour infra-red and multispectral as well as thermal photographs have been also used in Poland. For analog data handling the following equipment is available:

- stereoscopes, interpretoscopes, zoom-transfer-scopes, stereocomparators Zeiss Jena and Zeiss Oberkochen,
- microdensitometers,
- optical additive colour viewers AC-90, AC-70 NAC, MSP-4 Zeiss Jena,
- analog and electronics Multi Colour Data Processing System NAC.

Digital data processing is based on the 2 PAAC System (OVAAC8) which is used for interactive analysis of multispectral digital and analog data. Microcomputer IBM PC/AT are used for digital interpretation of data collected on a floppy disc or CCT. The following thematic and topographic work have been done:

- map making and updating in the scales 1:500 000, 1:200 000, 1:100 000, 1:50 000 using TM Landsat, SPOT, Soviet satellite photographs,
- rock discrimination, mineral resource evaluation, natural hazard assessment, landforms mapping,
- ground water targeting, hydrographic mapping,
- vegetation monitoring, crops classification on the basis of statistical methods, forest sanitary, forest economic classes determination,
- land use inventories, site investigations, soil investigations,
- pollution assessment, landscape disturbance detection.

A few remote sensing experiments named TELEFOTO and TELEGEO have been done so far in Poland since 1977. Different kind of equipment and level of data collection have been used simultaneously: MSS, TM Landsat, SALUT-6 orbital station, aircraft (2.5 - 10 km) equipped with RC-10, MKF-6, MSK-4, MB-490 NAC Cameras; helicopters with spectrometers, in the field ground data collection has been carried out. OPOLIS is an interdisciplinary research and application institution; it employs following experienced specialists: photogrammetrists, cartographers,

computer electronics experts, geographers, agricultural and forest interpreters. The OPOLIS organizes the low-cost training courses in the field of remote sensing applications. OPOLIS teams have also run the projects in the following developing countries: Vietnam, Mongolia, Cuba, Libya, Algeria, Somalia, Iraq, Sudan, Turkey, Nigeria.

4. Research and Development

- a) A new method of photo-triangulation adjustment, called PHOTONET 86 has been developed. The method is based on simultaneous adjustment of geodetic and photogrammetric measurements with refinement of exterior orientation elements.
- b) Adaptation of the stereocomparators (Zeiss Jena Stecometer Opton PSK-2 and mechanical plotters (Wild A-8 and A-10) to the analytical purposes through connection to the IBM PS computers in on-line procedure.
- c) Zeiss Jena stereocomparator STECO 18x18 was provided with analogue-to-digital converter for automatic measurements registration.
- d) Counters to Zeiss Jena stecometer C was constructed which is used instead of Coordimeter F.
- f) Two systems of aerotriangulation adjustment have been developed: first called AERONET is based on the method of independent bundles and uses 18M PC XT/AT computer, second called BUND is based on G. Schut method of independent bundles.
- g) For satellite photographs triangulation SPACE BLOCK SYSTEM was developed.
- h) For analytical aerial triangulation measurements using precision stereocomparator connected with microcomputer-system NADZOR SG of supervision of observations was developed. The similar system NADZOR AG for semi-analytical aerial triangulation was also prepared.
- i) For numerical on-line processing system MASOWKA SG was developed based on precision stereocomparator, microcomputer and known (from adjustment of aerial triangulation) orientation elements of photographs. The similar system MASOWKA AG but based on analogue stereoplotter and independent model measurements was also prepared.
- j) The calculation algorithms was programmed on various computers: PARABLOK--for determination of the displacement based on block adjustment of pseudostereograms taken from time base; STEREOGRAM-- analytical model solution with simultaneously executed conditions of collinearity and coplanarity; KALIBRACJA--program for field calibration of terrestrial and aerial cameras; KOREKCJA--program for geometrical corrections of TV, radar and scanner imageries.

- k) The set of programs: KP25-KP29, SPOC: DTMT, TRIN, FOTO for geometric corrections of aerial scanner imagery have been also developed.
- 1) Various programs for volume computations, based on DMT, for processing of terrestrial photographs and similar computations, have been worked out.
- m) Zeiss-Jena Topocart B/Orthophot B and Topocart C/Orthophot C instrument systems were modified. Now these instruments are used for production of stereomate also.
- n) For measuring of visible and near infrared radiation the spectroalbedometer was constructed.
- o) The technology for orthophoto production base on differential rectification of digitized aerial photos using minicomputers was developed.

5. Education

Photogrammetric education for geodetists and surveyors is given in Poland in the following three different levels:

- 1) high school or technical college--for Survey Technicians and/or Technologists,
- 2) post high school education of 4 years for Bachelor of Surveying (is provided only for persons who works professionally in geodesy),
- 3) university of 5 years for Master of Surveying.

The middle level of photogrammetry is provided at 28 technical high schools, which teach the survey technicians.

The university education in the field of Surveying and Geodesy in Poland is provided at three technical universities and three agriculture academics. There are two Faculties of Geodesy, and at the agriculture academics: the Faculties of Geodesy and Drainage/or Agriculture Facilities). Yearly, about 300 students begin study in all above mentioned universities and academies. But only about 40 students specialize in photogrammetry and remote sensing, and only 20 students is graduated yearly. The scope of photogrammetric education is carefully adjusted to fulfil of passive and active photogrammetrists. Foreigners are educated also at the university level. We have students from some Asiatic and African countries.

The photogrammetric university staff is following: one full professor, 3 associate professors, 8 readers, 35 doctors.

Last years the following postgraduate studies were organized at the universities:

- 1. Engineering photogrammetry,
- 2. Architectural photogrammetry,
- 3. Remote sensing for environment protection,
- 4. Remote sensing in agriculture and forestry.

The study last one year, and are studies with obligatory meeting every month for a few days at the university. They serve to educate the engineers of various disciplines and have both theoretical and practical courses. For such courses guest lecturers are also invited.

The university studies in geology, cartography and geography include photogrammetry and remote sensing courses also.

6. Publications

In the period of 1976-1986 there were elaborated 10 textbooks and 1009 articles concerning photogrammetry and remote sensing.

The following are the bibliographical data for textbooks in a chronological order:

- 1) Swiatkiewicz A.: Fotogrametria. Podrecznik dla studentow Geodezji i Urzadzen Rolnych Akademii Rolniczych. PWN: Warszawa 1977, s. 329.
- 2) Rudowski G.: Termowizja i jej zastosowanie. Wyd. WKL. W-wa 1978.
- 3) Sitek Z.: Fotogrametria inzynierska. Skrypty uczelniane nr 676, wyd. AGH Krakow 1979.
- 4) Swiatkiewicz A.: Fotogrametria. Zasady i zastosowanie w gospodarce rolnej i wodnej. PWN Warszawa 1979 wyd. 2.
- 5) Kaczynski R.: Instrumenty stereofotogrametryczne. Skrypt WAT W-wa 1980.
- 6) Sitek Z.: Fotogrametria z fotografia techniczna, PWN Warszawa 1981.
- 7) Kaczynski R., Mroczek, Sanecki J.: Rozpoznanie obrazowe. MON, W-wa 1982.
- 8) Swiatkiewicz A.: Fotogrametria-zasady i zastosowania w gospodarce rolnej i wodnej. PWN W-wa 1983.
- 9) Sitek Z.: Elementy fotogrametrii z fotografia techniczna. PWN Warszawa 1984.

10) Beker L., Kaczynski R.: Fotorafia i fotogrametria podwodna. WNT, W-wa 1985.

The technical and scientific works were printed in 20 national periodicals, 24 serial publications and in 76 other, occasional booklets. Works prepared by polish authors were printed also in 16 publications abroad. The table below shows the thematical classification of publications according to the domains of ISPRS commissions (some papers thematically belong to more than one commission).

year of -	ISPRS Commission number							
issue	I	11	III	IV	V	VI	VII	
1976	9	3	5	13	8	9	31	
1977	8	13	6	27	58	9	45	
1978	8	14	6	19	8	33	29	
1979	7	7	10	9	44	4	10	
1980	10	8	10	16	11	8	32	
1981	9	6	11	10	24	13	11	
1982	11	4	8	15	19	14	13	
1983	7	3	11	6	6	3	17	
1984	18	6	29	15	16	5	48	
1985	16	2	23	19	10	9	58	
1986	11	3	4	6	12	3	10	

Detailed information about national publications concerning photogrammetry and remote sensing can be found in the thematic bibliography which have been elaborated by our national society. First part of this bibliography was published in the proceedings of ISPRS commission VI in 1976, and the second part covering period 1976-1986 and the supplement to the first part were published by the University of Mining and Metallurgy in Cracow in 1987.

Beside the above mentioned, there are thematical bibliographies edited by "Center of professional, scientific, technical and economical information" which cover fields of geodesy (with photogrammetry and remote sensing), geography and geology.

7. Professional Subjects

Two professional organizations are active in Poland:

7.1. POLISH SOCIETY OF PHOTOGRAMMETRY AND REMOTE SENSING (PSPRS)—is the scientific section of POLISH GEODETIC ASSOCIATION (SGP). The activity of PSPRS is based on statutes of POLISH SOCIETY OF PHOTOGRAMMETRY (PSP) founded in 1930. In 1984 PSP took name PSPRS. The area of activity of PSPRS is POLISH PEOPLE'S REPUBLIC. PSPRS can be the

member of other scientific associations in the country and abroad. PSPRS continues the activity of PSP which was interrupted in 1939.

The aims of PSPRS are:

- a) activity in the field of photogrammetry and remote sensing together with various technical application,
- b) popularization and promotion of photogrammetric and remote sensing methods in different scientific and technical fields,
- c) exchange, publish and circulate any experiences within the country and abroad.

The supreme authority of the Society is the General Assembly. The General Assembly consist of all members of the Society, and every three years the President and by separate voting the Council of the Society are elected.

In 1987 number of active specialists in the Society was 142.

PSPRS is a member of the Main Technical Organization in Poland (NOT--it is federation scientific, and technical associations).

Legislative basis of the professional activities of PSPRS is statutes law issued 27 October 1932 (Dz. U. R. P. Nr 94, poz. 808) and amended 9 June 1982 (M. P. Nr 17, poz. 144).

Main Technical Organization (NOT) and Polish Geodetic Association (SGP) have established the awards consisted a monetary grant to the author of outstanding merit also on photogrammetry, photointerpretation or remote sensing.

7.2. POLISH GEOGRAPHICAL SOCIETY (PTG)--COMMISSION OF PHOTOINTERPRETATION is active in Poland on the basic of PTG Statutes. The objective of the Commission is the activity on photointerpretation field particularly for searching geographical environment. The number of members of the Commission is about 70. They are members of PTG.

8. Addresses

- 8.1. Organizations other than education and research
- 1) Regional Enterprises of Geodesy and Cartography (OPGK): 15-005 BIALYSTOK, ul. Sienkiewicza 84; 80-952 GDANSK, ul. Miszewskiego 17; 40-950 KATOWICE, ul. Kosshutha 9; 31-530 KRAKOW, ul. Grzegorzecka 10; 20-072 LUBLIN, ul. Czechowska 2; 90-746 LODZ, ul. Zakatna 18/20; 35-959 RZESZOW, ul. Geodetow 1; 70-508 SZCZECIN, ul. H. Poboznego 5; 53-125 WROCLAW, ul. Kasztanowa 18/20.

- 2) City Geodetic Enterprises: KPG 30-086 KRAKOW, ul. Halczyna 16; LMPG 90-101 LODZ, ul. Moniuszki 5; PPG 61-740 POZNAN, ul. Gronowa 20, WPG 00-955 WARSZAWA, Nowy Swiat 2.
- 3) Other enterprises: State Enterprise of Geodesy and Cartography--PPGK 00-950 WARSZAWA, ul. Jasna 2/4; Geoprojekt 00-895 WARSZAWA, ul. Biala 2; Mining Surveying Office Belchaow, PIOTRKOW TRYBUNALSKI p.o.b. 1442; Laboratories of Preservation of Monuments (PKZ) 02-958 WARSZAWA-WILANOW, ul. Wiertnicza 2.

8.2. Education and research

Photogrammetric Departments of Technical Universities: 30-059 KRAKOW, Al. Mickiewicza 30; 00-661 WARSZAWA, Pl. Jednosci Robotniczej 1.

Photogrammetric Departments of Agriculture Academies: 30-059 KRAKOW, A1. Mickiewicza 24/28; 10-957 OLSZTYN-KORTOWO b1. 52; 02-975 WARSZAWA-Ursynow, u1. Nowoursynowska 166; 50-363 WROCLAW P1. Grunwaldzki 24.

Other universities where photogrammetry and remote sensing is active are: Gdansk University, 80-952 GDANSK, ul. Miszewskiego 17 Jagiellonic University, 31-044 KRAKOW, ul. Grodzka 64; A. Mickiewicz University 61-701 POZNAN, ul. Fredry 10; Warsow University--Photointerpretation Laboratory, 00-927 WARSZAWA, Krakowskie Przedmiescie 30 and Photogeology 02-089 WARSZAWA, ul. Zwirki i Wigury 93; Wroclaw Technical University, 54-028 WROCLAW, ul. Rajska 6.

Research Institution:

Institute of Geodesy and Cartography--Photogrammetric Department and Remote Sensing Centre (OPOLIS) 00-950 WARSZAWA, ul. Jasna 2/4; Geology Department--Polish Academy of Sciences 02-089 WARSZAWA, ul. Zwirki i Wigury 93; Geological Institute 00-975 WARSZAWA, ul. Rakowiecka 4; Stettin Institute of Technology 70-326 SZCZECIN, Al. Piastow 80.

/09599

A Comparison Between the Variability Structure of the Remotely Sensed Sea-Surface Temperature and Pigment Distributions

43070006a Kyoto Selections from INTERNATIONAL ARCHIVES OF PHOTOGRAMMETRY AND REMOTE SENSING in English Vol 27, 1988 pp 252-260

[Article by Mati Kahru, Institute of Thermophysics and Electrophysics, Estonian Academy of Sciences, Paldiski Rd. 1, Tallinn, 200031, USSR, Commission VII]

[Text] Introduction

Since the work of Platt (1972) spectral analysis has been widely used for the interpretation of the plankton variability in the ocean. It has been assumed that the shape of the variance spectra (e.g., its slope in the log-log plot in relation to wavenumber k) can provide clues to discover the mechanisms, governing the distribution of plankton. After the initial flush of papers (Denman and Platt, 1975; Denman, 1976 and many others) the enthusiasm gradually decreased. Initial theories, set forth to explain the variance spectra of chlorophyll (index of phytoplankton abundance) gave inconsistent results. Some theories (Denman and Platt, 1976; Denman, et al., 1977) predicted a brake from shallower to steeper slopes with increasing wavenumbers. Another (Fasham, 1978), on the contrary, predicted flattening of the chlorophyll spectrum with increasing wavenumbers for a positive net growth rate. Platt (1978) concluded that if there was any merit in the concept of a spectral break at a critical wavenumber, the length of transects commonly used by shipboard patchiness studies was not sufficient. At the same time, the imagery of the Coastal Zone Color Scanner (CZCS), the principal source of synoptic maps of the "chlorophyll-like" pigments (Gordon and Morel, 1983), has not been studied by spectral analysis in a systematic way. By comparison, a number of papers have dealt with the variability structure of the sea surface temperature (SST) distributions obtained from the Advanced Very High Resolution Radiometer (AVHRR) (Deschamps, et al., 1981). It has been argued (Lesieur and Sadourny, 1981; Fasham, 1978; Army and Flament, 1985) that spectral slopes per se are only weak constraints for testing theories on the structure of flows

or the control of phytoplankton patchiness. In this regard, comparison of the pigment and SST spectra should yield more meaningful information.

In this paper the spatial variance spectra of the near-surface pigment concentrations (from CZCS) and SST (from AVHRR) are analyzed. Most of the images originate from the California Current area, a few from the North and the Baltic Seas.

Methods

The CZCS and AVHRR images were processed at the Jet Propulsion Laboratory (Pasadena, California) by M. Abbott and P. Zion using software developed in the University of Miami (Abbott and Zion, 1985). After correction for geographic errors, a 1024-by-1024 pixel array was removed from each satellite pass. Geophysical algorithms were then applied to derive SST and near-surface chlorophyll-like pigments. SST was estimated using the channel 4 (10 to 11.5 um) brightness temperature. The pigment concentration was derived using the Gordon algorithms (Gordon and Morel, 1983) as implemented in the Miami software. With both the SST and pigment concentrations, small absolute errors do not concern us since for spectral calculations only the relative spatial patterns are important. The SST and pigment images were then resampled and remapped to an equal area of 512-by-512 pixels. The remapped arrays have an approximate grid size of 1.1 x 1.1 km and are directly comparable over time and between sensors.

Series of parallel transects were extracted in the north-to-south and/or west-to-east directions from cloud-free areas. The distance between neighboring transects was usually 5 pixels. Each series contained up to 75 transects of equal length. The transects were trend corrected and tapered with the split cosine bell. The spectra were calculated with FFT and the Parzen lag window using FORTRAN subroutines from the NAGFLIB package. The calculation of bivariate spectra was similar in principle, the final results being the squared coherency spectrum estimates with their confidence bounds at the 95 percent level. Due to the finite length and resolution of the transects, the spectra are reliable for the wavelength range of 2-100 km. The variance spectra were integrated in several wavenumber bands, yielding a decomposition of the total variance into contributions at different scales. The mean spectral slopes were then calculated between these bands. All of the statistics were averaged over sets of parallel transects or spectra.

Autospectra of Pigment and SST Spatial Variance

A characteristic feature of the pigment data was an obvious increase in variance with the increase of the mean pigment concentration. The SST data showed no relationship between the mean and variance. Examples of the spectra of spatial variance are shown on Figure 1 with the statistics given in Tables 1, 2.

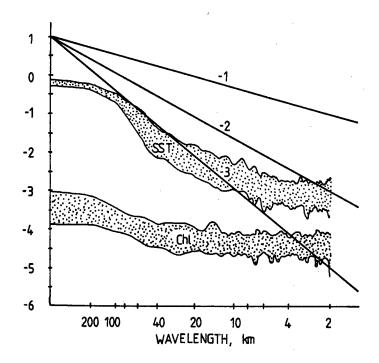


Figure 1. Envelopes of the variance spectra of temperature (SST) and pigment concentration (Ch1) for 28 parallel north-south transects in the California current area, 2 November 1981.

Table 1. Statistics of the sets of phytoplankton pigment spectra calculated from parallel transects from the California Current (CC) and other areas.

[mg/m3] 73, 3-10, 5 10, 0-2, 2 73, CC 81-04-04 0, 29 -2, 42 -1, 89 CC 81-04-04 0, 26 -2, 05 -2, 05 CC 81-04-04 0, 31 -1, 75 -2, 08 CC 81-04-21 0, 46 -1, 81 -0, 05 CC 81-05-08 0, 09 -2, 08 -0, 08 CC 81-05-08 0, 01 -2, 19 -0, 26 CC 81-05-08 1, 60 -2, 84 -2, 16 North Sea 80-06-06 1, 36 -2, 42 -0, 84 North Sea 80-06-06 1, 25 -2, 42 -0, 25 CC 81-06-15 0, 08 -0, 88 -0, 41 CC 81-06-15 0, 08 -1, 68 -0, 13 CC 81-06-16 0, 05 -1, 00 0, 10 CC 81-06-16 0, 05 -1, 00 0, 10 CC 81-06-16 0, 05 -1, 36 -0, 01 Baltic 79-06-19 1, 61 -0, 63 -0, 87 Baltic 79-06-19 2, 13 -0, 93 -0, 67 CC 81-07-07 1, 00 -2, 13 -2, 37 CC 81-07-08 1, 10 -2, 43 -2, 24 CC 81-11-02 0, 08 -0, 85 -0, 01 CC 81-11-03 0, 14 -0, 93 0, 04 CC 81-11-03 0, 14 -1, 00 0, 16 CC 81-11-03 0, 14 -1, 00 0, 24 CC 81-11-03 0, 17 -1, 80 -0, 24	_	Date	Mean		pectral sl			
CC 81-04-04 0.29 -2.42 -1.89 CC 81-04-04 0.28 -2.05 -2.05 CC 81-04-04 0.31 -1.75 -2.08 CC 81-04-21 0.46 -1.81 -0.05 CC 81-05-08 0.09 -2.08 -0.08 CC 81-05-08 1.60 -2.42 -0.26 CC 81-05-08 1.60 -2.84 -2.16 North Sea 80-06-06 1.36 -2.42 -0.84 North Sea 80-06-06 1.25 -2.42 -0.25 CC 81-06-15 0.08 -0.88 -0.41 CC 81-06-15 0.08 -1.68 -0.13 CC 81-06-16 0.05 -1.00 0.10 CC 81-06-16 0.05 -1.36 -0.01 Baltic 79-06-19 1.61 -0.63 -0.87 Baltic 79-06-19 2.13 -0.93 -0.67 CC 81-07-08 1.10 -2.43 -2.24 CC 81-11-02 0.08 -0.75 -0.07 CC 81-11-02 0.09 -1.43 -0.01 CC 81-11-03 0.14 -0.93 0.04 CC 81-11-03 0.14 -0.93 0.04 CC 81-11-03 0.14 -1.00 0.16 CC 81-11-03 0.14 -1.65 0.03 CC 81-11-03 0.17 -1.80 -0.24	Area	(yy-mm-dd)		wavelength ranges in km				
CC 81-04-04 0. 28 -2. 05 -2. 05 CC 81-04-04 0. 31 -1. 75 -2. 08 CC 81-04-21 0. 46 -1. 81 -0. 05 CC 81-05-08 0. 09 -2. 08 -0. 08 CC 81-05-08 0. 01 -2. 19 -0. 26 CC 81-05-08 1. 60 -2. 84 -2. 16 North Sea 80-06-06 1. 36 -2. 42 -0. 84 North Sea 80-06-06 1. 25 -2. 42 -0. 25 CC 81-06-15 0. 08 -0. 88 -0. 41 CC 81-06-15 0. 08 -1. 68 -0. 13 CC 81-06-16 0. 05 -1. 00 0. 10 CC 81-06-16 0. 05 -1. 36 -0. 01 Baltic 79-06-19 1. 61 -0. 63 -0. 67 CC 81-07-07 1. 00 -2. 13 -2. 37 CC 81-07-08 1. 10 -2. 43 -2. 24 CC 81-10-2 0. 08 -0. 75 -0. 07 CC 81-11-02 0. 08 -0. 85 -0. 10 CC 81-11-02 0. 08 -0. 85 -0. 10 CC 81-11-03 0. 14 -0. 93 0. 04 CC 81-11-03 0. 14 -1. 00 0. 16 CC 81-11-03 0. 17 -1. 80 -0. 24			[mg/m3]	73, 3-10, 5	10. 0-2. 2	73. 3-2. 2		
CC 81-04-04 0.31 -1.75 -2.08 CC 81-04-21 0.46 -1.81 -0.05 CC 81-05-08 0.09 -2.08 -0.08 CC 81-05-08 0.01 -2.19 -0.26 CC 81-05-08 1.60 -2.84 -2.16 North Sea 80-06-06 1.36 -2.42 -0.84 North Sea 80-06-06 1.25 -2.42 -0.25 CC 81-06-15 0.08 -0.88 -0.41 CC 81-06-15 0.08 -1.68 -0.13 CC 81-06-16 0.05 -1.00 0.10 CC 81-06-16 0.05 -1.00 0.10 CC 81-06-19 1.61 -0.63 -0.87 Baltic 79-06-19 1.61 -0.63 -0.87 CC 81-07-07 1.00 -2.13 -2.37 CC 81-07-08 1.10 -2.43 -2.24 CC 81-11-02 0.08 -0.75 -0.07 CC 81-11-02 0.09 -1.43 -0.01 CC 81-11-03 0.14 -0.93 0.04 CC 81-11-03 0.14 -0.93 0.04 CC 81-11-03 0.14 -1.00 0.16 CC 81-11-03 0.18 -1.65 0.03 CC 81-11-03 0.17 -1.80 -0.24	CC	81-04-04	0. 29	-2.42	-1.89	-2.08		
CC 81-04-21 0.46 -1.81 -0.05 CC 81-05-08 0.09 -2.08 -0.08 CC 81-05-08 1.60 -2.19 -0.26 CC 81-05-08 1.60 -2.84 -2.16 North Sea 80-06-06 1.35 -2.42 -0.84 North Sea 80-06-06 1.25 -2.42 -0.25 CC 81-06-15 0.08 -0.88 -0.41 CC 81-06-15 0.08 -1.68 -0.13 CC 81-06-16 0.05 -1.00 0.10 CC 81-06-16 0.05 -1.00 0.10 CC 81-06-19 1.61 -0.63 -0.87 Baltic 79-06-19 2.13 -0.93 -0.67 CC 81-07-07 1.00 -2.13 -2.37 CC 81-07-08 1.10 -2.43 -2.24 CC 81-11-02 0.08 -0.75 -0.07 CC 81-11-02 0.08 -0.85 -0.10 CC 81-11-03 0.14 -0.93 0.04 CC 81-11-03 0.14 -0.93 0.04 CC 81-11-03 0.14 -1.00 0.16 CC 81-11-03 0.18 -1.65 0.03 CC 81-11-03 0.17 -1.80 -0.24	CC	81-04-04	0. 28	-2.05	-2.05	-1.99		
CC 81-05-08 0.09 -2.08 -0.08 CC 81-05-08 0.01 -2.19 -0.26 CC 81-05-08 1.60 -2.84 -2.16 North Sea 80-06-06 1.36 -2.42 -0.84 North Sea 80-06-06 1.25 -2.42 -0.25 CC 81-06-15 0.08 -0.88 -0.41 CC 81-06-15 0.08 -1.68 -0.13 CC 81-06-16 0.05 -1.00 0.10 CC 81-06-16 0.05 -1.00 0.10 CC 81-06-19 1.61 -0.63 -0.87 Baltic 79-06-19 2.13 -0.93 -0.67 CC 81-07-07 1.00 -2.13 -2.37 CC 81-07-08 1.10 -2.43 -2.24 CC 81-11-02 0.08 -0.75 -0.07 CC 81-11-02 0.08 -0.75 -0.07 CC 81-11-03 0.14 -0.93 0.04 CC 81-11-03 0.14 -0.93 0.04 CC 81-11-03 0.18 -1.65 0.03 CC 81-11-03 0.17 -1.80 -0.24	CC	81-04-04	0.31	-1.75	-2.08	-1.96		
CC 81-05-08 0.01 -2.19 -0.26 CC 81-05-08 1.60 -2.84 -2.16 North Sea 80-06-06 1.36 -2.42 -0.84 North Sea 80-06-06 1.25 -2.42 -0.25 CC 81-06-15 0.08 -0.88 -0.41 CC 81-06-15 0.08 -1.68 -0.13 CC 81-06-16 0.05 -1.00 0.10 CC 81-06-16 0.05 -1.00 0.10 CC 81-06-19 1.61 -0.63 -0.01 Baltic 79-06-19 2.13 -0.93 -0.67 CC 81-07-07 1.00 -2.13 -2.37 CC 81-07-08 1.10 -2.43 -2.24 CC 81-11-02 0.08 -0.75 -0.07 CC 81-11-02 0.08 -0.75 -0.07 CC 81-11-02 0.08 -0.85 -0.10 CC 81-11-02 0.08 -0.85 -0.10 CC 81-11-03 0.14 -0.93 0.04 CC 81-11-03 0.14 -1.00 0.16 CC 81-11-03 0.18 -1.65 0.03 CC 81-11-03 0.17 -1.80 -0.24	CC	81-04-21	0.46	-1.81	-0.05	-0.94		
CC 81-05-08 1.60 -2.84 -2.16 North Sea 80-06-06 1.36 -2.42 -0.84 North Sea 80-06-06 1.25 -2.42 -0.25 CC 81-06-15 0.08 -0.88 -0.41 CC 81-06-15 0.08 -1.68 -0.13 CC 81-06-16 0.05 -1.00 0.10 CC 81-06-16 0.05 -1.36 -0.01 Baltic 79-06-19 1.61 -0.63 -0.87 Baltic 79-06-19 2.13 -0.93 -0.67 CC 81-07-07 1.00 -2.13 -2.37 CC 81-07-08 1.10 -2.43 -2.24 CC 81-11-02 0.08 -0.75 -0.07 CC 81-11-02 0.09 -1.43 -0.01 CC 81-11-03 0.14 -0.93 0.04 CC 81-11-03 0.14 -0.93 0.04 CC 81-11-03 0.18 -1.65 0.03 CC 81-11-03 0.17 -1.80 -0.24	CC	81-05-08	0.09	-2.08	-0.08	-1.15		
North Sea 80-06-06 1.36 -2.42 -0.84 North Sea 80-06-06 1.25 -2.42 -0.25 CC 81-06-15 0.08 -0.88 -0.41 CC 81-06-15 0.08 -1.68 -0.13 CC 81-06-16 0.05 -1.00 0.10 CC 81-06-16 0.05 -1.36 -0.01 Baltic 79-06-19 1.61 -0.63 -0.87 Baltic 79-06-19 2.13 -0.93 -0.67 CC 81-07-07 1.00 -2.13 -2.37 CC 81-07-08 1.10 -2.43 -2.24 CC 81-11-02 0.08 -0.75 -0.07 CC 81-11-02 0.09 -1.43 -0.01 CC 81-11-03 0.14 -0.93 0.04 CC 81-11-03 0.14 -0.93 0.04 CC 81-11-03 0.18 -1.65 0.03 CC 81-11-03 0.17 -1.80 -0.24	CC	81-05-08	0.01	-2.19	-0. 26	-1.36		
North Sea 80-06-06 1.25 -2.42 -0.25 CC 81-06-15 0.08 -0.88 -0.41 CC 81-06-15 0.08 -1.68 -0.13 CC 81-06-16 0.05 -1.00 0.10 CC 81-06-16 0.05 -1.36 -0.01 Baltic 79-06-19 1.61 -0.63 -0.87 Baltic 79-06-19 2.13 -0.93 -0.67 CC 81-07-07 1.00 -2.13 -2.37 CC 81-07-08 1.10 -2.43 -2.24 CC 81-11-02 0.08 -0.75 -0.07 CC 81-11-02 0.09 -1.43 -0.01 CC 81-11-03 0.14 -0.93 0.04 CC 81-11-03 0.14 -0.93 0.04 CC 81-11-03 0.14 -1.00 0.16 CC 81-11-03 0.14 -1.00 0.16 CC 81-11-03 0.17 -1.80 -0.24	CC	81-05-08	1.60	-2.84	-2.16	-2. 39		
CC 81-06-15 0.08 -0.88 -0.41 CC 81-06-15 0.08 -1.68 -0.13 CC 81-06-16 0.05 -1.00 0.10 CC 81-06-16 0.05 -1.36 -0.01 Baltic 79-06-19 1.61 -0.63 -0.87 Baltic 79-06-19 2.13 -0.93 -0.67 CC 81-07-07 1.00 -2.13 -2.37 CC 81-07-08 1.10 -2.43 -2.24 CC 81-11-02 0.08 -0.75 -0.07 CC 81-11-02 0.09 -1.43 -0.01 CC 81-11-02 0.08 -0.85 -0.10 CC 81-11-03 0.14 -0.93 0.04 CC 81-11-03 0.14 -1.00 0.16 CC 81-11-03 0.18 -1.65 0.03 CC 81-11-03 0.17 -1.80 -0.24	North Sea	80-06-06	1.36	-2. 42	-0.84	-1.44		
CC 81-06-15 0.08 -1.68 -0.13 CC 81-06-16 0.05 -1.00 0.10 CC 81-06-16 0.05 -1.36 -0.01 Baltic 79-06-19 1.61 -0.63 -0.87 Baltic 79-06-19 2.13 -0.93 -0.67 CC 81-07-07 1.00 -2.13 -2.37 CC 81-07-08 1.10 -2.43 -2.24 CC 81-11-02 0.08 -0.75 -0.07 CC 81-11-02 0.09 -1.43 -0.01 CC 81-11-03 0.14 -0.93 0.04 CC 81-11-03 0.14 -0.93 0.04 CC 81-11-03 0.18 -1.65 0.03 CC 81-11-03 0.17 -1.80 -0.24	North Sea	80-06-06	1.25	~2. 42	-0. 25	-1.33		
CC 81-06-16 0.05 -1.00 0.10 CC 81-06-16 0.05 -1.36 -0.01 Baltic 79-06-19 1.61 -0.63 -0.87 Baltic 79-06-19 2.13 -0.93 -0.67 CC 81-07-07 1.00 -2.13 -2.37 CC 81-07-08 1.10 -2.43 -2.24 CC 81-11-02 0.08 -0.75 -0.07 CC 81-11-02 0.09 -1.43 -0.01 CC 81-11-03 0.14 -0.93 0.04 CC 81-11-03 0.14 -0.93 0.04 CC 81-11-03 0.14 -1.00 0.16 CC 81-11-03 0.18 -1.65 0.03 CC 81-11-03 0.17 -1.80 -0.24	CC	81-06-15	0.08	-0.88	-0.41	-0, 50		
CC 81-06-16 0.05 -1.36 -0.01 Baltic 79-06-19 1.61 -0.63 -0.87 Baltic 79-06-19 2.13 -0.93 -0.67 CC 81-07-07 1.00 -2.13 -2.37 CC 81-07-08 1.10 -2.43 -2.24 CC 81-11-02 0.08 -0.75 -0.07 CC 81-11-02 0.09 -1.43 -0.01 CC 81-11-02 0.08 -0.85 -0.10 CC 81-11-03 0.14 -0.93 0.04 CC 81-11-03 0.14 -1.00 0.16 CC 81-11-03 0.18 -1.65 0.03 CC 81-11-03 0.17 -1.80 -0.24	CC	81-06-15	0.08	-1.68	-0.13	-0.78		
Baltic 79-06-19 1.61 -0.63 -0.87 Baltic 79-06-19 2.13 -0.93 -0.67 CC 81-07-07 1.00 -2.13 -2.37 CC 81-07-08 1.10 -2.43 -2.24 CC 81-11-02 0.08 -0.75 -0.07 CC 81-11-02 0.09 -1.43 -0.01 CC 81-11-02 0.08 -0.85 -0.10 CC 81-11-03 0.14 -0.93 0.04 CC 81-11-03 0.14 -1.00 0.16 CC 81-11-03 0.18 -1.65 0.03 CC 81-11-03 0.17 -1.80 -0.24	CC	81-06-16	0. 05	-1.00	0.10	-0, 43		
Baltic 79-06-19 2.13 -0.93 -0.67 CC 81-07-07 1.00 -2.13 -2.37 CC 81-07-08 1.10 -2.43 -2.24 CC 81-11-02 0.08 -0.75 -0.07 CC 81-11-02 0.09 -1.43 -0.01 CC 81-11-02 0.08 -0.85 -0.10 CC 81-11-03 0.14 -0.93 0.04 CC 81-11-03 0.14 -1.00 0.16 CC 81-11-03 0.18 -1.65 0.03 CC 81-11-03 0.17 -1.80 -0.24	CC	81-06-16	0.05	-1.36	-0.01	-0. 72		
CC 81-07-07 1.00 -2.13 -2.37 CC 81-07-08 1.10 -2.43 -2.24 CC 81-11-02 0.08 -0.75 -0.07 CC 81-11-02 0.09 -1.43 -0.01 CC 81-11-03 0.08 -0.85 -0.10 CC 81-11-03 0.14 -0.93 0.04 CC 81-11-03 0.14 -1.00 0.16 CC 81-11-03 0.18 -1.65 0.03 CC 81-11-03 0.17 -1.80 -0.24	Baltic	79-06-19	1.61	-0, 63	-0.87	-0.63		
CC 81-07-08 1.10 -2.43 -2.24 CC 81-11-02 0.08 -0.75 -0.07 CC 81-11-02 0.09 -1.43 -0.01 CC 81-11-02 0.08 -0.85 -0.10 CC 81-11-03 0.14 -0.93 0.04 CC 81-11-03 0.14 -1.00 0.16 CC 81-11-03 0.18 -1.65 0.03 CC 81-11-03 0.17 -1.80 -0.24	Baltic	79-06-19	2. 13	-0.93	-0.67	-0.74		
CC 81-11-02 0.08 -0.75 -0.07 CC 81-11-02 0.09 -1.43 -0.01 CC 81-11-02 0.08 -0.85 -0.10 CC 81-11-03 0.14 -0.93 0.04 CC 81-11-03 0.14 -1.00 0.16 CC 81-11-03 0.18 -1.65 0.03 CC 81-11-03 0.17 -1.80 -0.24	CC	81-07-07	1.00	-2, 13	-2.37	-2. 33		
CC 81-11-02 0.09 -1.43 -0.01 CC 81-11-02 0.08 -0.85 -0.10 CC 81-11-03 0.14 -0.93 0.04 CC 81-11-03 0.14 -1.00 0.16 CC 81-11-03 0.18 -1.65 0.03 CC 81-11-03 0.17 -1.80 -0.24	CC	81-07-08	1.10	-2, 43	-2. 24	-2.36		
CC 81-11-02 0.08 -0.85 -0.10 CC 81-11-03 0.14 -0.93 0.04 CC 81-11-03 0.14 -1.00 0.16 CC 81-11-03 0.18 -1.65 0.03 CC 81-11-03 0.17 -1.80 -0.24	CC	81-11-02	0.08	~0.75	-0.07	-0. 34		
CC 81-11-03 0.14 -0.93 0.04 CC 81-11-03 0.14 -1.00 0.16 CC 81-11-03 0.18 -1.65 0.03 CC 81-11-03 0.17 -1.80 -0.24	CC	81-11-02	0.09	-1.43	-0.01	-0.67		
CC 81-11-03 0.14 -1.00 0.16 CC 81-11-03 0.18 -1.65 0.03 CC 81-11-03 0.17 -1.80 -0.24	CC	81-11-02	0.08	-0.85	-0.10	-0.46		
CC 81-11-03 0.18 -1.65 0.03 CC 81-11-03 0.17 -1.80 -0.24	CC	81-11-03	0.14	-0.93	0.04	-0. 42		
CC 81-11-03 0.18 -1.65 0.03 CC 81-11-03 0.17 -1.80 -0.24	CC	81-11-03	0.14	-1.00	0.16	-0.45		
CC 81-11-03 0.17 -1.80 -0.24					0.03	-0.79		
					-0. 24	-0. 89		
Mean: 0.53 -1.64 -0.69		Mean:	0.53	-1.64	-0.69	-1.13		

Table 2. Statistics of the sets of SST spectra calculated from parallel transects from the California current area.

Date	Mean		pectral sl	-
(yy-mm-dd)		wavele	ngth range	s in Km
	[C·]	73. 3-10. 5	10.0-2.2	73. 3-2. 2
81-04-04	7.19	-1.84	-1.06	-1.59
81-04-21	9.44	-2. 26	-0, 65	~1.60
81-05-07	10. 22	-2.94	-1.03	-2. 28
81-05-08	10. 31	-2.56	-0.39	-1.70
81-05-09	10.75	-2.10	-1.55	-1.83
81-05-09	11.43	-2.51	-0.33	-1.52
81-06-16	15, 13	-2. 39	-1.81	-1.94
81-06-16	15.01	-2.74	-0.13	-1.54
81-07-08	13.16	-2.72	-1.08	-2. 32
81-07-08	11.66	-2.97	-0.98	-2.32
81-07-10	12.59	-2, 85	-1.14	-2. 22
81-07-12	12, 59	-2.51	-1.10	-2.04
81-07-15	12.77	-3.10	-0.93	~2.30
81-11-02	18.42	-2.51	-0.58	-1.66
81-11-03	18, 65	-2.47	-0.93	-1.68
81-11-03	17. 78	-2, 38	-0, 35	-1.48
81-11-03	18.18	-2.56	-0.39	-1.64
Mean:	13. 25	-2.55	-0.85	-1.86

All the SST spectra were quite similar in shape with steep slopes flattening with the increase of wavenumbers. The pigment spectra were much more variable but both seemed to have a bimodal distribution of the slopes (Figure 2), corresponding to the presence or absence of offshore filaments ("squirts" or "jets") in the California current (see Abbott and Zion, 1985). Steep pigment spectra (slopes -2...-2.5) corresponded to transects across systems of filaments and were associated with higher mean concentration. In case of oligotrophic conditions with low pigment levels and low variability, the pigment spectra were close to the white noise spectrum (slopes between 0 and -1). Surprisingly, the two pigment spectra from the Baltic Sea were also almost flat (slopes between -0.5 and -1). From many in situ transects of pigment and plankton concentration in the Baltic (Kahru, unpublished) there has been no evidence of this kind of flat spectra. Therefore the Baltic Sea data must be treated with caution as the algorithms of pigment retrieval were not reliable for Morel Case 2 waters (Gordon and Morel, 1985). In 70 percent of the cases, the SST spectra were significantly steeper (in the wavelength range 73.3-2.2 km) than the corresponding pigment spectra, and for the rest the difference in the slopes was insignificant.

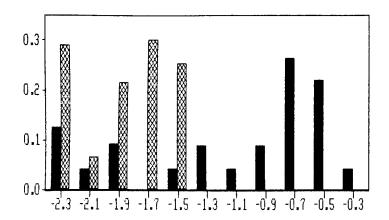


Figure 2. Frequency histograms of pigment (solid) and SST (hatched) spectral slopes from the CC area in the wavelength band $73.3-2.2~\rm km$.

Only a few sets of pigment spectra happened to be consistent with the Platt-Denman prediction of the spectra steepening towards the smaller scales. On the contrary, most of the pigment spectra (22 of 24 sets) became shallower and not steeper along wavelengths from 73.3 to 4.5 km. The same was true for most of the SST spectra (16 out of 17 sets). Between the wavelengths from 31.4 to 2.2 km the averaged spectral slopes flattened for 66 percent of the pigment spectra and for 94 percent of the SST spectra. The grand mean slope monotonously flattened with increasing wavenumbers.

Coherence Between the Pigment and SST Distributions

A general feature of the squared coherency spectra between the pigment and SST distributions in the California current area was their significant coherency on the longer wavelengths, and a drop to nonsignificant or spurious coherency starting from some characteristic wavelength (Figure 3). Averaging over each set of spectra, I calculated the minimal coherence length (hereafter, coherence length), defined as the mean wavelength) at which the lower 95 percent confidence limits of the coherency spectra first reach zero when moving from lower towards higher wavenumbers. For a few pairs of transects where the coherency was insignificant even at the longest scales, the coherence length was assumed to be equal to the length of the transects.

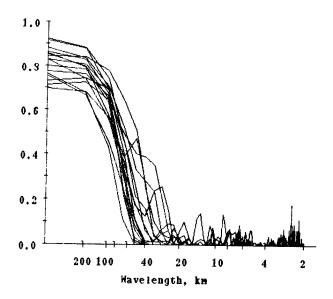


Figure 3. Lower 95 percent confidence limits of the squared coherency spectra between pigment and SST patterns from 16 north-south transects in the California current area, 8 July 1981.

The coherence lengths for pairs of pigment and SST images ranged from 27.6 km to over 500 km (Table 3). As could be expected, the coherence length is inversely related to the squared coherency at longer wavelengths. Although structures with wavelengths below the coherence length (e.g., fronts) may have a one-to-one correspondence between the distributions of pigments and SST, on the average, only the longer wavelengths are significantly correlated. The shortest coherence lengths belong to sets of north-south transects across the cross-shelf filaments in the California current system, the longest--to the oligotrophic oceanic conditions. In case of the filaments, coherency is highly anisotropic: higher across the filaments than along the filaments (cf. coherence lengths 172 vs. 321 km). In case of the lowvariability conditions, coherency is isotropic (cf. coherence lengths 330 vs. 389 km). The squared coherency is obviously higher when more variance is present on longer scales. The same relationship is manifest in the significant correlation between the coherence length and the spectral slopes of the pigment and SST autospectra. The general relationship is: the more variance there is on the longer scales, the steeper the autospectra, the higher the coherency, and the smaller the coherence length.

Table 3. Characteristics of the squared coherency spectra, averaged over sets of spectra, for pairs of pigment and SST images from the California Current area.

Date	Time	Coherence			erency on	
(yy-mm-dd)	lag	length	£	ollowing	wavelengt	hs:
,,,,	(h)	(Km)	73.3 km	31.4 km	20.0 km	14.7 Km
81-04-04	7	74. 6	0. 24	0. 33	0. 27	0. 25
81-04-21	7	341.1	0.14	0. 13	0. 12	0. 24
81-05-08	40	87.4	0. 45	0. 26	0. 24	0.17
81-05-08	7	172. 5	0. 29	0. 30	0. 24	0.17
81-05-08	7	320. 9	0.16	0. 25	0. 21	0.19
81-06-16	4	330.1	0. 17	0.14	0.10	0.10
81-06-16	4	388. 6	0. 25	0. 15	0.12	0. 12
81-07-07	8	30. 5	0.76	0. 52	0. 35	0. 15
81-07-08	4	27.6	0.81	0. 52	0. 35	0. 31
81-11-02	3	382. 9	0. 11	0.11	0.12	0. 12
81-11-03	4	376. 7	0.18	0.16	0. 12	0.10
81-11-03	4	536. 3	0.14	0.18	0. 09	0.14
81-06-15	20	416.8	0.15	0. 11	0. 09	0. 09
Average:	9. 2	268. 2	0. 30	0. 24	0. 19	0. 17
Minimum:	3	27.6	0.11	0, 11	0. 09	0. 09
Maximum:	40	536. 3	0.81	0. 52	0. 35	0. 31

To determine the influence of the time lag between the pigment and SST distributions, the decorrelation between a pigment image and a sequence of SST images with increasing time separation was examined. All of the image sequences happened to be from the high variability situations. The decrease of coherency with increasing time separation looks rather regular (Figure 4): a fast decorrelation period during the first 2 days followed by a slower decrease in the next days. The nearly linear trends could be used to correct all the pigment/SST coherence data to zero time lags. However, the assumption of equal decorrelation rate cannot be substantiated for different conditions. It is likely that the time separation between pigment and the corresponding SST images was not a major cause for the comparatively low coherency.

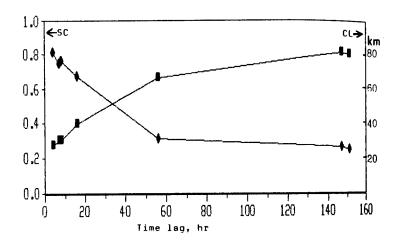


Figure 4. Decorrelation of pigment and SST patterns with increasing time separation: decrease of the squared coherency (SC) and increase of the coherence length (CL). The data points are connected for sake of clarity, they are not all from the same sequence of images.

A few calculations of the squared coherency between successive pigment images showed the same general relationship: higher coherency and lower coherence length with higher mean concentration and higher variance. For the time lag of 1 day the coherence length for successive pigment images ranged from about 40 km to more than 300 km.

Discussion

The pigment variance spectra, obtained here from the CZCS images, are in a number of ways different from the majority of spectra, obtained from shipboard chlorophyll measurements on shorter length scales. For example, 58 percent of the sets of pigment spectra, mostly from the oligotrophic conditions, had mean slopes between 0 and -1. It is important but by no means easy to distinguish between the real world and the artificial effects of data processing on the calculated spectra.

The data set from the California Current area clearly shows the existence of two hydrographic regimes. The regime with the offshore filaments is characterized by higher mean pigment concentration, high pigment variability on longer space scales, steep pigment and SST spectra, higher squared coherency between SST/pigment and successive pigment patterns, and shorter coherence lengths. The second regime represents typical oceanic (oligotrophic) conditions and has low mean pigment level and low pigment variability, especially on longer space scales. The coherency with the respective SST patterns and ensuing pigment images is low, and the coherence length is greater than 300 km. It is clear that the signal to noise ratio of the CZCS algorithms deteriorates in case of very low pigment concentrations. If the noise was primarily on high frequencies, this could tend to flatten the spectra. At the same time, the "-1" power law is also predicted by Bennett and Denman (1985) as the equilibrium after a sufficiently long time lag from an initial perturbation. This is certainly consistent with the California Current data where the offshore moving filaments of nutrient-rich water are probably the most important perturbations. could be conjectured that after the initial input of nutrients by the filaments, most of the pigment variance is generated on the longer space scales (% 10-100 km), resulting in "red" variance spectra (power laws "-2" and steeper). Subsequent stirring and mixing cause the pigment variance to cascade to ever higher wavenumbers, leading to "-1" spectra. The further flattening of the pigment spectra could be the effect of high-frequency noise from measurement and processing errors at low pigment concentrations. Chlorophyll transects with very low large-scale variability have also been observed by in situ measurements in Lake Tahoe (Abbott, et al., 1982). Thus, apart from measurement errors, "noisy" pigment variance spectra with low large-scale variability may be typical for equilibrium-like conditions, away from strong nutrient inputs. In these conditions the SST need not carry any information about the nutrient status of the water, thus, resulting in low coherence between the SST and pigment patterns. In fact, many of the large scale pigment patterns of the "oligotrophic" cases that did not match the SST

patterns looked quite real. In the high variability case the coherency between the pigment and SST patterns is not different from that between successive SST patterns with a similar time separation. In cases of negligible pigment/SST coherency the SST/SST coherency, though also lower, remains significant.

Acknowledgments. The author is indebted to M. R. Abbott and P. M. Zion for providing the images and to M. R. Abbott and K. L. Denman for helpful discussions.

References

Abbott, M. R., T. M. Powell, and P. J. Richerson (1982). The relationship of environmental variability to the spatial patterns of phytoplankton biomass in Lake Tahoe. "J. Plankton Res.," 4, 927-941.

Abbott, M. R. and P. M. Zion (1985). Satellite observations of phytoplankton variability during an upwelling event. "Cont. Shelf Res.," 4, 661-680.

Armi, L. and P. Flament (1985). Cautionary remarks on the spectral interpretation of turbulent flows. "JGR," 90, 11779-11782.

Bennett, A. F. and K. L. Denman (1985). Phytoplankton patchiness: inferences from particle statistics. "J. Mar. Res.," 43, 307-335.

Denman, K. L. (1976). Covariability of chlorophyll and temperature in the sea. "Deep Sea Res.," 23, 539-550.

Denman, K. L. and T. Platt (1975). Coherences in the horizontal distributions of phytoplankton and temperature in the upper ocean. "Mem. Soc. roy. sci. Liege," 6th series, 7, 19-30.

Denman, K. L. and T. Platt (1976). The variance spectrum of phytoplankton in the ocean. "J. Mar. Res.," 34, 593-601.

Denman, K. L., A. Okubo, and T. Platt (1977). The chlorophyll fluctuation spectrum in the sea. "Limnol. Oceanogr.," 22, 1033-1038.

Deschamps, P. Y., R. Frouin, and L. Wald (1981). Satellite determinations of the mesoscale variability of the sea surface temperature. "J. Phys. Oceanogr.," 11, 864-870.

Fasham, M. J. (1978). The statistical and mathematical analysis of plankton patchiness. "Ann. Rev. Oceanogr. Mar. Biol.," 16, 43-79.

Gordon, H. R. and A. Y. Morel (1983). Remote assessment of ocean color for interpretation of satellite visible imagery: a review. Springer-Verlag, N. Y., 114 pp.

Lesieur M. and R. Sadourny (1981). Satellite-sensed turbulent ocean structure. "Nature", 294, 673.

Platt, T. (1972). Local phytoplankton abundance and turbulence. "Deep-Sea Res.," 19, 183-187.

Platt, T. (1978). Spectral analysis of spatial structure in phytoplankton populations. In: "Spatial pattern in plankton communities," J. H. Steele, editor, Plenum, New York, pp 73-84.

/09599

A Study on Information Analysis Aids for Sea Surface Temperature Image Data

43070006b Kyoto Selections from INTERNATIONAL ARCHIVES OF PHOTOGRAMMETRY AND REMOTE SENSING in English Vol 27, 1988 pp 288-293

[Article by Hajime Koshiishi, Masao Naka, Hiromichi Yamamoto, Kohtaro Matsumoto, and Kohzo Homma, National Aerospace Laboratory, 7-44-1 Jindaijihigashi-machi, Chofu, Tokyo 182, Japan; Satsuki Matsumura, Far Seas Fisheries Research Laboratory, 5-7-1 Orido, Shimizu, Shizuoka 424, Japan; Hideo Takahashi, Hideo Tameishi, and Yoshihiro Okada, Japan Fisheries Information Service Center, 2-9-7 Ikenohata, Taito-ku, Tokyo 110, Japan; and Ken-ichi Okamoto, Radio Research Laboratories, 893-1 Hirai, Kashima-cho, Kashima-gun, Ibaraki 314, Japan; Commission Number: VII]

[Excerpts] Abstract

Sea surface temperature (SST) charts obtained from a satellite includes various oceanic conditions such as fronts, ocean currents, eddies, etc. In extracting these oceanic conditions, simplified processing and high accuracy of the processed results are important. Technology of knowledge based processing is applicable to these problems. In this study, a feasibility study on information analysis aids for SST image data using this technology has been performed. This paper also describes implementation of the prototype knowledge based system.

1. Introduction

Observation of the ocean from Earth orbital altitudes by satellite is extremely effective for obtaining global spatial structures and temporal changes which are difficult by ship observation. The fishery is particularly dependent on ocean observation. In searching fishing grounds, fishermen typically rely on experience of experts because the constant movement of fish in vast seas and time changes of oceanic phenomena make conventional searching by fishing boats prohibitive. Remote sensing by satellite opens up many possibilities for dealing with these problems and it is expected that large economic effects will be

achieved, and much research has been done both on industrial applications and in the fields of hydrodynamics and ocean physics. 1

For extracting these oceanic conditions, much accumulated knowledge and experience from conventional ocean observation by ship and other methods have been and will be indispensable. However, this knowledge is not necessarily available in a form that matches conventional data processing procedures by computers. On the other hand, the knowledge based processing has great possibilities of dealing with an ill-defined problem which has ill-structure of data information and rather requires many interactions between the system and users. In other words, the knowledge based processing is able to introduce expert experience and knowledge for oceans and fisheries. Therefore, the efficient application of the knowledge based processing technology is anticipated to serve as an analysis procedure for extracting oceanic conditions from the SST chart.

2. Analysis of SST Charts

For fishery, water temperature is one of the most important environmental conditions, and a suitable water temperature zone differs by a kind of fish. Direction and speed of ocean currents and eddies are also important factors in predicting a profitable fishing ground. Satellite image data is very effective for identifying the position and form of ocean currents, eddies, and fronts by water temperature distribution. Seawater temperature data from an infrared radiometer installed on a satellite is used with data measured by ship to draw up the SST distribution chart.

In the current experimental operation system, by putting a transparent paper with land and longitude-attitude lines on the SST image that is displayed on a CRT display by a computer, the characteristic values of oceanic conditions, such as a warm and cold water mass, eddies, and tongue-like intrusions of the Kuroshio and the Oyashio etc. are drawn (see Figure 1). Essentials to this process are many processing procedures dealing with trial and error on the basis of knowledge and experience on oceans and fisheries, image enhancement by judging the existence and size of clouds using multitemporal image data, and others. And some parts of these processes cannot be completely systematized in a machine processing form and is in need of large work loads.

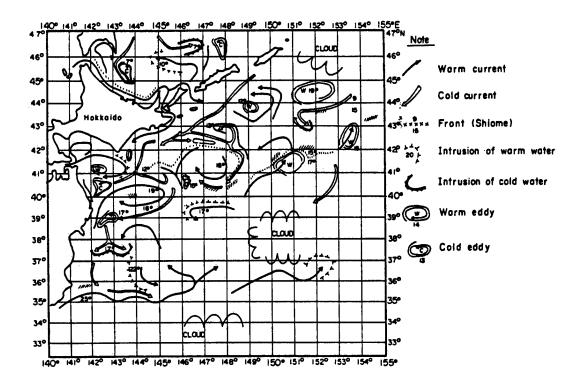


Figure 1. Oceanic Conditions Chart

3. Systematization of Analysis Support for SST Charts

In analyzing the satellite image data and extracting the oceanic conditions from SST charts, short processing time, objective results, and simplified processing are necessary. A reasonable method for meeting these requirements is to systematize in a computer system the tasks described in the foregoing paragraphs. In other words, the computer processing that is able to introduce expert knowledge and experience on oceans and fisheries is adequate for these needs.

In the systematization, an analysis of existing expert knowledge and experience used in the process of recognizing oceanic conditions are important for the feasibility of the system. An example of this analysis is shown in Table 1, in which only main items for estimation processing of fronts are listed up. In addition to these items, about 50 items have been analyzed for the first stage of systematization. They are knowledge information of the other oceanic conditions, attribute information for satellite image data, output information of the analysis result, and system information needed for systematizing oceanic conditions analysis.

Table 1. Knowledge Information for SST Analysis Aids System

kn.1	Fronts are based on inequality: temperature-difference / distance > x.
kn.2	x differs with each position generally.
kn.3	Temperature-difference and distance depend on the sea area.
kn.4	Distances are taken toward the normal line of the front.
kn.5	Fronts exist in the offing rather than in coastal zone.
kn.6	Several fronts sometimes concentrate in parallel.
kn.7	Temperature-slope is large where fronts concentrate.
kn.8	Fronts are formed in curve and intermittent.
kn.9	Front lines do not meet.
kn.10	Fronts agree with the direction of an isotherm.
kn.11	There are sea areas where fronts easily occur.
	Fronts are apt to occur east and west rather than north and south.

Among this knowledge information, some items are resolved into more detailed processing procedures and corresponded to algorithms for image processing and pattern recognition. To code the information and algorithms for computer use, a language must be selected that fits the characteristics of each type of information.

4. System Configuration

On the basis of the feasibility study, an aid system for extracting oceanic conditions from the SST, which can introduce expert knowledge and experience on oceans and fisheries, was constituted as shown in Figure 2. The system is able to be operated under a general purpose operating system in consideration of development environment of image processing and pattern recognition softwares. The implementation of the knowledge data base, the drive and control of analysis processing system, and user interface are done using a command procedure and list processing language considering run-time environment.

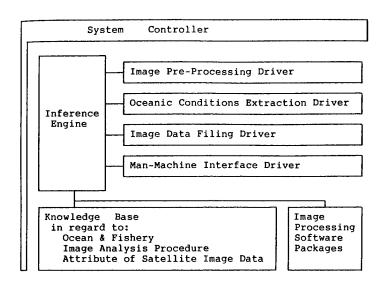


Figure 2. System of Information Analysis Aids for SST Image Data

In this system, both of the image pre-processing driver and the oceanic conditions extraction driver control image pre-processing and pattern recognition software packages under the inference engine. The packages are described in FORTRAN language for intending the utilization of established softwares which have exchangeabilities with general purpose image processing systems. And the image data filing driver controls image data input/output based on a standard image data format, parameter spaces needed for setting the necessary parameters for image preprocessing and pattern recognition, and so on. Moreover, the manmachine interface driver processes the demand of selecting image data, checking parameters for image input/output and file, and explaining system activities for users. And the display format for the man-machine interface can be customized for the user by use of system commands. Figure 3, the general flow of operation of a prototype system is shown. An example of display information for user interface is shown in Figure 4.

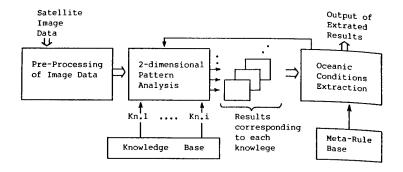


Figure 3. General Flow Chart of the System

```
*** Front Extraction Aid System ***

Outline of the System:

O System starts and screen changes by pressing execution key.

O Use help function if necessary.

O Return to any step when necessary.

O Extraction procedure is as follows:

1. Execute edge operator to detect candidates for fronts.

2. Infer whether each candidate is a front using knowledge rules.

3. Output results of front chart.

4. Store image results in file.
```

Figure 4. Example of Display Information for User Interface

An experimental result of the front extraction by this system is shown in Figure 5 [omitted]. As the input data to the system in this experiment, the SST chart obtained from NOAA infrared image data was used. Data of the area around Japan with 512 pixels by 512 lines of 8 bits per pixel were processed. The extracted result of the front can be displayed in colors.

Concluding Remarks

The system in this study can extract oceanic conditions with two dimensional patterns from SST charts using expert knowledge base on oceans and fisheries in a reasonably short time. The system has the following remarkable features: powerful support for analyzing marine observation satellite (MOS) image data and producing oceanography charts, high system performance using expert knowledge base on oceanography and fishery, and flexibility for the future system expansion.

Following the prototype system on the basis of the feasibility study, the advanced knowledge based system is planned. The future developmental stages of the system are as follows: extraction of oceanic conditions with a higher accuracy by using image sequence analysis, and production of fisheries oceanography charts with predicted fishing grounds and oceanic conditions.

This study is being conducted with a supply of MOS-1 satellite data from the National Space Development Agency of Japan.

References

- 1. "Conceptual Design Study of Real Time Reporting System on Oceanic Conditions," National Aerospace Laboratory, NAL SP-2T, Oct 1984.
- 2. Hideo Tameishi, "Evolution and Development of Eddies Observed by AVHRR Images and Fishing Ground," Sora to Umi, Note of the Society of Airborne & Satellite Physical & Fishery Oceanography, Vol 8, 1986, pp 1-13.

/09599

Interpretation of Remote Sensing Data From Eastern Areas of the Baltic

43070006c Kyoto Selections from INTERNATIONAL ARCHIVES OF PHOTOGRAMMETRY AND REMOTE SENSING in English Vol 27, 1988 pp 360-365

[Article by J. Lokk, Institute of Thermophysics and Electrophysics, Acad. of Sci. of the Estonian SSR, Paldiski Rd. 1, Tallinn 200031, USSR, VII Commission; V. Pelevin and V. Solomakha, Institute of Oceanology, Acad. of Sci. of the USSR, Krasikov Str. 23, Moscow 117218, USSR, VII Commission]

[Text] A method for the determination of concentrations of optically active substances (phytopigments, suspended and yellow matter) in waters with high concentrations and unequal indices of optically active substances is suggested. The method has been worked out relying on the Baltic Sea phenomenon but it can also be applied to other water bodies (seas as well as internal ones) of similar parameters.

Possible ways of applying remote sensing to the admixture concentration determination in the eastern Baltic waters are considered. It is known that the waters there are highly trophic and strongly subjected to human impact. In most papers devoted to the interpretation of spectral aerocosmic information on the sea surface, empiric relations between one or two characteristics of upward radiation spectrum and the chlorophyll "a" concentration were reached (Clark, 1981; Smith and Baker 1982; Shifrin, 1983, Shturm, 1984; Sugihara, Kishino and Okami, 1985). In the present paper an attempt of a more profound use of the upward radiation spectrum has been made. Let us consider the coefficient of the sea surface spectral brightness equal to

 $R = \frac{L_{SN} - L_{ZN}}{L_{ON}}$ (Lokk and Pelevin, 1978; Pelevin, 1978), where L_{SN} is

the brightness of the upward radiation above the sea surface, $L_{2\lambda}$ the sky brightness in the zenith, $L_{0\lambda}$ the brightness of the white diffuser, placed horizontally above the sea surface, f=0.02 the value of the Frenel reflection coefficient for the smooth water surface and normal light beam inclination, λ the light wavelength. To determine the

spectra of ρ_{λ} , $L_{3\lambda}$, $L_{3\lambda}$ and $L_{0\lambda}$ were directly measured. The experimental values of ρ_{λ} were obtained in the Baltic in 1986 and 1987 using the spectroradiometer with a set of interferencial lightfilters:

$$\lambda_{4} = 381 \text{ nm};
 \lambda_{2} = 438 \text{ nm};
 \lambda_{3} = 500 \text{ nm};
 \lambda_{4} = 555 \text{ nm};
 \lambda_{5} = 596 \text{ nm};
 \lambda_{6} = 670 \text{ nm}.$$

For calculations the formula of spectral brightness coefficient most directly connecting the parameter with the hydrooptical characteristic of the water, was chosen (Lokk and Pelevin, 1978):

$$\rho_{\lambda} = K \frac{b_{\delta \lambda}}{a_{\omega \lambda} + a_{y\lambda} + a_{p\lambda} + a_{o} + b_{\delta \lambda}}, \qquad (1)$$

where b_{k} is the coefficient of light backscattering; a_{wk} , a_{pk} , a_{gk} , a_{o} the coefficients of absorption in pure water, plankton pigments, dissolved organic "yellow" matter, suspended matter (excluding pigments, phytoplankton), κ =0.11 (Pelevin, 1978). It is believed (Pelevina, 1980) that the coefficient of absorption in the dissolved organic ("yellow") matter changes with the spectrum as

$$ay = ay \cdot \exp K(\lambda - \lambda),$$

where $K = 0.0148 \div 0.0152 \text{ m}^{-1}$. In calculations $K = 0.015 \text{ m}^{-1}$ and $\lambda = 500 \text{ nm}$. It is presumed that the construction of absorption in phytoplankton pigments is proportional to the chlorophyll "a" concentration C mg·m⁻³:

$$a_{p\lambda} = a_{p\lambda}^* \cdot c \quad \mathbf{M}^{-1}$$
.

After the analysis of various publications (Jerlov, 1970; Ochakovskij, et al., 1974; Popov, Fedorov and Orlov, 1979; Optics of Ocean, 1983) the following coefficient values were adopted:

$$a_{p394}^* = 0.036 \text{ m}^2 \cdot \text{mg}^{-1}; \quad a_{p438}^* = 0.059 \text{ m}^2 \cdot \text{mg}^{-1};$$

 $\vec{a_{psoo}} = 0.042 \text{ m}^2 \cdot \text{mg}^{-1}$ for specific absorption in pigments

and
$$a_{\omega} = 0.014 \text{ m}^{-1}$$
; $a_{\omega 438} = 0.011 \text{ m}^{-1}$; $a_{\omega 500} = 0.021 \text{ m}^{-1}$;

$$a_{\omega 555} = 0.053 \,\mathrm{m}^{-1}$$
; $a_{\omega 596} = 0.15 \,\mathrm{m}^{-1}$ in pure water (on natural

basis). The spectral dependence bbl in condition of the additive contribution of backscattering by large bbl and small bbsl fractions of suspended matter is selected as follows (Optics of Ocean, 1983):

$$b_{\ell,\lambda} = b_{\ell\omega 500} \cdot \left(\frac{500}{\lambda}\right)^{4.3} + b_{\ell\lambda 500} \cdot \left(\frac{500}{\lambda}\right)^{0.3} + b_{\ell5500} \cdot \left(\frac{500}{\lambda}\right)^{4.7}$$

The coefficient of light backscattering in pure water is $\ell_{\omega}500 = 0.001$ m⁻¹ (Popov, Feodorov and Orlov, 1979). It was suggested that within the interval of 500 nm $< \lambda < 600$ nm the special absorption in pigments $\alpha_{\rho\lambda}^*$ changes according to the law exp $[0.015 (\lambda_{\bullet} - \lambda)]$. The light absorption in suspended matter α_{o} (excluding the absorption in pigments) for calculations is considered non-selective. This way, the light absorption in pigments and dissolved yellow matter α_{λ} changes on the spectrum

$$a_{\lambda} = a_{y\lambda} + a_{p\lambda} = a_{500} \cdot \exp[0.045 \cdot (500 - \lambda)]$$
.

At wavelengths 500 nm < λ < 600 nm equation (1) is expressed as follows:

$$\rho_{\lambda} = K \frac{b_{\delta\lambda}}{a_{\omega\lambda} + a_{500} \cdot exp[0.015(500 - \lambda)] + a_{v} + b_{\delta\lambda}}$$
 (2)

For λ < 500 nm, where the spectral way of the curves $a_{y\lambda}$ and $a_{p\lambda}$ differs considerably, equation (1) has the form

$$\rho_{\lambda} = K \frac{b_{k\lambda}}{a_{\omega\lambda} + (1 - \frac{1}{2}) \cdot a_{500} \cdot exp[0.045(500 - \lambda)] + \frac{1}{2} \cdot a_{500} \cdot N_{\lambda} + b_{k\lambda}}, \quad (3)$$
where $\frac{a_{\rho 500}}{a_{500}}$; $N_{\lambda} = \frac{a_{\rho k}^{*}}{a_{\rho 500}^{*}}$

The reverse task - the determination of the unknown parameters **bll** 500, **ll** 500, **ag500**, **ap500**, **ao** for measuring **pl**;, was solved by a computer, relying on the principle of minimizing the discrepancies of the measured values of **pl**; and of the calculated values of **pl**; obtained from (2) - (3). The procedure of calculation is as follows. Firstly the calculation values of **bll** 500, **ll** 5500, **a** 500, **a** 60 for

 $\sum_{i=3}^{5} |\rho_{\lambda_i} - \rho_{\lambda_i}| = 0$ are found according to linear equations system

(2). Simultaneously according to system (3) by way of the modification of α_{500} and ξ , the values of α_{p500} and α_{y500} for which the maximum

values of the difference modulus $\frac{2}{k \cdot k} | \rho_{\lambda k} - \rho_{\lambda k}|$ are the smallest, are determined. The following conditions are satisfied:

666500, 665500,
$$a_{500}$$
, $a_{0} > 0$; $0 \le \xi \le 1$.

The results of calculations and measurements for stations showed in Figure 1, are summarized in Table.

As one can see, the calculated values of the chlorophyll concentration are in good agreement with the concentrations measured in samples. The precision achieved meets totally the economic needs as well as the requirements for the studies of the large-scale variability of water

mass and substance distribution in coastal areas. An analogous precision was reached for other optically active substances (suspended and yellow matter) in the water. The algorithm like that may be applied to investigations from low-flying carriers, where the influence of the atmosphere is inessential.

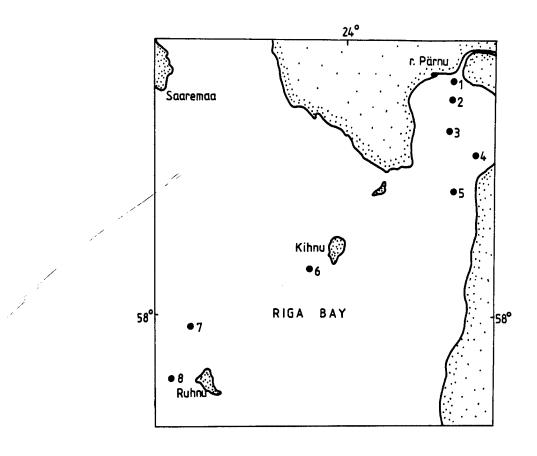


Figure 1. The Area of Sampling and Remote Measurements

Table. The Measured and Calculated Values of Optical Parameters and Chlorophyll Concentration

	λ(nm)					m-1				C (mg·m ⁻³)			
Station	383	438	500	555	596	a_{δ}	00	$a_{\mathfrak{o}}$	a _{y5500}	bel 500	665500	calc.	meas.
i measured calculated	0.007 0.008	0.016 0.015	0.026 0.026	0.040 0.040	0.045 0.045	1.	10	0.11	0.80	0.38	0.01	7.3	9.0
2 measured calculated	0.013 0.013	0.022 0.022	0.036 0.036	0.054 0.054	0.062 0.062	1.	56	0.06	1.00	0.76	0.04	13.2	9.2
3 measured calculated	0.015 0.013	0.020 0.022	0.038 0.038	0.056 0.056	0.061 0.061	0.	91	0.01	0.66	0.49	0.01	6.1	7.3
4 measured calculated	0.008 0.008	0.012 0.012	0.020 0.020	0.033 0.033	0.037 0.037	0.	89	0.02	0.44	0.19	0.02	10.8	8.5
5 measured calculated	0.006 0.005	0.007 0.008	0.014 0.014	0.023 0.023	0.025 0.025	0.	75	0.06	0.42	0.12	0.00	7.9	8.7
6 measured calculated	0.003 0.003	0.005 0.005	0.007 0.007	0.010 0.010	0.008 0.00 8	0.	35	0.01	0.20	0.00	0.03	3.5	2.8
7 measured calculated	0.004 0.003	0.003 0.004	0.007 0.007	0.012 0.012	0.012 0.012	0.	52	0.02	0.23	0.04	0.00	6.9	2.7
8 measured calculated	0.003 0.003	0.003 0.003	0.005 0.005	0.007 0.007	0.006 0.006	0.	30	0.08	0.12	0.02	0.00	4.2	3.2

References

- 1. Clark, D. K., 1981. Phytoplankton pigment algorithms for the NIMBUS-7 CZCS. Oceanogr. from space. Plenum Press, p 226-237.
- 2. Smith, R. C. and Baker, K. S., 1982. Oceanic chlorophyll concentrations as determined by satellite. Marine Biology, No 66, p 269-279.
- 3. Shifrin, K. S., 1983. Introduction to the optics of ocean. Leningrad, Gidrometeoizdat, 278 pp (in Russian).
- 4. Shturm, B., 1984. Atmospherical correction for remote sensing data and suspended matter quantity determination in sea surface layers. Remote sensing in meteorology, oceanography and hydrology (Ed. by Kreknell, A. P.). Moscow, Mir, 535 pp (in Russian).
- 5. Sugihara, S., Kishino, M., and Okami, N., 1985. Estimation of water quality parameters from irradiance reflectance using optical model. J. of the Oceanographical Society of Japan, Vol 41, 399 pp.
- 6. Lokk, J. and Pelevin, V., 1978. The interpretation of the upwelling radiation based on the Baltic sea. Proc. 11th Conf. Baltic Oceanogr. Rostock, p 589-599.
- 7. Pelevin, V. N., 1978. Evaluation of suspended matter and chlorophyll concentration in the sea on upward radiation spectrum measured from a helicopter. Okeanologija, Vol 18, No 3, p 421-424 (in Russian).

- 8. Pelevina, M. A., 1980. Methods and results of measurements of light spectral absorption in dissolved organic "yellow" matter in the Baltic Sea waters. Light fields in ocean. Moscow, Institute of Oceanology, Acad. Sci. USSR, 340 pp (in Russian).
- 9. Jerlov, N., 1970. Optical oceanography (Transl. from English, ed. by Ochakovskij, Y. E.). Moscow, Mir, 223 pp (in Russian).
- 10. Ochakovskiy, Y. E., Pelevin, V. N., Karlsen, G. G., et al., 1974. Distribution of natural radiation in ocean. Hydrophysical and hydrooptical investigations in the Atlantic and Pacific ocean. Moscow, Nauka, p 166-190 (in Russian).
- 11. Popov, N. I., Fedorov, K. N., and Orlov, V. M., 1979. Marine water (ed. by Monin, A. S.). Moscow, Nauka, 327 pp (in Russian).
- 12. Optics of Ocean., 1983. Physical optics of ocean (ed. by Monin, A. S.). Moscow, Nauka, 372 pp (in Russian).

/09599

Development of Borehole Scanner for Underground Geological Survey

43070006d Kyoto Selections from INTERNATIONAL ARCHIVES OF PHOTOGRAMMETRY AND REMOTE SENSING in English Vol 27, 1988 pp 391-395

[Article by Shunji Murai, Institute of Industrial Science, Univ. of Tokyo, 7-22-1, Roppongi, Minatoku, Tokyo, Japan; Chikaosa Tanimoto, Dept. of Civil Engineering, Univ. of Kyoto, Yoshihonda-machi, Sakyoku, Kyoto, Japan; Yoshitaka Matsumoto, Core Co., Ltd., 4-3-2-206, Shiba, Minatoku, Tokyo, Japan; Koji Nagata, Institute of Technology, Shimizu Construction Co., 3-4-17, Etchujima, Kotoku, Tokyo, Japan; Commission VII]

[Excerpts] Abstract

The borehole scanner has been developed by the authors to obtain digital imagery of inner wall of a borehole for geological survey. As compared with the existing borehole TV camera system, the following significant advantages were obtained.

- 1) Continuous color image of inner wall of the whole borehole can be obtained in digital form, while the TV camera system produces only a partial image in analogue form.
- 2) The speed of data acquisition is very high of 36 m/hour, while TV system is only 2 m/hour.
- 3) Digital image analysis can be effectively applied to extract useful information on rock characteristics underdams, power plants, etc.

Introduction

For the construction of facilities in/on rocks such as tunnels, dams and power plants, the advance geological evaluation is of major importance. Up to now the conventional methods for such an investigation of geology and fractures in rock have been to bore in through the surface and lower a TV camera to examine the borehole wall.

However, the type of borehole TV camera system exhibits the following disadvantages because the TV camera must be rotated approximately 40 degree for each shot at the same borehole level to obtain the full view of the wall.

- 1) Excessive observation time is required.
- 2) Each photograph taken by the TV system must be manually rearranged into a mosaic.
- 3) The image quality is not uniform in a TV scene due to shding and illumination effects.

As a result, there has been a strong demand for the development of a new system that would improve observation speed with continuous image of a good quality.

Borehole Scanner

The borehole scanner is composed of the following units as shown in Figure 1.

- 1) Scanner
- 2) Control Unit
- 3) Cable Unit

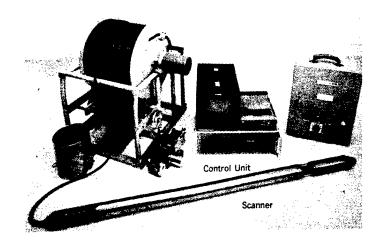


Figure 1. Borehole Scanner System

The scanner is composed of a light, a rotating mirror, an optroelectronic converter with R, G, B channels, a compass, a data transmitter and an amplifier, as shown in Figure 2.

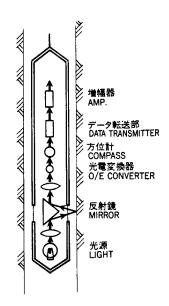


Figure 2. Scanner

The scanner is carefully lowered into a borehole with a size of 66 mm or 86 mm in diameter and a mirror rotates rapidly to collect the reflected light through the observation window from 360 degree around the borehole wall. Data obtained by the scanner are transmitted to the surface control unit and recorded in a video tape or a digital magnetic tape for reproduction on a monitor system or for data processing.

Figure 3 [omitted] shows the borehole scanner system on site.

Performance of borehole Scanner

a. Observation speed

The borehole scanner achieves observation speed of 36 m/hour, 15 times faster than is possible with the conventional TV camera system.

b. Image quality

The borehole scanner provides substantially full scale and continuous video color images of the inner wall of a borehole for the angle of 360 degree in real time, which can be monitored on the ground. The image quality is uniform on an image because of a constant angle of illumination. Even under turvid water level, the image quality is kept excellent due to the short distance between the rotating mirror and the inner wall. The resolution is 0.1 mm on the surface of the wall.

c. Recording method

VTR and digital recording are available. VTR recording system utilizes commercially available video tape which permits geological analysis or

evaluation by geologists away from the site. The analysis efficiency can be improved with the continuous scanned images of 360 degree view angle in a scrolling manner.

Table 1 shows the comparison of performance between the borehole scanner and the existing borehole TV camera.

Table 1. Comparison Between Borehole Scanner and TV Camera

	Borehole Scanner	TV Camera
View angle	Continuous 360°	Intermittent 40°
Observatin speed	36 m/hour	1-2 m/hour
Analysis efficiency	10-50 m/day	1-2 m/day
Recording method	VTR and digital	VTR
Resolution	recording 0.1 mm	0.1 mm
Max. observation depth	200 m	200 m
Borehole diameter	66-86 mm	66-86 mm

Figure 4 [omitted] and Figure 5 [omitted] show the comparison of the two images taken by the borehole scanner and the TV camera respectively. Much better image can be obtained by the borehole scanner.

Applications

The following applications have been carried out using the borehole scanner.

- a. Advance geological investigations for facilities in/on rocks such as dams, nuclear power plants, subsurface power plants, underground crude oil storage caverns and nuclear waste repositories.
- b. Maintenance and quality inspections for massive concrete structures such as dams, etc.
- c. Grouting efficiency evaluations for dams.
- d. Evaluations for soil efficiency improvements in soil foundations.

Figure 6 [omitted] shows very big open cracks in black tone in the rock of chart.

Figure 7 [omitted] shows a layer of quatz in the rock of granite with a number of cracks.

Conclusions

The underground remote sensing has been carried out with the borehole scanner which has been developed by the authors.

The borehole scanner has been producing outstanding images with high evaluation from the users.

Further development for a special image processing for geological survey should be made.

/09599

An Improving Multispectral Recording Set Analysis Method

43070006e Kyoto Selections from INTERNATIONAL ARCHIVES OF PHOTOGRAMMETRY AND REMOTE SENSING in English Vol 27, 1988 pp 406-415

[Article by Prof. dr. eng. Nicolae Oprescu, Eng. Constantin Borduselu, Institutul de Geodezie, Fotogrammetrie, Cartografie si Organizarea Teritoriului, 79662, Bd. Expozitiei nr. 1 A, sector 1, Bucuresti, Romania, Commission VII]

[Excerpts] Abstract: An analytical method to select the best combination out of a multispectral image set is presented, starting from the spectral signature of a certain class of the study. Parameters established analytically are then used in an analogical process using MSP-4C multispectral projector (made in Carl Zeiss Jena - The German Democratic Republic) to obtain the best resolution of an involved spectral class.

The MSP-4C multispectral projector made by Carl Zeiss Jena (DDR) is meant for the multispectral and/or multitemporal analysis of the records taken by MSK 6 or MSK 4 cameras mounted on aircrafts and space platforms, or LANDSAT, SPOT, etc. records.

The MSP-4C has four independent projection optical channels. In this way, almost unlimited combinations of simple images, colours and projection luminosity are possible.

Every optical channel contains (Figure 1):

- A special illumination device with a concave mirror, a halogen lamp (24 V/250 W), two heat absorbtive filters and four condenser lenses;
- A film holder for plane films with dimensions up to 70x91 mm, with a good horizontalization and with elimination of Newton's rings properties;
- A shutter for every channel which does not change the thermic equilibrium in the film holder;

- Seven colour filters setted on a rosette;
- A panchromatic projective lens, corrected for aberrations;
- Electric engine units to adjust contrast, image translation and rotation, and scale correction.

The images supplied by the four channels are projected on a 350x455 mm screen, five times enlarged by a mirror, under a 4.75 degree projection angle.

The main purpose of this device is to transform the little density differences (tones of gray) of the black and white images taken by the six camera channels (spectral bands) in contrasting colour tones into mixed images, using colour and neutral filters adequately combined.

The CIE 1931 chromaticity diagram, on which the areas denoting the same colour name (according to Kelly and Judd) are represented, is well covered by the colour shade areas derived from an all possible filter combination set.

The visual interpretation of the remote sensing multispectral or multitemporal images is difficult enough as compared the conventional photographic material interpretation. Besides reliable processing techniques, we must know these image interpretation requirements very well, and we must have a great experience on the field works. The main interpretation problem requires the specific information contents in many images to be combined (extracted) according to our purpose in order to be easily grasped from the mixed image.

During supervised analysis using MSP-4C multispectral projector, some problems are to be solved, in order to avoid subjective factor as much as possible. These problems are:

- 1. Selection of the strip set containing the maximum information (Figures 3 a, 3 b);
- 2. Filter combination selection among MSP-4C available set, so that the resulted image colour should emphasize the wanted phenomenon as well as possible (Figures 4, 5).

So, to get the best colour composite in three bands, it is necessary to select the best one out of 20 possibilities (${\rm C}^3_6$). Each band can have any colour, so we'll have 3276 different possibilities for image colour presentation.

Considering the three dimensional space defined by any spectral band triplet, the associated variance-covariance matrix defines an ellipsoid, in this space. In this case, only the computation and the ordering of

the determinants which correspond to every 3 x 3 main submatrix from M variance-covariance matrix are required. Then, the band triplets associated with these determinants will be decreasingly ordered depending on the information content. This method, proposed by Sheffield in 1985 has a great advantage, the elimination of the possibility to choose a spectral band triplet closely correlated. The logical scheme of the computational programme which can solve the above problem can be found in the Appendix (Figure 3).

The second great problem refers to the set of best filter combination chosen from the device's set of filters to:

- emphasize the class of interest for a maximum colour contrast;
- have the possibility to obtain again the same colour image, at a new analysis;
- reduce the human operator's subjective factor.

The available inputs are:

- selected multispectral photographical records using the maximum volume ellipsoid method;
- spectral signature of the involved classes (that is gray tone intervals of these classes in each image);
- the device optical characteristics:
- -- the spectral radiation distribution of the sources;
- -- the colour filter transmittance curves;
- -- the neutral filter transmittance curves and the heat filter curves.

The chosen set of filters should provide, within a metric chromatic space, the maximum distance between the colours (a maximum difference of colouring, respectively). In this case, it is better to consider colours in CIE 1976 (L*, u*, v*) three dimensional space.

The colour difference will be:

$$\Delta E = [(\Delta L^*)^2 + (\Delta u^*)^2 + (\Delta v^*)^2]^{\frac{1}{2}}$$

The first term represents the psychometric lightness difference:

$$L^* = 116 \left(\frac{Y}{Y_0} \right)^{1/3} - 16 \tag{1}$$

and the other two terms represent CIE 1976 psychometric chromaticity difference

$$u^* = 13 L^* (u' - u'_n); v^* = 13 L^* (v' - v'_n)$$
 (2)

where:

$$u' = \frac{4x}{x + 15y + 3z}$$
; $v' = \frac{9y}{x + 15y + 3z}$ (3)

and $\mathbf{Y_n}$, $\mathbf{Y_n}$ are computed in a similar way, using $\mathbf{X_n}$, $\mathbf{Y_n}$, $\mathbf{Z_n}$ which correspond to the source.

X, Y, Z are three stimulus values of the considered colour and are given by the following expressions:

$$X = K \int_{\lambda} C(\lambda) \bar{x}(\lambda) d\lambda$$

$$Y = K \int_{\lambda} C(\lambda) \bar{y}(\lambda) d\lambda$$

$$Z = K \int_{\lambda} C(\lambda) \bar{z}(\lambda) d\lambda$$
(4)

x, y, z represent three stimulus spectral values.

The colour stimulus function: $f(\lambda) = S(\lambda) G(\lambda)$

The transmittance:

Gfc = the colour filter spectral transmittance from MSP-4C Gfn = the neutral filter spectral transmittance from MSP-4C

Git = the heat absorbtion filter spectral transmittance

Eq = the film transmittance in the area (or areas) of the considered class.

$$Gtg = \left(1 - \frac{\text{the level of gray}}{255}\right)$$

 $S(\lambda)$ = the spectral power distribution of the illuminating source.

The K constant =
$$\frac{100}{\int_{\lambda} S(\lambda) \overline{y}(\lambda) d\lambda}$$

projector's/

Because on the multispectral display we receive the light from three channels, it results:

$$x = \frac{K}{3} \int_{\lambda} S(\lambda) \left[G_{4}(\lambda) + G_{2}(\lambda) + G_{3}(\lambda) \right] \overline{x}(\lambda) d\lambda$$

$$Y = \frac{K}{3} \int_{\lambda} S(\lambda) \left[G_{4}(\lambda) + G_{2}(\lambda) + G_{3}(\lambda) \right] \overline{y}(\lambda) d\lambda$$

$$Z = \frac{K}{3} \int_{\lambda} S(\lambda) \left[G_{1}(\lambda) + G_{2}(\lambda) + G_{3}(\lambda) \right] \overline{z}(\lambda) d\lambda$$

$$X_{n} = \frac{K}{3} \int_{\lambda} S(\lambda) \cdot 3 \cdot \overline{x}(\lambda) d\lambda$$

$$Y_{n} = \frac{K}{3} \int_{\lambda} S(\lambda) \cdot 3 \cdot \overline{y}(\lambda) d\lambda$$

$$Z_{n} = \frac{K}{3} \int_{\lambda} S(\lambda) \cdot 3 \cdot \overline{z}(\lambda) d\lambda$$

For a certain set of filter the algorithm takes into consideration the computation of the X, Y, Z three stimulus and of the L*, u*, v* for the considered class and for the whole remainder image is made from 5 to 5 mm.

Finally, the COLOUR subroutine computes Δ E* (the average distance between colours in CIE 1976 (L*, u*, v*) metric space, from the class of interest to the remainder image.

As the general algorithm computes all colouring possibilities, it is necessary to eliminate those combinations which do not give significant distances in the considered metric space.

Further on, the average distances are computed for the rest of filter sets, and these are decreasingly ordered, the maximum value giving the best filter combination.

The method is not yet implemented and experimented, that's why the results are not presented here. Because this problem is analytically treated, we expect an improvement of the processing resolution for the multispectral and multitemporal images given by the remote sensing records.

References

Colwell, R. N. (Editor in chief) 1983 Manual of Remote Sensing, Second edition, Chap. 17 Data Processing and Reprocessing, Chap. 19 Remote Sensing Software Systems. American Society of Photogrammetry, The Sheridan Press, USA.

Grum, F., Bartleson, C. J., et al., 1980 Optical Radiation Measurements, Vol 2, Color Measurement, Academic Press, USA.

Rothery, D. A., 1987 Cover Deccorelation Stretching as an Aid to Image Interpretation, International Journal of Remote Sensing, Vol 8, No 9, Taylor Francis, USA.

Sheffield, C., 1986 Selecting Band Combination from Multispectral Data, P. E. R. S., Vol 51, No 6.

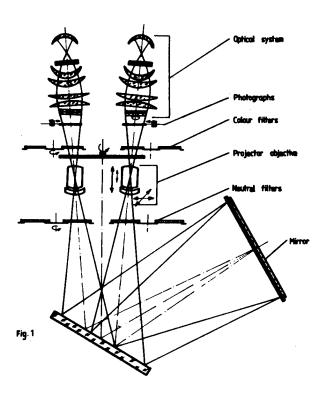


Figure 1. The Optical Configuration of Multispectral Projector MSP-4C

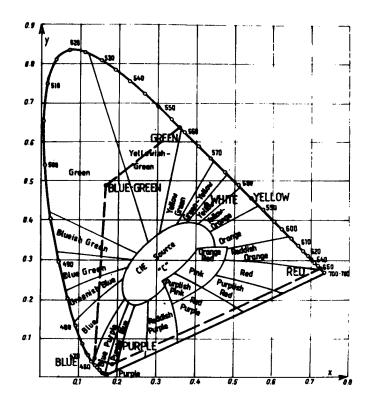


Figure 2. The position of the colour filters in the CIE 1931 chromaticity diagram and the aree of possible colours defined by these. In addition are illustrated the common names of colors assigued to various areas of the CIE 1931 chromaticity.

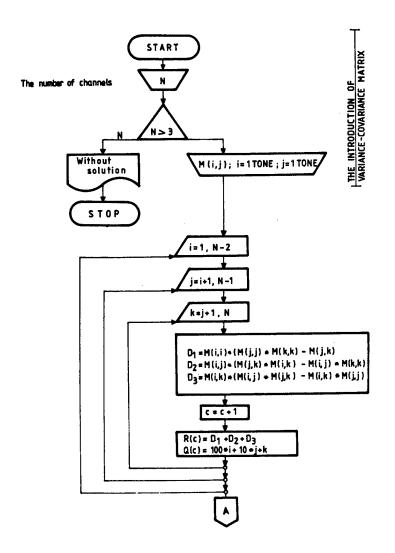


Figure 3a. The selection of the best triplet of channels

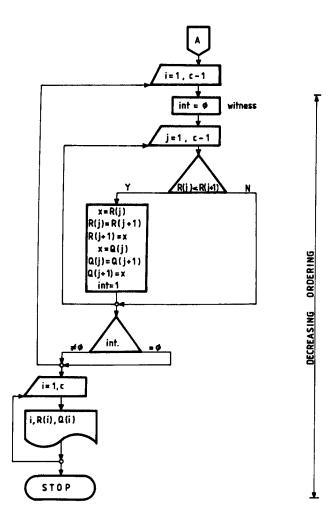


Figure 3b.

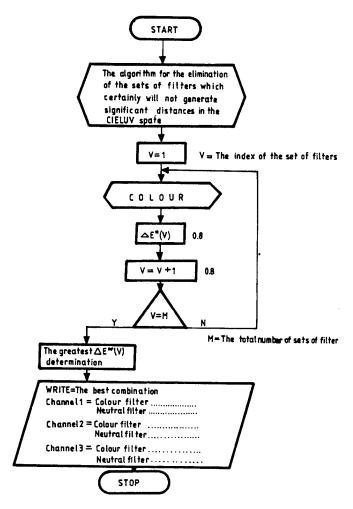


Figure 4. An algorithm for the best set of filters determination so that the color contrast between the class of interest and the remainder image to be maximum

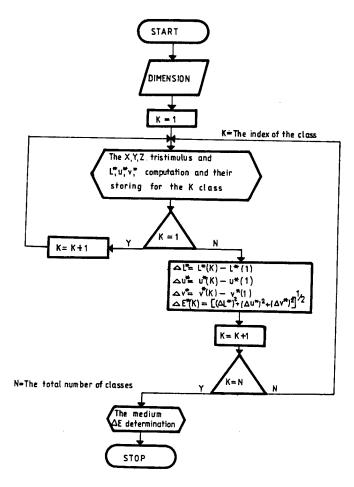


Figure 5. A computational algorithm for the mean distance between the class of interest and the others classes, in the CIELUV space (the color subroutine)

/09599

Development of a Field Radiometer as a Ground Truth Equipment for the Japanese ERS-1

43070006f Kyoto Selections from INTERNATIONAL ARCHIVES OF PHOTOGRAMMETRY AND REMOTE SENSING in English Vol 27, 1988 pp 718-727

[Article by Yasushi Yamaguchi and Isao Sato, Geological Survey of Japan, Higashi 1-1-3, Tsukuba, Ibaraki 305, Japan and Tsutomu Ohkura, Optical Science Co., Ltd., Nakano-kamimachi 3-20-4, Hachioji, Tokyo 192, Japan, Commission VII]

[Excerpts] Abstract

A new field radiometer has been developed to provide ground truth data for the optical sensor of the Japanese ERS-1 (Earth Resources Satellite), which is scheduled to be launched in 1992. This radiometer has two motor-driven filter wheels, each of which can contain up to eight filters and corresponds to the silicon and lead-sulphide detectors respectively. The same field of view exactly is guaranteed to all the spectral bands, because only one aperture is used to observe a target. It takes approximately twenty seconds to perform one continuous measurement for the seven spectral bands equivalent to the ERS-1 sensor. A portable lap-top computer controls the radiometer and records measured results on a floppy disc. An officially-calibrated lamp and a standard reflection plate mounted on an optical bench were also prepared for the purpose of absolute energy calibration of the radiometer. Preliminary investigation has shown that this newly developed radiometer can provide reliable spectral data.

1. Introduction

The Japanese ERS-1 (Earth Resources Satellite) is scheduled to be launched in 1992 and will be equipped with both an eight-band optical sensor and an L-band SAR (Technology Research Association of Resources Remote Sensing System, 1986). The optical sensor has four bands in the visible to near-infrared (VNIR; 0.4-1.1 um) region and four bands in the short-wavelength-infrared (SWIR; 1.1-2.5 um) region respectively (Table 1). The VNIR bands have the similar bandpasses to those of the Landsat

TM. The bands 3 and 4 are selected for stereoscopic imaging along the nadir track of the satellite. The SWIR bands are particularly of interest to geologists because of their expected capability to discriminate among some lithologic units.

Yamaguchi (1987, 1988) has already discussed possible data processing techniques for lithologic and vegetation discrimination using the optical sensor data of the ERS-1. His discussions based upon reflectance data obtained by the high-resolution spectroradiometer prior to actual measurements by the satellite sensor, because the sensor is currently being manufactured. The reflectance spectra with spectral resolution of 2 nm in the 0.35-1.0 um region and 4 nm in the 1.0-2.5 um region were convolved into hypothetical sensor responses. However, spectral measurements by such a spectroradiometer as well as the subsequent convolution process are somewhat time consuming and are not an efficient way to get enough sensor responses for statistical investigation. Instead, a field radiometer with the same bandpasses as the ERS-1 sensor should greatly help evaluate capability of the satellite sensor prior to its operation.

After the satellite becomes operational, the field radiometer will be able to provide ground truth data in various applications. In some data processing concepts, ground reflectance measurements are indispensable for "reflectance calibration" of images (e.g., Elvidge and Lyon, 1985; Roberts, et al., 1987). If we can assume a linear nature between the recorded digital numbers in a magnetic tape and ground reflectance, it is easy to convert the digital numbers into reflectance using field targets with enough spatial distribution (Marsh and Lyon, 1980). Kepper, et al., (1986) reported that the reflectance calibrated image was composed of fewer image units than an uncalibrated image and these units corresponded more closely to the mapped geologic formations. Some field radiometers have already been developed as ground truth tools for the Landsat sensors, but some modifications have been desired in their specifications. For these reasons, we have developed a new field radiometer for the ERS-1 optical sensor.

2. Specification of the New Radiometer

There are some user requirements for a field radiometer. First of all, it has to be portable, i.e., it has to be operated in field by batteries and its weight should not be too great. The newly developed radiometer consists of the optical head and the battery unit as shown in Figure 1 [omitted]. The radiometer can be operated by the DC 12V battery, which is rechargeable from AC 100V or 200V power supply and lasts about 3.5 hours in case of continuous measurements. Voltage of the battery can be checked by the analog-meter on the battery unit. A lap-top personal computer (NEC PC-98LT) is used for control of the radiometer and can work about 4 hours in field with its internal battery. As the total weight of the radiometer including the battery unit and the computer is

about 15 kilograms, two persons are needed to carry and operate it in field.

This radiometer has two filter wheels in the optical head as shown in Figure 2. Each wheel can contain up to eight interference filters and corresponds to the silicon and lead-sulphide detectors respectively. Therefore, up to eight spectral bands in the VNIR region and another eight bands in the SWIR region are available. At present, three filters in the VNIR region and four filters in the SWIR region whose bandpasses are similar to those of the ERS-1 optical sensor (Figure 3) have been installed. The filter wheels are automatically rotated by pulse motors in order to accomplish shorter measurement time. During field operations, illumination conditions are always changing. Thus, the shorter the time necessary for a measurement, the less influence from fluctuations of illumination conditions. It takes about twenty seconds to perform one continuous measurement for the seven spectral bands.

Other requirements for a field equipment are easy operation and a reliable recording medium. It is also desired that a measured result can be checked immediately in field. Otherwise, we cannot recognize a failure of measurements until returning to a laboratory from a field survey. For these reasons, it was decided to use a lap-top personal computer for control of the radiometer. The optical head is connected to the computer through the battery unit by RS232C interface (Figure 1). We can easily operate the radiometer using the computer keyboard and can check the result immediately on the liquid-crystal display. Measured data can be recorded on a 3.5-inch floppy disc.

An important advantage of this radiometer is that there is only one observation aperture in the optical head. Generally speaking, geologic targets such as surface rocks of soils are quite inhomogeneous even within a field of view of a radiometer. Thus, it is important to carry out a spectral measurement in the same field of view exactly for the different spectral bands when we discuss a spectral response pattern of a particular target. Many of the previously developed radiometers measure a target with different fields of view using multiple apertures. If there is significant inhomogeneity in the target, such systems might cause a problem that each spectral band measures different areas with different spectral properties. In order to avoid it, the optical head of the newly developed radiometer has only one objective aperture (Figure 2) as to guarantee the same field of view to all the spectral bands. The field of view can be checked through the sighting telescope. When we start a measurement, the light path to the telescope is closed automatically and the incident ray is directed to the filters. The radiometer also has four different types of irises as shown in Table 2. The most appropriate iris for the measurement is chosen by rotating the iris wheel.

3. Calibration Using a Standard Lamp on an Optical Bench

An optical bench (Figure 4 [omitted]) has been prepared for the purpose of performing absolute energy calibration of the radiometer. An officially-calibrated illumination lamp is mounted on the optical bench, a distance of fifty centimeters from a standard reflection plate (Figure 5). This is the same material as the reference plate being used in field measurements, i.e., an aluminum plate with thin coating of barium-sulphate on the surface.

Using this optical bench, we can easily get calibration factors to convert readings obtained by the radiometer into absolute energy values. Calibration factors are stored on a floppy disc as a data file and are called when energy conversion is required. An integrating sphere with barium-sulphate coating on its internal surface is also prepared. It will be possible to monitor irradiance from the sun using the calibration factors and the integrating sphere equipped at the objective aperture of the radiometer. This capability will allow us to evaluate the satellite data and correct atmospheric effects after the satellite sensor becomes operational.

4. Reliability of the Radiometer in Spectral Measurements

Some measurements have been carried out as a test of the radiometer. Firstly, the repeatability of measurements and the effect of temperature were examined by changing the temperature at 0, 25, and 40 degrees celcius. The dark current did not exceed 0 plus or minus 1 percent of readings in any cases. It was also shown that the fluctuation of the measurements was not more than two percent of the readings when measured over the white reference plate in any cases of the three temperatures tested.

Next, reliability of the radiometer was tested by comparing the measurement results to the spectra obtained by the high-resolution spectroradiometer over the same targets. Figure 6 shows the typical reflectance spectrum of kaolinite; an important clay mineral in hydrothermally-altered areas. This spectrum was then convolved into the hypothetical response pattern through the filters installed in the radiometer by multiplying the filter transmittance curves (Figure 3). The same target was also measured by the radiometer. As shown in Table 3, these two response patterns coincided sufficiently well. Namely, kaolinite shows high response except the bands 7 and 8 in the SWIR region because of the characteristic absorption at 2.2 um due to the existence of hydroxyl. Many other measurements have also shown good coincidence between the response patterns obtained by these two methods. Consequently, it can be concluded that the newly developed radiometer would provide reliable spectral data as the ground truth to the ERS-1 optical sensor.

5. Conclusion

A new field radiometer has been developed as a ground truth equipment for the optical sensor of the Japanese ERS-1. As a result of the preliminary investigation, it has been shown that the radiometer worked sufficiently well with enough reliability in spectral measurements. It will be possible to get enough sensor response patterns for statistical investigation of the ERS-1 sensor prior to its launching. After the satellite becomes operational, this radiometer will be used to collect ground truth data in various applications.

The filter wheels in the radiometer can contain up to sixteen filters, more than the seven spectral bands of the ERS-1 sensor. So, such usage as identification of clay minerals using filters with the specific bandpasses in the SWIR region might be possible in future. This is another possible application of the radiometer as a field tool for exploration geology (e.g., Gladwell, et al., 1983).

The authors would like to express their gratitude to H. Tsu, H. Hase and M. Urai of the Geological Survey of Japan for their help in this research. The first author thanks R. J. P. Lyon of the Stanford University for his valuable suggestions. This research was funded as a part of the ERS-1 project promoted by the Agency of Industrial Science and Technology, Ministry of International Trade and Industry of Japan.

6. References

Elvidge, C. D. and Lyon, R. J. P., 1985, Influence of rock-soil spectral variation on the assessment of green biomass. Remote Sensing of Environment, v.17, p 265-279.

Gladwell, D. R., Lett, R. E., and Lawrence, P., 1983, Application of reflectance spectrometry to mineral exploration using portable radiometers. Economic Geology, v.78, p 699-710.

Kepper, J. C., Lugaski, T. P., and MacDonald, J. S., 1986, Discrimination of lithologic units, alteration patterns and major structural blocks in the Tonopah, Nevada area using Thematic Mapper data. In Proc. Fifth Thematic Conf. on Remote Sensing for Exploration Geology, Environmental Research Institute of Michigan, Ann Arbor, MI, p 97-115.

Marsh, S. E. and Lyon, R. J. P., 1980, Quantitative relationships of near-surface spectra to Landsat radiometric data. Remote Sensing of Environment, V.10, p 241-261.

Roberts, D. A., Yamaguchi, Y. and Lyon, R. J. P., 1987, Comparison of various techniques for calibration of AIS data. In Proc. of the Second Airborne Imaging Spectrometer Data Analysis Workshop, Jet Propulsion Laboratory, Pasadena, CA, p 21-30.

Technology Research Association of Resources Remote Sensing system, 1986, RRSS News, n.2, p 1 (in Japanese).

Yamaguchi, Y., 1987, Possible techniques for lithologic discrimination using the short-wavelength-infrared bands of the Japanese ERS-1. Remote Sensing of Environment, v.23, p 117-129.

Yamaguchi, Y., 1988, Spectral indices for vegetation and rock type discrimination using the optical sensor of the Japanese ERS-1. In Proc. Sixth Thematic Conf. on Remote Sensing for Exploration Geology, Environmental Research Institute of Michigan, Ann Arbor, MI, in press.

Table 1. Bandpasses of the Optical Sensor of the ERS-1

Band	Bandcenter (nm)	Bandwidth	(nm)		
1	560	80			
2	660	60			
3	810	100	stereo		
4	810	100	stereo		
5	1650	110			
6	2060	110			
7	2190	120			
8	2340	130			

Table 2. Shape and Size of the Irises in the Radiometer

Iris no.	shape	size(mm)	FOV	
1	square	8 x 8	4.6	
2	square	4 x 4	2.3°	
3	square	2 x 2	1.15°	
4	circle	ø 1.5	0.86°	
5	rectangle	1.5 x 8	$0.86 \times 4.6^{\circ}$	
6	(closed)	-	-	

Table 3. Comparison of the responses to kaolinite powder whose reflectance spectrum is shown in Figure 6. Notice that these measurement results coincide well each other. (a) Measurement results by the new field radiometer. An average of ten measurements. (b) Hypothetical responses convolved from the reflectance data obtained by the high-resolution spectroradiometer. An average of four spectra.

	Band 1	Band 2	Band 3	Band 5	Band 6	Band 7	Band 8
(a)	79.99	86.00	86.78	89.39	79.92	54.34	54.59
(p)	82.27	88.02	91.60	95.03	83.00	54.04	56.10

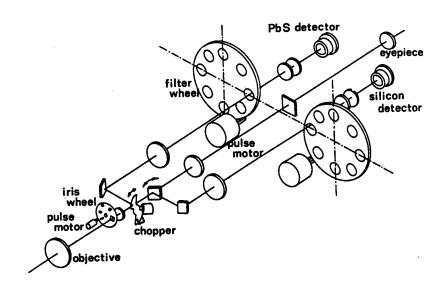


Figure 2. The optical system in the optical head of the radiometer. Notice two filter wheels and the only one aperture for observation.

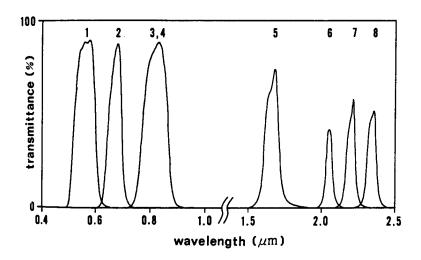


Figure 3. Transmittance curves of the filters installed.

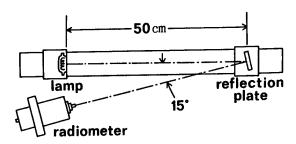


Figure 5. The arrangement for calibration of the radiometer using the optical bench.

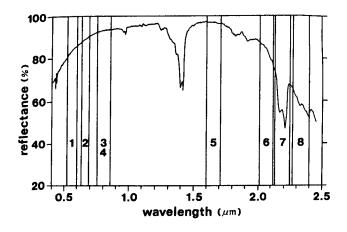


Figure 6. A reflectance spectrum of kaolinite powder obtained by a high-resolution spectroradiometer and the bandpasses of the ERS-1 shown in Table 1.

/09599

Application of Aerial Side-Looking Radar Imagery in China

43070006g Kyoto Selections from INTERNATIONAL ARCHIVES OF PHOTOGRAMMETRY AND REMOTE SENSING in English Vol 27, 1988 pp 728-736

[Article by Yang Pinghe and Wang Lianke, China Aviation Remote Sensing Corporation, P. O. Box 9221, Beijing, The People's Republic of China]

[Excerpts] China made a relatively late start to employ microwave remote sensing technique and has by now only achieved preliminary results. The following is a presentation of the application of the side-looking radar imagery in China.

The Institute of Electronics of the Chinese Academy of Sciences and Shanghai Jiaotong University are the major institutions in China engaged in developing side-looking radar. In 1980, the Institute of Electronics of the Chinese Academy of Sciences conducted an imaging flight-test of its own-developed synthetic aperture side-looking radar (x-band), covering an area of 2,000 square kilometers, and obtained fairly clear terrain target imagery of the test area, with a scale factor being 1:150,000 and system resolution being 15m.

A real aperture side-looking radar system (Ka-band) developed by Shanghai Jiaotong University underwent a flight-test over Hangzhou Gulf in March 1987 and was used in the comprehensive remote sensing flights for flood prevention and disaster fighting over the Yongding River acrossing Beijing and Tianjin in July and August of the same year. During the several dozens of successful sorties, both the airborne display and the display of the ground reception system showed clear imagery and proved to be an effective means for real-time monitoring in struggle against flood in China.

The Ka-band multipolarized real aperture side-looking radar jointly developed by East China Institute of Chemical Technology, Sheng Mei Radio Factory and Dalian Surface Vessel Institute was employed in microwave remote sensing surveys of the distribution of water-clogging plants first in a region of Taiyuan, Shanxi in January 1986 and then in Nansi Lake and the mid-reaches of the main stream of Huaihe River in

Anhui in August 1987. It was also used in a side-looking radar remote sensing survey over the multi-metallogenic provinces in Tongling, Anqing, and Luzhong. Consequently, an area of 5,000 square kilometers was covered and HH polarized radar imagery of the above regions were obtained, with azimuth resolution being less than 20m and range resolution being less than 15m.

The 25th Institute of the Ministry of Astronautic Industry has developed a quasi-coherent SAR and RAR dual-modular imaging radar and carried out a number of successful flight-tests over Jinxi, Liaoning, in September, 1986.

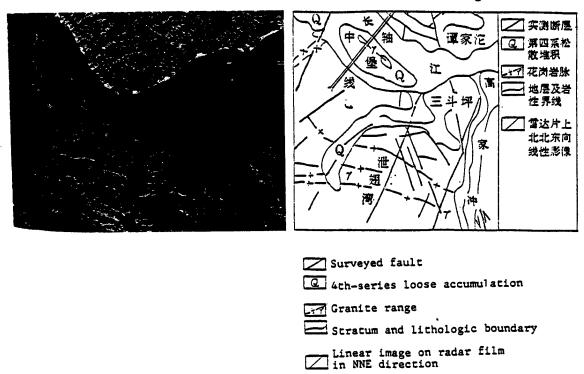
China Aviation Remote Sensing Services Corporation introduced, in 1984, an X-band earth resources side-looking radar imaging system, thus enabling China's microwave remote sensing technique to enter a stage of practical employment. Since then, broad areas have been surveyed and mapped for the respective remote sensing or research institutions of Hunan Geologic Branch, the Ministry of Geology and Mineral Resources, the State Seismological Bureau, the Ministry of Water Resources and Electric Power, the Ministry of Forestry, the Ministry of Coal Industry, etc., and satisfactory results have been achieved.

- 1. Application in Geologic Survey
- A. Distinct Structure Interpretation Result

To meet the construction needs of the Three Gorges Project, the Remote Sensing Centre of the Ministry of Geology and Mineral Resources acquired, in January 1985, from China Aviation Remote Sensing Services Corporation, side-looking airborne radar imagery covering 20,000 square kilometers from Wanxian County to Yichang City with a scale factor of 1:100,000. The said imagery, with clear images and abundant information, turned out to be of excellent quality, particularly in respect of linear structures. Many new discoveries were made through comparing the information recorded in original documents with the results obtained from the interpretation of linear structures, rock avalanche, land-slip and mud-rock flow and the estimation of flooded areas and economic losses.

Side-Looking Radar Imagery of San Dou Ping

A Graph Based on Geologic Interpretation of Side-Looking Radar Imagery of San Dou Ping



There are 46 faults of more than 20km each in length interpreted from the imagery, of which only 13 existed on old geologic maps and the other 33 are newly discovered. This result sufficiently demonstrates the significant practical value of microwave remote sensing technique to geologic researches.

The newly discovered faults have drawn considerable attention of the specialists and authoritative departments concerned as they provide sounder scientific basis for the biggest hydraulic engineering site selection and dam foundation stability evaluation.

After performing geologic interpretation of the x-band aerial sidelooking radar imagery of Bashang grassland North of the Great Wall, we have come to know that side-looking radar imagery, due to its directional effect, is sensitive to minor terrene fluctuations and capable of giving prominence to fine terrene features. Furthermore, thanks to its continuous coverage of large areas, the radar imagery may accumulate the fine terrain differences over a long distance, thereby enhancing linear appearance. This macroscopic and comprehensive display, in conjunction with side-looking technique, enhances the appearances of the geologic features that cannot be easily seen on visible light photographs and helps interpret linear structures. The systematic remote sensing interpretation results exhibit that the linear structure density shown on the structure maps acquired from side-looking radar imagery is obviously higher than that on satellite and aerial photographs.

B. Feasible, Whereas Difficult Lithological Interpretation

The variation of imagery colour tones is the indicating feature for distinguishing rocks. As far as visible light photography band is concerned, the variations of the colour tones (or colours) on the photographs record mainly the difference in spectral reflectance of ground objects, reflect the chemical properties of geologic bodies and can help distinguish the rocks of different chemical properties and rock alteration. Whereas the variations of colour tones on side-looking radar imagery primarily reflect the differences in such physical features as ground location and roughness of geologic bodies. differences are often influenced by soils, vegetations, humanity and other factors, thus causing some difficulties to lithological interpretation by using side-looking radar imagery. Therefore, it is hard to evaluate the geologic sense of the colour tone differences found on side-looking radar imagery. Nevertheless, some rocks can still be distinguished with the help of the characteristic that the side-looking radar imagery gives prominence to fine terrene features. We have distinguished metamorphic rocks and volcanic rock in the Bashang grassland by referring to the clear metamorphic lineations in N-W direction and the obvious fine lamination patterns.

Hunan Remote Sensing Centre has made a step forward in employing sidelooking radar imagery to revise and compile geologic maps. They have established geologic lithological interpretation signs in Chenzhou Region by means of X-band side-looking radar imagery.

The Aerosurveying Remote Sensing Corporation of the Ministry of Coal Industry employs side-looking radar imagery of the east slope of the Luliang Mountain Range in lithological interpretation and has made the following summary: The important question of lithological interpretation is to investigate the surface roughness of rocks of different types. By comparing land survey result with imagery to determine the relative elevation of the surface roughness of various rocks and their grey level on imagery, as well as referring to the macro-geomorphic features, hydrographic features, pattern structure, lamination, etc., of various rocks, many kinds of geologic bodies can be interpreted. For example, they have, in the above-mentioned area, distinguished 9 kinds of geologic bodies, namely, granite of the Archean Era, alkaline complex of the Mesozoic Era, dyke rocks, metamorphic rocks, C-P coal-series stratum, detrital rock series of marinecontinental facies, P2-T continental facies red fragmental rocks, Q3 loess and Q4 loose accumulation.

C. Application in Mineral Deposit Research

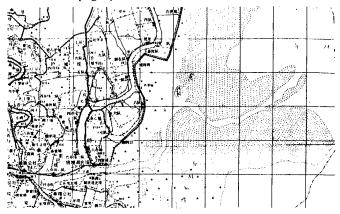
The Aerosurveying Remote Sensing Corporation of the Ministry of Coal Industry has conducted exploratory application research using sidelooking radar imagery (covering approximately 2,000 square kilometers) of Taiyuan West Mountain Coal Field. The interpretation and analysis of the radar imagery has made detailed research conclusions available now for optimum pitch angle selection, survey direction selection, geologic interpretation signs, fault structure interpretation result, coal distribution images, etc. They have read out from the radar imagery of the West Mountain region more than 100 linear structures, the majority of which correspond to the fault structures already known. With the fault structures of different grades clearly shown on imagery in a broad sense, the law of distribution of such mineral deposits as coal field can be clearly observed. At present, MSS visible light photographs and thermal infrared imagery cannot do so well as the radar imagery. big fault at Xishe, about 80km in length, is Class 1 structure controlling the west boundary of the coal field. On the imagery, it is shown as a banded image of 1km in width. After interpreting the fault structures, we have come to the conclusion that the radar imagery containing broad information and having high resolution is more suitable for regional structure research such as coal fields.

Hunan Remote Sensing Centre has gained much in utilizing side-looking radar imagery of Chenzhou area for prospecting and set contours of four long-term minerogenetic provinces. After performing geologic interpretation of side-looking radar imagery and satellite imagery, they have, based on the remote sensing imagery and the geologic and exploration results, made comprehensive analysis and worked out the contours of the four long-term minerogenetic provinces in Chenzhou-Guilin region, namely, Huangzujiang, Yazhixian, Changchengling and Litian.

2. Application in Map Revision and Compilation

The Surveying and Mapping Team of Hunan Geologic and Mineral Branch, by using 1:100,000 side-looking radar imagery, has updated the existing 1:200,000 topographical map and hydrographic map and compiled "Map of Dongting Lake" displaying the present water area of the lake, current names of places and transportation network. On the basis of this map, they have added hydraulic engineering key elements and compiled "Hydraulic Engineering Map of Dongting Lake" which serves as the basic map for comprehensive tackling of the lake, flood prevention, dyke building, cropland arrangement, land utilization, course control and hydraulic engineering planning, and plays an important role for the hydraulic construction and land management in Hunan Province.

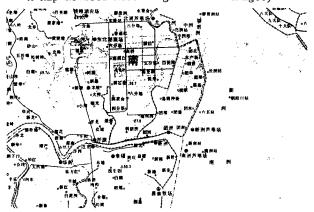
Topographical Map Before Revision



Side-Looking Radar Imagery



A Map Revised According to Radar Imagery



The above examples have proved that it is greatly advantageous to use side-looking radar imagery to revise and compile maps for cloudprevailent plains and lakes. However, it is possible to employ sidelooking radar imagery for revising and compiling maps of hilly land and mountain areas? A few remote sensing surveying and mapping institutions in China have the following point of view: Such features as upside down configuration, overlapping and shadowing of side-looking radar imagery impose certain difficulties upon overhead imaging. Therefore, at present, side-looking radar imagery must be employed in conjunction with other means (e.g., visible light photographs). For revising and compiling maps of gently undulated land, topographic information acquired lately and the newly obtained ground objects' information can be used. However, it is now still difficult to use side-looking radar imagery to revise and compile maps of mountain areas and more efforts ought to be made to seek for the possibility of using computer to process the digitized radar imagery converted from images to digital data so as to increase the geometric precision of imagery required by map compilation.

3. Application in Flood Control and Disaster Relief

Aerial microwave remote sensing made positive contributions in flood control and disaster relief work in Liaoning, China.

In August, 1985, flood occurred in Liaoning Province, the Liaohe River overflowed its banks and its dykes were breached in many places. Panjin City, Shuguang oil field and many other important factories in that region were threatened by the flood. In order to know the condition of the disaster at the lower reaches of the river, the National Flood Control Headquarters issued an instruction of conducting microwave surveying and mapping over the area. Upon receiving the order on August 28, China Aviation Remote Sensing Services Corp. started to image the flooded area of 110,000 square kilometers using side-looking airborne radar, and then performed ground imagery processing, mosaics, quick interpretation and estimation of essentials, etc. It took them only 22 hours to complete all of the jobs. As a result, they supplied 1:100,000 and 1:50,000 radar images, flooded area graphs and other valuable data. The timely and accurate supply of the flood distribution imagery by China Aviation Remote Sensing Services Corporation enabled the National Flood Control Headquarters to take flood diversion and rescuing measures at right moment. Consequently, the raid of 4th flood peak was effectively withstood and economic losses greatly reduced. For this, China Aviation Remote Sensing Services Corp. won high praise from governmental officials concerned.

The Remote Sensing Centre of the Ministry of Water Resources and Electric Power carried out visual interpretation and used computer for auto-identification of the flood condition in Liaohe River-Panjin region in accordance with the side-looking radar imagery, and worked out

1:25,000 graphs and pseudo colour radar imagery showing the flood condition in the region.

This was the first time for the side-looking airborne radar to be used in China to investigate flood condition and to direct flood control and disaster relief work. The results have shown the following evident characteristics:

- (1) The radar is highly mobile and can quickly produce microwave imagery and timely provide flooding information.
- (2) Radar imagery has higher resolution, contains more information and can supply the details required in struggle against various disasters.
- (3) Microwave imagery clearly indicates water-land boundaries and is conducive to investigating the scope of flooded area.
- (4) Side-looking radar imagery of plain areas has very small geometric distortion and needs not be geometrically calibrated when in use, thus saving a lot of time for flood condition investigation and reducing workload.

The following is a piece of side-looking radar imagery of the flood condition in Panjin area processed by computer. [omitted]

4. Application in Forestry Investigation and Other Fields

In the year of 1985, the Institute of Forestry Investigation and Planning of the Ministry of Forestry conducted research work in Shaxian County, Fujian Province, on the response of soils and forests to microwave imagery using X-band side-looking radar imagery. The detection interpretation and land survey offered the following results:

It is possible to perform visual interpretation of soil types on 1:50,000 radar imagery and there exist potentialities in distinction of forest types and investigation of forest resources. The following are a few pieces of information gathered from practical research:

- (1) The accuracy of soil interpretation can reach 90 percent and above;
- (2) The accuracy of Grade 3 forest interpretation can reach 85 percent and above;
- (3) It is not difficult to locate and draw the contours of forest boundaries and compartment network;
- (4) It is fruitful to locate contours of small compartments on radar imagery.

China has large areas of virgin forests and there is a good prospect of employing microwave remote sensing technique to investigate forest resources.

The Research Institute of Chinese National Seismological Bureau has made seismological and resources development researches on Hainan Island and Leizhou Peninsula using side-looking radar imagery.

China State Surveys and Mapping Branch and the Hydraulic Research Team of the Ministry of Geology and Mineral Resources have conducted studies on map measurement and water location respectively using side-looking radar imagery.

Microwave remote sensing is an informational technique having broad prospects and has manifested its incomparable strength firstly in geology and flood monitoring. Should it be used in conjunction with visible light remote sensing and infrared remote sensing, achievements will definitely be made in many more fields. Remote sensing is a new technique which is under comprehensive development all over the world. Only through further strengthening international cooperation and research, can the superiority of remote sensing in quick supply, macroscopic display and abundant accumulation of information be exhibited and enhanced. We wish to join hands with friends the world over to work for developing the remote sensing technique and advancing the worldwide progress of sciences.

/09599 END